Development and Implementation of Multi-User Detection (MUD) Strategies for Shallow Water Acoustic Network (SWAN) Telemetry

By

Hong Kwang, Yeo

A Thesis Submitted for the Degree of Doctor of Philosophy in the

Faculty of Engineering, University of Newcastle upon Tyne

November, 2001

Department of Electrical and
Electronic Engineering
The University of Newcastle
Upon Tyne
Merz Court
Newcastle Upon Tyne
NE1 7RU
United Kingdom

Abstract

This thesis describes the development and implementation multi-user detection strategies for phase coherent Shallow Water Acoustic Network (SWAN) communication. Sea-trial experiments were carried out in the North Sea, 8 km near Noordwijk, Netherlands.

The present demand for shallow water acoustic networks (SWAN) is driven by the need for environmental and other data acquisition from fixed and mobile measuring platforms located in the continental sea. Such networks require new, reliable and bandwidth-efficient data communication systems, which maximises the use of the underwater channel for simultaneous transmissions. However, horizontal-link digital acoustic communication is limited by both environmental and system factors.

Underwater acoustic channels are characterised by multipath propagation, which is due to the signal reflection from the sea surface and the sea bottom. Due to wave motion, the multipath components undergo time-varying propagation delays, which result in signal fading and phase fluctuations in the received signal. Another problem with horizontal-link communication is that of the Doppler effect that arises as a result of relative motion between the transmitter and receiver. Receivers employing array processing with adaptive decision feedback equalisation schemes have been shown to be effective to tackle these problems. However, in a phase coherent SWAN, the base-station receiver has the added task of mitigating the effect of co-channel interference from other users in the network. Although various multiple access protocols can be implemented to help ease the co-channel interferences, they usually utilises a significant amount of the limited channel resources.

The constraints of SWAN communication lead to the need for multi-user detection strategies. The thesis proposes a number of novel multi-user detection strategies and presents the software architecture and practical implementation of these phase coherent multi-user receiver structures.

Both simulation data and experimental real data were used to compare the performances of the proposed receiver structures. Successful implementation of the receiver system was demonstrated by field trial results for ranges up to 5km.

Table of Contents

List of Publications Arising From This Work

i.) Conference Papers

1. H. K. Yeo, B. S. Sharif, A. E. Adams and O. R. Hinton, "Analysis of a Multi-Element Multi-User receiver for a Shallow Water Acoustic Network (SWAN) based on Recursive Successive Interference Cancellation (RSIC) Technique," *IEEE Proceedings Ocean Conference*, vol. 3, pg. 1537-1541, September 1999.

2. H. K. Yeo, B. S. Sharif, A. E. Adams and O. R. Hinton, "Multi-user Detection for a Time-Variant Multipath Environment," *IEEE Proceedings of the 2000 International Symposium for Underwater Technology*, pg. 399-404, May 2000.

3. H. K. Yeo, B. S. Sharif, A. E. Adams and O. R. Hinton, "Comparison of adaptive algorithms performances for a multistage multi-user receiver structure," *IEEE Ocean Proceedings 2000*, vol. 3, pg. 2019-2023, September 2000.

ii.) Journal Papers

4. H. K. Yeo, B. S. Sharif, A. E. Adams and O. R. Hinton, "An improved RLS algorithm for time-variant underwater acoustic communications," *IEE Electronics Letter*, vol. 36, No. 2, pg. 191-192, 20th January 2000.

5. H. K. Yeo, B. S. Sharif, A. E. Adams and O. R. Hinton, "Performances of Multi-Element Multi-User detection strategies in Shallow Water Acoustic Network (SWAN)", *IEEE Journal of Ocean Engineering*, vol. 26, Issue 4, pg. 604-611, October 2001.

6. H. K. Yeo, B. S. Sharif, A. E. Adams and O. R. Hinton, "Implementation of Multi-user Detection Strategies for Coherent Underwater Acoustic Communication", *IEEE Journal of Ocean Engineering*, vol. 27, Issue 1, pg. 17-27, January 2002.

Acknowledgements

I would like to acknowledge the encouragement and support from Prof. B. S. Sharif, Mr. A. E. Adams and Professor O. R. Hinton during the period of this research work.

Thanks also to the research partners, Dr. Alain Plasiant and Dr. Xavier Cristol from Thomson Marconi System (France); Otello Gasparini, Marco V. A. and Claudio A. (former) from DUNE (Italy), Machteld G. M. De Kroon, Fritz V. D. Knapp from TNO (Netherlands), Michel Tinga (Former), Sonja (Former) and Stephen Fischer from Rijkswaterstaat (Netherlands) for their contributions toward the success of the research project.

Special thanks to the funding support from the European Community MAST III project for the research project.

I would like to thank my parents and family members for their encouragement and support, both during the course of this work and in life, without which I will not be what I am today.

This work is dedicated to my wonderful and beautiful wife, Qian Geng, who has stuck with me through time of difficulties and despair, not to mention times of joy and laughter. Her endless encouragement had given me the strength to persevere on.

Last but not least to Him, for "... I am what I am by the grace of the Lord."

"High in the mountains a spring pours its life into a tiny stream which begins a whispering journey. It is joined to another stream, which soon becomes a part of an even stronger current. Carried and carrying, supported and supporting; the growing, travelling and mingling continue until finally the stream, swept joyfully along with its brothers and sisters goes tumbling, rushing, racing and roaring into the Great Body to fulfil its destiny and to become – fulfilled..."

– Author unknown

List of Symbols and Abbreviations

υ	Target radial speed away or towards the receiver
ADC	Analogue to Digital Converter
AM	Amplitude modulation
bps	Bits per second
B_w	Bandwidth
BPSK	Binary Phase Shift Keying
c	Velocity of sound in water
CCI	Co-Channel Interference
cm	Centimetre
dB / km	Decibel Per Kilometre
DC	Direct Current
DCT	Discrete Cosine Transform
DQC	Data Quality Check
DPCM	Direct Pulse Code Modulation
DS – SS	Direct Sequence Spread Spectrum
ELF	Extremely Low Frequency
EM	Electromagnetic Wave
f_c	Transmitted centre frequency
f_s	Transmission sampling rate
FDCT	Forward Discrete Cosine Transform
FDMA	Frequency Division Multiple Access
FIR	Finite-duration Impulse Response
FSK	Frequency Shift Keying
GB	Giga bytes
GUI	Graphical User Interface
HOS	Higher Order Statistics
Hz	Hertz
ICU	Interference Cancellation Unit
ICM	Interference Cancellation Modules

IDCT	Inverse Discrete Cosine Transform
IIR	Infinite-duration Impulse Response
ISI	Inter Symbol Interference
JPEG	Joint Photographic Experts Group
kbps	Kilo Bits Per Second
km	Kilometre
kHz	Kilohertz
LAN	Local Area Network
LFM	Linear Frequency Modulation
m	Meter
MAI	Multiple Access Interference
ML	Maximum Length
MLSR	Maximum Length Sequence Register
MB	Mega bytes
MEMU	Multi-Element Multi-User
MESU	Multi-Element Single-User
M – FSK	Multiple Frequency Shift Keying
MHz	Mega Hertz
min	Minutes
ML	Maximum Likelihood
MMSE	Minimum Mean Square Error
MPN	"MeetPost Noordwijk" – Research and monitoring platform, positioned at 9 km off the coast off Noordwijk, Netherlands
M-PSK	M-ary Phase Shift Keying
MUD	Multi-User Detection
OSI	Open System Interconnection
P_{er}	Packet Error Rate
PLL	Phase Lock Loop
PSK	Phase Shift Keying
PRN	Packet Radio Network
QAM	Quadrature Amplitude Modulation
QPSK	Quadrature Phase Shift Keying
R_c	Coded Data Rate

R_d	Data rate
RF	Radio Frequency
rms	Root Mean Square
Rx	Reception
s	Seconds
SCSI	Small Computer System Interface
sps	Symbols Per Second
SUD	Single User Detection
TDMA	Time Division Multiple Access
Tx	Transmitter or transmission
Tx1	Transmitter 1
Tx2	Transmitter 2
T_o	Frame total duration
T_g	Guard time between frames
λ	Wavelength

NB: Notations with [] signifies cross-references and notations with () signifies equations.

List of Figures

List of Tables

List of Appendix Figures

List of Appendix Tables

Chapter 1 Introduction

1.1 Multi Access Channel

The idea of several transmitters sending information simultaneously via a communication channel dates back to Thomas A. Edison in 1873, with the invention of the duplex [1.1]. Simultaneous transmission of two telegraphic messages travelling in the same direction through the same wire was enabled with this revolutionary system. The messages were encoded by changing the polarity of one, while a change of absolute value was performed for the other.

In modern day context, multiple access communication exists in numerous situations. Mobile telephones transmitting to a base station, local area networks, packet-radio networks are just few of the examples of multiple access communication. The common feature in these communications is the use of a common channel through which transmissions take place. The receiver usually observes a superposition of signals sent by the active transmitters, as shown in Figure 1-1.

The translation of the concept of multiple access communication to underwater communications, employing sound propagation, is an ongoing active research area that is an immense task beset by many problems [1.2].

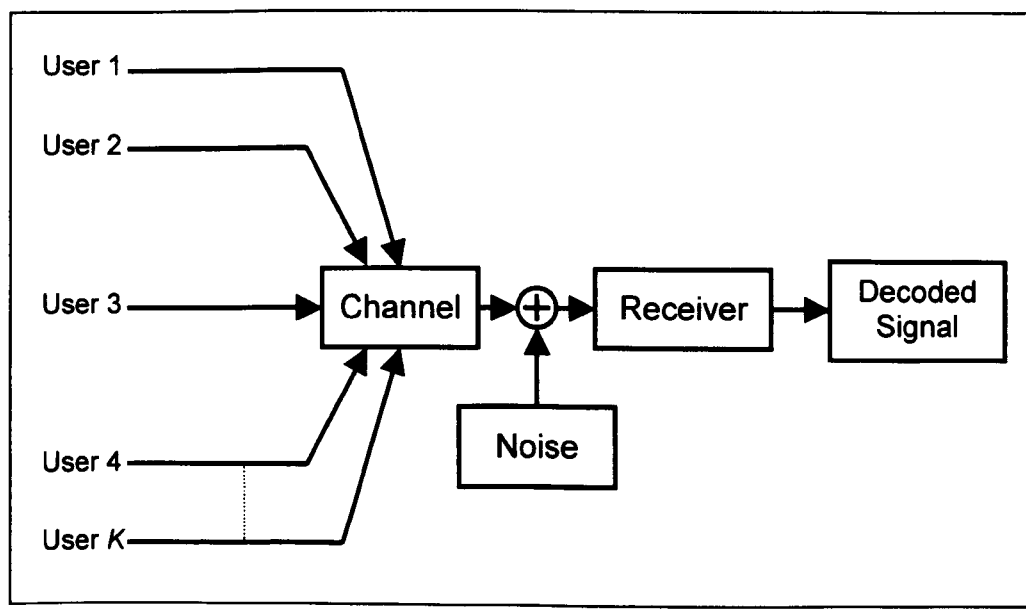

Figure 1-1 Multi access communication model

1.2 Background of Underwater Acoustic Communication

Sound waves are the principal means for long-distance wireless communication in the ocean. Electromagnetic (EM) waves, carried by wires or fibres on the ocean bottom, offer high reliability and useful bandwidth. However in wireless mode, EM waves do not propagate over long distances underwater, except in the Extremely Low Frequency (ELF).

The history of underwater sound wave propagation can be traced back several centuries to the fundamental discoveries and accomplishments of scientists in many diverse fields. Towards the end of the 15th century, Leonardo da Vinci wrote [1.4]:

"*If you cause your ship to stop, and place the head of a long tube in the water and place the outer extremity to your ears, you will hear ships at a great distance from you*".

In 1687, Sir Isaac Newton published the first treatment of the theory of sound, where he was able to relate the propagation of sound in fluids to measurable physical quantities such as density and elasticity [1.5]. In 1827, a Swiss physicist, Daniel Colladon, and a French mathematician, Charles Sturm, measured the speed of sound in water at Lake Geneva in Switzerland. Although they only used a simple light flash, coupled with the sounding of an underwater bell, to obtain the measurement, the value obtained was close to the accepted value today [1.5]. Lord Rayleigh established the basis for acoustic theory in 1877 [1.6]. His work covered the generation, propagation, and reception of sound in a rigorous manner. The first practical application of underwater sound came into use in the late 19th century. Ships employing a submarine bell and by timing the interval between the sound of the bell and a foghorn, sent off simultaneously in parallel, a second ship could then determine its position from the ship where the foghorn and bell were installed.

In the 20th century, there was considerable progress in improving underwater acoustic communication both for military and civilian purposes. An extensive historical review of the development of practical acoustic applications for both World Wars is well documented in [1.7]-[1.8]. Coverage of underwater acoustic communication prior to 1967 is recorded in [1.9]. A comprehensive review of acoustic telemetry prior to 1983 is referenced in [1.10].

1.3 Recent Advances in Underwater Acoustic Communication

1.3.1 Telemetry Systems

Recent techniques that have advanced the field of underwater acoustic communication are highlighted in this section. One pioneer for an underwater communication system, which did not employ diversity techniques was the Gertrude system [1.11]. This system was used for communication with submarines. It used analogue amplitude modulation (AM), and with careful placement of the hydrophones, compensation for multipath propagation from distinct angles of arrival was achieved. The single-sideband Gertrude system is still in operation for diver communication systems [1.12]. These perform well for vertical or ultra-short horizontal links environments, with negligible multipath propagation. The development of digital systems, not employing diversity techniques, was reported as early as 1960 [1.13]-[1.14]. The Benthic digital system described in [1.15] allows 4800 bps transmission. Since no diversity technique was adopted, data transmission was performed vertically through the water column in order to minimise multipath propagation effects.

The above systems were not really suitable for horizontal shallow water channels which exhibits severely delay spread due to multipath propagation. Alternative systems that were based on noncoherent digital modulation, Frequency Shift Keying (FSK), had been traditionally accepted as the only alternative for shallow water channels which exhibit rapid phase variation. Although noncoherent detection eliminates the need for carrier phase tracking, it does not solve the problem of multipath propagation. In order to combat the problem of inter-symbol interference (ISI), the noncoherent FSK system had to employ guard times, which were inserted between each successive transmitted data, to ensure that the reverberation effects were kept minimal at the receiver. Noncoherent receiver systems are usually classified by their explicit diversity technique, where explicit diversity could be characterised by intentionally transmitting the data through distinct subchannels in time, frequency, geometric space, or waveform space. Due to the independence of the subchannel fading processes, the channel error probability decreases exponentially in the number of transmissions, or diversity order [1.16]. The digital acoustic telemetry system described in [1.17] was one communication link that used explicit diversity technique. This system was designed to operate in frequency-selective multipath fading environments having extreme phase

instability. Coded data using multiple FSK (M-FSK) was adopted for data transmissions operating in the 45-55 kHz band. A 30 kHz header tone was used for coarse, word synchronisation and a continuous 60 kHz pilot tone was used for Doppler tracking. In one of the implementations of a digital acoustic telemetry system, a 400 bps digital coded data stream was transmitted with an (8,4) Hamming code. The Hamming codeword elements were selected from eight tones spanning at 2 kHz per each baud period. The receiver then performed an estimation of the Doppler shift using a phase-locked loop (PLL) whose output was used to adapt the down-conversion nominal carrier, which was at 50 kHz. The hopping pattern was then tracked in order to determine the frequency span for the current active word and inverse Fast Fourier Transform (FFT) was used to extract the squared magnitudes of the received gated tones. Retrieval of the 8-bit code word was achieved with non-coherent soft decision detection. Apart from this system, several commercial systems following the digital acoustic telemetry format that allowed reliable transmission through severe reverberant multipath channels with low system complexity were reported in [1.18]. Provided the PLL was successful in tracking the pilot tone, such systems could tolerate Doppler shift for up to 600 Hz. The Doppler compensation performance deteriorated to 20-25 Hz when the pilot PLL lost lock on the received signal. Another noncoherent M-FSK telemetry system operating in the 20-30 kHz band with maximum throughput of 5kbps was reported in [1.19]. Here the frequency band was divided into 16 subbands, in each of these subbands a 4-FSK data signal was transmitted. The system reported successful implementation for telemetry over a 4 km horizontal shallow water channel and a 3 km deep ocean vertical path. In the case of a 700 m shallow water path, the error probabilities for the transmitted uncoded data were recorded in the order of $10^{-2} - 10^{-3}$.

With the aim of increasing the usage of the bandwidth-limited underwater channel, research focus shifted from noncoherent modulation technique to phase-coherent techniques such as Phase Shift-Keying (PSK) and Quadrature Amplitude Modulation (QAM). These methods encode data information into the phase as well as the amplitude of the transmitted signal.

One of the earliest phase-coherent systems for underwater acoustic communication was reported in [1.20] where ISI was compensated by a coherent echo cancellation technique. Adaptive equalisation adopted for high-speed underwater acoustic communication was reported in the early 1990s [1.21]. In a short-range communication

link of ~60 m the system reported in [1.22] had a throughput of 500 kbps, with an operating carrier frequency of 1 Mhz. The main application of this system was for undersea robotic maintenance of submerged platforms. A 16-QAM data format was used with an adaptive equaliser adopting the Least Mean Square (LMS) algorithm. The error probability was in the range of 10^{-7} which was measured over the averaged acquired data packets. The vertical link image transmission system developed by [1.23] used a phase non-coherent differential PSK (DPSK), with Least Mean Square (LMS) adaptive equalisation, operating at 20 kHz carrier frequency with a data throughput of 16 kbps for surface transmission over 6.5 km. The error probability achieved from field trials was in the range of 10^{-4} with a Signal-to-Noise Ratio (SNR) of 15 dB.

A network telemetry system for shallow water medium ranges was developed in [1.24], where direct-sequence spread spectrum (DS-SS) technique was adopted to aid rejection of multipath propagation effects. This system had a data throughput of 600 bps, a spreading bandwidth of 10 kHz, with a 30 kHz carrier frequency band. Another development in network telemetry system was reported in [1.25], using a Quadrature PSK (QPSK) modulation data format with data throughput of 5 kbps. This system was configured for a six-node network operating with a 15 kHz frequency band. The problem of ISI was tackled using a decision feedback equaliser using the Recursive Least Square (RLS) algorithm.

1.3.2 Signal Processing Methods for Multipath and Doppler Compensation

To achieve high data rate transmission, telemetry systems based on phase-coherent data signalling method had to deal with the ISI problem that result from multipath propagation effect. One of the earliest records of pure phase-coherent data transmission with ISI compensation was reported in [1.26]. The signal processing method was based on joint synchronisation and a fractionally spaced decision-feedback equalisation technique adopting the RLS adaptive algorithm. This system was demonstrated through field tests to exhibit a data throughput of 2 kbps over long range channel, 20 km, and 40 kbps in medium range channel, 5 km. Array processing was adopted in [1.27] to eliminate or reduce multipath propagation. This approach seeks the use of an array of transmitters to excite a single path of propagation. Rejection of ISI was dealt with by careful positioning of a long receiving array. The channel medium was deemed rapidly

changing for an adaptive equaliser to perform tracking in order to achieve the minimum point of the error performance surface. The system of [1.27] employed a long array of receiver elements to compensate for possible errors. Both Binary and Quaternary DPSK data signal were used, with data throughput of 10 kbps and 20 kbps respectively. Error probability was recorded to be in the range of $10^{-2} - 10^{-3}$. It was concluded that this type of configuration was found to be operationally more effective in short range communication.

An adaptive beamforming method used as a means of ISI rejection was reported in [1.28]-[1.29]. The adaptive beamformer uses a decision-feedback equaliser operating with the LMS algorithm to steer towards the signal of interest, while nulling other interfering signals. This system was tested in shallow water with a data throughput of 10 kbps with error probability in the range of 10^{-2} without equalisation and 10^{-3} with adaptive equalisation. Recently, a Doppler compensation scheme adopting block-based interpolation with decision-feedback equalisation was proposed in [1.30]. The Doppler compensation was obtained by measuring the Doppler shift between two a priori known Linear Frequency Modulated (LFM) 'chirp' signals in the received data packet. An interpolator structure was then used to perform a sampling rate conversion of the input samples in order to compensate for the Doppler shift. With a data throughput of 10 kbps, an error probability was reported to be in the range of $10^{-3} - 10^{-4}$. However, this block-based system assumed that Doppler shift variations are relatively small, under some circumstances this assumption does not stand. An alternative, decision directed Maximum Likelihood (ML) cost function used to estimate Doppler shift has been proposed [1.31]. This system offers a real-time signal processing approach compared to the block based processing as the received signal can be processed immediately whereas the block-based system requires a buffer to hold the received data between each LFM signal prior to Doppler compensation.

1.3.3 Signal Processing Methods for Multiuser Interference Cancellation

Network communication research had sparked increased interest in recent years due to the need for environmental data acquisition from fixed and mobile measuring platforms located in the continental sea, as shown in Figure 1-2. Apart from resolving the problem of ISI arising from multipath propagation, Doppler shifts, environmental noise etc, the

receiver in such scenarios has the additional task of mitigating the effects of co-channel interference from other users in the network system. Therefore multiuser communication techniques [1.32] have to be considered for such underwater acoustic communication applications. Although Frequency Division Multiple Access (FDMA) or Time Division Multiple Access (TDMA) may be consider for underwater acoustic communication in such circumstances, both these techniques exhibits their own problems. In a bandwidth-limited channel, the network users are usually confined to sharing the same frequency band for data signalling. Therefore, the FDMA technique, which operates in orthogonal spectrum bands, will be wasting the already limited channel resources. TDMA technique is subjected to the problem of efficient time-slot allocation, which arises due to the long propagation delay. One possible solution to multi-user underwater network communication is to adopt Code Division Multiple Access (CDMA), where multiple users are allowed to transmit simultaneously both in frequency and time. However, adopting CDMA technique reduces overall data throughput. One recent multiuser detection technique adopting CDMA was reported in [1.33]. The fundamental principle of this multiuser system was an extension from the system of [1.26], where array processing, joint synchronisation, channel equalisation in the form of decision-feedback equalisation was adopted. Multiuser interference cancellation was performed via feedback filters in a cross over manner.

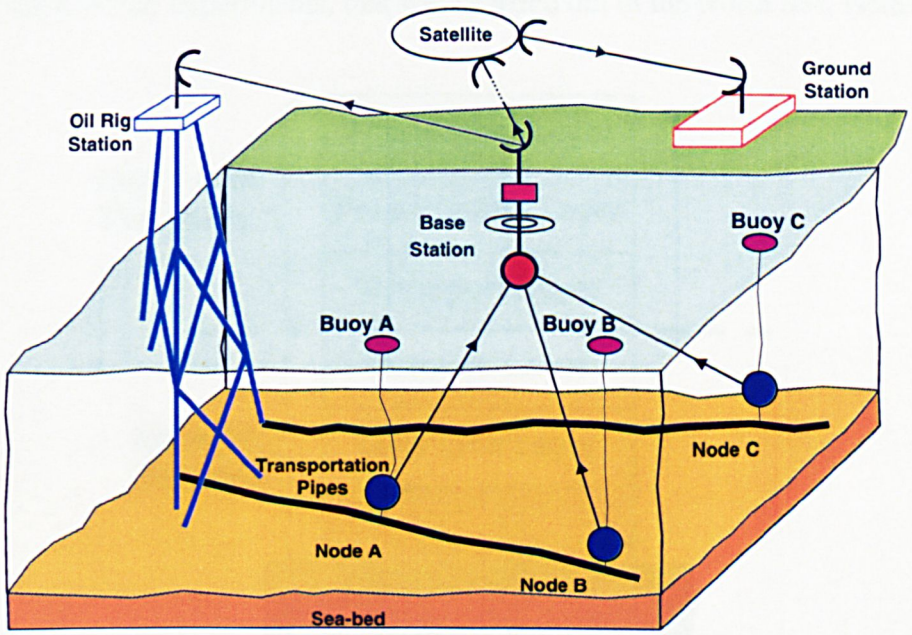

Figure 1-2 An example of shallow water acoustic network communication

1.4 Research project objectives

1.4.1 Scope of Research Project

The primary objective of this research work, Shallow Water Acoustic Network (SWAN), is to advance the understanding of phase coherent communication in shallow water acoustic networks at the physical layer level in the communication hierarchy of the Open System Interconnection (OSI) model, as shown in Figure 1-3. This involves the development and implementation of innovative software based adaptive multi-user receiver systems for achieving signal separation in the presence of co-channel interference (CCI) or multiple access interference (MAI) for horizontal-link network transmission and reception in a time-varying underwater channel medium, as shown in Figure 1-4. Apart from mitigating the effects of MAI, the base station receiver system has also, at the same time to resolve the problems that were highlighted in section 1.3.3. In order to achieve these goals, a study and performance comparison of the adaptive filtering algorithms adopted in the decision-feedback equaliser (DFE) receiver structures were carried out. From the foundation of the adaptive DFE receiver structures, novel methods of phase-coherent multi-user detection strategies were developed which accomplishes the main aim of this research project. The developed multi-user receiver systems were tested with both simulated network communication scenarios and sea-trial experiments, that were carried out in the North Sea, Netherlands.

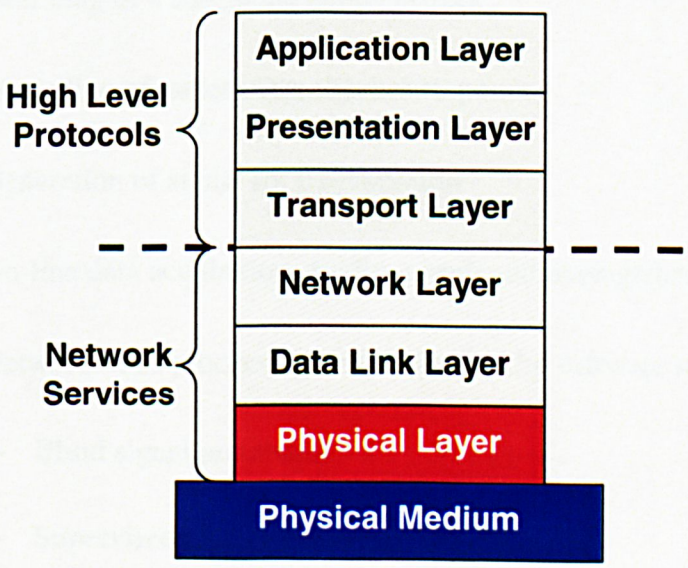

Figure 1-3 Open System Interconnection (OSI) model

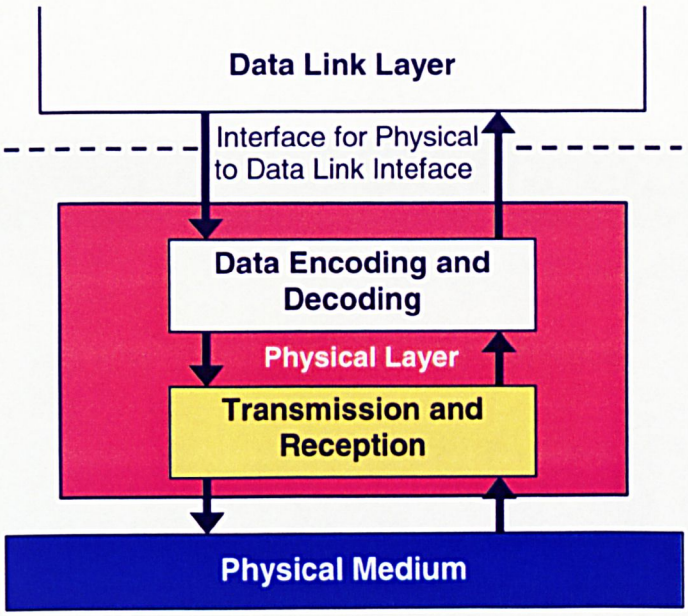

Figure 1-4 Functions of physical layer

1.4.2 Research Project Partnership

Shallow Water Acoustic Network (SWAN) is a collaborated research project between five working group partners, as listed in Table 1-1. Sponsored by the European Community MAST III project – SWAN (MAS3-CT97-0107SWAN), the general structure of the 36 months duration research project concerns:

- Outlining of a communication network
- Modelling of underwater channel response
- Generation of signal for transmission
- On-line data acquisition, quality-check and management from sea-trials
- Network node processing and evaluation by software receiver entailing
  - Blind signal processing,
  - Supervised signal processing
  - Multi User Detection (MUD) strategies

Partners	Country	Project Tasks
Dune Ingegneria dei Sistemi Sri (Project Co-ordinator)	Italy	• General Network Outline • Signal Processing - Blind signal processing - Generation of Transmission signals
Thomson Marconi Sonar	Netherlands	• Underwater channel modelling - Deterministic channel modelling - Stochastic channel modelling
University of Newcastle	United Kingdom	• Signal Processing - Supervised signal processing - Generation of Transmission signals • Multi-user detection strategies
Rijkswatersaat	Netherlands	• Deployment of Experiment • Environmental measurement
TNO Institute of Applied Physics	Netherlands	• Data On-line Acquisition • Data Quality Check • Data Management

Table 1-1 List of working group partners

1.5 Outline of Thesis

Chapter 2 provides a review of underwater communications. Emphasis is placed on the various natural variables, which affects shallow water acoustic communication.

Chapter 3 considers various methods, for data transmission in a band-width limited channel. The chapter discusses the advantages and disadvantages of multiple access techniques and network theory. The second part of the chapter describes the various signal coding techniques for use in the sea-trials. In the last section, a geometrical multipath deterministic channel model was used to study the effects of signal multipath propagation through a shallow water channel. Provided that the channel is slowly changing, the deterministic channel model can provide a good estimation of transmission loss during signal propagation through the shallow water medium.

Chapter 4 presents a treatment of both supervised and blind adaptive algorithms. The use of adaptive filtering algorithms is one of the main driving forces behind successful retrieval of transmitted signals. These algorithms operate by continuously seeking the minimum point of the error-performance in order to assure that optimisation is achieved. However, as the shallow water channel medium is time-variant, the adaptive algorithm has the added task of tracking the minimum point of an error performance surface that is not fixed. In this chapter, several of the well established supervised adaptive algorithms are investigated. An improved version of the RLS algorithm, with an improved rate of convergence and tracking is presented. In the second part of the chapter, blind Higher Order Statistics (HOS) algorithms which belongs to a sub-family of the blind deconvolution algorithms, are investigated [1.34]-[1.35]. Blind algorithms can be viewed as a self-organised learning processes [1.36], self-organised in the sense that the deconvolution is performed in the absence of a training sequence.

The last section of the chapter concentrates on making a comparison of the supervised and blind algorithms by assessing the rate of global convergence and tracking properties of the adaptive algorithms.

Chapter 5 describes the design and development of the multi-user detection strategies for underwater acoustic communications. Adaptive decision feedback equalisation employing array processing provides the basic building block for single user communication. From this foundation, several novel methods of multi-user detection

schemes for multiple access interference cancellation are proposed and developed. The validity of the multi-user receiver structures is tested via simulations for equal and unequal power reception scenarios using the channel model of chapter 3.

Chapter 6 describes the experimental, configuration for the both the first and second sea-trials held in the North Sea, Netherlands. The software design and implementation for the receiver structures is also presented.

Chapter 7 presents the results obtained from the North Sea trials. The results not only demonstrate the successful implementation of the software based receiver structures that were developed, but also highlight various modifications and enhancements to further improve the system.

Chapter 8 concludes the thesis with a summary and provides a discussion of the possible practical deployment of SWAN and suggestions to improve future work in underwater network communication.

Chapter 2 Acoustic Signal Transmission in Shallow Water Medium

2.1 Introduction

The boundaries and the volume properties in shallow water form a complex medium for the propagation of acoustic signals. In the process of transmission, the acoustic signal arriving at the receiver is delayed, distorted and weakened. Therefore, an understanding of the transmission of acoustic signals in underwater communication is needed to facilitate the design and development of novel yet reliable multi-user detection (MUD) receiver structures as discussed in chapter 6.

In this chapter, emphasis is placed on the effects that are most detrimental to the successful transmission of acoustic signals for shallow underwater communication.

2.2 Refraction

Sound velocity in the sea varies with the temperature, depth, and salinity [2.1]. From numerous experimental results and theoretical considerations, the sound velocity can be expressed as

$$c = 1449 + 4.6T - 0.055T^2 + 0.0003T^3 \qquad (2.1)$$

$$+(1.39 - 0.012T)(S - 35) + 0.017h$$

where c, T, S and h are the sound speed, in ms^{-1}, temperature, in $^{\circ}C$, salinity, in parts per thousand and depth, in m, respectively. As the sound velocity varies with the environmental parameters, the acoustic signals will be refracted according to Snell's law. Assuming an acoustic signal is transmitted at angle, $\theta(h_i)$ from a source at depth, h_i. Upon interacting with a media boundary, the differing acoustic impedance, from the refracted angle, $\theta(h_r)$, and depth, h_r can be expressed as

$$\frac{\sin(\theta(h_i))}{\sin(\theta(h_r))} = \frac{c(h_i)}{c(h_r)} \qquad (2.2)$$

2.3 Multipath Propagation

Multipath propagation occurs whenever there is more than one path arriving at the receiver. This phenomenon is normally caused by channel boundary reflections, both from the sea surface and sea-bottom, and volume scattering of the acoustic signal by reflective objects in the sea ocean, as illustrated in Figure 2-1. The effects of multipath propagation on the transmitted acoustic signals are numerous. The received signals tend to suffer from fluctuations both in phase and amplitude, resulting in reduced probability of signal detection during periods of fading. The other problem caused by multipath propagation is the degradation of phases and amplitudes between array receivers resulting in a reduced output gain in the arrays. Due to the sweeping by the underwater current, the movement of the transmitter and receiver causes the multipath components to undergo frequency broadening which results in Doppler effects.

2.3.1 Reflection Loss at the Sea surface

The propagation of signals in underwater acoustic communications is greatly influenced by the sea surface, which acts as both a reflector and scatterer of sound. In a calm sea surface situation, the acoustic signals may be reflected without any scattering. The lossless reflection is due to the large impedance mismatch of the air to water interface that give rise to a surface reflection coefficient of nearly -1. In such circumstances the acoustic signal with intensity, I_i, suffers no loss from the reflected intensity, I_r, defined by the surface loss coefficient, in dB,

$$\upsilon_r = 10\log_{10}\left(\frac{I_r}{I_i}\right) \tag{2.3}$$

In the case where the sea surface is rough, the acoustic signals are reflected randomly resulting in a smeared signal reception with intensity loss at the receiver.

The Rayleigh parameter, P, is used as a measurement of the acoustic roughness of the sea surface and is defined by [2.2]

$$P = \frac{2\pi\sigma\sin\theta}{\lambda} \tag{2.4}$$

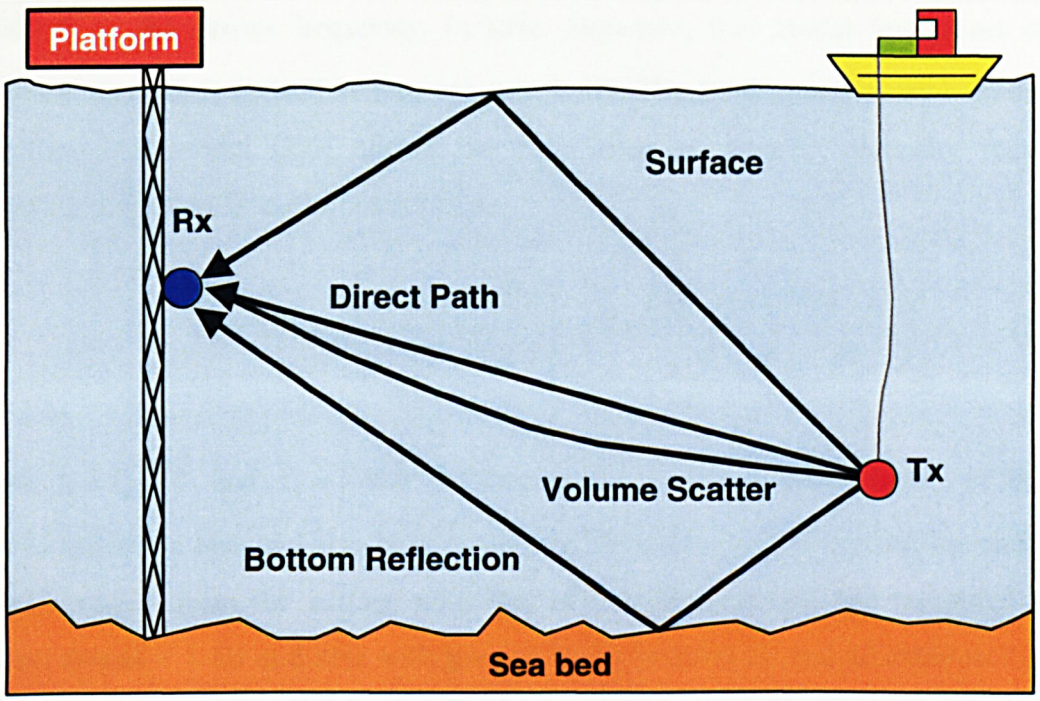

Figure 2-1 Acoustic signal undergoing multipath propagation from boundaries and volume scattering

where θ is the incident grazing angle, in degrees, of the sound upon the sea surface, λ is the wavelength and σ is the r.m.s. wave height (crest to trough), in ft, inter-related by the windspeed, w, in knots, as [2.3]

$$\sigma = 0.005 w^{2.5} \tag{2.5}$$

It was found empirically that when $P << 1$, that is $\sigma \sin\theta < \lambda/8$, the sea surface may be considered smooth; when $P >> 1$, the sea surface is considered rough [2.4].

Many other authors have also presented investigations on the characterisation of the sea surface reflection loss. Marsh et al. [2.5] extended the work of the Rayleigh parameter to account for the scattering from randomly irregular surfaces, the surface reflection loss was derived assuming a small grazing angle and is expressed as

$$\upsilon_r = -10 \log_{10}[1 - 0.0234 (f_c \sigma)^{3/2}] \tag{2.6}$$

where f_c is the carrier frequency, in kHz. However, this model falls short of the accountability when reflection loss exceeds 3 dB. The Beckmann-Spizzichino surface reflection loss model [2.6] allows the calculation of acoustic intensity reduction following reflection from the sea surface,

$$\upsilon_r = 10\log_{10}\left[\frac{(1+(f_c/f_1)^2)}{(1+(f_c/f_2)^2)}\right] - \left(1+\frac{(90-w)}{60}\right)\left(\frac{(90-\theta)}{30}\right)^2 \qquad (2.7)$$

where $f_1 = f_2\sqrt{10}$ and $f_2 = 378w^{-2}$. Other works in the characterisation of the sea surface reflection loss had also been presented. Patterson [2.7] compared the energy of pulses returned from the surface with that of the direct arrival and measured a sea surface loss of ~ 1 dB at 8 kHz with grazing angle between 22 and 52 degrees. Using a similar technique, Urick and Saxton [2.8] measured a sea surface loss of ~ 3 dB at 25 kHz with grazing angle between 4 and 19 degrees. Reports from Libermann [2.9], using the Lloyd mirror effect and observing the depth of the minima as f_c is varied, also presented similar results as [2.8] for 30 kHz acoustic signal with grazing angle of 8 degrees and wave heights of 0.2-0.8 ft. From the results obtained by these authors, it appears that the sea surface loss is less than 1 dB at $f_c < 1$ kHz and rises to about 3 dB at 25 and 30 kHz.

2.3.2 Reflection Loss at the Sea Bottom

The sea bottom is in many aspects similar to the sea surface, serving both as a reflector and scatterer of acoustic signal. However, the analysis of sea bottom reflection loss is much more complicated due to the fact that the sea bottom is often layered, with a density and a sound velocity that changes gradually or abruptly with depth. Thus the impedance mismatch between the water and the sea bottom may see a portion of the incident acoustic energy being transmitted into the bottom and a portion of the energy being reflected. The energy that is transmitted into the bottom may encounter layers of different materials, resulting in reflections and transmission at each boundary. Eventually, the energy reflected within the bottom returns to the water and recombines with the acoustic signal reflected from the water-bottom interface. The resultant reflection coefficient from a layered bottom constitutes losses in energy level and phase fluctuation relative to the incident wave, as shown in Figure 2-2.

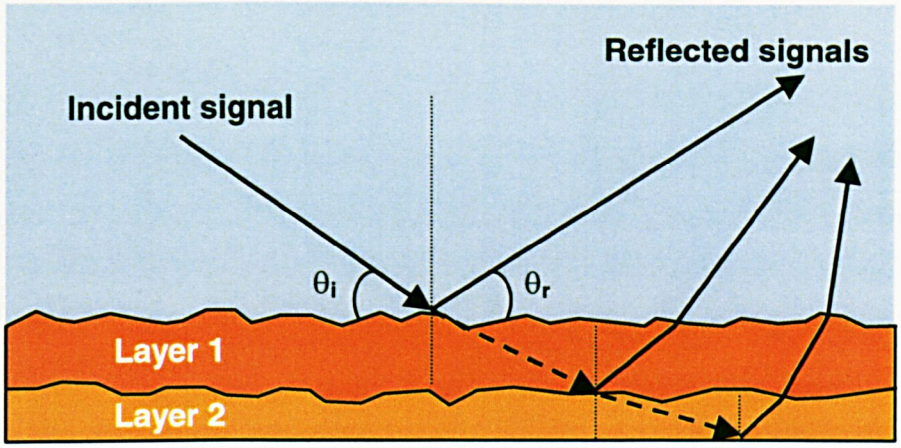

Figure 2-2 Effects of reflected acoustic signals from water-bottom interface

Assuming a nonlayered sea bottom, the Rayleigh reflection coefficient, defined by [2.10], is given as

$$P = \frac{(Z_2/Z_1)\sin\theta_i - \sin\theta_r}{(Z_2/Z_1)\sin\theta_i + \sin\theta_r} \tag{2.8}$$

where Z_2/Z_1 is the ratio of the characteristics impedance of the sea bottom and water, θ_i and θ_r is the incidence and reflected angle respectively.

Numerous experimental measurements for the acoustic signal loss in the sea bottom have been made [2.11], and the attenuation coefficient, β, in dB/m, is related to the carrier frequency by

$$\beta = kf_c^n \tag{2.9}$$

where k and n are empirical constants.

Due to the multilayered sediments at the sea bottom, the received acoustic signal that would have undergone multipath propagation via the sea bottom may end up with an enhanced energy from some angles and frequencies while a diminished energy in others. Therefore the reflection loss at the sea bottom generally suffers a higher attenuation than that of the reflection loss from the sea surface.

2.4 Reverberation

The causes of reverberation have been attributed to several environmental properties as reported in [2.12]. Urick [2.12] reported three main types of scatterers induced reverberation in the sea-ocean. The first type, known as volume reverberation, is caused by the inhomogeneities of the underwater environmental properties that form discontinuities in the physical properties of the underwater acoustic medium. Therefore the transmitted acoustic signals are usually intercepted and re-radiated in varying portions. The second and third type of scatterers induced reverberation are that of the sea surface and bottom reverberation, where scatterers are located near the boundaries. Since a two dimensional distribution of scatterers is involved, the two types of reverberation may be analytically considered together as surface reverberation [2.12].

2.4.1 Boundaries Scattering

The fundamental ratio which reverberation depends on is the scattering strength. Several methods are used to quantify the scattering strength. Urick and Hoover [2.13] beamed up short pulses of acoustic signals at 60 kHz via a directional transmitter, to the sea surface at different grazing angles and the transmitted signals were then observed by a narrow beam receiver. The method adopted by Chapman and Harris [2.14], using explosive sound sources with non-directional receiver reception was deemed more suitable for lower frequencies operation. The results from these experimental measurements showed a strong variation at low frequencies and grazing angles, where $P << 1$, while no variation were observed at higher frequencies and grazing angles, $P >> 1$. The work of [2.14] expressed the scattering strength, S, in dB, as

$$S = 3.3\log_{10}\frac{\theta}{30} - 4.24\log_{10} E + 2.6 \qquad (2.10)$$

where

$$E = 158(wf_c)^{1/3} \qquad (2.11)$$

2.5 Ambient Noise

Ambient noises in the ocean are unwanted acoustic signals, which interfere with the operation of underwater acoustic signal communications. The sources of ambient noise can be contributed by both nature and man-made activities with different sources exhibiting different directional and spectral characteristics. Typically, these sources of shallow water noise are highly variable both in time and place. While the wind and the biological properties are the main causes for natural noises, man-made noise may be characterised by shipping and industrial noises.

2.5.1 Turbulence Related Noise

The compendium for the characterisation of ambient noise spectral levels for the open ocean, published by Wenz [2.15], considered noise effects in terms of their spectral density and shows the dominant effects in different frequency bands. For operating frequency, $f_c < 10$ Hz, turbulence in the sea can induce pressure fluctuations sensed by hydrophones. As the noise is pseudo rather than the result of acoustic signal propagation, its spectral level will depend on the size, shape and motion of the hydrophone. However, this noise is frequently of little significance to underwater acoustic communication, which usually operate at much higher frequencies. The turbulence noise spectrum level, NSL_1, for frequency, f_c in kHz, may be expressed, in dB re 1 μPa, empirically as [2.10],

$$NSL_1 = 17 - 30(\log_{10} f_c) \qquad (2.12)$$

2.5.2 Distant Shipping Noise

For frequencies in the range of $10 \le f_c \le 100\text{Hz}$, distant shipping noises are in most cases, the dominant cause. Noise generated by surface ship can be distributed broadly in frequency [2.16] but is shaped by the low-pass characteristic of the sea when propagating over long distances [2.17]. The shipping noise spectrum level, NSL_2, in this frequency band may vary up to 10 dB between light (scale 0) and heavy shipping (scale 1) density, *D*, and can be expressed as [2.10],

$$NSL_2 = 40 + 20(D - 0.5) + 26\log_{10} f_c - 60\log_{10}(0.03 + f_c) \qquad (2.13)$$

2.5.3 Sea Surface Noise

At a higher frequency range of $100 < f_c \leq 10^4$ Hz, the formation and oscillation of subsurface air bubbles, generated by the breaking waves, parameterised by wind force, is the dominant factor for ambient noise in shallow water communication [2.18]. The noise spectral level decreases at a rate of 15 to 17 dB per decade for $f_c > 100$ Hz. The surface agitated noise spectrum level, NSL_3, for wind-speed w, in ms^{-1}, may be expressed as [2.10],

$$NSL_3 = 50 + 7.5w^{1/2} + 20\log_{10} f_c - 40\log_{10}(0.4 + f_c) \qquad (2.14)$$

2.5.4 Molecular Noise

For frequencies above the range of $f_c > 10^4$ Hz, ambient noise is dominated by the noise from molecular agitation. This thermal noise level increases at a rate of ~20 dB per decade and is expressed as [2.10],

$$NSL_4 = -15 + 20\log_{10} f_c \qquad (2.15)$$

2.5.5 Noise Spectrum Level

The overall noise spectrum level, NL, or the intensity attributed to a spectrum measurement bandwidth of 1 Hz, is the power sum of the noise spectrums from (2.12) to (2.15). To allow for an actual transmission bandwidth of B_d Hz, the total noise level is given by [2.10],

$$NL = NSL_1 + NSL_2 + NSL_3 + NSL_4 + 10\log_{10} B_d \qquad (2.16)$$

2.6 Transmission Loss

In the process of propagating through the shallow water medium, due to transmission losses, the acoustic signal experiences a decrease in the received power intensity. The transmission loss can be considered as the sum of the spreading loss and attenuation loss, which includes absorption and scattering loss.

2.6.1 Spreading Loss

Spreading loss is associated with the weakening of the acoustic signal as it spreads outwardly from the source. In an unbounded acoustic communication medium, the spreading loss of the transmitted acoustic signal is fundamentally associated by the spherical loss. This type of loss follows an inverse square law where the intensity of the transmission loss increases at the square of the range. The spherical loss, TL_{spher}, at range R_i, with reference to the intensity, R_o, at 1m, is expressed as [2.12],

$$TL_{spher} = 20\log_{10}(R_i / R_o) \tag{2.17}$$

In the case of shallow water acoustic communication where the medium is bounded by the sea surface and sea floor, resulting in the medium acting as an acoustic waveguide, the spreading loss is not spherical because the acoustic signal can no longer cross the boundaries. The spreading loss of this kind which exists between mid-range and long-ranges, is termed cylindrical loss and the loss, TL_{cylind}, is expressed as [2.12],

$$TL_{cylind} = 10\log_{10}(R_i / R_o) \tag{2.18}$$

2.6.2 Attenuation Loss

When propagating through the shallow water medium, the transmitted acoustic signal experiences a loss in energy with each unit distance travelled. The attenuation losses are contributed by several environmental factors [2.19]. Frequencies in excess of 1 MHz tends to suffer attenuation loss caused mainly by the viscous friction, where the acoustic energy is converted into heat energy. The ionic relaxation process of the magnesium sulphates that are present in the sea had been identified as the main cause of attenuation loss in frequencies, $f_c \leq 100$ kHz [2.10]. At frequencies, $f_c \leq 700$ Hz, boric acid relaxation, despite its smaller concentration in the seawater, also contributes to the attenuation loss.

The attenuation factor, α, in dBm^{-1}, derived by Fisher and Simmons [2.20] is the summed contribution from freshwater attenuation, α_f, magnesium sulphate relaxation, α_m, and boric acid relaxation, α_b, and is expressed as

$$\alpha = \alpha_f + \alpha_m + \alpha_b \tag{2.19}$$

Freshwater attenuation, $\alpha_f = [(2.1\times10^{-10})(T-38)^2 + (1.3\times10^{-7})]f_c^2$

Magnesium sulphate relaxation, $\alpha_m = \dfrac{50(T+1)(2S\times10^{-5})f_c^2}{2500(T+1)^2 + f_c^2}$

Boric acids relaxation, $\alpha_b = \dfrac{(1.2\times10^{-4})(10^{(T-4)/100})f_c^2}{(10^{(T-4)/100})^2 + f_c^2}$

where, S is the salinity, in (%) and T is temperature, in ^{o}C.

The total transmission loss, TL_{Total}, in dB, attributed to the spreading and attenuation loss for range R, in m, is given as [2.12],

$$TL_{Total} = \kappa \log_{10} R + \alpha R \tag{2.20}$$

where the constant κ has a value of 10 or 20 when either the cylindrical or spherical loss is considered respectively.

The semi-empirical expressions published by Marsh and Schulkin [2.21] provided a rough prediction for the transmission loss for frequency ranges, $0.1 \le f_c \le 10$ kHz. For short distances such that $R < H$, where H is defined by $1/8(h+L)^2$ and *h*, *L* are the channel depth and layer depth respectively; the transmission loss, TL_{Short}, in dB, is expressed as [2.12],

$$TL_{Short} = \kappa \log_{10} R + \alpha R + 60 - \beta \tag{2.21}$$

where the "near-field anomaly", β, is dependent on the sea-state and bottom type, given in Appendix I. At medium distances such that $H \le R \le 8H$, the transmission loss, TL_{Medium}, is expressed as [2.12],

$$TL_{Medium} = 15\log_{10} R + \alpha R + b_T\left(\frac{R}{H} - 1\right) + 5\log_{10} H + 60 - \beta \tag{2.22}$$

where b_T is the attenuation coefficient in dB, refer to Appendix II. Finally for long distances such that $R > 8H$, the transmission loss, TL_{Long}, is expressed as [2.12],

$$TL_{Long} = 10\log_{10} R + \alpha R + b_T\left(\frac{R}{H} - 1\right) + 10\log_{10} H + 64.5 - \beta \qquad (2.23)$$

Therefore, while (2.20) gives a generalised equation for the total transmission loss contributed by spreading loss and attenuation loss, (2.21) to (2.23) take into account the effects of spherical loss near the source and cylindrical loss at greater distances.

2.7 Sonar Equation for Point-to-Point Transmission

The sonar equation for the single way transmission allows the characterisation of the power level for the transmitting equipment and the shallow water medium so that the received acoustic signals can be detected and demodulated [2.4]. The source power level, SL, is easily obtained by simple considerations of the losses that are described in section 2.4 to 2.6, and is given by

$$SL = NL + TL + DT - DI \qquad (2.24)$$

where NL is the summed noise spectrum described in section 2.5; TL is the transmission loss presented in section 2.6; DT is the detection threshold and DI is the directivity index of the transmitting hydrophone.

2.8 Summary

The objective of this chapter was to provide a review of the under water communication environment where emphasis was placed on the various natural variables, which are detrimental towards shallow water acoustic communication.

The effects of multipath propagation are a major problem that affects the received acoustic signals. The fluctuations both in phase and amplitude often result in a reduced probability of signal detection during periods of fading. The other problem posed by multipath propagation is the degradation of phases and amplitudes between array receivers resulting in a reduced output gain in the arrays.

While the effect of transmission loss caused by spreading and attenuation loss can be rectified by increasing the source power level, the challenging task is to keep the source power level constant at all transmitting positions, such that the received acoustic signals are detectable at the furthest distance. This will inevitably lead to the "near-far" problem in coherent multi-user communication. Therefore in the following chapters of the thesis methods are developed in order to mitigate the effects of multipath propagation and MAI for shallow water acoustic network.

Chapter 3 Network Communication Analysis

3.1 Introduction

The environmental factors in shallow water attribute to the detrimental effects for reliable transmission of acoustic signals were outlined in chapter 2. Apart from resolving the problem of intersymbol interference (ISI), caused by multipath propagation, the base-station receiver had the added task of mitigating the effects of multiple access interference from other unintended users in the network.

This chapter outlines the network configurations for shallow water acoustic network (SWAN), which shows that multiple transmissions arriving simultaneously at a receiver can result in data packet collision. This is followed by highlighting the practical difficulties of implementing three reported multiple access techniques, which can be adopted for the enhancement of data transmission in a bandwidth limited SWAN. The problem engulfing network communication then leads to the resolving of data packet collision by multiple access interference cancellation techniques, which is the focal point of chapter 6. The latter part of the chapter is devoted to the discussion and analysis of signal coding that has been used in the sea-trials. Finally the chapter analysed a geometrical multipath deterministic channel model that was used to investigate the effects of signal multipath propagation through a shallow water channel. Provided that the channel is slowly changing, the deterministic channel model can provide a good estimation of transmission loss in signal propagation through the shallow water medium.

3.2 Network Configuration

The shallow water Acoustic Local Area Network (ALAN) topology of [3.1] is in many aspects, similar to the packet radio network (PRN) of [3.2]. The main difference between these two topologies is that the PRN uses a single thread forwarding scheme and a single data channel. The ALAN also adopts a virtual circuit that forwards packets from the source to destination and multiple frequencies accommodating the use of selective-repeat, go-back-N and store-and-forward protocols. Transmission of acoustic signal in water has a propagating velocity which is much slower than that of the EM waves in air. Therefore adopting the PRN in ALAN would results in delay between data

packets of up to tens of seconds. Furthermore, the accommodating of multiple frequencies in the ALAN topology is severely limited by bandwidth limitation. Therefore a compromise between these topologies need to be addressed. This section furnishes a discussion of the proposed network configuration for the SWAN project [3.3], which outlines the presence of multiple users arriving simultaneously at a receiver.

3.2.1 Packet Relay Network

For an available bandwidth, W, the channel capacity, C, constrained by the Shannon limit for error-free transmission is defined as [3.4]

$$C = W\log_2\left(1+\frac{P}{W\eta}\right) \tag{3.1}$$

where P and η are the average received signal power and ambient noise respectively. And the signal-to-noise ratio (SNR) is defined as

$$SNR = 10\log_{10}\left(\frac{P}{W\eta}\right) \tag{3.2}$$

Whilst this definition is viable for system design, the problem of data packet collision need also to be addressed. Assuming that a data packet originating from node *A* must reach node *G* by successive hops through the network nodes of Figure 3-1. Instead of utilising the multiple frequencies [3.1], which entails a minimum usage of three carrier frequencies for a similar network layout, the total available bandwidth in the network is partitioned into two disjoint bands, F_{c1} and F_{c2}. Each node always transmits omnidirectionally either on a band F_{c1} or F_{c2} and receives omnidirectionally via the other band F_{c2} or F_{c1}. The data packet from node *A* at time instant *(1)*, in band F_{c1} will be processed as:

- Transmission by node *A* is received by nodes *B* and *D* in band F_{c1};
- Node *B* and *D* starts transmitting in band F_{c2} at time instant *(2)*;
- Transmission from node *B* is received by nodes *A* and *F*;

- Transmission from node *D* is received by nodes *A* and *E*;
- At time instant *(3)*, node *E* starts transmission on F_{c1} ;
- Data packet transmission from nodes *E* and *F* is received by node *G* which result in data collision.

In this packet relay network analysis of inter-node data packet transmission, after the initialisation phase, each node transmits in a continuous mode. Frequency Division Multiple Access (FDMA) technique is employed using two bands F_{c1} and F_{c2} to discriminate reception from transmission. Time Division Multiple Access (TDMA) is only employed for interleaving the transmitted packet streams relative to the messages . Figure 3-1 indicates that a node may receive simultaneous messages from other distinct nodes resulting in data packet collision. Although adopting the transmission protocols of [3.2] would decrease the possibilities of simultaneous reception at a node, adopting the PRN would result in large delay between data packets.

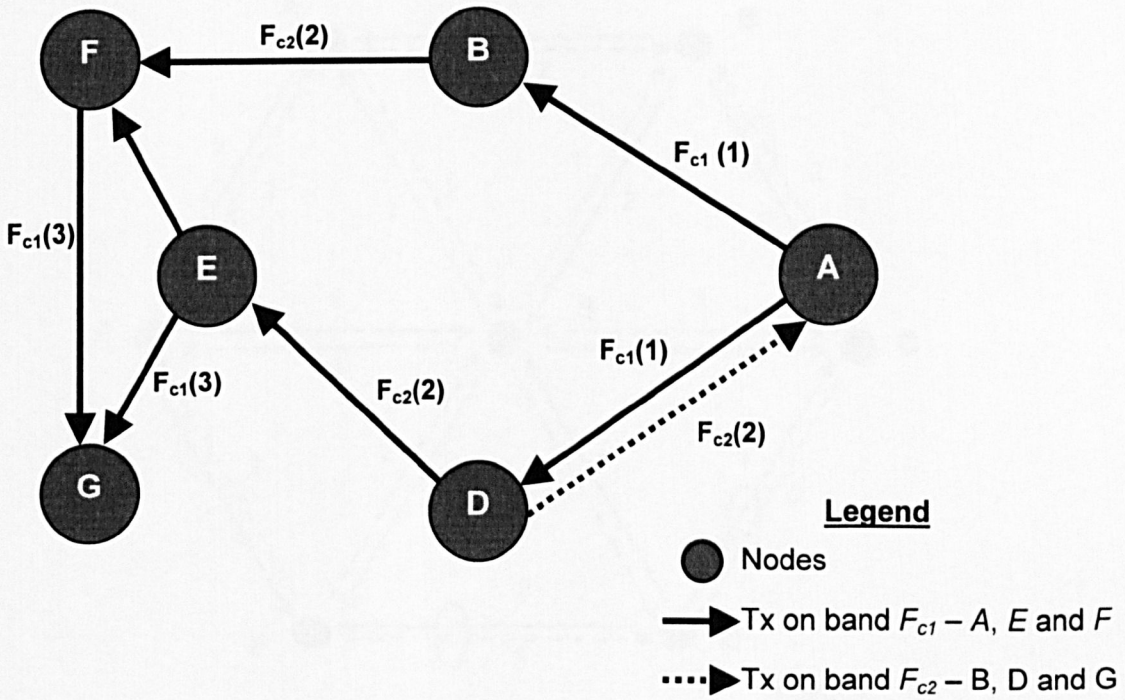

Figure 3-1 Packet relay and star network

3.2.2 Star Network

A star network is illustrated in Figure 3-2 with one central node, *S*, and peripheral nodes *A* to *F*. Each of the peripheral nodes may be associated to a Benthic station for data collection [1.15]. The central node may be equipped with radio frequency (RF) equipment hosted in a buoy or on a fixed surface platform for data relay to the shore. The central node *S* transmits to (receives from) all peripheral nodes on band $F_{c1}(F_{c2})$. The messages on the circled paths between peripheral nodes cannot be received because each peripheral node is set to receive only on band F_{c2}.

Reception of simultaneous messages between two peripheral nodes may occur through the central node *S*. The central node is then subjected to multiple access interference (MAI) reception from the peripheral nodes. In Figure 3-2, direct communications between adjacent peripheral nodes is allowed. Now the central node transmits only control and command messages on a small service band F_{c3} and receives on bands F_{c1} and F_{c2}.

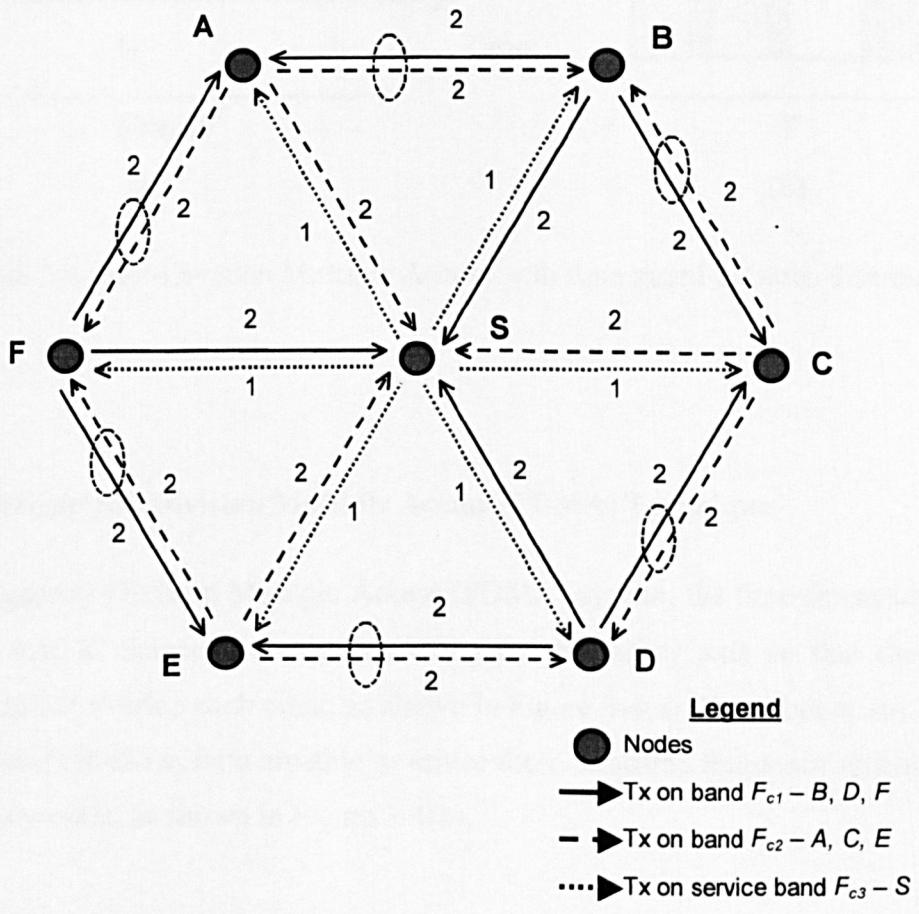

Figure 3-2 Star network with nodes-to-centre communications

3.3 Multiple Access Techniques

3.3.1 Time Division Multiple Access (TDMA) Technique

In a Time Division Multiple Access (TDMA) system, the time plane is divided into K discrete timeslots in a round-robin fashion, contiguous along the time axis, as shown in Figure 3-3. Each user in the system transmits signal energy in the allocated timeslots with low duty cycle.

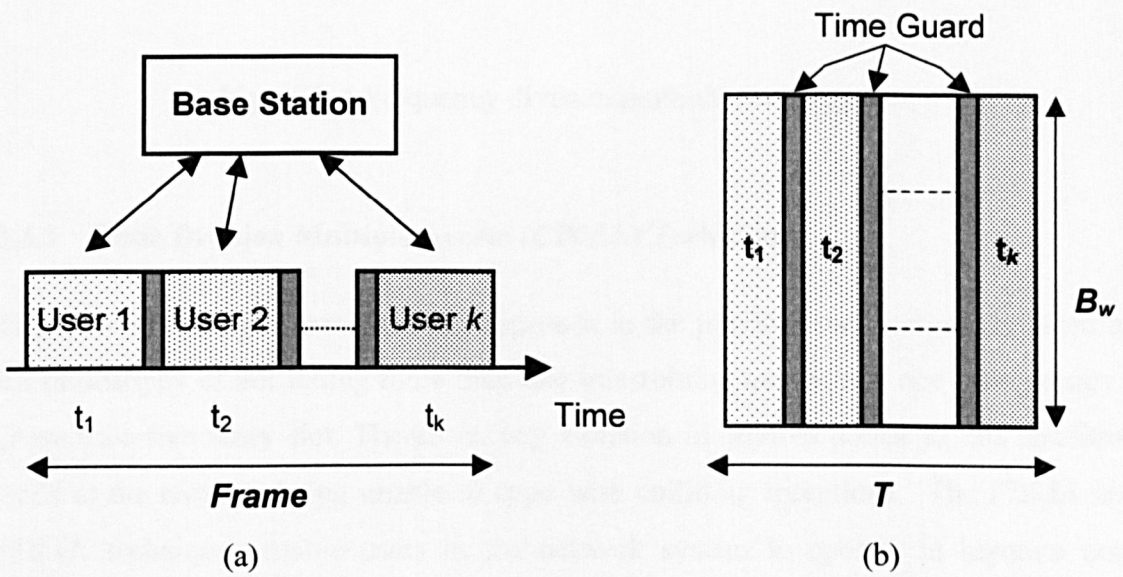

Figure 3-3Time-Division Multiple Access with time guard between discrete slots

3.3.2 Frequency Division Multiple Access (FDMA) Technique

In a Frequency Division Multiple Access (FDMA) system, the time-frequency plane is divided into K channels, contiguous along the frequency axis so that the resulting spectra do not overlap each other, as shown in Figure 3-4(a). Therefore at any particular time T, users in the system are able to utilise these allocated frequency channels with a 100% duty cycle, as shown in Figure 3-4(b).

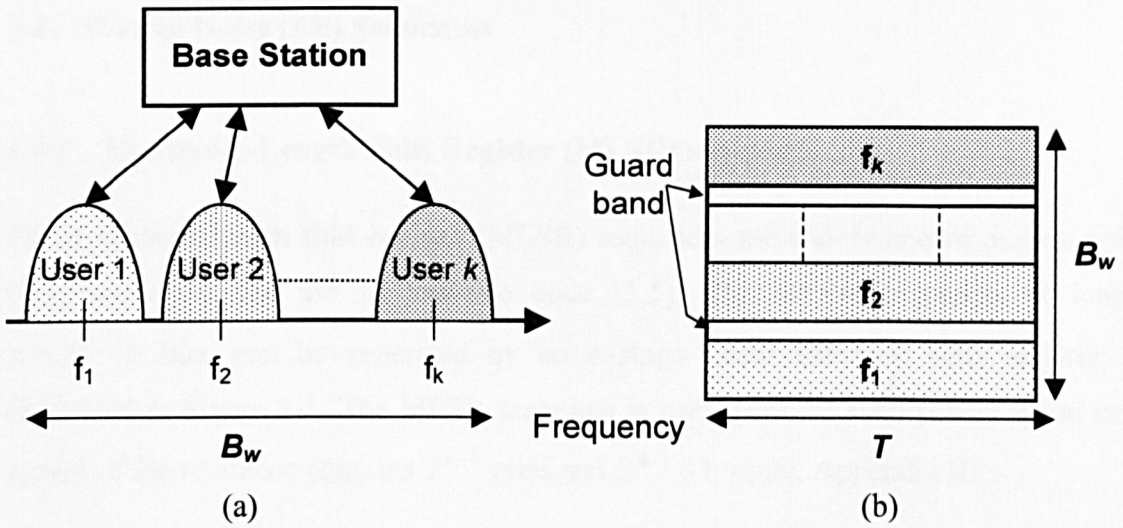

Figure 3-4 Frequency division multiple access system

3.3.3 Code Division Multiple Access (CDMA) Technique

The non-interfering channel sharing approach in the previous two sections is based on the philosophy of not letting more than one transmitting user at any one time occupy a given time-frequency slot. Therefore, any violation in random access to this condition leads to the receiver being unable to cope with colliding receptions. The FDMA and TDMA techniques enable users in the network system to operate in separate non-interfering channels where the signals transmitted by all users are mutually orthogonal. As discussed in network configuration of section 3.2 and due to non-ideal channel propagation effects, TDMA technique requires long duration of guard time insertion, while the FDMA technique adopts wide spectral guard bands between data packets transmission to avoid co-channel interference. These multiple access technique strategies waste the bandwidth limited channel resources as the number of users are greater than the number of co-current active users at any given time. Code Division Multiple Access (CDMA) technique transmits the data stream by spreading the data with a set of signature waveform, obtained from pseudo-noise (PN) sequences. The signature waveforms overlap each other in both time and frequency. Coding orthogonality ensures that the users are transparent to each other. However, one major disadvantage of introducing spread spectrum signals in SWAN is at the expense of reduced data throughput in a bandwidth-limited channel.

3.4 Pseudo-Noise (PN) Sequences

3.4.1 Maximum-Length Shift Register (MLSR) sequence

The maximum-length shift-register (MLSR) sequences are widely known pseudo noise (PN) sequences for use in low-rate code [3.5]. The MLSR sequence, of length $n = 2^m - 1$ bits, can be generated by an *m*-stage linear feedback shift register, as illustrated in Figure 3-5. The MLSR sequence is itself periodic with period n and each period of the sequence contains 2^{m-1} ones and $2^{m-1} - 1$ zeros, Appendix III .

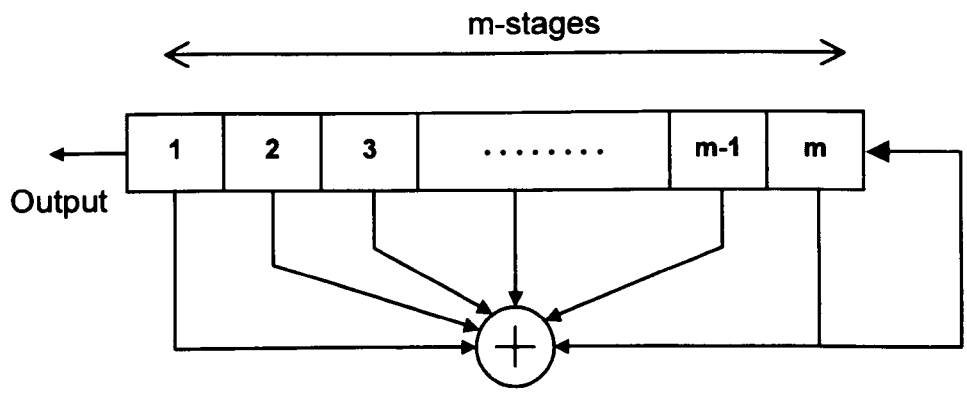

Figure 3-5 *M*-stage shift register with linear feedback

One important characteristic of the periodic PN sequence is its periodic auto-correlation function, which is defined as

$$r(j) = \sum_{i=1}^{n} (2b_i - 1)(2b_{i+j} - 1) \qquad 0 \le j \le n-1 \qquad (3.3)$$

where b_i is the element $\{0,1\}$. A pseudo-random sequence should have an auto-correlation function with the property that $r(0) = n$ and $r(j) = 0$ for $1 \le j \le n-1$. The periodic auto-correlation function of the MLSR sequence can be expressed as

$$r(j) = \begin{cases} n & j = 0 \\ -1 & 1 \le j \le n-1 \end{cases} \tag{3.4}$$

It can be seen from (3.4) that for large value of n, the size of the off-peak value relative to the peak value is small. Therefore the MLSR sequence can be considered to be ideal in terms of its autocorrelation function.

In order to cater for coherent network communication, the PN sequences for users should ideally be mutually orthogonal to each other so that the cross-correlation between the PN sequences is low. Although, the MLSR sequence possesses good autocorrelation property, it suffers from relatively large peaks between any pair of MLSR sequence in the cross correlation property [3.6]. Even though there is a possibility of selecting a small subset of the MLSR sequence that have low cross-correlation peak values, this subset of sequences is too small for network communication.

3.4.2 Gold code sequences

A set of periodic PN sequences with good cross-correlation properties were proposed by Gold [3.7]-[3.8]. Gold proved that for certain MLSR sequences, known as preferred sequence, exhibits a three-valued cross-correlation function of value existed as:

$$\{-1, -v(j), v(j)-2\} \tag{3.5}$$

where

$$v(j) = \begin{cases} 2^{(j+1)/2} + 1 & \text{odd } j \\ 2^{(j+2)/2} + 1 & \text{even } j \end{cases} \tag{3.6}$$

Therefore a total of $n+2$ sequences can be obtained for a pair of sequences of length $n = 2^m - 1$ bits, known as Gold sequence.

3.5 M-PSK Modulation

3.5.1 Binary Phase-Shift Keying (BPSK) Modulation

In a Binary Phase Shift Keying (BPSK) scheme [3.9], the modulating data signal shifts the phase of the carrier waveform into one of the two possible state, either π or 0, corresponding to binary symbols ± 1.

$$s_i(t) = \sqrt{\frac{2E}{T}}\cos[2\pi f_c t + \phi_i(t)] \tag{3.7}$$

where E, T are the symbol energy and symbol time duration $0 \le t \le T$, and the phase term $\phi_i(t)$ have M discrete values given by,

$$\phi_i(t) = \frac{2\pi i}{M} \qquad i = 1,\ldots,M \tag{3.8}$$

A typical BPSK waveform is shown in Figure 3-6 with abrupt changes at the symbol transitions.

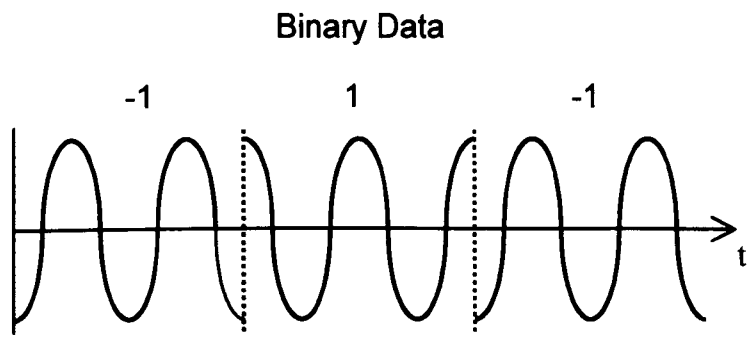

Figure 3-6 Signalling information for Binary Phase Shift Keying

Modulated BPSK signal wave is generated by simply applying the incoming binary data, in bipolar form, and the sinusoidal carrier to a product modulator, as shown in Figure 3-7.

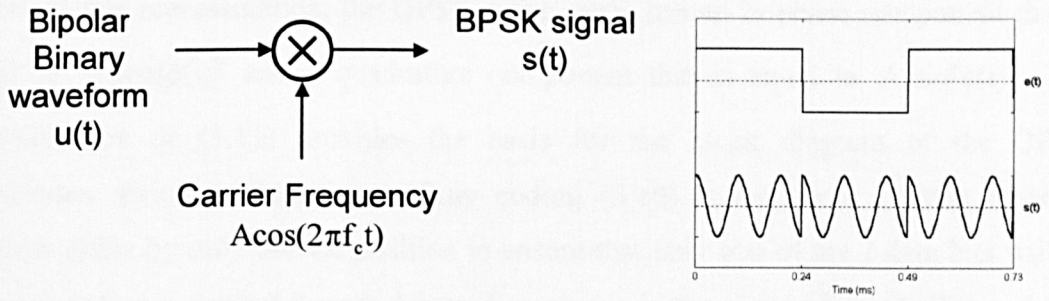

Figure 3-7 Generation scheme for Binary Phase Shift Keying (BPSK)

3.5.2 Quadrature PSK (QPSK) Modulation

In the BPSK scheme, only one of the two possible signals can be transmitted during each signalling interval, therefore leading to a theoretical bandwidth efficiency of 1 bps/Hz. The other approach to increase the bandwidth efficiency is then to adopt *M*-ary coding. In Quadrature PSK (QPSK) with level $M = 2^2$, one of the four possible signal waveforms

$$s(t) = \begin{cases} A_c\cos\left(2\pi f_c t - \dfrac{3\pi}{4}\right) \\ A_c\cos\left(2\pi f_c t - \dfrac{\pi}{4}\right) \\ A_c\cos\left(2\pi f_c t + \dfrac{\pi}{4}\right) \\ A_c\cos\left(2\pi f_c t + \dfrac{3\pi}{4}\right) \end{cases} \tag{3.9}$$

is transmitted during each symbol interval with each signal uniquely related to 2 bits/symbol, therefore increasing the efficiency to twice that of the BPSK scheme. In a general form, s(t) signal wave can be represented in the form

$$s(t) = A_c\cos\left[2\pi f_c t + \phi(t)\right] \tag{3.10}$$

where the phase $\phi(t)$ assumes the values of (3.9) for each input dibit data stream. By expanding the term of (3.10), the equation can be re-written as

$$s(t) = A_c\cos[\phi(t)]\cos\left(2\pi f_c t\right) - A_c\sin[\phi(t)]\sin\left(2\pi f_c t\right) \tag{3.11}$$

Based on this representation, the QPSK wave, $s(t)$, has an in-phase component that is equal to $A_c\cos[\phi(t)]$ and a quadrature component that is equal to $A_c\sin[\phi(t)]$. The representation of (3.11) provides the basis for the block diagram of the QPSK transmitter, shown in Figure 3-8. Gray coding [3.10] is employed so that adjacent symbols differ by only one bit position to ensure that only one of the 2 data bits will be erroneous when a symbol error is detected, as shown in the phasor diagram Figure 3-9.

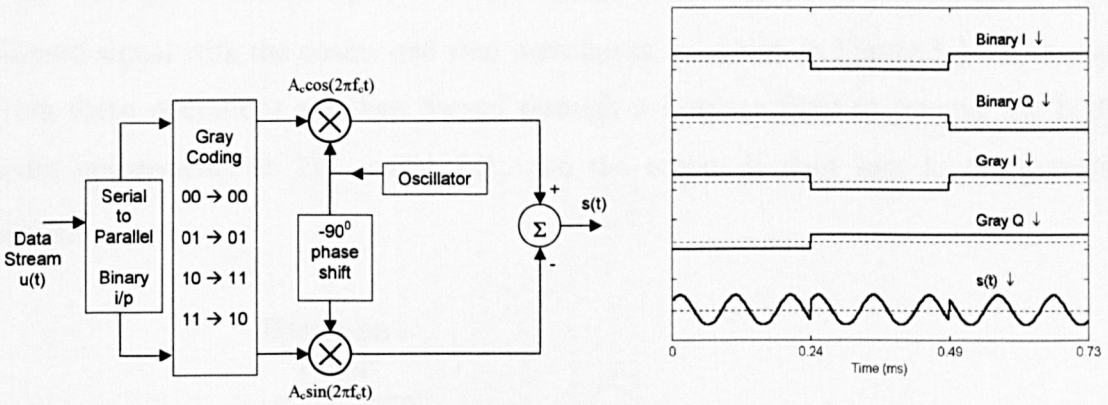

Figure 3-8 Block diagram of a QPSK transmitter

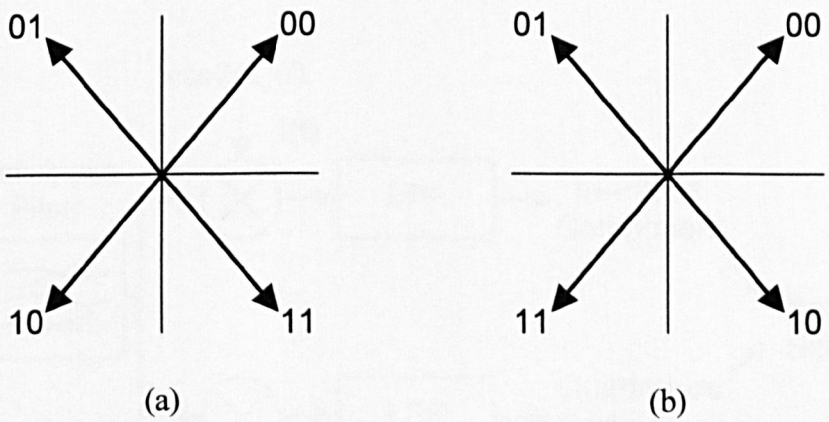

Figure 3-9 (a) Binary coded versus (b) Gray-coded phasor diagram

3.6 Error Performance of M-PSK systems

The demodulation of the BPSK and QPSK coding is carried out in an identical fashion as to the transmission procedure. The received signal is first passed through a bandpass filter centred at f_c to remove the unwanted noise and interference spectrum at the cutoff frequency of the bandwidth boundaries, BW_L and BW_H. Figure 3-10 shows the demodulation scheme for a single component for the BPSK scheme, which is multiplied by a cosine waveform. In the QPSK scheme, the signal is then separated into its In-Phase and Quadrature components, I(t) and Q(t), by simply multiplying the bandpass filtered signal with the cosine and sine waveforms, as shown in Figure 3-11. The ouput from these operations are then passed through a lowpass filter to remove the higher order components at $2f_c$, $\cos(4\pi f_c t)$, and the output is then sent to the detection scheme.

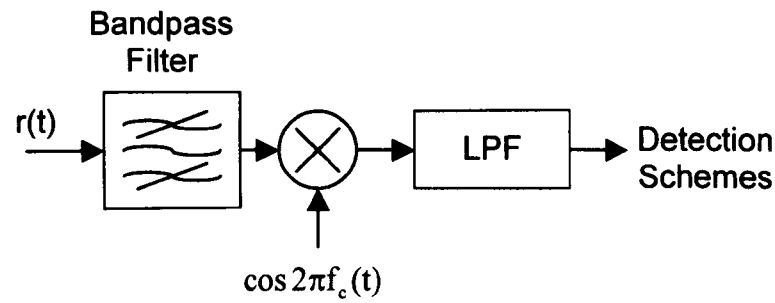

Figure 3-10 BPSK demodulation

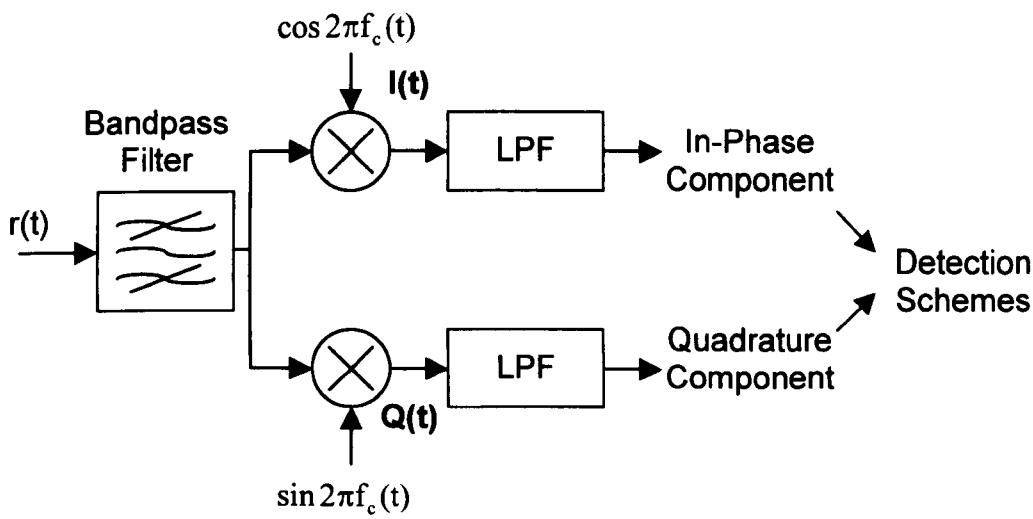

Figure 3-11 QPSK demodulation

For the BPSK signals, which is antipodal, the bit error probability, P_B, [3.11] is given as

$$P_B = Q\left(\sqrt{\frac{2E_b}{N_o}}\right) \tag{3.12}$$

where Q, E_b and N_o are the complementary error function, bit energy and noise power. Since QPSK bit stream is partitioned into I and Q components, with each stream being modulated at half of the bit rate of the original stream, it can be characterised as two orthogonal BPSK channels. If the magnitude of the original QPSK vector has a value of A_c, the magnitude of the I and Q components will each has a value of $A_c/2$, as shown in Figure 3-12. Therefore, if the QPSK signals has a bit rate of R bits/s and an average power of S watts, the individual BPSK components will be half the bit rate and power.

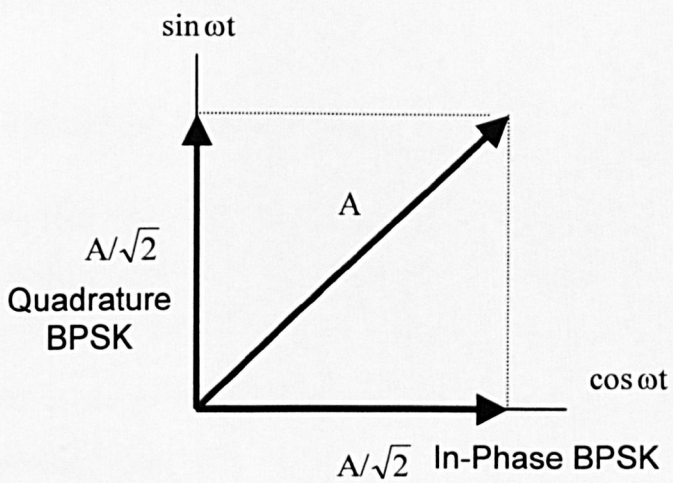

Figure 3-12 In-Phase and Quadrature BPSK components of QPSK scheme

From the ratio of the average signal power to average noise power ratio, SNR, given as

$$\frac{E_b}{N_o} = \frac{S}{N_o}\left(\frac{1}{R}\right) \tag{3.13}$$

It can be seen from that error probability of the QPSK is equal to that of the BPSK. However, it was noted by [3.11], that symbol error probability, P_e, between BPSK and QPSK is different. When utilising the Gray code assignment, the bit error probability for *M*-ary PSK was shown by [3.13] to be

$$P_B \approx \frac{P_e}{\log_2 M} \tag{3.14}$$

For large SNR, the symbol error probability for coherently detected *M*-ary PSK is expressed as [3.10].

$$P_e(M) \approx 2Q\left(\sqrt{\frac{2E_s}{N_o}} \sin\frac{\pi}{M}\right) \tag{3.15}$$

where E_s is the energy per symbol, $E_b(\log_2 M)$. Therefore, it is seen from this analysis that QPSK is the preferred signal coding over the BPSK coding technique in a band limited underwater acoustic channel.

3.7 Geometrical Multipath Channel Model

The underwater medium can be characterised as a time-varying multipath channel where the amplitude and time of arrival observed at the receiver changes with time. Considering a unit impulse, $\delta(t)$, is being transmitted through a time-varying channel, at sampling instant t_s, the observed signal at the receiver may consists of a series of train pulses, as shown in Figure 3-13.

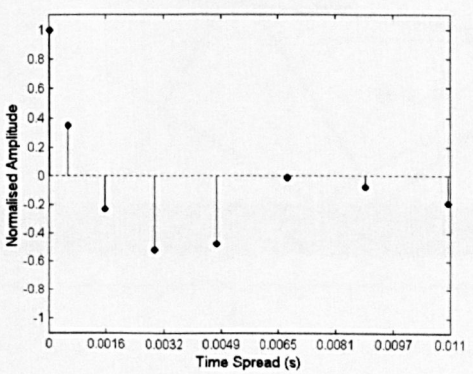

Figure 3-13 Example of a multipath channel

The transmitted signal, $s(t)$, can be expressed in a general form

$$s(t) = \mathrm{Re}[u(t)e^{j\omega t}] \tag{3.16}$$

As the transmitted signal propagates over the multipath channel, as shown in Figure 3-14, each resultant path will possess an attenuation factor, a, and delay time, τ. For an infinite number of paths, $n = \infty$, the observed signal at the receiver can be expressed as

$$x(t) = \sum_{n=1}^{\infty} a_n(t)s(t - \tau_n(t)) \tag{3.17}$$

Extending (3.17) to the case of continuous waveform gives

$$x(t) = \int_{-\infty}^{\infty} a(\tau;t)s(t - \tau)d\tau \tag{3.18}$$

where $a(\tau;t)$ denotes the signal attenuation and time delay τ at time t. By substituting (3.16) into (3.18) yields

$$x(t) = \mathrm{Re}\left[\left\{\int_{-\infty}^{\infty} a(\tau;t)e^{-j\omega\tau}u(t - \tau)d\tau\right\}e^{j\omega t}\right] \tag{3.19}$$

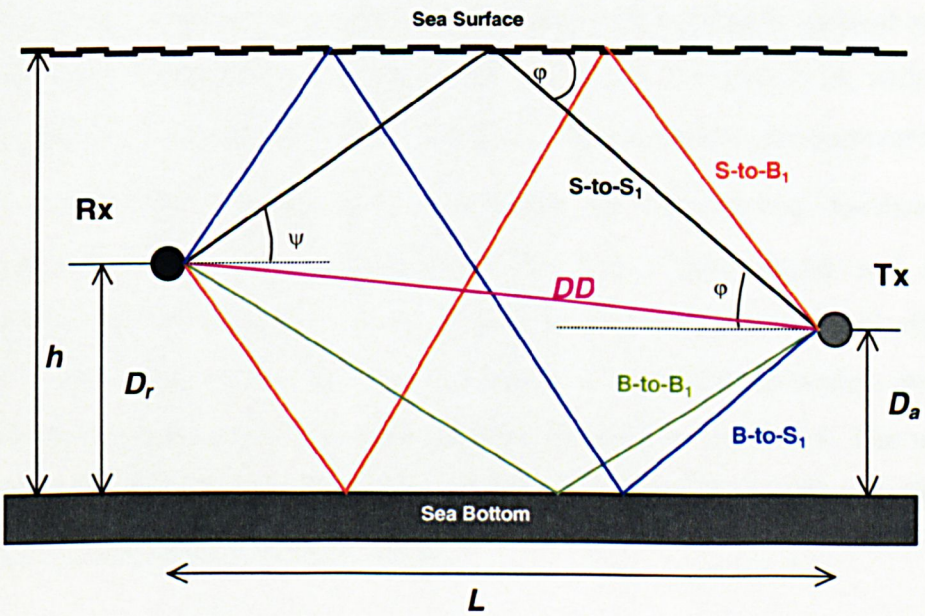

Figure 3-14 Multipath propagation of an underwater acoustic channel model

As the inner term of (3.19) is the response to an equivalent lowpass channel to the equivalent lowpass signal, $s(t)$, it is apparent that the low-pass time-variant impulse response, $h(\tau;t)$ is equal to

$$h(\tau;t) = a(\tau;t)e^{-j\omega\tau} \tag{3.20}$$

or more formally $h(\tau;t)$ represents the response of the channel at time t due to an impulse applied at time $(t-\tau)$. Therefore the equivalent baseband received signal, $x_b(t)$, is

$$x_b(t) = \sum_{n=1}^{\infty} a_n(t)e^{-j\omega\tau_n(t)}u(t-\tau_n(t)) \tag{3.21}$$

In the case when unmodulated carrier is transmitted then $u(t) = 1$ for t, (3.21) is reduced to

$$x_b(t) = \sum_{n=1}^{\infty} a_n(t)e^{-j\omega\tau_n(t)} \tag{3.22}$$

3.7.1 Simulated Results

From the basis of (3.22), a deterministic geometrical multipath channel model was analysed [3.14]. Taking the channel geometry, as shown in Figure 3-14, with a uniform channel depth, h, and constant sound speed, c. The transmitter and receiver depth, D_a and D_r respectively are separated by a horizontal transmission distance, L. The transmitted signal can be classified into the direct path signal and multi-path components, refer to Appendix V. To investigate the multipath channel effects for a sample system under various distance conditions, a computer simulation analysis was performed in Microsoft C++ using the parameters given in Table 3-1. The wind speed was assumed to 25 knots, which corresponds to a sea state condition 5 [3.16], with computed reflection coefficient, $\bar{r} = 0.32$.

System Parameters	
Carrier Frequency	f_c = 10 kHz
Frequency Bandwidth	B_w = 8 – 12 kHz
Data rate	4 k symbol/s
Channel Parameters	
Channel Depth	18m
Tx Depth	9m
Rx Depth	9m
Wind Speed	25 knots
Sound Speed	1500 m/s
Distances between Tx and Rx under investigation	
500m, 2km, 5km and 10km	

Table 3-1 System parameter for channel impulse simulation

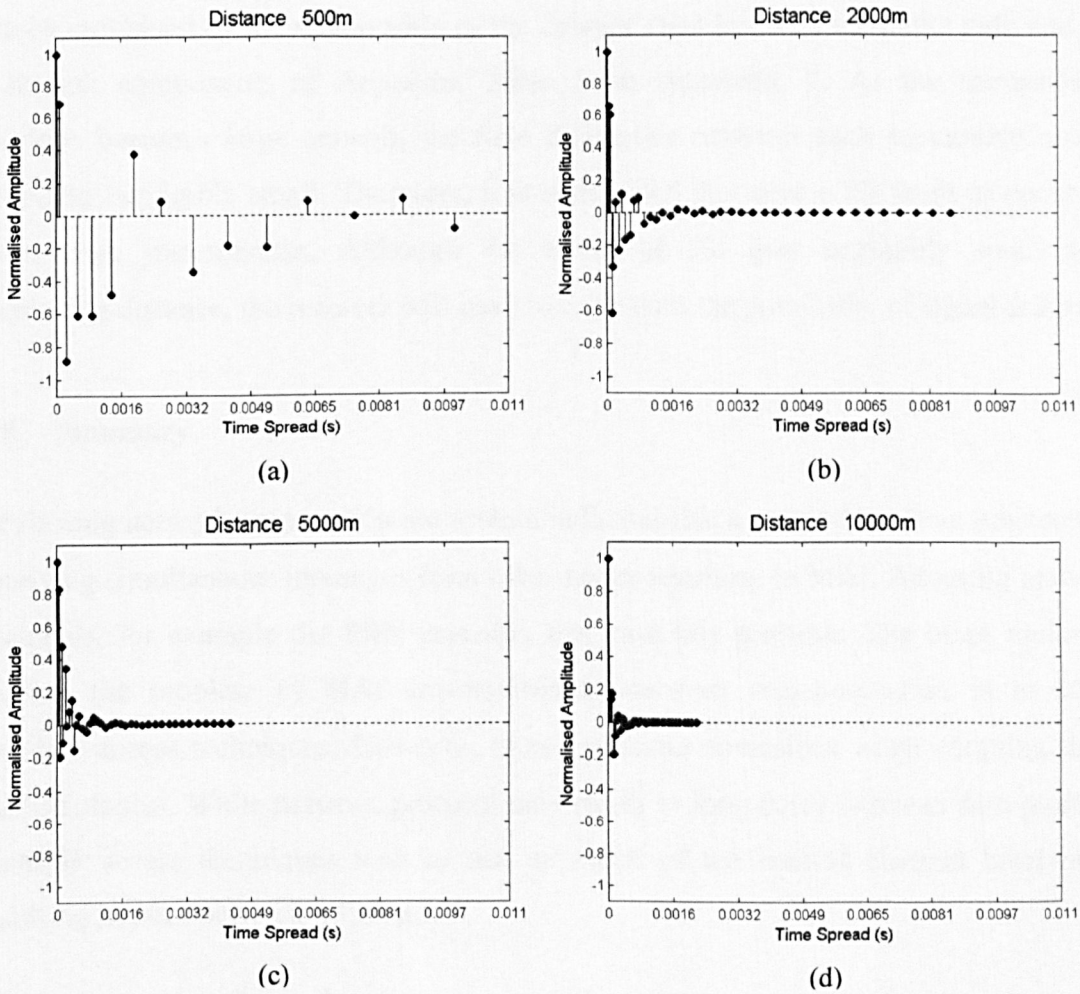

Figure 3-15 Channel impulses at (a) 500m (b) 2km (c) 5km (d) 10km

Figure 3-15 shows the computed impulse response, normalised by the direct path, for the various distances at 500m, 2km, 5km and 10km. It can be seen from Figure 3-15(a) that the multipath time spread for the short-range transmission at 500m exhibits severe ISI which spans for ~28 symbols. The reciprocal of the multipath spread is a measure of the coherence bandwidth, (Δf), of the channel [3.12], which is given as

$$(\Delta f_c) \approx \frac{1}{T_{multi}} \tag{3.23}$$

where T_{multi} is the multipath spread. If (Δf) is large in comparison to the transmitted bandwidth, the signal undergoes frequency non-selective fading. On the other hand, if (Δf) is small, the transmitted signal suffers from frequency selective fading. From the multipath intensity plots in Figure 3-15, it was observed that as the transmission distance increases from 500m to 10km, the multipath time spread grew smaller. This can be explained by the relationship of the delayed time between the direct path and the multipath components of Appendix Table 4, in Appendix V. As the transmission distance becomes large enough, the time difference between each successive arrival becomes, negligibly small. Therefore, it is anticipated that severe ISI tends to occur for short-range transmission. Although the effect of ISI gets negligibly small with increasing distance, the receiver will have to cope with the possibility of signal fading.

3.8 Summary

Reviewing network communication system indicates that a network node is subjected to receiving simultaneous messages from other nodes resulting in MAI. Adopting network protocols, for example the PRN protocol, can ease this problem. The other option in solving the problem of MAI encountered in network communication is to adopt multiple access techniques. However, there are some downsides when adopting these methodologies. While network protocol may result in long delay between data packets, multiple access techniques tend to use up much of the limited channel bandwidth, resulting in poor network efficiency.

The investigation of signal coding was carried out in the second part of the chapter. It was seen that the error probability of QPSK modulation scheme with Gray-coding is equal to that of the BPSK, therefore enabling the system to increase its bits transmission

per second to twice of the available bandwidth. Therefore, QPSK modulation scheme is the preferred signal coding over the BPSK coding technique in a band limited underwater acoustic channel.

Finally, a geometrical multipath channel model was descibed for a shallow water channel depth of 18m. The channel model provided an insight to the effects of ISI on the transmitted acoustic signal. It is anticipated that severe ISI tends to occur at short-range transmission. As the effect of ISI gets negligibly small with increasing distance, the receiver will have to cope with the possibility of signal fading.

Chapter 4 Supervised and Blind Adaptive Equalisation

4.1 Introduction

The phenomenon of ISI and background noise can deteriorate the performance of the receiver. Therefore the role of an adaptive equaliser is to resolve distortion introduced by the channel while minimising the effect of additive noise prior to the detection input. Adaptive filtering is the main driving force behind successful retrieval of received signals by continuously seeking the minimum point of the error performance surface in order to assure that optimisation is achieved. However, as the shallow water channel medium is time-variant, the adaptive algorithms have the added task of tracking the minimum point that is no longer fixed.

Two approaches are investigated in this chapter to deal with the time variant channel:

1. Supervised adaptive algorithms: These algorithms uses a priori known training sequence, embedded before the data sequence, to adjust the equaliser tap weight coefficients in order to achieve a desired local minima in the error-performance surface. This unimodal nature can assure convergence of the algorithm. When switching to the decision-directed mode, the algorithm uses the estimated data to modify and update the error performance surface in a multimodal nature [4.1]. In this section, several classical supervised algorithms are investigated. Due to the instability performance of the standard RLS algorithm in tracking a time-variant channel, an improved RLS (IRLS) algorithm [4.2] is presented which exhibits good convergence yet at the same time achieves better tracking properties.
2. Blind deconvolution: This can be viewed as a self-organised learning process [4.9]. Self-organised in the sense that deconvolution is performed in the absence of a prior known training sequence. A sub-family of the blind deconvolution algorithms, Implicit Higher Order Statistics (HOS), which exploit the HOS of the received signal is considered mainly due to its fast computation.

Performance comparison of both supervised and blind adaptive algorithms are presented in section 4.4, using both simulated and experimental data for a single-user scenario. The performances of the algorithms are assessed by comparing the rate of convergence and tracking property for practical implementation. From the results obtained from

simulation and experimental data, the IRLS algorithm exhibits better convergence and tracking property as compared to the other classes of algorithms. The last section discusses the feasibility of the adaptive algorithms for practical implementation in underwater acoustic communication.

4.2 Supervised Adaptive Equalisations

4.2.1 Stochastic Least Mean Square (LMS) algorithm

The Least Mean Square (LMS) algorithm, first proposed by Widrow and Hoff [4.4], is a stochastic implementation of the steepest-descent algorithm and is the most widely used adaptive filtering algorithm in practice due to its simplicity and robustness in signal processing.

4.2.1.1 Mean Square Error criterion

The concept of a cost function is the optimisation of the filters. It defines the transformation from a vector space spanned by the elements of the coefficient vector into the space of a real scalar [4.5]. There are two points that need to be considered when selecting a cost function:

1. The cost function must be mathematically tractable
2. The cost function should have a single minimum or maximum point, so that the optimum set of filter parameters could be selected unambiguously

The tractability of the cost function allows the analysis of the filter and also simplifies the development of the algorithm for adjustment of the filter parameters. The number of minima (or maxima) points for a cost function is closely related to the filter structure. The IIR filter involves both feedforward and feedback section, where portions of the filter output and possibly other internal variables in the filter are fed back to the input [4.6]. In general, unless it is properly designed, the feedback in IIR filters results in

many minima (or maxima) points, which give rise to instability with the result of filter oscillation. On the other hand, FIR filters are inherently stable because the structure involves the use of only the forward path, which has a single minima (or maxima) point once the proper cost function is used [4.7],[4.8]. Therefore attention is confined to FIR filters in this chapter.

A highly popular and simple cost function that satisfies the above two conditions, is the mean-square error, ξ, which is defined as the mean-square value of an estimation error [4.8] expressed as

$$\xi = E[|e(n)^2|] \tag{4.1}$$

where $E[\cdot]$ denotes the statistical expectation. The estimation error $e(n)$ is the difference between the desired response $d(n)$ and the output value $y(n)$ in discrete time, shown in the basic transversal filter in Figure 4-1 and is expressed as

$$e(n) = d(n) - y(n) \tag{4.2}$$

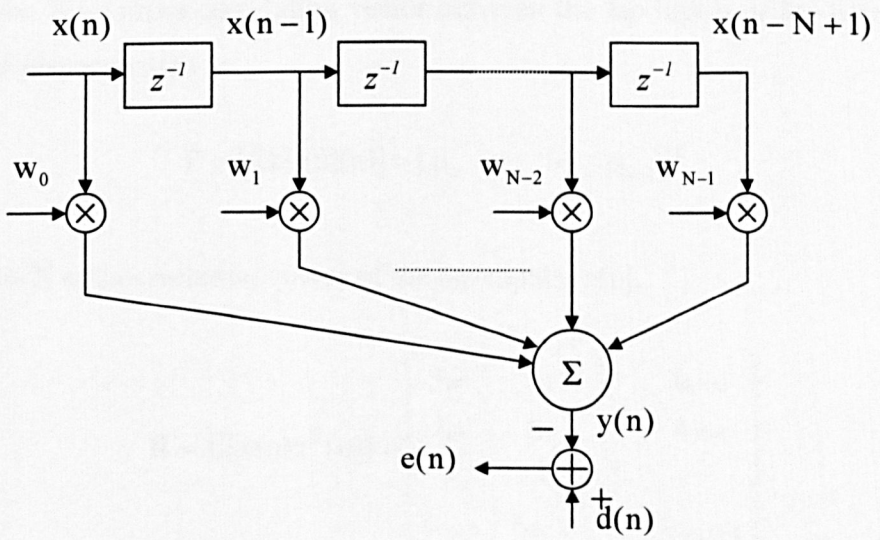

Figure 4-1 Transversal Filter

4.2.1.2 Optimal Weight Values: Wiener-Hopf Equation

Considering the basic transversal filter shown in Figure 4-1. The sampled filter input, $\mathbf{x}(n)$ and the tap-weights, $\mathbf{w}$, are defined as column vectors

$$\mathbf{x}(n) = [x(n) \quad x(n-1) \quad \cdots \quad x(n-N+1)]^T \tag{4.3}$$

and

$$\mathbf{w} = [w_0 \quad w_1 \quad \cdots \quad w_{N-1}]^T \tag{4.4}$$

where the superscript T stands for transpose. The filter output is

$$y(n) = \sum_{i=0}^{N-1} w_i x(n-i) = \mathbf{w}^T\mathbf{x}(n) = \mathbf{x}(n)\mathbf{w}^T \tag{4.5}$$

where N is the number of tap weights used in the filter. Substituting (4.5) in (4.2) yields

$$e(n) = d(n) - \mathbf{x}(n)\mathbf{w}^T \tag{4.6}$$

And the cost function in (4.1) can then be expanded to

$$\xi = E[d^2(n)] - \mathbf{w}^T E[\mathbf{x}(n)d(n)] - E[d(n)\mathbf{x}^T(n)]\mathbf{w} + \mathbf{w}^T E[\mathbf{x}(n)\mathbf{x}^T(n)]\mathbf{w} \tag{4.7}$$

Defining the $N \times 1$ cross-correlation vector between the tap inputs of the filter, $\mathbf{x}(n)$ and the desired response $d(n)$ as

$$\mathbf{P} = E[\mathbf{x}(n)d(n)] = [p_0 \quad p_1 \quad \cdots \quad p_{N-1}]^T \tag{4.8}$$

and the $N \times N$ autocorrelation vector of the tap inputs, $\mathbf{x}(n)$,

$$\mathbf{R} = E[\mathbf{x}(n)\mathbf{x}^T(n)] = \begin{bmatrix} r_{00} & r_{01} & \cdots & r_{0,N-1} \\ r_{10} & r_{11} & \cdots & r_{1,N-1} \\ \vdots & \vdots & \ddots & \vdots \\ r_{N-1,0} & r_{N-1,1} & \cdots & r_{N-1,N-1} \end{bmatrix} \tag{4.9}$$

Noting that $E[d(n)\mathbf{x}^T(n)] = \mathbf{P}^T$ and $\mathbf{w}^T\mathbf{P} = \mathbf{P}^T\mathbf{w}$, the cost function in (4.1) is obtained as

$$\xi = E[d^2(n)] - 2\mathbf{w}^T\mathbf{P} + \mathbf{w}^T\mathbf{R}\mathbf{w} \tag{4.10}$$

The optimal set of weight values, $\mathbf{w}_{opt}$, is obtained when $E[d^2(n)]$ is a minimum, which is achieved by differentiating the cost function of (4.10) with respect to the weight vector to zero:-

$$\nabla\xi = \frac{\partial\xi}{\partial\mathbf{w}} = 2\mathbf{R}\mathbf{w}_{opt} - 2\mathbf{P} = 0 \tag{4.11}$$

where ∇ is the gradient operator defined as the column vector.

$$\nabla = \begin{bmatrix} \frac{\partial}{\partial w_0} \\ \frac{\partial}{\partial w_1} \\ \vdots \\ \frac{\partial}{\partial w_{N-1}} \end{bmatrix} \tag{4.12}$$

From which $$\mathbf{w}_{opt} = \mathbf{R}^{-1}\mathbf{P} \tag{4.13}$$

is the expression for the Wiener-Hopf equation [4.9].

4.2.1.3 Solving of Wiener-Hopf Equation: Least Mean Square algorithm

The optimum set of weight coefficient values, $\mathbf{w}_{opt}$, can be obtained by solving (4.13) directly. Although straightforward, acquisition of the autocorrelation matrix, $\mathbf{R}$, and cross-correlation matrix, $\mathbf{P}$, which are not known a *priori*, requires an offset of substantial computational load for matrix inversion. Due to the time-variant nature of the underwater channel, both $\mathbf{R}$ and $\mathbf{P}$ changes with time and so the optimum weight vector needs to be updated frequently. Therefore a different approach of finding w_{opt} is desirable. While the *Newton's* algorithm method searches the zeros of a function [4.5], the *steepest-descent* method uses a deterministic gradient iterative method of optimisation for searching the minimum value of the mean squared error [4.10].

According to (4.11), if w(k) is the tap-weight vector at time index *n*, it can be updated by:

$$\mathbf{w}(n+1) = \mathbf{w}(n) - \mu\nabla\xi(n) \tag{4.14}$$

where μ is a positive step-size parameter. The LMS algorithm simply replaces the cost function of (4.1) by its instantaneous coarse estimate $\xi(n) = e^2(n)$ [4.4]. Substituting $\xi(n) = e^2(n)$ into (4.14), the tap-weight vector at time index *n*, is obtained as

$$\mathbf{w}(n+1) = \mathbf{w}(n) - \mu\nabla e^2(n) \tag{4.15}$$

The *i* th element (tap weights) of the gradient vector $\nabla e^2(n)$ is

$$\frac{\partial e^2(n)}{\partial w_i} = 2e(n)\frac{\partial e(n)}{\partial w_i} \tag{4.16}$$

Substituting (4.2) for the last factor on the right hand side of (4.16) and noting that d(n) is independent of w_i yields

$$\frac{\partial e^2(n)}{\partial w_i} = -2e(n)\frac{\partial y(n)}{\partial w_i} \tag{4.17}$$

And substituting for y(n) from (4.5),

$$\frac{\partial e^2(n)}{\partial w_i} = -2e(n)x(n-i) \tag{4.18}$$

Using (4.12) and (4.18), the expression in (4.15) is obtained as

$$\mathbf{w}(n+1) = \mathbf{w}(n) + 2\mu e(n)\mathbf{x}(n) \tag{4.19}$$

This is the tap-weight adaptation for the LMS algorithm by which the correction that is applied to the current estimate of the tap-weight vector, w(n). Using these notations, the LMS algorithm may be written in complex notation to reflect the data, estimated error and tap-weight adaptation for MPSK modulation, as depicted in Table 4-1. The subscripts *I* and *Q* denote the "in-phase" (real) and "quadrature" (imaginary)

components respectively. Figure 4-2 shows the cross-coupled signal-flow representation of the complex error and output signals and Figure 4-3 illustrates the cross-coupled signal-flow for the tap-weight adaptation. The combination of the pair of signal-flow diagrams constitutes the canonical model of the complex LMS algorithm that is equivalent to a set of four real LMS algorithms with cross-coupling between them.

Parameters N = Number of taps for $n = 0,1,2,...,N-1$

μ = Step-size parameters

Initial Conditions Tap-Weights

$$w_I(0) = 0 \qquad w_Q(0) = 0$$

For each time instant, n = 0,1, 2, ... , N – 1 compute

1. Complex filter output:

$$y_I(n) = \mathbf{w}_I^T(n)\mathbf{x}_I(n) - \mathbf{w}_Q^T(n)\mathbf{x}_Q(n)$$

$$y_Q(n) = \mathbf{w}_I^T(n)\mathbf{x}_Q(n) + \mathbf{w}_Q^T(n)\mathbf{x}_I(n)$$

2. Complex Error Estimation:

$$e_I(n) = d_I(n) - y_I(n) \qquad e_Q(n) = d_Q(n) - y_Q(n)$$

3. Complex Tap-weight adaptation:

$$\mathbf{w}_I(n+1) = \mathbf{w}_I(n) + \mu[e_I(n)\mathbf{x}_I(n) + e_Q(n)\mathbf{x}_Q(n)]$$

$$\mathbf{w}_Q(n+1) = \mathbf{w}_Q(n) + \mu[e_I(n)\mathbf{x}_Q(n) - e_Q(n)\mathbf{x}_I(n)]$$

Table 4-1 Adaptation of the canonical complex LMS algorithm

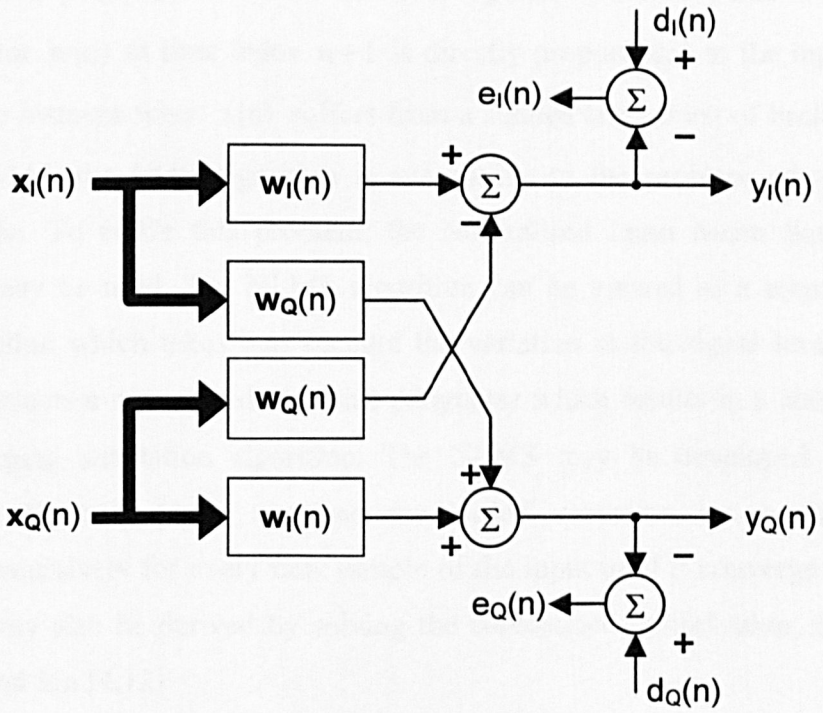

Figure 4-2 Error and output signal-flow representation of the complex LMS algorithm

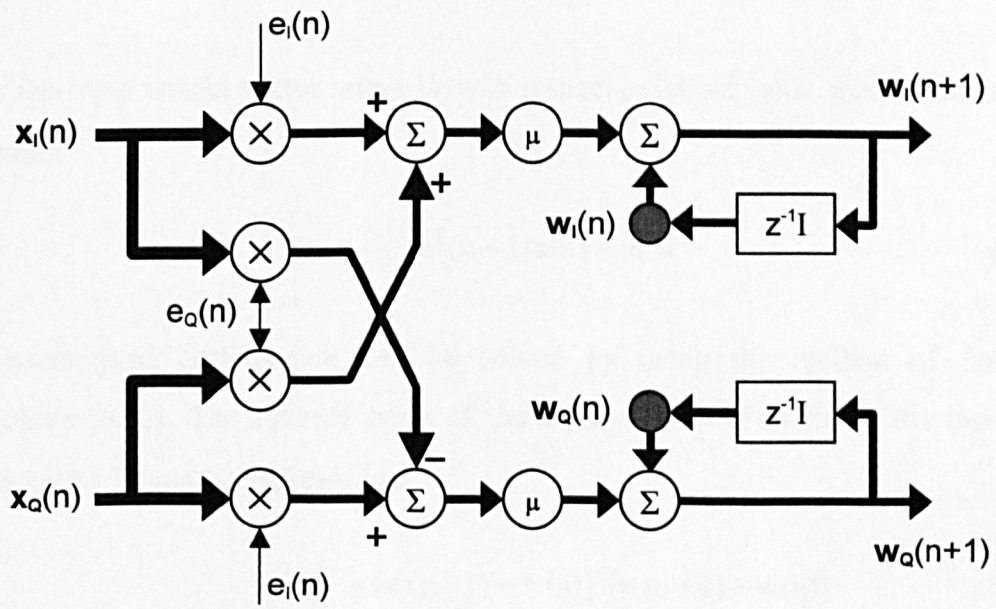

Figure 4-3 Tap-weight update signal-flow representation of the complex LMS algorithm

4.2.2 Normalised Least Mean Square (NLMS) algorithm

The adaptation $\mu\mathbf{x}(n)e(n)$ factor, of the LMS algorithm, in (4.19) that is applied to the weight vector $\mathbf{w}(n)$ at time index $n+1$ is directly proportional to the input-tap vector $\mathbf{x}(n)$. In the instance when $\mathbf{x}(n)$ suffers from a sudden large burst of background noise or strong MAI, the LMS algorithm is susceptible to the problem of gradient noise amplification. To tackle this problem, the Normalised Least Mean Square (NLMS) algorithm may be used. The NLMS algorithm can be viewed as a companion to the LMS algorithm which takes into account the variation in the signal level at the filter input and selects a normalised step-size parameter which results in a stable as well as fast converging adaptation algorithm. The NLMS may be developed from several viewpoints. Nitzberg [4.11] obtained the NLMS recursion by running the LMS algorithm recursively for every new sample of the input until it converges. The NLMS recursion may also be derived by solving the constrained optimisation, formulated by Goodwin and Sin [4.12]:

Given the tap-input weight vector $\mathbf{x}(n)$ and the desired output decision $d(n)$, the weight vector $\mathbf{w}(n+1)$ is determined so as to minimise the squared Euclidean norm of the difference

$$\eta(n) = \mathbf{w}(n+1) - \mathbf{w}(n) \tag{4.20}$$

in the tap-input weight vector $\mathbf{w}(n+1)$ with respect to its old value $\mathbf{w}(n)$, subject to the constraint

$$\mathbf{w}^T(n+1)\mathbf{x}(n) = d(n) \tag{4.21}$$

The constrained optimisation can be solved by using the method of *Lagrange multipliers* [4.13]. The squared norm of the change $\eta(n)$ of (4.20) in the tap-weight vector $\mathbf{w}(n+1)$ can be expressed as

$$\|\eta(n)\|^2 = [\mathbf{w}(n+1) - \mathbf{w}(n)]^T[\mathbf{w}(n+1) - \mathbf{w}(n)] \tag{4.22}$$

$$= \sum_{k=0}^{N-1} |\mathbf{w}_k(n+1) - \mathbf{w}_k(n)|^2$$

From (4.21) and (4.22), the cost function can then be stated as

$$\xi = \sum_{k=0}^{N-1} (\mathbf{w}_k(n+1) - \mathbf{w}_k(n))^2 \tag{4.23}$$

The optimum set of values of $\mathbf{w}_k(n+1)$ is obtained by differentiating the cost function and setting the results to zero. Hence (4.23) yields

$$2[\mathbf{w}_k(n+1) - \mathbf{w}_k(n)] = \lambda \mathbf{x}(n-k) \tag{4.24}$$

where λ is the *Lagrange multiplier*. The unknown λ is solved by multiplying both sides of (4.24) by $x(n-k)$ and summing over the values of $k = 0$ to $N-1$. The result from (4.24) is therefore

$$\lambda = \frac{2}{\sum_{k=0}^{N-1} |\mathbf{x}(n-k)|^2} \left[\sum_{k=0}^{N-1} \mathbf{w}_k(n+1)\mathbf{x}(n-k) - \sum_{k=0}^{N-1} \mathbf{w}_k(n)\mathbf{x}(n-k) \right] \tag{4.25}$$

$$= \frac{2}{\|\mathbf{x}(n)\|^2} \left[\mathbf{w}^T(n+1)\mathbf{x}(n) - \mathbf{w}^T(n)\mathbf{x}(n) \right]$$

where $\|\mathbf{x}(n)\|$ is the Euclidean norm of the input-tap vector $\mathbf{x}(n)$. Applying the definition of estimation error from (4.6) and the constraint from (4.21) to (4.25),

$$\lambda = \frac{2}{\|\mathbf{x}(n)\|^2} e(n) \tag{4.26}$$

A vector form equivalent can be written by substituting (4.26) into (4.24),

$$\eta(n) = \mathbf{w}(n+1) - \mathbf{w}(n) \tag{4.27}$$

$$= \frac{1}{\|\mathbf{x}(n)\|^2} e(n)$$

A positive step-size parameter, μ, is introduced to (4.27) in order to control the tap-weight from one iteration to the next without changing its direction. Therefore changing (4.27) to

$$\eta(n) = \mathbf{w}(n+1) - \mathbf{w}(n) \tag{4.28}$$

$$= \frac{\mu}{\|\mathbf{x}(n)\|^2} e(n)$$

The recursion for the NLMS algorithm can then be expressed as

$$\mathbf{w}(n+1) = \mathbf{w}(n) + \frac{\mu}{\|\mathbf{x}(n)\|^2} \mathbf{x}(n)e(n) \tag{4.29}$$

The tap-weight vector $\mathbf{w}(n+1)$ computed at time index $n+1$ is updated in such a way that the tap-weights exhibit minimum change with respect to the known $\mathbf{w}(n)$ at time index n. Hence the NLMS algorithm can be seen as a manifestation of the principle of minimal disturbance which states that, in the light of new input data, the parameters of an adaptive system should be disturbed in a minimal fashion [4.14].

The NLMS algorithm introduces a problem of its own when overcoming the problem of gradient noise amplification that is associated with the LMS algorithm. In the instance of a large input-tap vector, $\mathbf{x}(n)$, the NLMS algorithm is able to normalise the correction vector, $\mathbf{x}(n)e(n)$, with respect to the squared Euclidean norm of the input-tap vector, $\mathbf{x}(n)$. However in the instance when $\mathbf{x}(n)$ is small, numerical difficulties may arise due to the division by a small value of the squared norm $\|\mathbf{x}(n)\|^2$. To ensure that numerical difficulties does not arises, a slight modification is made to the recursion of (4.29) by introducing a small scalar value, σ, yielding

$$\mathbf{w}(n+1) = \mathbf{w}(n) + \frac{\mu}{\sigma + \|\mathbf{x}(n)\|^2} \mathbf{x}(n)e(n) \tag{4.30}$$

Thus, the NLMS algorithm can be seen as a modification of the LMS algorithm that normalises the tap-weight vector with respect to the squared Euclidean norm of the input-tap vector. The complex notation of the NLMS adaptive algorithm for a MPSK modulation scheme is depicted in Table 4-2.

Parameters N = Number of taps for $n = 0,1,2,\ldots,N-1$

μ = Step-size parameters

α = Small positive constant $\alpha > 0$

Initial Conditions Tap-Weights

$$w_I(0) = 0 \qquad w_Q(0) = 0$$

For each time instant, n = 0,1, 2, ... , N – 1 compute

1. Complex filter output:

$$y_I(n) = \mathbf{w}_I^T(n)\mathbf{x}_I(n) - \mathbf{w}_Q^T(n)\mathbf{x}_Q(n)$$

$$y_Q(n) = \mathbf{w}_I^T(n)\mathbf{x}_Q(n) + \mathbf{w}_Q^T(n)\mathbf{x}_I(n)$$

2. Complex Error Estimation:

$$e_I(n) = d_I(n) - y_I(n) \qquad e_Q(n) = d_Q(n) - y_Q(n)$$

3. Complex Tap-weight adaptation:

$$\mathbf{w}_I(n+1) = \mathbf{w}_I(n) + \mu\left[\frac{1}{\alpha + \|\mathbf{x}_I(n)\|^2} e_I(n)\mathbf{x}_I(n) + \frac{1}{\alpha + \|\mathbf{x}_Q(n)\|^2} e_Q(n)\mathbf{x}_Q(n)\right]$$

$$\mathbf{w}_Q(n+1) = \mathbf{w}_Q(n) + \mu\left[\frac{1}{\alpha + \|\mathbf{x}_Q(n)\|^2} e_I(n)\mathbf{x}_Q(n) - \frac{1}{\alpha + \|\mathbf{x}_I(n)\|^2} e_Q(n)\mathbf{x}_I(n)\right]$$

Table 4-2 Adaptation of the complex NLMS algorithm

4.2.3 Variable Step-Size LMS algorithm

The step-size parameter, μ, plays a significant part in governing the performances of the LMS algorithm, by which the rate of convergence changes in proportion to the step-size parameter. Therefore, a large μ is required to minimise the transient time of the LMS algorithm. However, a small μ is needed to achieve a small misadjustment, which is a measure of the amount of MSE that deviates from the minimum mean-squared error produced by the Wiener filter. The Variable Step-Size LMS (VSLMS) algorithm, which is based on the method of steepest descent utilises an independent step-size parameter for each tap-weight update and is therefore an effective solution to these conflicting requirements [4.15].

Following the formulation of the LMS tap-weight vector recursion of (4.15), a similar approach of obtaining the optimum step-size parameter for the VSLMS algorithm can be expressed as

$$\mu_k(n) = \mu_k(n\text{-}1) - \beta \frac{\delta \xi}{\delta \mu_k(n-1)} \tag{4.31}$$

where β is a small positive adaptation parameter. From the analogy of the LMS algorithm, the stochastic gradient recursion of (4.31) is

$$\mu_k(n) = \mu_k(n\text{-}1) - \beta \frac{\delta e^2(n)}{\delta \mu_k(n-1)} \tag{4.32}$$

Using (4.16), the last factor on the right hand side of (4.32) can be obtained as

$$\frac{\delta e^2(n)}{\delta \mu_k(n-1)} = 2e(n) \frac{\delta e(n)}{\delta \mu_k(n-1)} \tag{4.33}$$

$$= -2e(n)x_k(n) \frac{\delta w_k(n)}{\delta \mu_k(n-1)}$$

According to the LMS algorithm, the tap-weight, $\mathbf{w}_k(n)$, is related to the step-size recursion, $\mu_k(n-1)$,

$$w_k(n) = w_k(n-1) + 2\mu_k(n-1)e(n-1)x_k(n-1) \tag{4.34}$$

By differentiating (4.34) with respect to $\mu_k(n-1)$ and substituting to (4.33) yields

$$\frac{\delta e^2(n)}{\delta \mu_k(n-1)} = -g_k(n)g_k(n-1) \tag{4.35}$$

where $g_k(n)$ is defined as

$$g_k(n) = -2e(n)x_k(n) \tag{4.36}$$

By substituting (4.35) to (4.32), the stochastic gradient recursion of the VSLMS algorithm can be expressed as

$$\mu_k(n) = \mu_k(n\text{-}1) + \beta g_k(n)g_k(n-1) \tag{4.37}$$

where β is a small positive step-size parameter. Although, the optimality of the VSLMS algorithm may be obtained by solving rigorously for a set of unknown step-size parameters [4.16]-[4.17], such solutions are lengthy and also require an offset of substantial computational load. A simple yet effective method of solving the set of unknown step-size parameters is to initialise a set of upper and lower limits, μ_{max} and μ_{min} respectively, for the step-size parameters. This is to ensure that the step-size parameter does not become too large (resulting in system instability) or too small (resulting in a slow response to a sudden change to the data due to the time-variant environment). Table 4-3 summarises the complex implementation of the VSLMS algorithm.

Parameters N = Number of taps for $n = 0,1,2,...,N-1$

μ_{max} = Maximum step-size value

μ_{min} = Minimum step-size value $\Big\}\ 0 < \mu_{min} < \mu_{max}$

g = Stochastic gradient terms

β = Small positive step-size parameter $\gamma > 0$

Initial Conditions Tap-Weights

$$w_I(0) = 0 \qquad w_Q(0) = 0$$

Step-size parameters

$$\mu_I(0) = \mu_{max} \qquad \mu_I(0) = \mu_{max}$$

For each time instant, n = 0,1, 2, ... , N – 1 compute

1. Complex filter output:

$$y_I(n) = \mathbf{w}_I^T(n)\mathbf{x}_I(n) - \mathbf{w}_Q^T(n)\mathbf{x}_Q(n)$$

$$y_Q(n) = \mathbf{w}_I^T(n)\mathbf{x}_Q(n) + \mathbf{w}_Q^T(n)\mathbf{x}_I(n)$$

2. Complex Error Estimation:

$$e_I(n) = d_I(n) - y_I(n) \qquad e_Q(n) = d_Q(n) - y_Q(n)$$

3. Complex Step-Size adaptation:

$$g^*(n) = e^*(n)x^*(n-1)$$

$$\mu^*(n) = \mu^*(n-1) + \beta g^*(n)g^*(n-1)$$

Conditions

$$\text{if } \mu^*(n) > \mu_{max},\ \mu^*(n) = \mu_{max}$$

$$\text{if } \mu^*(n) < \mu_{min},\ \mu^*(n) = \mu_{min}$$

4. Complex Step-Size adaptation:

$$\mathbf{w}_I(n+1) = \mathbf{w}_I(n) + \mu^*\left[e_I(n)\mathbf{x}_I(n) + e_Q(n)\mathbf{x}_Q(n)\right]$$

$$\mathbf{w}_Q(n+1) = \mathbf{w}_Q(n) + \mu^*\left[e_I(n)\mathbf{x}_Q(n) - e_Q(n)\mathbf{x}_I(n)\right]$$

Table 4-3 Adaptation of the complex VSLMS

4.2.4 Kalman algorithm

Applications of Kalman adaptive filtering was first reported in the literature by Lawrence and Kaufman [4.18], where Kalman filtering was constructed into an equaliser to provide an estimation of the channel input. This was followed by Godard [4.19], who used a different approach in formulating the adaptive filtering problem by which a tap delay-line structure was introduced to estimate a state vector in Gaussian noise. This prompted other extensive investigations of the application of the Kalman adaptive algorithm.

A linear, discrete-time dynamical system signal-flow graph is shown in Figure 4-4 [4.20]. The state vector, $w(n)$, is defined as a set of quantities that is used to define the dynamical behaviour of the system. As $w(n)$ is generally unknown, a set of observation data, $d_o(n)$, is used to estimate it. The Kalman filtering problem for this linear system can be formulated by two equations: the processing equation, $w(n+1)$, which describes the dynamics of the system, and the measurement equation, $d(n)$, which describes the measurement error incurred in the system. From Figure 4-4, the processing and the measurement equations can be expressed as

$$\mathbf{w}(n+1) = \boldsymbol{\kappa}(n+1,n)\mathbf{w}(n) + \mathbf{v}_p(n) \tag{4.38}$$

and

$$\mathbf{d}_o(n) = \mathbf{r}(n)\mathbf{w}(n) + \mathbf{v}_m(n) \tag{4.39}$$

where $\boldsymbol{\kappa}(n+1,n)$ is a $N \times N$ transition matrix relating the state of the system at times $n+1$ and n, $\mathbf{r}(n)$ is the measurement matrix. The $N \times 1$ vectors, $\mathbf{v}_p(n)$ of (4.38), and $\mathbf{v}_m(n)$ of (4.39), are the process noise and the measurement noise respectively. The statistically independent vectors are modelled as a zero-mean, white noise processes whose correlation matrices are defined as

$$E[\mathbf{v}_p(n)\mathbf{v}_p^T(k)] = \begin{cases} \mathbf{Q}_p(n) & n = k \\ 0 & n \neq k \end{cases} \tag{4.40}$$

and

$$E[\mathbf{v}_m(n)\mathbf{v}_m^T(k)] = \begin{cases} \mathbf{Q}_m(n) & n = k \\ 0 & n \neq k \end{cases} \tag{4.41}$$

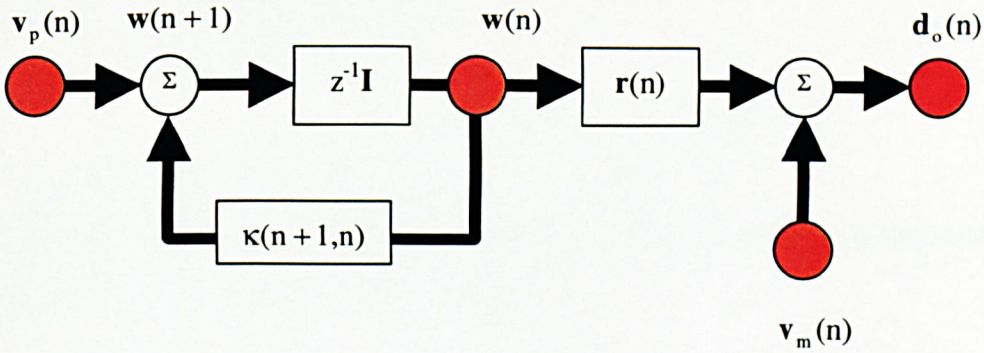

Figure 4-4 Signal-flow of a linear, discrete-time dynamical Kalman system

The Kalman filtering problem can be solved by the approach of the innovation process [4.21], which is defined as

$$\alpha(n) = \mathbf{d}_o(n) - \hat{\mathbf{d}}_o(n) \tag{4.42}$$

where $\hat{\mathbf{d}}_o(n)$ denotes the minimum mean-square estimate of the observed data $d_o(n)$ starting at time $n = 1$ extending to and including time $n-1$. From the minimum mean-square estimate of (4.39), the measurement noise vector is zero since $v_m(n)$ is orthogonal to the past observations, which gives

$$\hat{\mathbf{d}}_o(n) = \mathbf{r}(n)\mathbf{w}(n) \tag{4.43}$$

Substituting (4.43) to (4.42) gives the innovation process

$$\alpha(n) = \mathbf{d}_o(n) - \mathbf{r}(n)\mathbf{w}(n) \tag{4.44}$$

The correlation matrix of the innovation process is defined as [4.21]

$$\mathbf{R}(n) = \mathbf{r}(n)\mathbf{K}(n,n-1)\mathbf{r}^T(n) + \mathbf{Q}_m(n) \tag{4.45}$$

where $\mathbf{K}(n,n-1)$ is the predicted state-error correlation matrix, which was derived as the Riccati difference equation as

$$\mathbf{K}(n) = \mathbf{K}(n,n-1) - \boldsymbol{\kappa}(n,n+1)\mathbf{G}(n)\mathbf{r}(n)\mathbf{K}(n,n-1) \tag{4.46}$$

where $\mathbf{G}(n)$ is the Kalman gain given as

$$\mathbf{G}(n) = \boldsymbol{\kappa}(n+1,n)\mathbf{K}(n,n-1)\mathbf{r}^{H}(n)\mathbf{R}^{-1}(n) \tag{4.47}$$

The minimum mean-square estimate of (4.38) can be expressed as a linear combination of the sequence of innovations processes [4.9],

$$\mathbf{w}(i) = \sum_{k=1}^{n} \mathbf{B}_i(k)\boldsymbol{\alpha}(k) \tag{4.48}$$

where $\mathbf{B}_i(k)$ is given by

$$\mathbf{B}_i(k) = E[\mathbf{w}(i)\boldsymbol{\alpha}^{H}(k)]\mathbf{R}^{-1}(k) \tag{4.49}$$

For $i = n+1$, and substituting (4.49) to (4.48) yields

$$\mathbf{w}(n+1) = \sum_{k=1}^{n-1} E[\mathbf{w}(n+1)\boldsymbol{\alpha}^{H}(k)]\mathbf{R}^{-1}(k)\boldsymbol{\alpha}(k)$$

$$+E[\mathbf{w}(n+1)\boldsymbol{\alpha}^{H}(n)]\mathbf{R}^{-1}(n)\boldsymbol{\alpha}(n) \tag{4.50}$$

where the second term on the right hand side of (4.50), excluding the innovation process, is the raw expression of the Kalman gain of (4.47). It can also be seen that the summation first term of (4.50) can be rewritten as

$$\sum_{k=1}^{n-1} E[\mathbf{w}(n+1)\boldsymbol{\alpha}^{H}(k)]\mathbf{R}^{-1}(k)\boldsymbol{\alpha}(k) = \boldsymbol{\kappa}(n+1,n)\mathbf{w}(n) \tag{4.51}$$

Therefore (4.50) can be expressed as

$$\mathbf{w}(n+1) = \boldsymbol{\kappa}(n+1,n)\mathbf{w}(n) + \mathbf{G}(n)\boldsymbol{\alpha}(n) \tag{4.52}$$

The equations in that order of (4.47), (4.45), (4.43), (4.52) and (4.46) then define the Kalman's one step prediction algorithm. Implementation of the Kalman algorithm is summarised in Table 4-4.

Parameters N = Number of taps for $n = 0,1,2,...,N-1$

$\mathbf{Q}_m$, $\mathbf{Q}_p$= Correlation matrix for measurement and process noise

Initial Conditions Tap-Weights

$$w_I(0) = 0 \qquad w_Q(0) = 0$$

Measurement and Process noise

$$Q_m = \delta^{-1}I \quad Q_m = \chi^{-1}I \qquad \text{where } \delta < \chi$$

For each time instant, n = 0,1, 2, ... , N – 1 compute

1. Computation of complex Gain vector:

$$\mathbf{G}(n) = \frac{\mathbf{K}^*(n-1)\mathbf{r}^*(n)}{\mathbf{r}^*(n)\mathbf{K}^*(n-1)\mathbf{r}^{*H}(n) + \mathbf{Q}_m(n))}$$

2. Complex filter output:

$$y_I(n) = \mathbf{w}_I^T(n)\mathbf{r}_I(n) - \mathbf{w}_Q^T(n)\mathbf{r}_Q(n)$$

$$y_Q(n) = \mathbf{w}_I^T(n)\mathbf{r}_Q(n) + \mathbf{w}_Q^T(n)\mathbf{r}_I(n)$$

3. Complex Error Estimation:

$$\alpha^*(n) = d^*(n) - y^*(n)$$

4. Complex Tap-weight adaptation:

$$\mathbf{w}_I(n+1) = \mathbf{w}_I(n) + [\mathbf{G}_I(n)\alpha_I(n) + \mathbf{G}_Q(n)\alpha_Q(n)]$$

$$\mathbf{w}_Q(n+1) = \mathbf{w}_Q(n) + [\mathbf{G}_I(n)\alpha_Q(n) - \mathbf{G}_Q(n)\alpha_I(n)]$$

5. Complex input covariance matrix:

$$\mathbf{K}^*(n) = \mathbf{K}^*(n-1) - \mathbf{G}(n)\mathbf{r}^*(n)\mathbf{K}^*(n-1) + \mathbf{Q}_p$$

$$\mathbf{K}^*(n-1) = \mathbf{K}^*(n) + \mathbf{Q}_p$$

Table 4-4 Adaptation of the complex Kalman algorithm

4.2.5 Recursive Least Square (RLS) algorithm

The LMS algorithm method of tap-weight update strives to minimise the mean square of the estimation error, $\xi(n)$. The tap-weight parameters in the Recursive Least Square (RLS) algorithm are optimised by utilising information in the input data from time index, $n > 0$, till the present sample and minimising the sum of squared values of the error samples of the filter output such that the cost function, at any time index $n > 0$, can be minimised

$$\xi(n) = \sum_{k=1}^{n} \rho_n(k) e_n^2(k) \tag{4.53}$$

where $e^2(n)$ is the estimated error as defined in (4.2). The weighting factor, $\rho(k)$, with property,

$$0 < \rho_n(k) \leq 1 \qquad k = 1,2,...,n \tag{4.54}$$

is used to ensure that the data in the distant past are "forgotten" in order to allow the filter, when operating in a time-variant environment, the possibility of following the statistical variations of the input data [4.22]. The exponential weighting or forgetting factor is one of the commonly used weighting, which is defined by

$$\rho_n(k) = \lambda^{n-k} \qquad k = 1,2,...,n \tag{4.55}$$

where λ is a positive constant close to, but smaller than, 1.0. When $\lambda < 1.0$, the forgetting factor defined by (4.55) gives more weight to the recent data samples of the error estimates compared to the old ones, thus forgetting the past. Roughly speaking, the inverse of $1-\lambda$ is a measure of the memory of the algorithm. The case of $\lambda = 1.0$ corresponds to an infinite memory. From the perspective of practical signal processing, the forgetting factor is kept within a range $0.95 < \lambda < 1.0$ [4.23]. By substituting (4.55) in (4.53) and using matrix notation, the cost function is expressed as

$$\xi(n) = \mathbf{e}^T(n)\mathbf{\Lambda}(n)\mathbf{e}(n) \tag{4.56}$$

where $\mathbf{\Lambda}(n)$ is the diagonal matrix consisting of the forgetting factors

$$\mathbf{\Lambda}(n) = \begin{bmatrix} \lambda^{n-1} & 0 & 0 & \cdots & 0 \\ 0 & \lambda^{n-2} & 0 & \cdots & 0 \\ 0 & 0 & \lambda^{n-3} & \cdots & 0 \\ \vdots & \vdots & \vdots & \ddots & \vdots \\ 0 & 0 & 0 & \cdots & 1 \end{bmatrix} \tag{4.57}$$

The optimum tap-weight vector for which the cost function of (4.56) attains its minimum is defined by the normal equations written in matrix form

$$\mathbf{w}(n) = \mathbf{\Psi}_{\lambda}^{-1}(n)\boldsymbol{\theta}_{\lambda}(n) \tag{4.58}$$

where the $N \times N$ correlation vector is defined by

$$\mathbf{\Psi}_{\lambda}(n) = \mathbf{x}^{T}(n)\mathbf{\Lambda}(n)\mathbf{x}(n) \tag{4.59}$$

and the $N \times 1$ correlation vector is

$$\boldsymbol{\theta}_{\lambda}(n) = \mathbf{x}(n)\mathbf{\Lambda}(n)\mathbf{d}(n) \tag{4.60}$$

Applying the input data vector of (4.3) and expanding the summations in (4.59) and (4.60)

$$\mathbf{\Psi}_{\lambda}(n) = \mathbf{x}(n)\mathbf{x}^{T}(n) + \lambda\mathbf{x}(n-1)\mathbf{x}^{T}(n-1) + \lambda^{2}\mathbf{x}(n-2)\mathbf{x}^{T}(n-2) + \cdots \tag{4.61}$$

$$\boldsymbol{\theta}_{\lambda}(n) = \mathbf{x}(n)d(n) + \lambda\mathbf{x}(n-1)d(n) + \lambda^{2}\mathbf{x}(n-2)d(n) + \cdots \tag{4.62}$$

From the expression of (4.61) and (4.62), the recursion of the autocorrelation vector, $\mathbf{\Psi}_{\lambda}(n)$, and the cross-correlation vector, $\boldsymbol{\theta}_{\lambda}(n)$, can be obtained recursively as

$$\mathbf{\Psi}_{\lambda}(n) = \lambda\mathbf{\Psi}_{\lambda}(n-1) + \mathbf{x}^{T}(n)\mathbf{x}(n) \tag{4.63}$$

and

$$\boldsymbol{\theta}_{\lambda}(n) = \lambda\boldsymbol{\theta}_{\lambda}(n-1) + \mathbf{x}(n)d(n) \tag{4.64}$$

The resulting two recursions of (4.63) and (4.64) form the basis for the derivation of the RLS algorithm. In order to compute the tap-weights recursively and to avoid the long computational load of determining the inverse of the correlation matrix, the tap-weight vector can be computed by using matrix algebra, and in particular the *matrix inversion lemma* [4.24].

For an arbitrary non-singular $N \times N$ matrix $\mathbf{A}$, any $N \times 1$ vector $\mathbf{B}$ and a scalar α, the identity of the *matrix inversion lemma* can be expressed as

$$(\mathbf{A} + \alpha \mathbf{B}\mathbf{B}^{T})^{-1} = \mathbf{A}^{-1} - \frac{\alpha \mathbf{A}^{-1}\mathbf{B}\mathbf{B}^{T}\mathbf{A}^{-1}}{1 + \alpha \mathbf{B}^{T}\mathbf{A}^{-1}\mathbf{B}} \tag{4.65}$$

Let $\mathbf{A} = \lambda \boldsymbol{\Psi}_{\lambda}(n-1)$, $\mathbf{B} = \mathbf{x}(n)$ and $\alpha = 1$, the inverse of the correlation matrix of (4.63) can be evaluated as

$$\boldsymbol{\Psi}_{\lambda}^{-1}(n) = \lambda^{-1}\boldsymbol{\Psi}_{\lambda}^{-1}(n\text{-}1) - \frac{\lambda^{-2}\boldsymbol{\Psi}_{\lambda}^{-1}(n\text{-}1)\mathbf{x}(n)\mathbf{x}^{T}(n)\boldsymbol{\Psi}_{\lambda}^{-1}(n\text{-}1)}{1 + \lambda^{-1}\mathbf{x}(n)\boldsymbol{\Psi}_{\lambda}^{-1}(n\text{-}1)\mathbf{x}^{T}(n)} \tag{4.66}$$

To simplify computation, a column vector of dimension $N \times 1$ is defined

$$\mathbf{K}(n) = \frac{\lambda^{-1}\boldsymbol{\Psi}^{-1}(n\text{-}1)\mathbf{x}(n)}{1 + \lambda^{-1}\mathbf{x}(n)\boldsymbol{\Psi}^{-1}(n\text{-}1)\mathbf{x}^{T}(n)} \tag{4.67}$$

where $\mathbf{K}(n)$ known as the gain vector, is the transformation of the input-tap vector from the inverse of the correlation matrix $\boldsymbol{\Psi}_{\lambda}(n)$. Using these definitions, (4.66) can be rewritten as

$$\boldsymbol{\Psi}_{\lambda}^{-1}(n) = \lambda^{-1}[\boldsymbol{\Psi}_{\lambda}^{-1}(n-1) - \mathbf{K}(n)\mathbf{x}^{T}(n)\boldsymbol{\Psi}_{\lambda}^{-1}(n\text{-}1)] \tag{4.68}$$

Using (4.68) in (4.67) and rearranging gives

$$\mathbf{K}(n) = \boldsymbol{\Psi}_{\lambda}^{-1}(n)\mathbf{x}(n) \tag{4.69}$$

The recursive equation for the tap-weight vector of the RLS algorithm can be obtained by using (4.64) and (4.69) in (4.58)

$$\mathbf{w}(n) = \lambda\boldsymbol{\Psi}_{\lambda}^{-1}(n)\boldsymbol{\theta}_{\lambda}(n-1) + \boldsymbol{\Psi}_{\lambda}^{-1}(n)\mathbf{x}(n)d(n) \tag{4.70}$$

$$= \lambda\boldsymbol{\Psi}_{\lambda}^{-1}(n)\boldsymbol{\theta}_{\lambda}(n-1) + \mathbf{K}(n)d(n)$$

And substituting (4.68) in (4.70),

$$\mathbf{w}(n) = \boldsymbol{\Psi}_{\lambda}^{-1}(n-1)\boldsymbol{\theta}_{\lambda}(n-1) - \mathbf{K}(n)\mathbf{x}^{T}(n)\boldsymbol{\Psi}_{\lambda}^{-1}(n-1)\boldsymbol{\theta}_{\lambda}(n-1) + \mathbf{K}(n)d(n) \tag{4.71}$$

$$= \mathbf{w}(n-1) - \mathbf{K}(n)\mathbf{x}^{T}(n)\mathbf{w}(n-1) + \mathbf{K}(n)d(n)$$

$$= \mathbf{w}(n-1) + \mathbf{K}(n)\varepsilon(n)$$

where $\varepsilon(n)$ is the innovation defined as

$$\varepsilon(n) = [d(n) - \mathbf{x}^{T}(n)\mathbf{w}(n-1)] \tag{4.72}$$

Therefore, the amount of change to be made in the tap-weight at the *n*th iteration is determined by the product of the innovation, $\varepsilon(n)$, and the gain vector, $K(n)$. Figure 4-5 depicts a signal–flow diagram of the RLS algorithm and a summary of the complex RLS algorithm is illustrated in Table 4-5 [4.23].

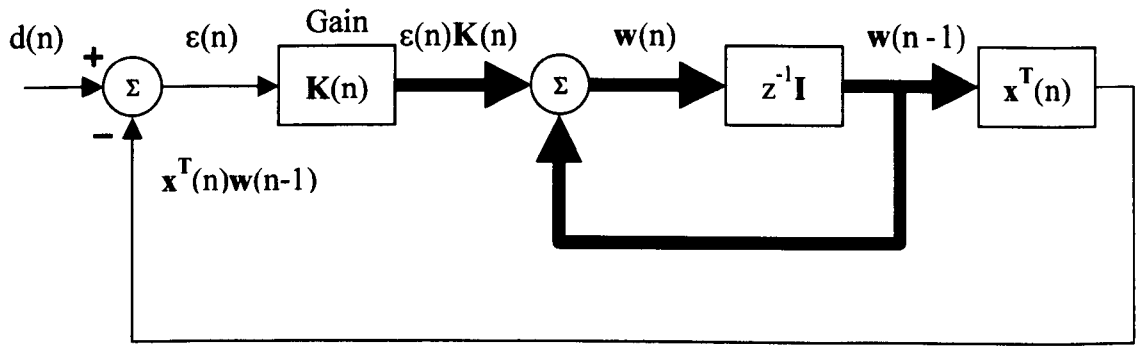

Figure 4-5 Signal flow of the RLS algorithm

Parameters N = Number of taps for $n = 0,1,2,...,N-1$

Initial Conditions Tap-Weights

$$w_I(0) = 0 \qquad w_Q(0) = 0$$

For each time instant, n = 0,1, 2, ... , N – 1 compute

1. Computation of complex Gain vector:

$$\upsilon^*(n) = \mathbf{x}^{*T}(n)\Psi_{*\lambda}^{-1}(n-1)$$

$$\kappa^*(n) = \lambda + \upsilon^*(n)\mathbf{x}^*(n)$$

$$\mathbf{K}^*(n) = \frac{\upsilon^*(n)}{\kappa^*(n)}$$

2. Complex filter output:

$$y_I(n) = \mathbf{w}_I^T(n)\mathbf{x}_I(n) - \mathbf{w}_Q^T(n)\mathbf{x}_Q(n)$$

$$y_Q(n) = \mathbf{w}_I^T(n)\mathbf{x}_Q(n) + \mathbf{w}_Q^T(n)\mathbf{x}_I(n)$$

3. Complex Error Estimation:

$$\varepsilon^*(n) = d^*(n) - y^*(n)$$

4. Complex Tap-weight adaptation:

$$\mathbf{w}_I(n) = \mathbf{w}_I(n-1) + [\mathbf{K}_I(n)\varepsilon_I(n) + \mathbf{K}_Q(n)\varepsilon_Q(n)]$$

$$\mathbf{w}_Q(n) = \mathbf{w}_Q(n-1) + [\mathbf{K}_I(n)\varepsilon_Q(n) - \mathbf{K}_Q(n)\varepsilon_I(n)]$$

6. Complex correlation matrix:

$$\Psi_{*\lambda}^{-1}(n) = \lambda^{-1}[\Psi_{*\lambda}^{-1}(n-1) - \mathbf{K}^*(n)\upsilon^*(n)\Psi_{*\lambda}^{-1}(n-1)]$$

Table 4-5 Adaptation of the standard RLS algorithm

4.2.6 Improved Recursive Least Square (IRLS) algorithm

The tracking capability of the RLS algorithm in a time-varying channel had been reported to be more inferior to the LMS and Kalman filtering algorithms [4.25]-[4.27]. Although recognising that the RLS algorithm is a special case of the Kalman filter, the reason for it not inheriting the good tracking property of the Kalman filter lies in the fundamental formulation of the cost function.

In formulating the RLS algorithm, the exponential weighting constant, ρ^{n-1}, from (4.53) is incorporated into the cost function [4.9]:

$$\xi(n) = \sum_{k=1}^{n} \rho_n(k) e_n^2(k) \tag{4.73}$$

This enables the filter to track the statistical variation in a time-variant environment and was reported by Sayed and Kailah [4.28]-[4.29] to be the root of the problem. Sayed and Kailah described the state-space model with a pair of equations given as

$$\mathbf{w}(n+1) = \lambda^{-1/2}\mathbf{w}(n) \tag{4.74}$$

$$d_o(n) = \mathbf{r}(n)\mathbf{w}(n) + \mathbf{v}_m(n) \tag{4.75}$$

where λ is the forgetting factor and (4.75) is identical to (4.39). Since the transition matrix, $\kappa(n+1,n)$, of (4.39) is time variant as compared to the transition matrix, $\lambda^{-1/2}$, of (4.74), which is governed by a constant multiple of the identity matrix equal to $\lambda^{-1/2}\mathrm{I}$, it can be seen that (4.74) is not the optimal way to estimate the unknown vector, $\mathbf{w}(n)$, in a time-varying channel.

In order to rectify this problem, an extension from the concept of the Kalman filtering algorithms is considered. The optimization criterion can be expressed as

$$\min_{\{\mathbf{w}(0),\mathbf{v}_p(n)\}} \xi\left[\mathbf{w}(0), \mathbf{v}_p(0), \mathbf{v}_p(1), \cdots, \mathbf{v}_p(n)\right] \tag{4.76}$$

where the cost function, ξ, is quadratic in its argument and is given by [4.29],

$$\xi = \left(\mathbf{w}(0)-\bar{\mathbf{w}}\right)^H \Pi_0^{-1}\left(\mathbf{w}(0)-\bar{\mathbf{w}}\right)+\sum_{n=0}^{N}\mathbf{v}_p(n)^H Q^{-1}(n)\mathbf{v}_p(n)+\sum_{n=0}^{N}\frac{|\mathbf{e}(n)|^2}{\sigma^2(n)} \quad (4.77)$$

In the cost function of (4.77), the unknown factors are the initial weight-vector $\mathbf{w}(0)$ and the process noise sequence, $v_p(n)$. The solution for the optimisation of the cost function in (4.76) was shown in [4.29], which gives an iterative procedure that provides recursive estimates of the successive weight vectors, $\mathbf{w}(n)$.

Assuming that the process and the measurement noises is a zero-mean white noise sequence with covariance matrix, $\mathbf{Q}(n)$, and variance σ^2 respectively. The initial state-vector, $\mathbf{w}(0)$, is assumed to be random with mean $\bar{\mathbf{w}}$ and covariance matrix Π_0, expressed as

$$E\left(\mathbf{w}(0)-\bar{\mathbf{w}}\right)\left(\mathbf{w}(0)-\bar{\mathbf{w}}\right)^H = \Pi_0 \quad (4.78)$$

With the assumption that the random variables, $\left\{\mathbf{v}_\mathbf{p}(n), \mathbf{v}_\mathbf{m}(n), \left(\mathbf{w}(0)-\bar{\mathbf{w}}\right)\right\}$, are uncorrelated to each other, the condition in (4.78) may be re-written as

$$E\begin{bmatrix}\mathbf{v}_\mathbf{p}(n)\\ \mathbf{v}_\mathbf{m}(n)\\ \left(\mathbf{w}(0)-\bar{\mathbf{w}}\right)\end{bmatrix}\begin{bmatrix}\mathbf{v}_\mathbf{p}(n)\\ \mathbf{v}_\mathbf{m}(n)\\ \left(\mathbf{w}(0)-\bar{\mathbf{w}}\right)\end{bmatrix}^H = \begin{bmatrix}\mathbf{Q}(n)\delta(n,m) & 0 & 0\\ 0 & \sigma^2(n)\delta(n,m) & 0\\ 0 & 0 & \Pi_0\\ 0 & 0 & 0\end{bmatrix} \quad (4.79)$$

where $\delta(n,m)$ is the *Kronecker* delta function, which is

$$\delta(n,m) = \begin{cases}1 & \text{for } n=m\\ 0 & \text{otherwise}\end{cases} \quad (4.80)$$

In a stationary environment, the measurement noise vector of the input covariance matrix in Table 4-4, is zero which results in $\mathbf{K}(n-1)=\mathbf{K}(n)$, and the modified RLS algorithm is reduced without involving a weighting factor [4.2]. A summary of the improved RLS algorithm is presented in Table 4-6.

Parameters N = Number of taps for $n = 0,1,2,\ldots,N-1$

Initial Conditions Tap-Weights

$$w_I(0) = 0 \qquad w_Q(0) = 0$$

For each time instant, n = 0,1, 2, ... , N – 1 compute

1. Computation of complex Gain vector:

$$\upsilon^*(n) = \mathbf{x}^{*T}(n)\Psi_{\lambda}^{-1}(n-1)$$

$$\mathbf{K}^*(n) = \frac{\upsilon^*(n)}{a + \upsilon^*(n)\mathbf{x}^*(n)}$$

2. Complex filter output:

$$y_I(n) = \mathbf{w}_I^T(n)\mathbf{x}_I(n) - \mathbf{w}_Q^T(n)\mathbf{x}_Q(n)$$

$$y_Q(n) = \mathbf{w}_I^T(n)\mathbf{x}_Q(n) + \mathbf{w}_Q^T(n)\mathbf{x}_I(n)$$

3. Complex Error Estimation:

$$\varepsilon^*(n) = d^*(n) - y^*(n)$$

4. Complex Tap-weight adaptation:

$$\mathbf{w}_I(n) = \mathbf{w}_I(n-1) + [\mathbf{K}_I(n)\varepsilon_I(n) + \mathbf{K}_Q(n)\varepsilon_Q(n)]$$

$$\mathbf{w}_Q(n) = \mathbf{w}_Q(n-1) + [\mathbf{K}_I(n)\varepsilon_Q(n) - \mathbf{K}_Q(n)\varepsilon_I(n)]$$

7. Complex correlation matrix:

$$\Psi_{\lambda}^{-1}(n) = \Psi_{\lambda}^{-1}(n-1) - \mathbf{K}(n)\mathbf{x}^T(n)\Psi_{\lambda}^{-1}(n-1)$$

Table 4-6 Adaptation of the improved RLS algorithm

4.3 Blind Adaptive Equalisation Algorithm

In the instance when the system is unknown and a precise knowledge of the input signal is not available, the effectiveness of the supervised adaptive equalisation techniques reduces. In this situation, adaptive blind deconvolution, which does not employ training sequence for the adjustments of the equaliser's tap weight may be employed to address this problem. The implicit Higher-order statistics (HOS) based algorithms is chosen for investigation due mainly to its computational simplicity.

4.3.1 Implicit Higher-Order Statistics (HOS) Algorithms

4.3.1.1 Decision-Directed Bussgang Algorithm

The fundamental principal of blind deconvolution is to determine an impulse response, c_i, of the ideal inverse filter, which can then be related to the impulse response of the unknown channel, h_i, such that

$$\sum_i c_i h_{\ell-i} = \delta_\ell \tag{4.81}$$

where δ_ℓ is the *Kronecker delta*:

$$\delta_\ell = \begin{cases} 1 & l = 0 \\ 0 & l \neq 0 \end{cases} \tag{4.82}$$

The simple inverse filter defined by (4.81) is an "ideal" case in the sense that it is able to reconstruct the received data correctly,

$$\sum_i c_i x(n-i) = \sum_\ell d(n-\ell) \sum_i c_i h_{\ell-i} \tag{4.83}$$

Theoretically, by applying the definition of (4.81) into (4.83), the desired signal can be retrieved as

$$\sum_i c_i x(n-i) = \sum_\ell \delta_\ell d(n-\ell) \tag{4.84}$$

$$= d(n)$$

As the underwater channel, h_n, is time-variant and unknown, (4.81) cannot be used to determine the inverse filter in order to retrieve the desired signal. Instead, an iterative deconvolution procedure can be used to compute the tap weights of the equalisers such that the convolution of c(n) and the received signal x(n) at time index *n* may yield a complete or partial removal of the ISI with a deconvolved sequence [4.30]

$$y(n) = \sum_{i=-L}^{L} c_i(n)x(n-i) \tag{4.85}$$

where $2L+1$ is the truncated length of the impulse response. Using (4.84), (4.85) is simplified as

$$y(n) = d(n) + q(n) \tag{4.86}$$

where q(n) is the convolved noise that represents the ISI resulting from the use of the approximate inverse filter. The output y(n) is then fed to a zero-memory non-linear estimator, which can then produce an estimate $\hat{d}(n)$ for the data sequence y(n) denoted by

$$\hat{d}(n) = \varphi(y(n)) \tag{4.87}$$

where $\varphi(.)$ is some non-linear function. This forms the basis for the discussion of the subsequent sub-topics of Bussgang algorithms. Assuming that the Bussgang algorithm has attained convergence in the received signal and the eye pattern has opened up, the adaptive equaliser can then switch to a decision directed mode of operation, and the MMSE control of the adaptive tap-weights for the equaliser can be exercised. A decision device can replace the condition in (4.87)

$$\hat{d}(n) = dec(y(n)) \tag{4.88}$$

The algorithm flow of the decision-directed algorithm is the same as the LMS algorithms of Table 4-1, with difference being the error estimation, which is updated as

$$e(n) = \hat{d}(n) - y(n) \tag{4.89}$$

4.3.1.2 Sato Algorithm

The pioneering work of blind equalisation for M-ary systems dates back to the work of Sato [4.31]. The Sato algorithm utilises a minimisation of the cost function of (4.1) in a nonconvex manner, meaning that the error performance surface attained by this method may have local minima in addition to a global minimum. This is in contrast with the cost function of the LMS algorithm in chapter 4.2.1, which is a convex (quadratic) function of the adaptive tap-weights and therefore having a well-defined minimum point. The cost function of the Sato algorithm can be expressed as

$$\xi = E[(\hat{d}(n) - y(n))^2] \tag{4.90}$$

where $y(n)$ is the filter output and $E[\cdot]$ denotes the statistical expectation. The zero-memory non-linear estimator is described as

$$\hat{d}(n) = \chi \text{sgn}(y(n)) \tag{4.91}$$

The sgn(.) is the signum function and the constant χ sets the gain of the equaliser defined by

$$\chi = \frac{E[x^2(n)]}{E[|x(n)|]} \tag{4.92}$$

Using (4.90) and (4.91), the error estimation is updated as

$$e(n) = \frac{E[x^2(n)]}{E[|x(n)|]} \text{sgn}(y(n)) - y(n) \tag{4.93}$$

4.3.1.3 Constant Modulus Algorithm

The family of constant modulus algorithms (CMA) was first introduced by Godard [4.32]. This type of blind equalisation algorithms was introduced for use in M-ary PSK digital communication systems. The Godard algorithm was designed to counter effect the deviations of the blind equaliser output from a constant modulus. The algorithm minimises the nonconvex cost function into the form of

$$\xi(n) = E[(|y(n)|^k - M_k)^2] \tag{4.94}$$

where k is an positive integer and M_k is a positive real constant defined by

$$M_k = \frac{E[|x(n)|^{2k}]}{E[|x(n)|^k]} \tag{4.95}$$

The tap-weight vector of the equaliser is adapted in accordance with the LMS algorithms of Table 4-1 [4.32] and the error update is defined as

$$e(n) = y(n)|y(n)|^{k-2}\left(M_k - |y(n)|^k\right) \tag{4.96}$$

In the case where $k = 1$, the cost function of (4.94) is deduced as

$$\xi(n) = E[(|y(n)| - M_1)^2] \tag{4.97}$$

where

$$M_1 = \frac{E[|x(n)|^2]}{E[|x(n)|]} \tag{4.98}$$

Using (4.98), the error update is given as

$$e(n) = \frac{y(n)}{|y(n)|}\left(M_1 - |y(n)|\right) \tag{4.99}$$

The Godard algorithm, in this case, was viewed as an extension from the Sato algorithm. When $k = 2$, the Godard algorithm is referred to as the constant modulus algorithm (CMA) [4.33]. The cost function of (4.94) is deduced as

$$\xi(n) = E[(|y(n)|^2 - M_2|)^2] \tag{4.100}$$

where

$$M_2 = \frac{E[|x(n)|^4]}{E[|x(n)|^2]} \tag{4.101}$$

And the error update is, using (4.101), given as

$$e(n) = y(n)\left(M_2 - |y(n)|^2\right) \tag{4.102}$$

4.4 Performance Comparison of the Adaptive Algorithms

In this section, both the supervised and blind adaptive algorithms are tested using simulated and sea-trial experimental data. First is the rate of convergence, which is defined as the required number of iterations by the adaptive algorithm to achieve convergence to the optimum minimum point in the error performance surface, or the Wiener solution. As the shallow water channel is time-variant, the adaptive algorithms have the added task of tracking the minimum point that is no longer fixed. The second criteria of assessment for the adaptive algorithms is to track statistical variations in the environment. A common figure of merit that is used to access the tracking capabilities of the algorithms is the mean-square deviation between the unknown input weight vector and the adjusted weight vector [4.34].

4.4.1 Decision Feedback Equaliser

An overview description of the receiver structure adopted for the simulation, adaptive Decision Feedback Equaliser (DFE) [4.35], is covered in this section. A detailed treatment of the DFE (single user detection) is discussed in sections 5.3 and 5.4, of chapter 5, respectively. The DFE, shown in Figure 4-6, consist of a feedforward and feedback filters, a training block and a decision block. Both the feedforward and feedback filters are realised as transversal finite impulse response (FIR) filters.

The DFE operates first in the training mode, which uses a priori known training sequence. Once training is completed, any channel characteristic variations are tracked by the decision directed mode. In decision directed mode, the decision block attempts to map the sampled data from the FIR filters onto the IQ constellation containing the most ideal symbol. In the process of mapping the symbol, an error is generated, where the error is the Euclidean distance between the received signal and the ideal value, of which the difference represents the complex error signal.

When the current received symbol is estimated, the ISI contribution of this symbol is removed from future received symbol, which means that once the decision device quantifies the input sampled data to the closest IQ constellation point, the filter can then calculate the ISI effect on subsequent symbols and attempt to compensate the input of the decision block. The output from the decision error is fed into the feedforward FIR filter, the output of which compensates the decision block. The feedback FIR filter is

responsible for cancelling the ISI effects on subsequent future symbols due to the current symbol.

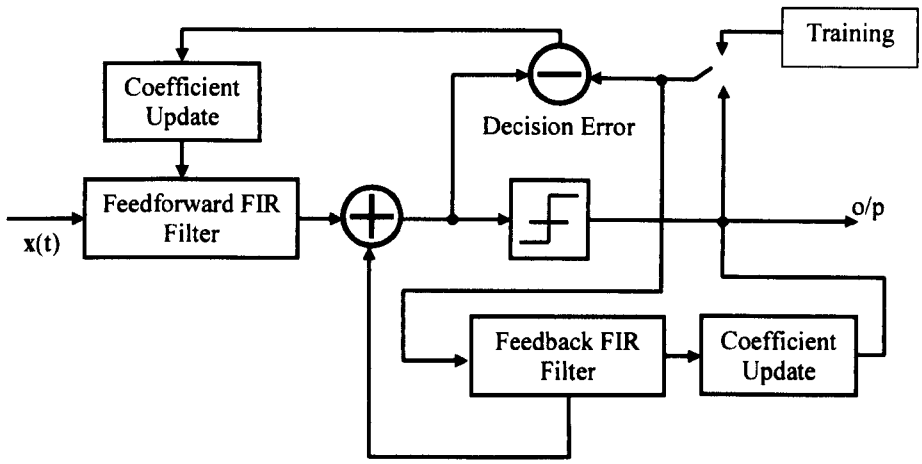

Figure 4-6 Block diagram of a Decision Feedback Equaliser

4.4.2 Simulated Results

Assuming that the channel is slowly changing or time-invariant, then the deterministic geometrical multipath channel model described in section 3.7 can be used to provide an estimation of transmission loss, due to multipath propagation, in the signal propagation through the shallow water medium. Uncorrelated AWGN was superimposed on the transmitted data packet to give input SNR = 10 dB.

The simulation results were obtained from a vertical 6-element array of equal spacing. A 511 bits BPSK PN sequence was used for the training of the adaptive equaliser and a 4096 sps QPSK data packet for performance tests. Clock synchronisation was assumed to have been achieved prior to training and demodulation of the data packet. A sampling frequency of 65.536 kHz was chosen to approximate with the settings of the receiver system for the sea-trials, described in chapter 6. The parameters used for the simulation are depicted in Table 4-7.

Both the forward and feedback filters of the adaptive equaliser uses 15 taps length respectively, refer to Appendix Figure 2 of Appendix VI for taps length selection. The tap coefficients of the adaptive algorithms were initially set to zero. The parameter values used by the adaptive algorithms are listed in Table 4-8, refer to Appendix Figure 3 – Figure 6 of Appendix VI for optimised parameters selection.

Frequency	B_w = 8 - 12 kHz
Carrier Frequency	F_c = 10 kHz
Modulation	Coherent QPSK
Channel Depth	18 m
Tx Depth for user	9 m
Rx Array Depth	First element at 6 m ref. to sea surface
No. of Elements	6
Channel	Geometrical Multipath Model
Distance	2000 m
Noise	AWGN
Training symbols	511
Data packet length	4096 (8192 bits) - Gray coded
Input SNR	10 dB

Table 4-7 Simulation parameters setting

	Algorithms	Parameters	Forward & Feedback values	
1.	LMS,NLMS	Step size, μ	0.007	0.005
2.	NLMS	Constant, α	0.0001	0.0001
3.	VSLMS	Step size, μ_{max}	0.009	0.007
		Step size, μ_{min}	0.005	0.003
4.	RLS	Forgetting factor, λ	0.98	0.98
5.	Sato, Godard	Step size, μ	0.006	0.004

Table 4-8 Algorithm parameter settings

4.4.2.1 Comparison of Supervised Adaptive Algorithms

The rate of convergence in the error performance surface during the training period for the supervised adaptive algorithms is shown in Figure 4-7. It can be seen that in a steady channel, most of the supervised algorithms achieves convergence by 150 symbol iterations, with improved convergence in the mean square error of the error performance surface occurring after 150 symbol. Both the LMS and normalised LMS algorithms were observed to be performing in roughly the same manner, both requiring the same number of symbol iteration to achieve convergence. The VSLMS algorithm, which was bounded by the upper and lower step-size values assure that convergence is relatively faster as compared to the LMS and normalised LMS algorithm. Both the Kalman and RLS algorithm, were also observed to perform roughly in the same manner, as the RLS can be considered as a class of the Kalman algorithm derived by using a state-space model that matches the RLS model [4.28]. By omitting the forgetting factor from the updating of the inverse correlation matrix, the improved RLS was observed to achieve convergence at 120 symbol iterations.

When switching from the training mode to the decision mode for continuous adjustment of the parameters of the adaptive filter, the mean-square deviation was used as a figure of merit for the tracking assessment [4.34], which is defined as

$$\chi(n) = E[\|\hat{w}(n)-w_u(n)\|^2]$$

$$= E[\|e(n)\|^2] \tag{4.103}$$

The computed MSE during the decision mode obtained by the supervised algorithms is shown in Figure 4-8. The tracking performance of the supervised algorithms was seen to be in tune with theoretical point-of-view of the algorithms when operating in a time-invariant channel. Figure 4-9 (a)-(f) shows the demodulated I-Q phase-constellation obtained by the various adaptive algorithms for the data packet. A packet error rate, $P_{er} = 0.0$ was obtained by all the supervised adaptive algorithms. The result of the computation of SINR (Signal to Interfering Noise Ratio), given as

$$\text{SINR(dB)} = -10\log_{10}\left(\frac{1}{N}\sum_{k=1}^{N} e_k^2\right) \tag{4.104}$$

where N denotes the number of symbols per data packet is depicted in Table 4-9. It is observed that the improved RLS algorithm had achieved a SINR of 16.35 dB, while the RLS achieves a SINR of 15.56 dB. From the computed SINR, the RLS algorithm had achieved better results over the LMS, normalised LMS and VSLMS algorithms with SINR 14.44 dB, 14.23 dB and 15.41 dB respectively. The main reason for this is that the multipath channel model used was deterministic and the statistical variation in the signal propagation can be regarded to be in a steady-state condition.

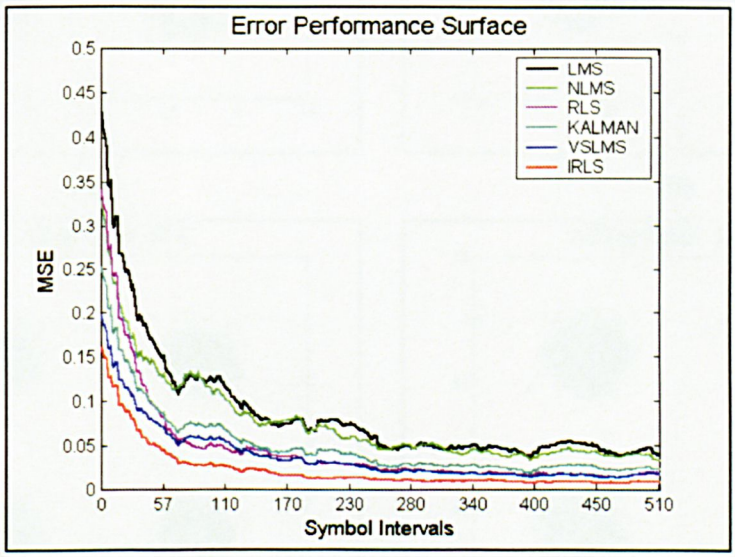

Figure 4-7 Error performance surface for supervised adaptive algorithms - training mode

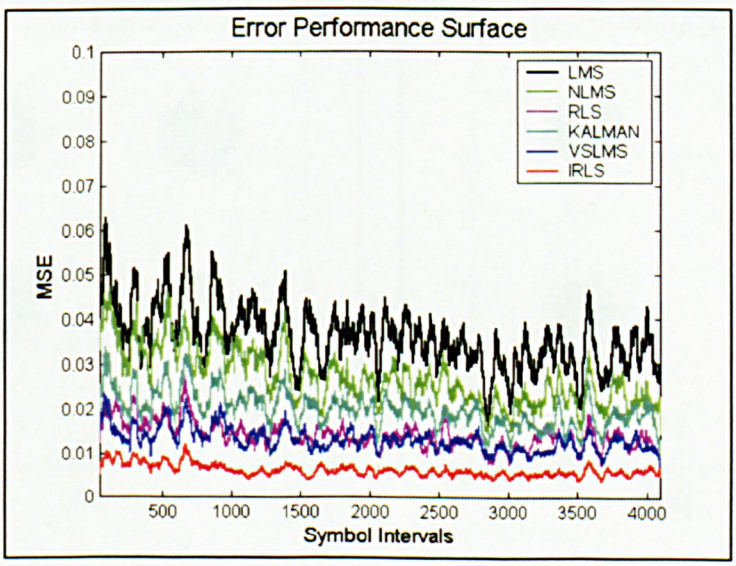

Figure 4-8 MSE plots for the supervised algorithms - decision directed mode

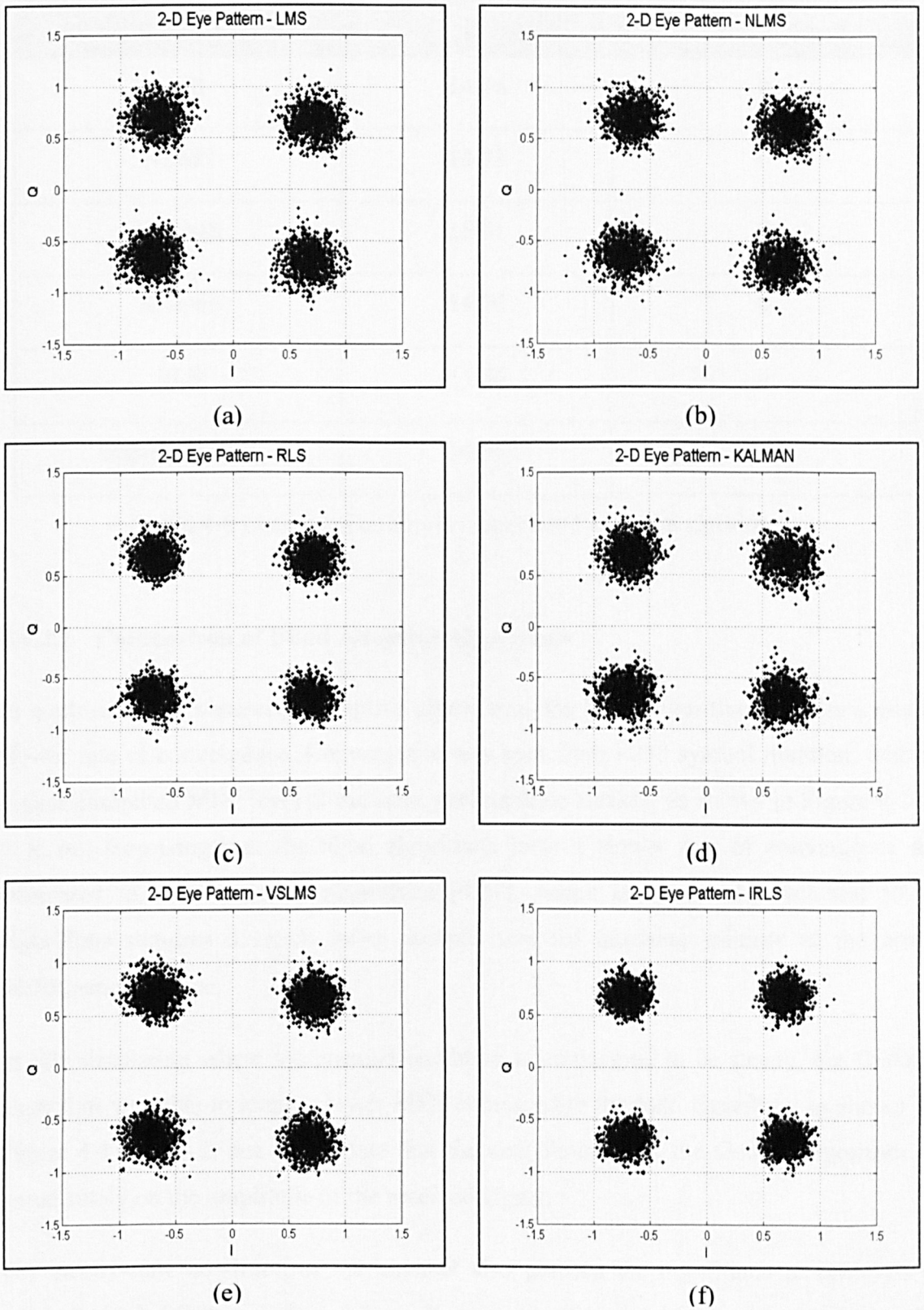

Figure 4-9 I-Q constellation for supervised adaptive algorithms

Supervised Algorithms	SINR (dB)	Packet Error Rate (P_{er})
LMS	14.44	0
NLMS	14.23	0
VSLMS	15.41	0
Kalman	14.70	0
RLS	15.56	0
Improved RLS	16.35	0

Table 4-9 Computed output for supervised adaptive algorithms

4.4.2.2 Comparison of Blind Adaptive Algorithms

In contrast to the supervised adaptive algorithms, the blind algorithm exhibits a much slower rate of convergence. Convergence was seen from ~230 symbol iteration, with a higher computed MSE level at the error performance surface, as shown in Figure 4-10. It is not surprising that the blind algorithms have a slower rate of convergence as compared to the supervised algorithms [4.37], which is due to the fact that HOS algorithms requires a much larger sample size for attaining minima at the error performance surface.

In this simulation where the channel condition is considered to be steady, the Godard algorithm was able to attain a lower MSE compared to the Sato algorithm, as shown in Figure 4-11. This is due to the fact that the cost function of the Godard algorithm is based solely on the amplitude of the received signal.

The steady-state condition of the channel also permits the algorithms to achieved a relatively high SINR with $P_{er} = 0.0$, as illustrated in Figure 4-12 (a)-(c) and Table 4-10. However, in a more hasher underwater environment, as will be discussed in the following section, the blind algorithm may not have sufficient time to reach a steady state, therefore it will not be able to track the statistical changes in the environment.

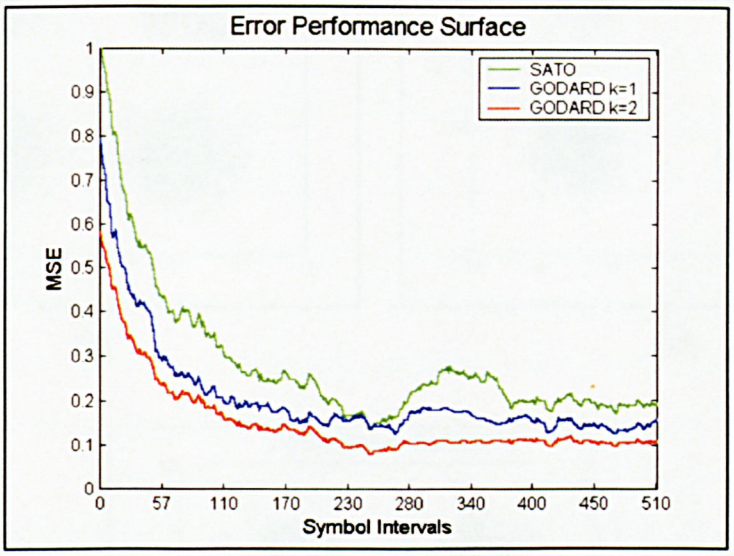

Figure 4-10 Error performance surface for blind adaptive algorithms - training mode

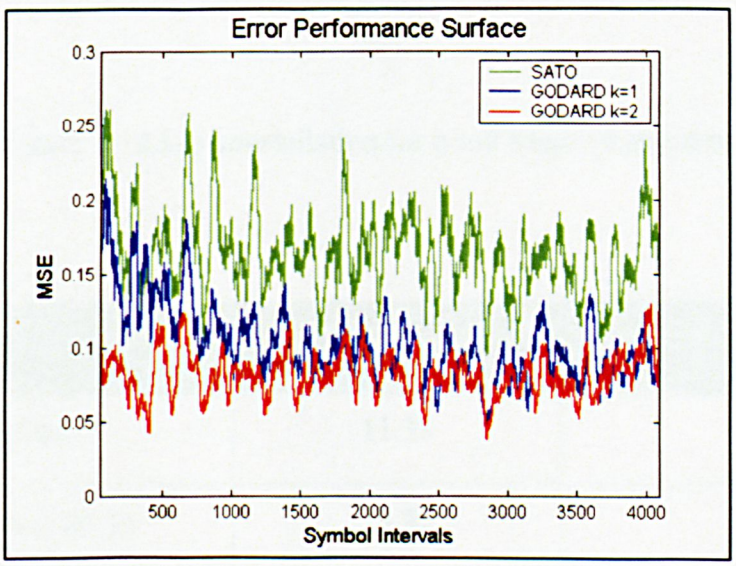

Figure 4-11 MSE plots for the blind algorithms - decision directed mode

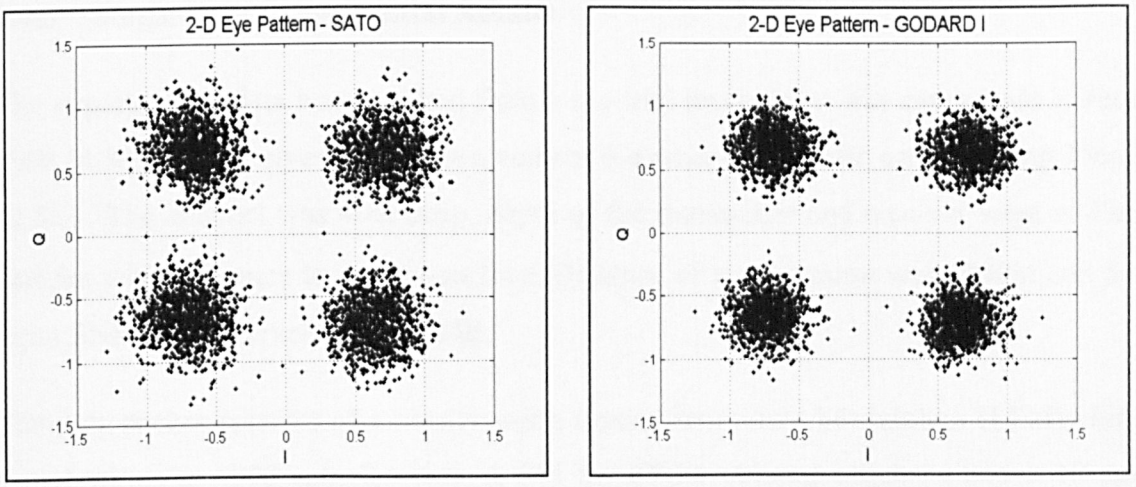

(a) (b)

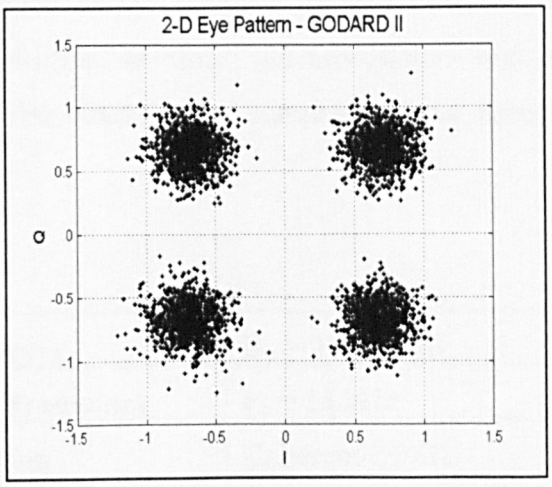

(c)

Figure 4-12 I-Q constellation for blind adaptive algorithms

Blind Algorithms	SINR (dB)	Packet Error Rate (P_{er})
Sato	11.38	0
Godard (k=1)	13.32	0
CMA (k=2)	13.93	0

Table 4-10 Computed output for blind adaptive algorithms

4.4.3 Single User Experimental Results

The experimental data was acquired from a sea-trial project that was carried out in June 1998 [4.36]. The receiver array uses a vertical 6-element setup with array spacing 25cm, (2.5λ). The channel was 40m deep, depth of the transmitter and receiver were at 30m and 5m with reference to the sea-surface. Distance of transmission was 1800m and the input SNR was observed to be ~20dB.

The data packet consists of a header using Linear Frequency Modulation (LFM) chirp signal which is 1000 samples long, a 511 bit BPSK training sequence and a 10ksps QPSK data packet. Time synchronisation was achieved by cross-correlating the chirp signal with a local signal at the receiver. In this case, the blind algorithms were considered to be semi-blind as time synchronisation was achieved prior to the convergence and data demodulation. A summary of the experimental setup is given Table 4-11.

Frequency	B_w = 10-20 kHz
Carrier Frequency	F_c = 15 kHz
Modulation	Coherent QPSK
Channel Depth	40 m
Tx Depth	30 m
Rx Array Depth	First element at 5 m ref. to sea surface
No. of Elements	6
Element Spacing	25 cm
Channel	North Sea (U. K.)
Header	Linear FM of length 1000
Training symbols	511
Data packet length	4096 (8192 bits) – Gray Coded
Distance	1800 m
Input SNR	20 dB

Table 4-11 Experimental parameters setting

The channel impulses shown in Figure 4-13 exhibit multipath spread of ~3.5ms, corresponding to an ISI of ~35 symbols. Therefore suggesting a longer feedback tap length to remove residual ISI. A 20 and 40 taps were used for the forward and feedback filters respectively for the adaptive equaliser, refer to Appendix Table 6 of Appendix VII for taps length selection. The tap coefficients of the adaptive algorithms were initially set to zero. The parameters used for the simulation are depicted in Table 4-12, refer to Appendix Table 7 of Appendix VII for optimised parameters selection.

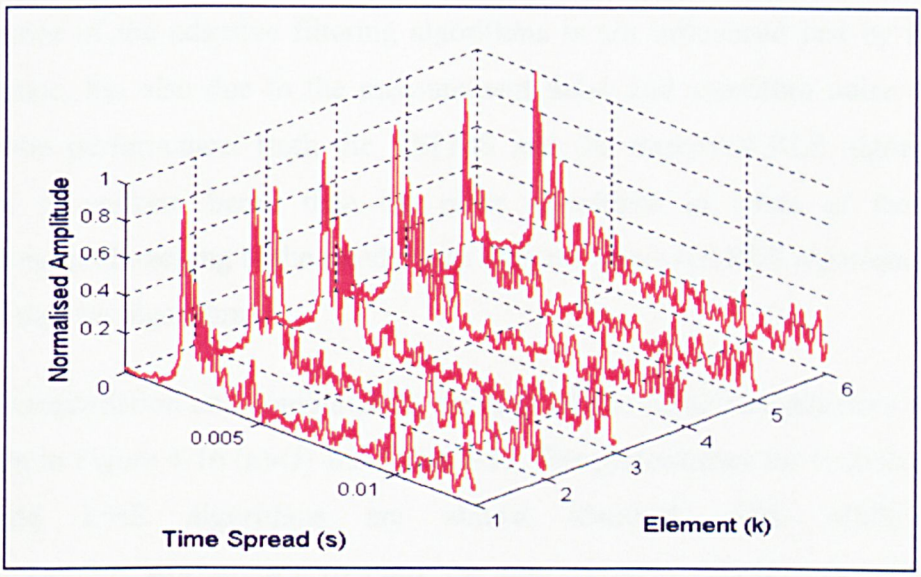

Figure 4-13 Channel impulses observed for k elements

	Algorithms	Parameters	Forward & Feedback values	
1.	LMS,NLMS	Step size, μ	0.005	0.003
2.	NLMS	Constant, α	0.0001	0.0001
3.	VSLMS	Step size, μ_{max}	0.007	0.005
		Step size, μ_{min}	0.003	0.001
4.	RLS	Forgetting factor, λ	0.98	0.98
5.	Sato, Godard	Step size, μ	0.004	0.002

Table 4-12 Algorithm parameter settings

4.4.3.1 Comparison of Supervised Adaptive Algorithms

From the results obtained for the rate of convergence, as shown in Figure 4-14, it is seen that the RLS algorithm has a better convergence than over the LMS and normalised LMS algorithms. However, the RLS algorithm has poor tracking capability compared to the LMS algorithms, as shown in Figure 4-15. Although the RLS algorithm has a better convergence in the transient state, it does not necessary imply that it will give good tracking performance in the steady state. This is due to the fact that the tracking performance of the adaptive filtering algorithms is not influenced just by the rate of convergence, but also due to the measurement noise and algorithm noise during the steady-state performance. Both the VSLMS and the improved RLS algorithm were observed to perform better than the other algorithms in terms of their rate of convergence and tracking in the steady state with the improved RLS algorithm being the better of the two algorithms.

The I-Q constellation and computed P_{er} for each of the supervised adaptive algorithms are shown in Figure 4-16 (a)-(f) and Table 4-13. The performance for both the LMS and normalised LMS algorithms are almost identical, with $SINR = 10.48dB$ ($P_{er} = 7.32 \times 10^{-4}$) and $SINR = 10.47dB$ ($P_{er} = 6.11 \times 10^{-4}$) respectively. This deduces that the LMS does not suffer from much gradient noise amplification in the input signal. The upper and lower bound step-size values ensure that the VSLMS achieves better $SINR = 11.65dB$ ($P_{er} = 2.44 \times 10^{-4}$). The RLS algorithm exhibited a poorer tracking property as compared to the Kalman algorithm, which reinforces the arguments in [4.28]. The computed SINR for both RLS and Kalman algorithm are 9.2dB ($P_{er} = 3.42 \times 10^{-4}$) and 10.76dB ($P_{er} = 3.66 \times 10^{-4}$) respectively. The computed SINR obtained by the improved RLS algorithm was 12.91 dB with $P_{er} = 0.0$.

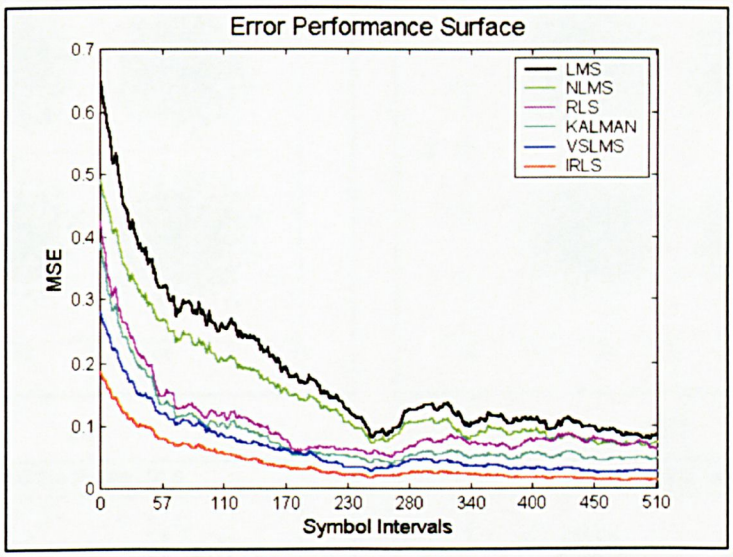

Figure 4-14 Error performance surface for blind adaptive algorithms - training mode

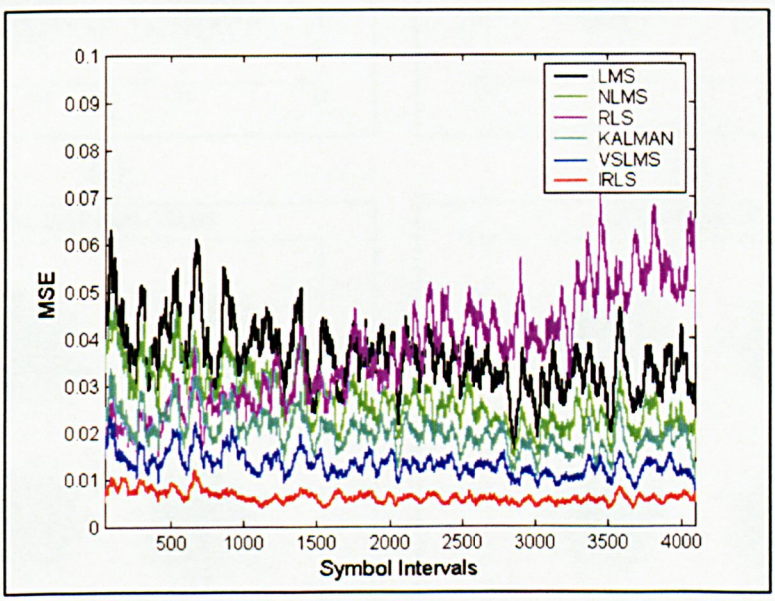

Figure 4-15 MSE plots for the supervised algorithms - decision directed mode

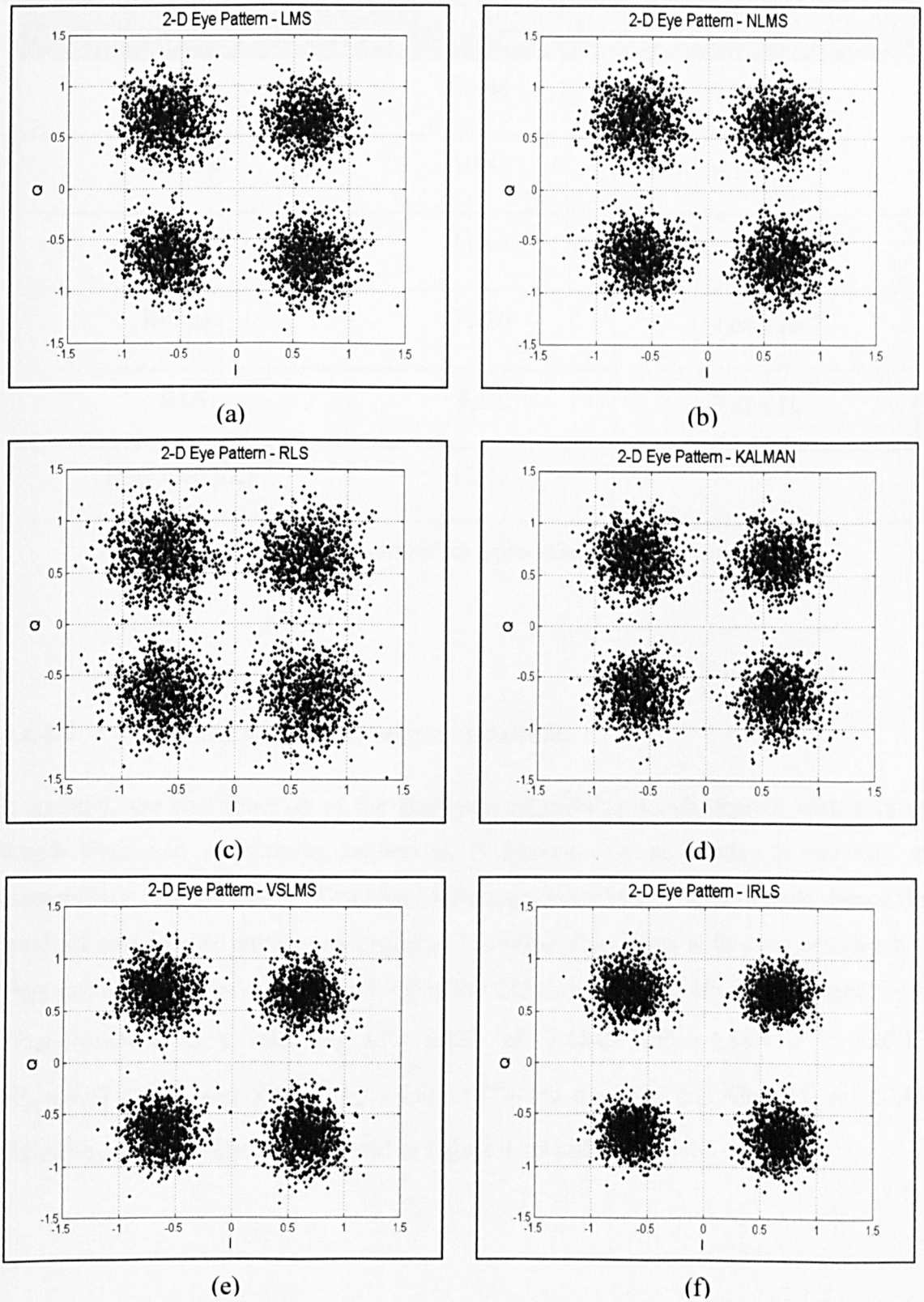

Figure 4-16 I-Q constellation for supervised adaptive algorithms

Supervised Algorithms	SINR (dB)	Packet Error Rate (P_{er})
LMS	10.48	7.32×10^{-4}
NLMS	10.47	6.11×10^{-4}
VSLMS	11.65	2.44×10^{-4}
Kalman	10.76	3.66×10^{-4}
RLS	9.20	3.42×10^{-3}
Improved RLS	12.91	0

Table 4-13 Computed output for supervised adaptive algorithms

4.4.3.2 Comparison of Blind Adaptive Algorithms

In general, the cost function of the Bussgang algorithms which operate with a finite length filter and no training sequences, is non-convex, as shown in the rate of convergence of Figure 4-17. Therefore, false local minima can be generated, hence the result of non-convex rate of convergence. The blind algorithms with poor convergence were not able to achieve good tracking in the decision mode, as shown in Figure 4-18. Thus resulting in a relatively low SINR of 7.65dB ($P_{er}=1.36\times10^{-2}$), 8.08dB ($P_{er}=8.67\times10^{-3}$) and 8.6dB ($P_{er}=4.88\times10^{-3}$) for the Sato and Godard and CMA algorithms respectively, as illustrated in Figure 4-19 and Table 4-14.

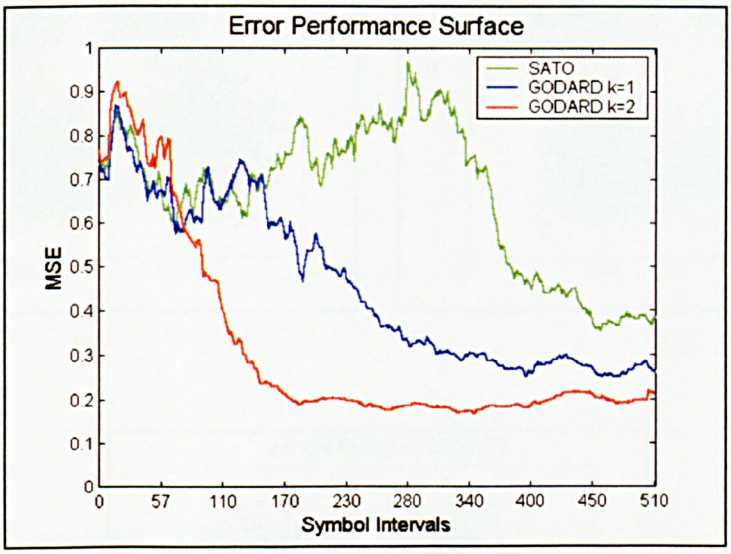

Figure 4-17 Error performance surface for blind adaptive algorithms - training mode

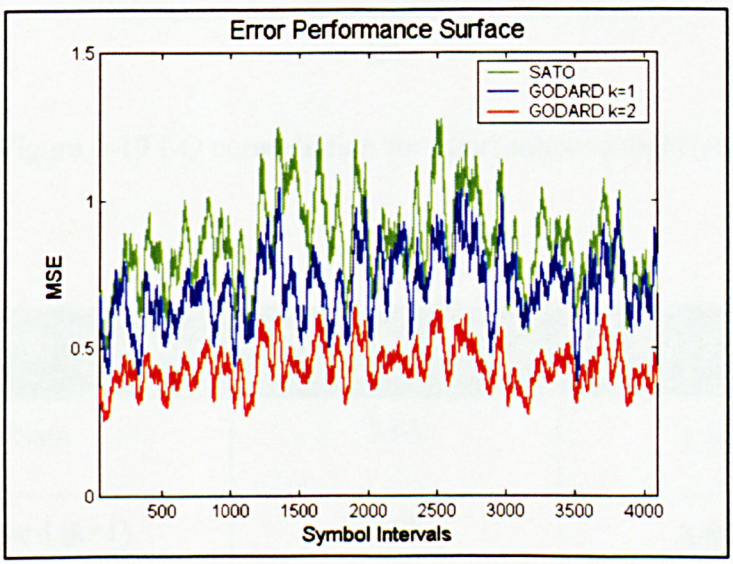

Figure 4-18 MSE plots for the supervised algorithms - decision directed mode

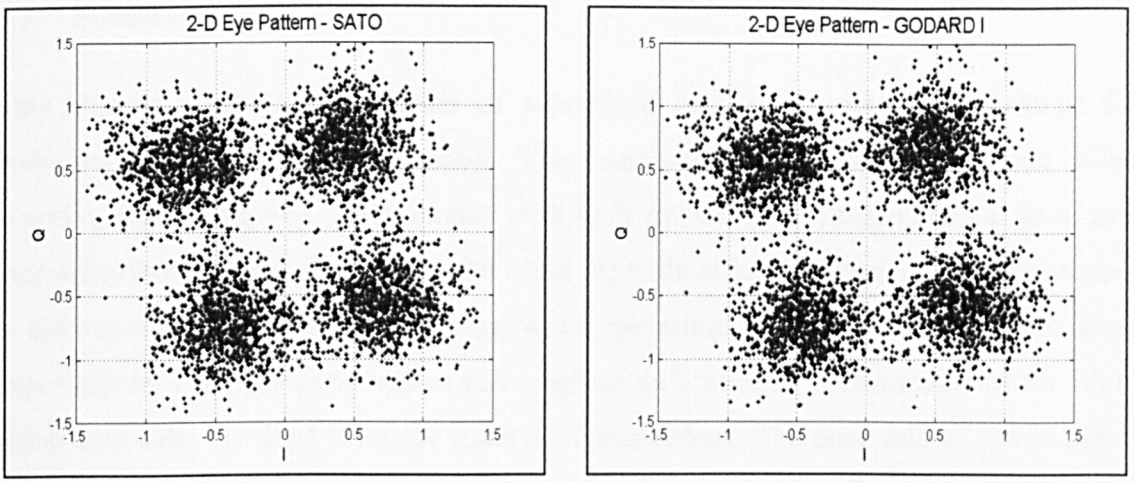

(a) (b)

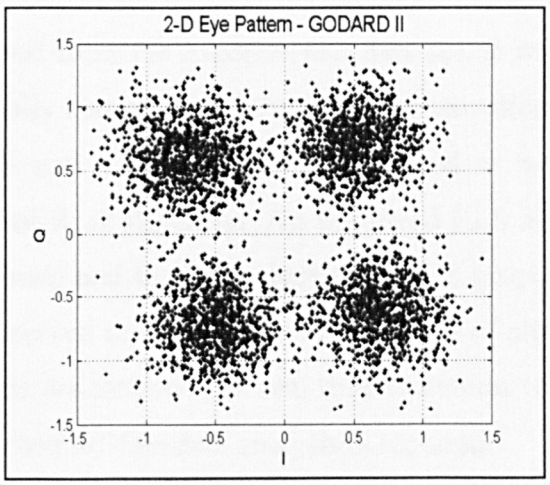

(c)

Figure 4-19 I-Q constellation for blind adaptive algorithms

Blind Algorithms	SINR (dB)	Packet Error Rate (P_{er})
Sato	7.65	1.36×10^{-2}
Godard (k=1)	8.08	8.67×10^{-3}
Godard (k=2) CMA	8.60	4.88×10^{-3}

Table 4-14 Computed output for blind adaptive algorithms

4.5 Summary

This chapter reviewed the classes of supervised and blind adaptive algorithms for underwater acoustic communication. The capability of the supervised and blind adaptive algorithms was demonstrated with both simulated and experimental data. In a time-invariant channel simulation, the blind algorithms have comparable performances to the supervised algorithms. However, when operating in a time-variant channel using experimental data, the poor rate of convergence and tracking performance of the blind algorithms falls far short from the supervised algorithms. The poor rate of convergence in the training mode was not acceptable to provide a good transient into the decision directed mode.

From the results obtained from the experimental data set, it was concluded that time-varying channel, especially that of an underwater communication channel, the classes of LMS, normalised LMS and VSLMS algorithms proved to be of a better choice as compared to the standard RLS algorithm. An improved RLS algorithm, which was an extension from the Kalman and the RLS algorithms, was proposed in this chapter and its performance was observed to surpass the other classes of algorithms. Generally, the class of LMS algorithms are attractive in real-time operation while the improved RLS algorithm is desirable when off-line data analysis is required.

Chapter 5 Design of Multi User Detection Strategies

5.1 Introduction

Initial work on multi-user detection strategies was demonstrated from the optimal multi-user receiver and its potential improvements in network system capacity and near-far resistance [5.1]. However, the optimal multi-user receiver was deemed far to complex to be implemented in a practical system, which has led to much research in alternative sub-optimal multi-user detection approaches. This chapter presents the design and development of novel multi-user detection strategies for the base-station receiver in underwater acoustic communications. Receiver structures adopting array processing with adaptive decision feedback equalisation (DFE) scheme provide the basic building block for single user communication. From here, several methods of multi-user detection (MUD) schemes for multiple access interference cancellation are proposed and developed. A new novel MUD strategy based on Recursive Successive Interference Cancellation (RSIC) technique, which offer better performance over other MUD strategies is being proposed in this chapter.

The validity of the multi-user receiver structures are then analysed from simulations for multi-user reception scenarios, which involve equal and unequal power reception.

The results from the simulated analysis not only highlighted the effectiveness of these multi-user detection schemes, but also pointed out the potential areas of weakness, which may exist in some of these multi-user detection schemes.

5.2 System Model

In the uplink communication model, shown in Figure 5-1, each user is observed to be arriving at the base station asynchronously. The data field of the transmitted data consists of a header, H_k, training sequence, TS_k, and variable data length. The header is used for initial "coarse" time synchronisation or clock recovery, and the training sequence is used to provide initial training to adapt the equaliser tap weights.

The received signal at the base-station can be expressed in complex form, $\mathbf{x}(t)$ where

$$\mathbf{x}(t) = \sum_{k=1}^{K} A_k h_k b_k (t - \tau_k) + n(t) \tag{5.1}$$

where $A_k(t)$, $h_k(t)$, $b_k(t)$ and τ_k denote, for each user *k*, the received amplitude, channel transfer function, transmitted bit sequence and time delay respectively, and $n(t)$ is the Additive White Gaussian Noise (AWGN). In order to model an asynchronous reception, consideration is given to the transmitted bit stream, b_k, of the *k*th user which takes the form

$$b_k \in \left\{\pm 1/\sqrt{2}; \pm 1/\sqrt{2};\right\} \tag{5.2}$$

Thus generalising (5.1) becomes

$$\mathbf{x}(t) = \sum_{k=1}^{K} \sum_{j=-M}^{M} A_k h_k b_k^j (t - jT - \tau_k) + n(t) \tag{5.3}$$

where T is the symbol duration. Symbol-epoch offsets are defined with respect to an arbitrary origin, $\tau_{ref} = 0$, which is the time origin of the first detected user at the base-station, as shown in Figure 5-1.

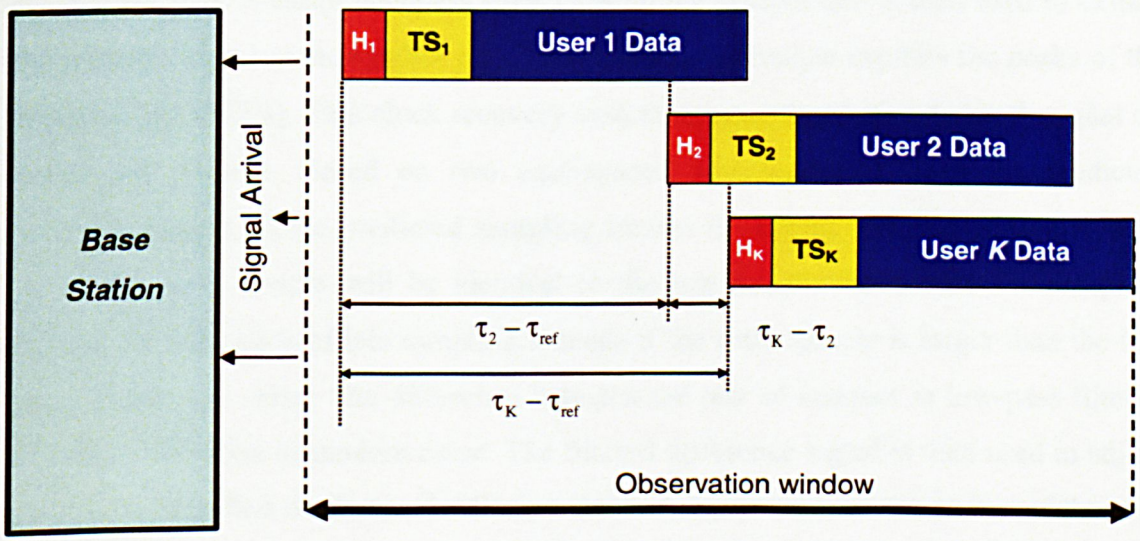

Figure 5-1 Observation window for the different time of arrival for uplink signal transmission

5.3 Receiver System Synchronisation

In a practical acoustic communication scenario, neither the PN code alignment nor the carrier frequency/phase can be known a priori, therefore this information has to be extracted by the receiver system from the received signal. Furthermore drifting of the clock causes inaccurate PN code alignment. Although stable time clocks can be used to synchronise the timing between the transmitter and receiver, there is always an initial timing uncertainty due to the range uncertainty. The other uncertainty in the carrier frequency/phase can be caused by a frequency drift in the transmitter/receiver oscillator or Doppler shift caused by the relative physical motion of the transmitter and receiver. Therefore the fundamental problem of coherent M-PSK receiver system is to perform both clock and carrier recovery for the transmitted signal. While clock recovery is needed to ensure synchronisation between the receiver and transmitter clocks, carrier recovery endeavours to align the receiver local oscillator with the transmitted carrier frequency that had been changed by the channel medium.

5.3.1 Clock Synchronisation

One of the most fundamental self-synchronising clock recovery systems is the squaring or times-two system [5.2]. When the down converted signal is squared, or passed through a non-linear rectifier, it possesses a periodic frequency domain component at the symbol rate. A tuned bandpass filter close to the symbol rate is then used to extract the periodic signal at the symbol rate. The early-late technique exploits the peaks of the received signal [5.3]. This clock recovery system squares the received signal so that all peaks are positive. Based on two equi-spaced samples taken from the predicted sampling instant, if the predicted sampling instant is aligned with the correct sample point, the early sample will be identical to the late sample taken after the sampling instant. An indication of late sampling is made if the early sample is larger than the late sample and vice versa. The difference between the pair of samples is low-pass filtered to reduce the effect of random noise. The filtered difference signal is then used to adjust a voltage-controlled oscillator (VCO) in order to delay or advance the arrival of the next clock impulse. Although these two self-synchronisation systems work well for binary modulation scheme, their main problem is the added complexity to the receiver design.

The other option for clock recovery is to transmit a separate short synchronising signal before the data packet itself. The process for achieving clock synchronisation is to transmit a priori known PN sequence to the receiver. The receiver then performs a cross-correlation of the known PN sequence with the received signal and then compares the output with a reference threshold, as shown in Figure 5-2. When the filtered output exceeds the reference threshold the receiver is then locked on to the received signal and clock synchronisation is accomplished. The receiver can then switch to the demodulation of the data, as illustrated in Figure 5-3.

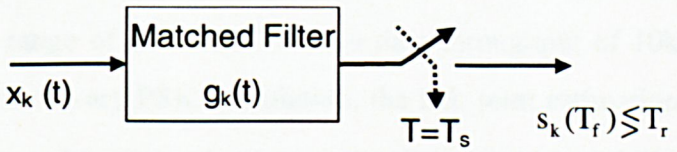

Figure 5-2 Matched filter time acquisition

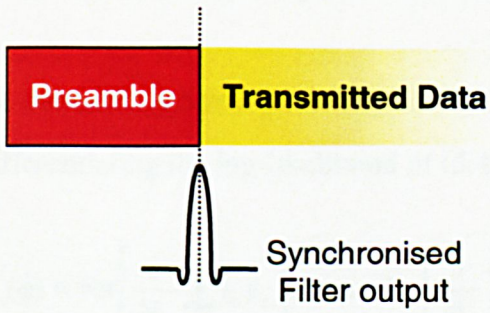

Figure 5-3 Data time synchronisation with preamble

5.3.2 Carrier and Doppler Compensation

A common problem related to the carrier frequency is the receiver's inability to solve phase ambiguities in the case of rotational symmetry. Although phase locking can be established for the QPSK modulation scheme at multiples of 90°, but without additional transmitted signal information it is not possible to resolve the angle at which phase lock has been achieved. The effect of coherent detection suffering from inaccurate carrier recovery is shown in Figure 5-4. This problem can be rectified with the transmission of a preamble signal to indicate the initial phase of the transmitted data.

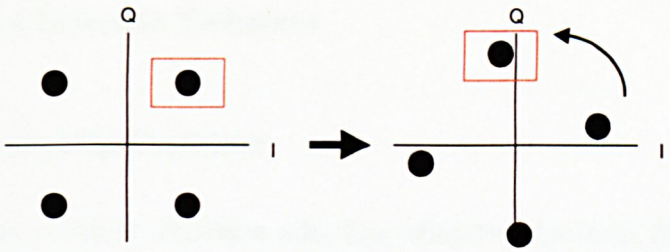

Figure 5-4 Coherent detection suffering from inaccurate carrier recovery

Carrier recovery techniques adopting decision-directed tracking was first described by Proakis [5.4]. A discrete time approach to the Maximum Likelihood (ML) joint estimation of carrier phase and symbol timing proposed by Sharif [5.5] reported an error probability in the range of $10^{-3}-10^{-4}$ with a data throughput of 10kbps. At time nT_s, where $T_s < 1/B_w$, for M-ary PSK modulation, the ML joint estimation of phase, ϕ, and symbol timing, τ, can be express by the log-likelihood function [5.4] given as

$$\Lambda_L(\phi,\tau) = \mathrm{Re}\left[\frac{e^{j\phi}}{N_o}\sum_n I_n^* y_n(\tau)\right] \tag{5.4}$$

where I_n^* and y_n are the complex decision and complex filter output. The ML estimate of ϕ can be found by differentiating the log-likelihood of (5.4),

$$\Lambda_L(\phi) = \mathrm{Re}\left[\frac{1}{N_o}\sum_n I_n y_n\right]\cos\phi - \mathrm{Im}\left[\frac{1}{N_o}\sum_n I_n y_n\right]\sin\phi \tag{5.5}$$

with respect to ϕ and equating the derivative to zero, giving

$$\phi_{ML} = -\tan^{-1}\left[\frac{\mathrm{Im}\left(\sum_n I_n y_n\right)}{\mathrm{Re}\left(\sum_n I_n y_n\right)}\right] \tag{5.6}$$

The solution to the symbol estimation, $\hat{\tau}_{ML}$, is given as

$$\hat{\tau}_{ML} = \sum_n I_n^* \frac{\delta}{\delta\tau}[y_n(\tau)] = 0 \tag{5.7}$$

5.4 Single-User Detection Technique

5.4.1 Adaptive Spatial Combiner

A phase-coherent receiver structure adopting adaptive decision feedback equalisation (DFE) for underwater acoustic communication was first documented in [5.6]. The primary task of the phase-coherent DFE for single-user detection (SUD), shown in Figure 5-5, is to equalise the ISI and perform phase tracking which result from multipath propagation and phase fluctuations. The multi-element feedforward equalisers are used to remove ISI and provide phase compensation. The feedback equaliser uses past decisions to update the tap weights to remove residual ISI.

The operation of the adaptive DFE is divided into two phases – the training mode and decision directed mode. In the training mode, a priori known training sequence which is embedded in the receiver system is used as the desired signals to provide initial training for adapting the equaliser tap weights. At the end of the training mode, the equaliser would have attained convergence close to the optimal values. The receiver then switches to the decision directed mode where the detected symbols are treated as the desired signal for further adaptation and equalisation so that variations in the channel can be tracked.

At time nT_s, where $T_s < 1/B_w$, the output at the forward equalisers of the adaptive DFE (used for removal of precursor ISI), for user K, after phase correction is

$$a_K(n) = \sum_{\ell=1}^{L} \mathbf{f}_K^{\ell} \mathbf{x}_K^{\ell}(n) e^{-j\hat{\theta}_K^{\ell}} \tag{5.8}$$

where $\mathbf{f}_K^{\ell}$, $\mathbf{x}_K^{\ell}$ and $\hat{\theta}_K^{\ell}$ are the filter coefficients, nT_s-spaced samples buffered in the feedforward filters and phase correction for user K at time nT_s and receiver element L. The output from the feedback filter, which suppresses the residual causal ISI, can then be expressed as

$$c_K(n) = \mathbf{d}_K \mathbf{q}_K(n) \tag{5.9}$$

where $\mathbf{d}_K(n)$ and $\mathbf{q}_K(n)$ are the row vector contents of the M most recent estimated symbol decisions and column vector coefficients of the feedback filters respectively. When the symbol is known by the receiver in the training mode, $\mathbf{d}_K(n)$ is expressed as

$$\mathbf{d}_K(n) = [\bar{d}_K(n-1) \quad \cdots \quad \bar{d}_K(n-M)]^* \tag{5.10}$$

and

$$\mathbf{d}_K(n) = [\hat{d}_K(n-1) \quad \cdots \quad \hat{d}_K(n-M)]^* \tag{5.11}$$

when the receiver switches over to the decision directed mode. The symbol error estimation can then be defined as

$$e_K^*(n) = \hat{d}_K^*(n) - \tilde{d}_K^*(n) \tag{5.12}$$

where $\tilde{d}_K^*(n)$ is the pre-decision variable. The corresponding mean square error (MSE) is depicted as

$$MSE_K = E\{|e_K^2(n)|\} \tag{5.13}$$

The main difference between an adaptive combiner and a beamformer is that the combiner seeks to minimise the error in the received data symbols while the beamformer seeks to null out interfering user's signal from the signal of interests [5.7]. The adaptive beamformer achieve improvements in the output signal-to-interference noise ratio (SINR) by manipulating nulls, or coherent cancellation, in the direction of the interfering signal whilst maintaining a lobe, or coherent summation, in the direction of the intended signal.

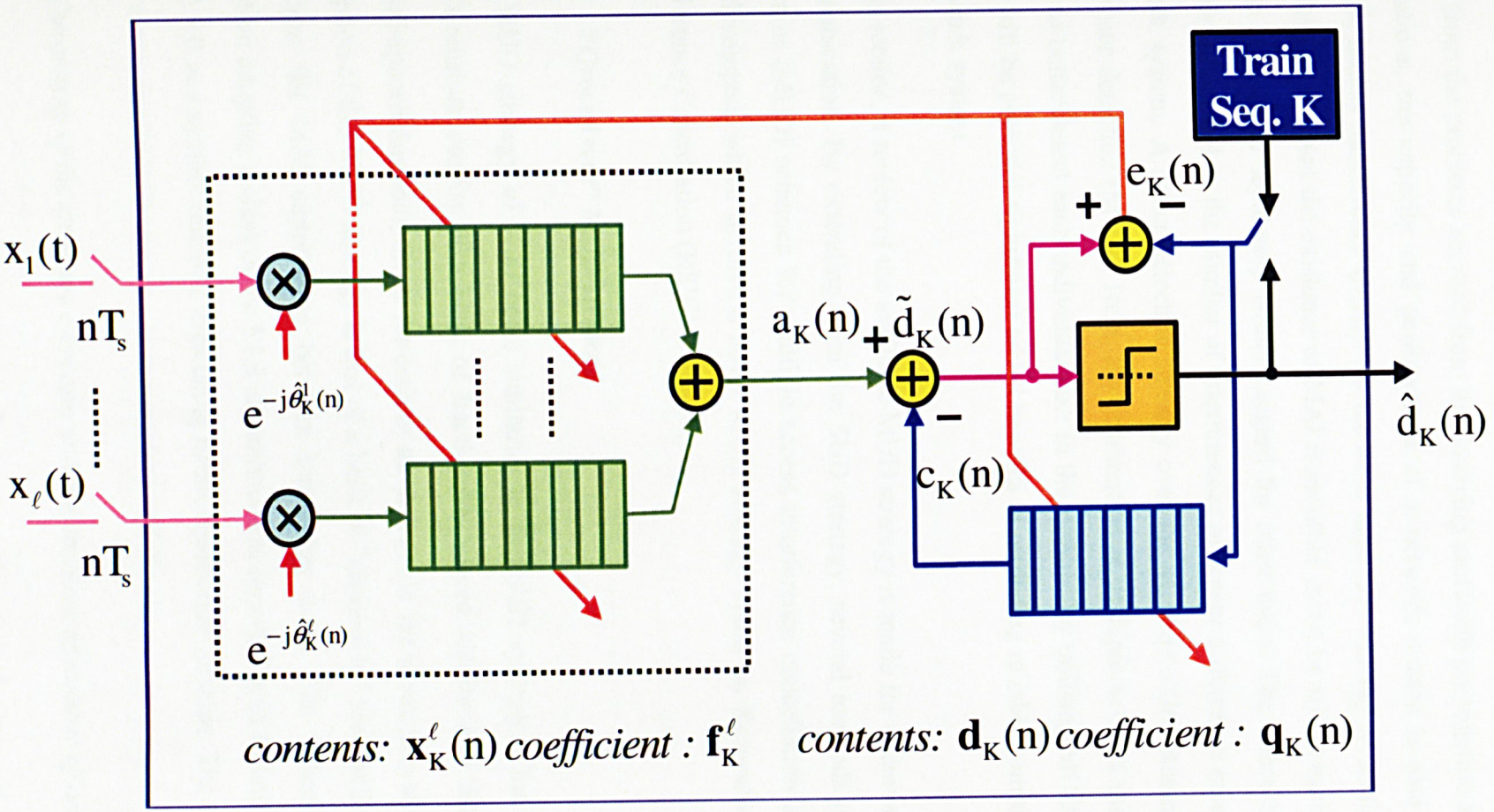

Figure 5-5 Single-user detection (SUD) receiver structure adopting decision feedback equalisation

5.5 Multi-User Detection (MUD) Strategies

Apart from the problems accrued from time-varying multipath propagation and Doppler fluctuations, the capacity and performance of a network system is also limited by multiple access interference (MAI). As the SUD detection strategy in section 5.4 does not take into account the existence of MAI from other users, by which each user in the system is detected separately without regard for other users. The effect of MAI will become substantial as the number of interferences or power differences increases in the network system. A better detection strategy over the SUD detection strategy is one of multi-user detection (MUD). Here, the information of multiple users is used jointly in order to better detect each individual user in the system. By utilising MUD algorithms, there will be potential significant added benefits in providing reliable communication in a network system.

In this section, a review of the available MUD strategy is made for underwater acoustic communication. By extending from the SUD strategy, several methods of multi-user detection (MUD) schemes for multiple access interference cancellation are proposed and developed, which involve a novel MUD strategy based on Recursive Successive Interference Cancellation (RSIC) technique.

5.5.1 "Cross-Over" MUD strategy

The MUD strategy of [5.8] bears similarity to the SUD strategy. This "cross-over" MUD receiver consist of a bank of fractionally spaced feedforward filters and nT_s symbol-spaced feedback filters for each of the K users in the network system. The main exception of this MUD strategy is that of a bank of "cross-over" feedback filters, which performs the MAI suppression between interfering users. The "cross-over" MUD structure adopting a class of the RLS algorithms was reported in [5.8] with packet error of $P_e = 0$ at a symbol rate of 2 ksps using BPSK modulation scheme. The complexity of the "cross-over" MUD structure is summarised as follows:

1.) Complexity of the structure increases with the increase of number of array sensor

2.) Time complexity per bit is linear to the number of users in the network system

5.5.2 Parallel Interference Cancellation (PIC) MUD strategy

Multi-user receiver structure based on parallel interference cancellation (PIC) estimates and subtracts all the MAI for *k* users concurrently [5.9]-[5.10]. Recent work in mobile communication has shown that the performance of PIC can be improved by performing an initial partial cancellation [5.11]-[5.13]. The partial cancellation involves multiplying the estimated symbol of each user with a factor less than unity prior to any interference cancellation. This takes into account the fact that the tentative decisions made in the earlier stages are less reliable than those of the later stages. However, employing these PIC schemes in underwater acoustic communications is unrealistic since these MUD structures, developed in mobile communications, do not take into account the predominant effects of ISI, phase fluctuations and Doppler effects encountered in the underwater acoustic environment.

To enhance the capability of the basic PIC structure, an *Mth*-stage MUD receiver structure based on weighted parallel interference cancellation (PIC) with adaptive DFE was proposed [5.14], as shown in Figure 5-6. The contents of each DFE block in Figure 5-6 are as depicted in Figure 5-5. The heavy lines (—) in Figure 5-6 represent the repeated structures for each element of the receiver array.

In stage 1 of the PIC structure, the initial bits/symbols for all users $k = 1,2,3,...K$, are estimated from the corresponding DFE units. The estimated bit decisions are then regenerated with a weighting factor and phase correction. The regenerated signal is then subtracted from the received signal at the receiver array elements. The modified received signal, having one fewer interfering signals, is then passed to the next stage for processing and the removal of a further user signal. This process of parallel decision estimation, regeneration, weighting and interference cancellation is repeated for *M* stages, where the last stage assumes that all MAI have been removed between users. The $t_b^{(M-1)}$ term in Figure 5-6 denotes the time delay of the received signal to be summed with the regenerated MAI signals of other users at the *(M-1)th* stage.

Assuming perfect delay estimation, (a buffer window is used to store the time reference for asynchronous reception), the signal that is fed to element ℓ of user *K*, at stage 2, after subtracting all MAI from other users in the interference cancellation unit (ICU) in stage 1, is expressed as:

$$\mathbf{x}_{K,2}(n) = \sum_{k=1}^{K} A_k^{\ell} b_k^{\ell}(n) e^{-j\theta_k^{\ell}} - \sum_{k=1}^{K-1} \hat{d}_{k,1} \alpha_{k,1}^{\ell} e^{-j\hat{\theta}_{k,1}^{\ell}} + \rho(n) \tag{5.14}$$

where the second term and third term are the regenerated MAI signal for all users, $k = 1,2,3,...(K-1)$, and the residual noise, respectively. $\hat{\theta}_{k,1}^{\ell}$ and $\alpha_{k,1}^{\ell}$ are the phase correction and scaled amplitude at element, ℓ, at stage 1.

Assuming perfect interference cancellation, the retrieved information from the adaptive DFE for user K from the output of stage M is decoded as,

$$\hat{d}_{K,M} = \mathrm{sgn}(\mathbf{x}_{K,(M-1)}(n)) \tag{5.15}$$

where the individual signal, that is fed to element ℓ of user K, is

$$\mathbf{x}_{K,(M-1)}(n) = \sum_{k=1}^{K} A_k^{\ell} b_k^{\ell}(n) e^{-j\theta_k^{\ell}} - \sum_{k=1}^{K-1} \hat{d}_{k,(M-1)} \alpha_{k,(M-1)}^{\ell}(n) e^{-j\hat{\theta}_{k,(M-1)}^{\ell}} \tag{5.16}$$

The retrieved information symbol from the output of the adaptive DFE for user K at stage M is decoded as

$$\hat{d}_{K,M}(n) = \mathrm{sgn}\left(\sum_{\ell=1}^{L} \mathbf{f}_{K,(M-1)}^{\ell} \mathbf{x}_{K,(M-1)}^{\ell}(n) . e^{-j\hat{\theta}_{K,(M-1)}^{\ell}} - c_{K,(M-1)}(n) \right) \tag{5.17}$$

In order for a new set of signals to be regenerated for better data estimation in the next stage, the PIC structure assumes that the decision of the previous stage has been estimated correctly. Therefore any estimation error, contributed by any user, will degenerate the removal of MAI for other users. This problem arises in a "near-far" scenario, where the received signal for the weak user, coupled with the strong MAI from the other users that are fed into the DFE structure, will encounter difficulties in estimating the data correctly. Therefore, it can be seen that the PIC receiver structure is more superior in a well-power-controlled channel, where all signals from separate users are at an almost equal power level.

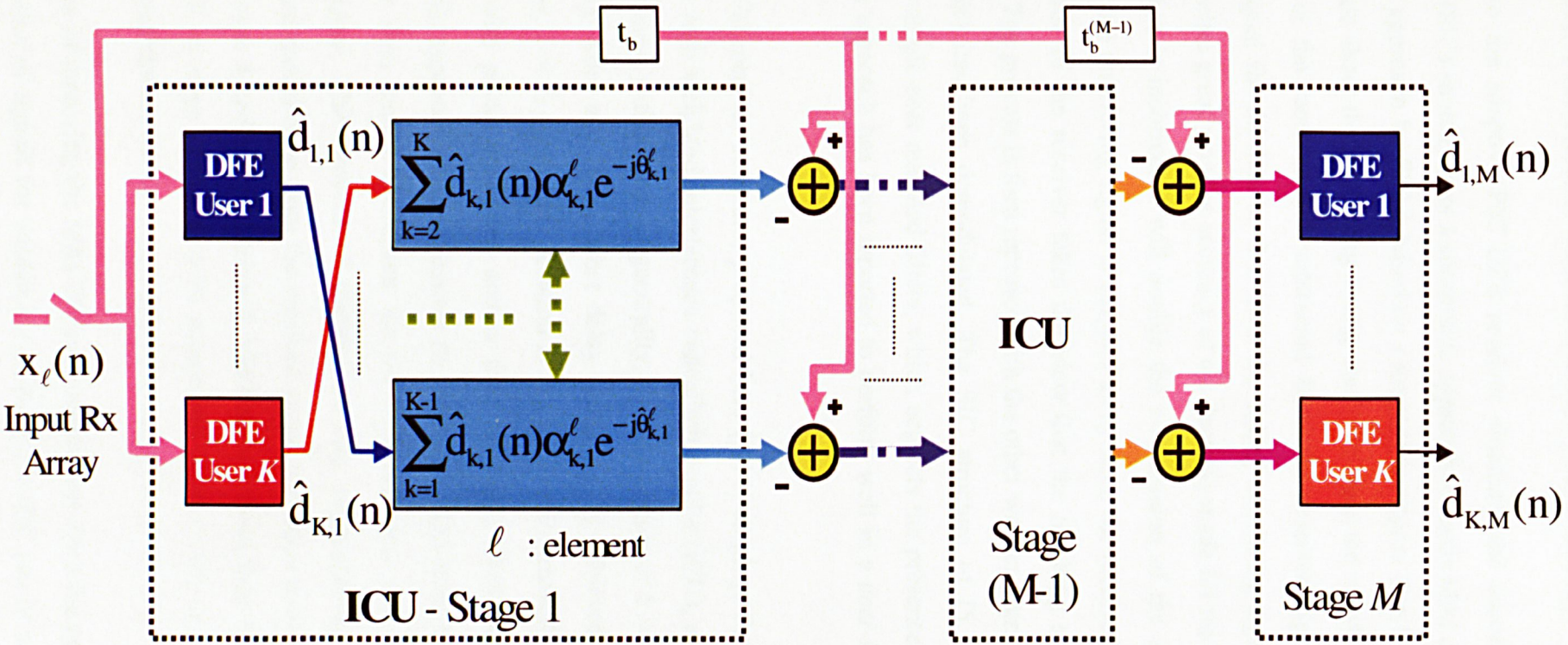

Figure 5-6 Parallel interference cancellation (PIC) MUD receiver structure

5.5.3 Successive Interference Cancellation (SIC) MUD strategy

In contrast to the adaptive PIC DFE receiver structure, the successive interference cancellation (SIC) strategy uses a successive approach towards MAI cancellation [5.15] - [5.17]. The approach for SIC is based on a simple but elegant idea [5.15]. If a decision has been made about the interfering strong user's bit, then the interfering signal can be regenerated at the receiver and subtracted from the received signal. The resulting subtracted signal should then be free from the strong interfering signal. However, this assumption relies greatly on the accuracy of the decision made for the interfering signal; if this decision is incorrect it will double the contribution of the interfering weaker signal. Once the interfering signal is stripped away from the received signal, the signal processing side of the receiver takes the view that the resulting signal contains one fewer users. The process is then repeated with the other weaker users, until the last user (weakest user) has been demodulated. The SIC structure of [5.15] uses decisions produced by single-user matched filters, which neglects the presence of the interfering signals. This approach has been reported to perform well in a near-far situation under AWGN.

The SIC MUD receiver structure, proposed here [5.14] employs the adaptive DFE in combination with weighted interference cancellation units (ICU), as shown in Figure 5-7. It is assumed, without loss of generality, that the powers of $k = 1,2, \ldots, K$ users are in descending order and that perfect delay estimation is achieved. In this case, the strongest user, $k = 1$, correct bit decision is regenerated by multiplying with a weight factor, α_1, with phase correction and is then subtracted from the received signal. Therefore, this approach aims to remove the strongest MAI from the received signal. The detector then makes a decision for the next strongest user ($k = 2$) from the subtracted signal. This process of decision-making, regeneration, weighting, phase correction, and cancellation from the received signal continues until the weakest or last user, K, has been decoded. The retrieved information symbol from the output of user K adaptive DFE in stage M can also be determined from (5.15) to (5.17), however, it should be noted that the MAI reductions are performed successively.

The technique of removing the MAI of the strongest user from the received signal aids in the estimation of signals for weaker users. Therefore SIC can be seen to be superior in a non-well-power-controlled channel. However, one prime disadvantage of such

system is that the strongest user does not benefit from the reduction of MAI, which means that the summed MAI effects from all other weaker users will, to a certain degree, affects the correct data estimation for the strongest user. The adaptive SIC MUD strategy can be described in the following algorithmic form:

1.) Obtain energy statistics from the received signal to rank users in descending power.

2.) Perform adaptive symbol estimation of strongest user (amplitude and phase).

3.) Estimated result is regenerated and cancelled from received signal.

4.) Subtracted received signal is passed to next weaker user for decoding.

5.) Repeat 1) to 4) until the last or weakest user K is decoded.

The practical implementation features of the SIC MUD can be summarised as follows:

1. Prior to adaptive signal processing, knowledge of the received power for all users in the network cell is required so that interference cancellation can be performed successively. Any errors in the estimation translates directly into additive interference for further decision making for weaker users.

2. Users weaker than the intended user are neglected for SIC.

3. The delay time for demodulation for SIC grows linearly with the number of users.

4. Time complexity per bit is linearly related to the number of users in the system.

The advantages of adopting the SIC strategy are straightforward [5.18]-[5.19]. Firstly, the receiver has the best chance of estimating the correct decision for the strongest user in the system. Secondly, removing the strongest user in the system gives the most benefit to the remaining weaker users. The SIC structure can be considered to be effective if the received power for users are widely variable. A major shortcoming of the adaptive SIC processor is that its performance is asymmetric, where users of equal received power are demodulated with disparate reliability. This is the opposite of the adaptive PIC, which means that the summed MAI effects from all other weaker users will, to a certain degree, affect correct data estimation.

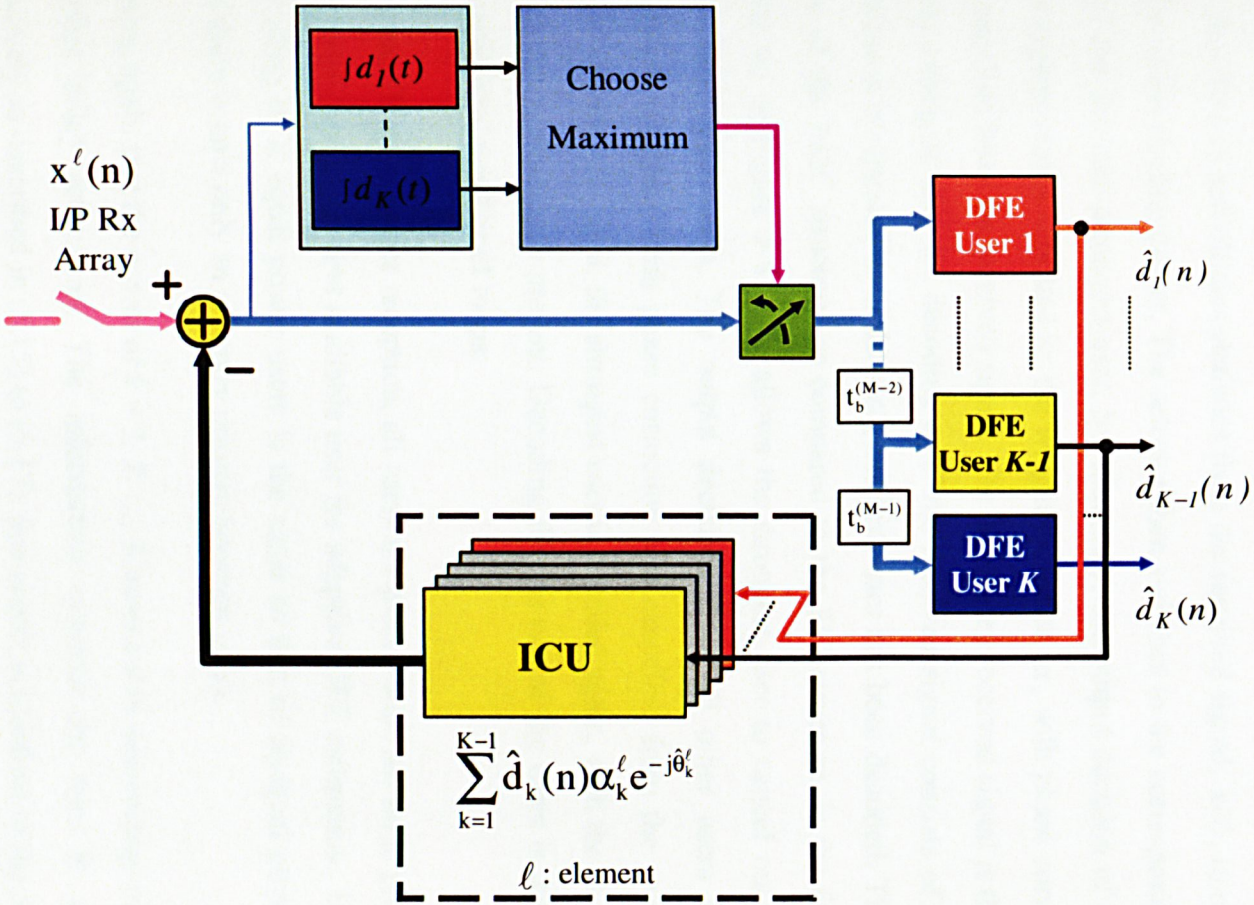

Figure 5-7 Successive interference cancellation (SIC) MUD receiver structure

5.5.4 Recursive Successive Interference Cancellation (RSIC) MUD strategy

In order to circumvent the short falls of the PIC and SIC structures, a new MUD technique of MAI cancellation based on recursive successive interference cancellation (RSIC) has been proposed in [5.20]-[5.21]. This RSIC structure is shown in Figure 5-8. In the case of unequal power reception, the receiver, having a priori knowledge of K users, first detects and obtains statistics from the received signal, $\mathbf{x}(t)$, to rank the users in order of descending power. The selector then switches to the corresponding adaptive DFE of the detected strongest user. Subsequently, the output decision of the strongest user is regenerated, multiplied by the weighting factor, α, with phase correction and is then cancelled from the received signal. The subtracted received signal is then passed to the next strongest user for decoding as if the received signal consists of $K - 1$ users. This process is repeated until the last (weakest) user has been decoded. The distinctive feature of the RSIC structure, as compared to the SIC structure, is the feedback loop labelled *(o)* in Figure 5-8. This allows the strongest user to cancel out the summed effects from other users. The output decisions from all other users are summed, regenerated, weighted with phase correction and cancelled from the received signal. With the subtracted signal, the strongest user is decoded again, with the assumption that only background noise is present. Decoding for the rest of the users is then performed for a predefined number of loops.

In the case of equal power reception, all users are placed with the same priority and the selector switches to the first available user for adaptive DFE estimation. The procedure of decoding of K equal power users is the same as that of unequal power reception, except there is now only an arbitrary priority between users.

Assuming again that the power of $k = 1, 2, \ldots, K$ users are in descending order and there is perfect delay estimation. The information symbols for user K are retrieved successively as described in (5.15) to (5.17), this aspect is identical to the SIC structure. During the loop back, the output symbol decisions for users $k = 2, 3, \ldots, K$, are summed, regenerated and cancelled from the received signal. The subtracted signal that is fed-back to user 1 can then be decoded free from MAI of other users. The output from the adaptive DFE of user 1 at $(M+1)$th stage can be expressed as

$$\hat{d}_{1,(M+1)} = \mathrm{sgn}(\mathbf{x}_{1,M}(n)) \tag{5.18}$$

where the signal, that is fed to element ℓ of user 1, is

where $$\mathbf{x}_{1,M}(n) = \sum_{k=1}^{K} A_k^{\ell} b_k^{\ell}(n) e^{-j\theta_k^{\ell}} - \sum_{k=2}^{K} \hat{d}_{k,M} \alpha_{k,M}^{\ell}(n) e^{-j\hat{\theta}_{k,M}^{\ell}} \tag{5.19}$$

Expanding (5.18) leads to

$$\hat{d}_{1,(M+1)}(n) = \mathrm{sgn}\left(\sum_{\ell=1}^{L} \mathbf{f}_{1,M}^{\ell} \mathbf{x}_{1,M}^{\ell}(n).e^{-j\hat{\theta}_{1,M}^{\ell}} - c_{1,M}(n) \right) \tag{5.20}$$

where $c_{1,M}(n)$ is for the removal of postcursor ISI for user 1 at stage *(M + 1)*. At stage *2M*, for a single loop-back, the retrieved information for user *K* is depicted as:

$$\hat{d}_{K,2M}(n) = \mathrm{sgn}\left(\sum_{\ell=1}^{L} \mathbf{f}_{K,(2M-1)}^{\ell} \mathbf{x}_{K,(2M-1)}^{\ell}(n).e^{-j\hat{\theta}_{K,(2M-1)}^{\ell}} - c_{K,(2M-1)}(n) \right) \tag{5.21}$$

where the input signal at element ℓ, for user *K*, is

$$\mathbf{x}_{K,(2M-1)}(n) = \sum_{k=1}^{K} A_k^{\ell} b_k^{\ell}(n) e^{-j\theta_k^{\ell}} - \sum_{k=1}^{K-1} \hat{d}_{k,(2M-1)} \alpha_{k,(2M-1)}^{\ell}(n) e^{-j\hat{\theta}_{k,(2M-1)}^{\ell}} \tag{5.22}$$

Operation of this detector can be described in the following algorithmic form:

i) Obtain statistics from the received signal to rank users in descending power. If the received powers are equal, switch to the DFE for the first available user. Process steps ii) to vii) of the algorithmic flow.

ii) Perform adaptive DFE symbol estimation of the strongest/first user (amplitude and phase).

iii) Estimated result is regenerated and cancelled from received signal.

iv) Subtracted received signal is passed to the next strongest user DFE for decoding.

v) *Repeat i) to iv) until the last or weakest user K is decoded.*

vi) *Decisions of all subsequent users are then summed, regenerated, cancelled from the received signal and fed back to the strongest user for MAI cancellation.*

vii) *Repeat ii) to v) where regeneration and MAI cancellation is performed for the next weaker user, k = 2, 3, 4, ... K for a pre-defined number of iterations.*

The advantages of implementing the adaptive RSIC structure are threefold. Firstly, the RSIC structure offers the flexibility to self-adapt to handle equal or unequal power reception. In the case of equal power reception, the RSIC structure operates identically as the PIC structure. Whereas in an unequal power reception, the recursive loop back feature allows the strongest user to benefit from the reduction of MAI from other users. Secondly, with the MAI reduced, the adaptive DFE block that is incorporated for each user can then effectively cope with the multipath fading propagation and inter-symbol interference (ISI). And finally, implementing the RSIC structure can effectively tackle the problem of power control inefficiency in horizontal-link SWAN communication. Therefore, the adaptive RSIC MUD structure manifests itself to be a superior candidate for implementation in SWAN for both well-power-controlled and non-well-power-controlled channels. From the analysis, the adaptive PIC receiver structure has a processing load of $(K \times M)$, whereas the adaptive SIC receiver structure has only a processing load of M. Although the adaptive RSIC receiver structure has an increased load, $(2M)$, compared to the SIC structure, it requires a much lower computational load than the PIC structure. One major gain of the RSIC over the SIC MUD structure is that users weaker than the intended user are accounted for by the loop-back feature.

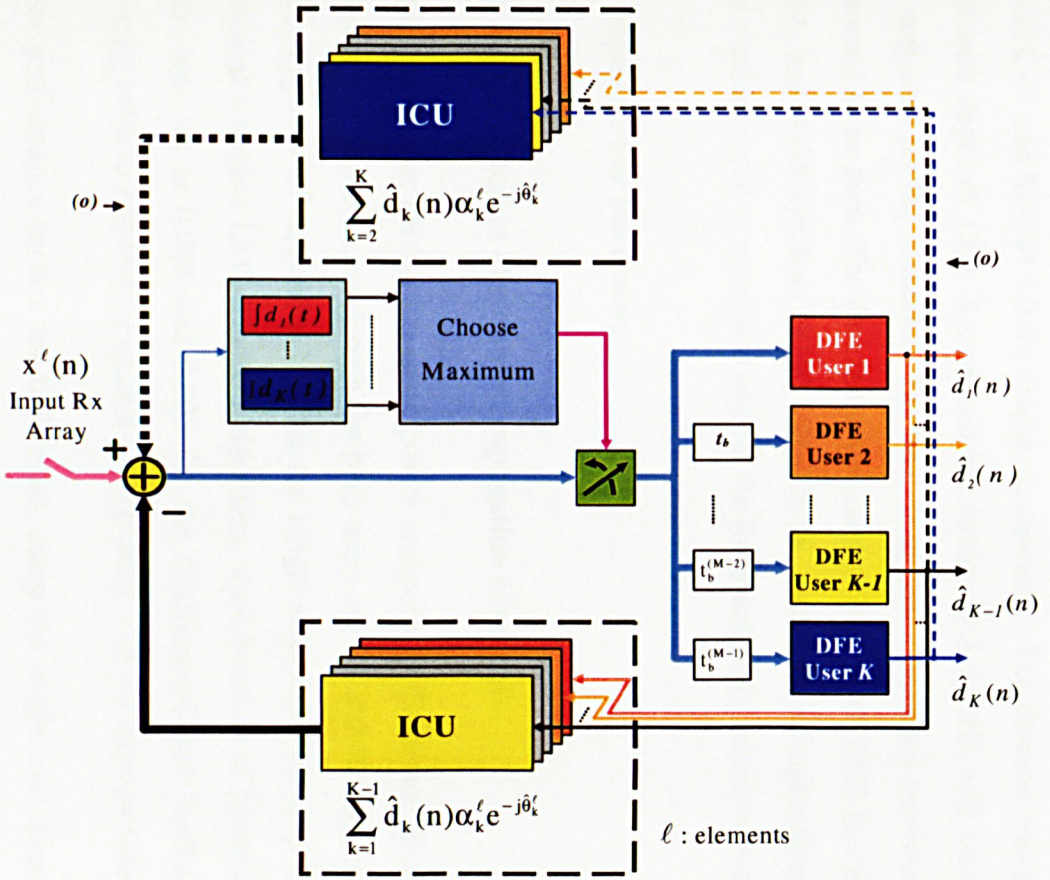

Figure 5-8 Recursive successive interference cancellation (RSIC) receiver structure

5.6 Comparison of the adaptive MUD strategies

The performances of the adaptive MUD strategies are tested against the single user detection strategy and the "cross-over" MUD detection strategy of [5.8]. Scenarios of a multi-user network which involves unequal-power ("near-far" effect) and equal power reception are considered here. The multipath channel model, consisting of the direct path and boundaries reflection paths, described in chapter 3.7 was used in the simulation. The simulation was carried out with a software receiver, written in Microsoft C++ and Matlab 5.0 for output visualisation. The channel was assumed to be uniform with depth of 18m. A common bandwidth of 8–12kHz with carrier frequency 10kHz was used for the scenarios. The time delay factor between received data packets was assumed to be zero. The data structure consists of a set of 1023 bits BPSK training sequence, and 4096 symbols (8192 bits) QPSK data with no spreading factor. A 6-element vertical receiver array was used at the front end of the receiver system.

5.6.1 Equal Power Reception

5.6.1.1 Performance in Multipath Propagation Channel

The user's parameter setting for equal power reception is illustrated in Table 5-1. The feedforward and feedback tap length for both users are 20 and 40 respectively, refer to Appendix Figure 7 of Appendix VIII for tap length selection. The step-size values for the canonical complex LMS adaptive algorithm, used because of faster computational purposes, was set at 0.008 and 0.006 for the feedforward and feedback filter taps respectively, refer to Appendix Figure 8 of Appendix VIII for stepsize selection.

The error performance surface for both users, using the single user detection strategy, was observed to converge during the training period of ~500 symbols, as shown in Figure 5-9. The SINR obtained for users 1 and 2 were 9.58 dB with $P_{er} = 3.7 \times 10^{-3}$ and 10.01 dB with $P_{er} = 2.4 \times 10^{-3}$ respectively. There was a slight improvement when the "cross-over" MUD strategy was used. The slight improvement in results was largely limited by the eigenvalue spread when using the LMS algorithm and was deemed to be unsatisfactory. The computed SINR obtained by the "cross-over" MUD strategy for user 1 and user 2 was 9.95 dB with $P_{er} = 2.2 \times 10^{-3}$ and 10.15 dB with $P_{er} = 1.95 \times 10^{-3}$

respectively, as shown in Figure 5-10. By removing interference concurrently before feeding the subtracted data to the next stage, the PIC strategy was able to take advantage of estimating the interference mitigated data. An improved SINR and P_{er} were observed for both users 1 and 2 with 10.78 dB, $P_{er} = 4.9 \times 10^{-4}$ and 10.81 dB, $P_{er} = 2.4 \times 10^{-4}$ respectively, as shown in Figure 5-11. Since the SIC strategy cancels co-channel interference successively, users of equal power tends to be decoded with disparate reliability. As the power for both users are equal, the SIC strategy switches to the first available user, user 1, for data estimation. Although an improvement was observed for user 2, with computed SINR 10.25 dB with $P_{er} = 1.5 \times 10^{-3}$, the interference contributed by user 2 hinders the data estimation for user 1, since no interference cancellation was performed for user 1. Thus the computed result for user 1 is identical to the results obtained by the single user detection strategy, as shown in Figure 5-12. By performing a single loop-back interference cancellation, the RSIC was able to obtain a better result as compared to the other MUD strategies for both user 1 and 2 with SINR of 11.36 dB with $P_{er} = 1.2 \times 10^{-4}$ and 11.22 dB with $P_{er} = 1.1 \times 10^{-4}$ respectively, as shown in Figure 5-13. A summary of the computed SINR and P_{er} for the various receiver structures is summarised in Table 5-2.

Figure 5-14 shows a plot of the computed SINR for user 2, of the various detection strategies as a function of diversity order. It was noted as the number of element increases, the computed SINR gap between the different structures begins to widen. At $L = 6$, the RSIC strategy gained an improvement of ~1.2 dB over the single user detection strategy, and ~0.4 dB over the PIC strategy. Thus, it is suggested that both the PIC and RSIC strategies are suitable candidates for network communication where equal power reception can be ensured.

Tx Depth for both		User 1 - 9 m and User 2 – 12 m
Rx Array Depth		First element at 8 m ref. to seabed
Channel		Multipath Channel Model
User 1	**Distance**	2000 m
	I/P SNR	13 dB
User 2	**Distance**	2000 m
	I/P SNR	13 dB

Table 5-1 Parameters for 2-user equal power reception

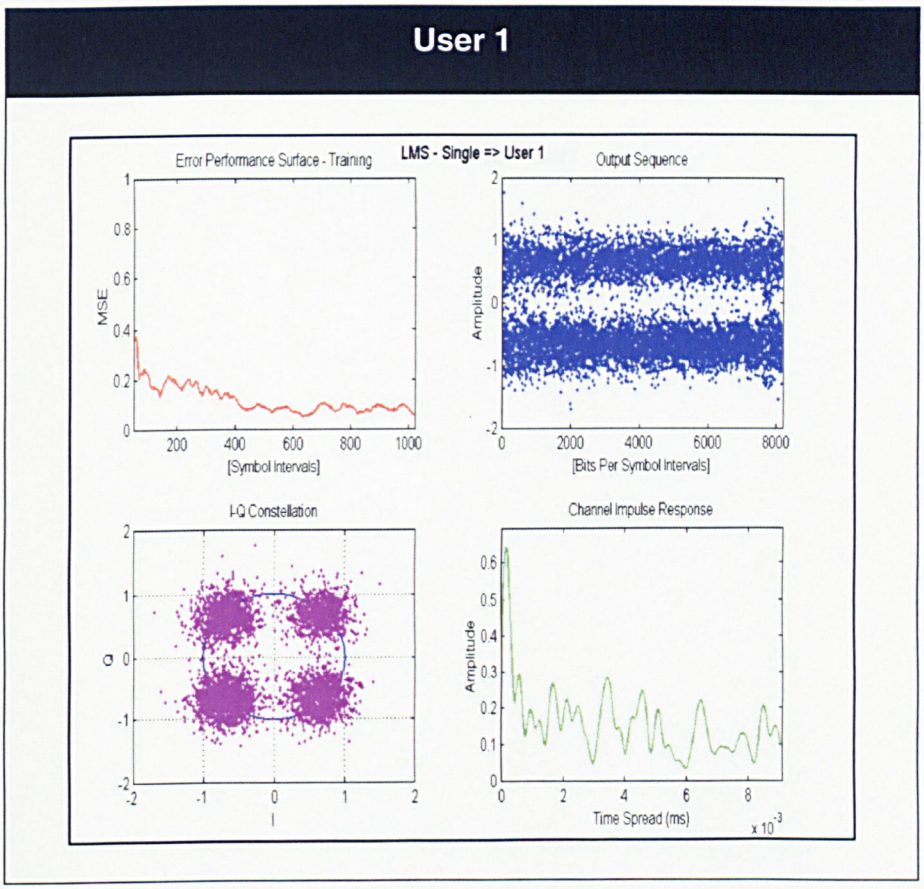

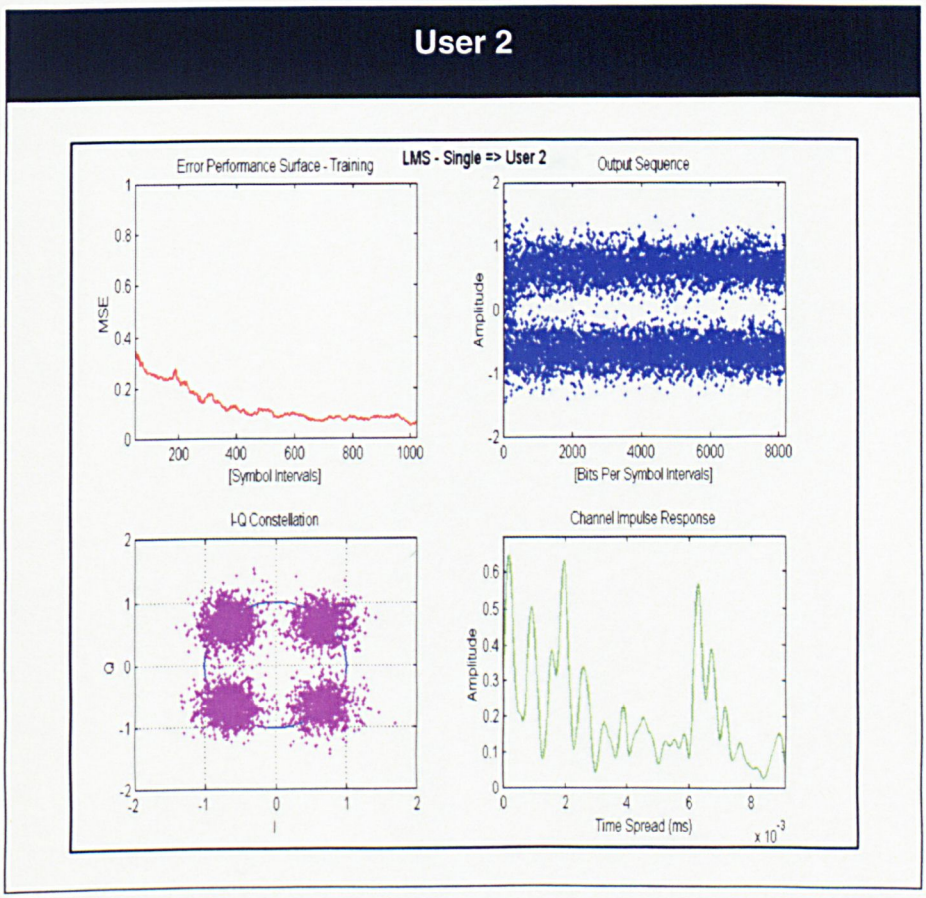

Figure 5-9 Single user detection strategy for equal power reception

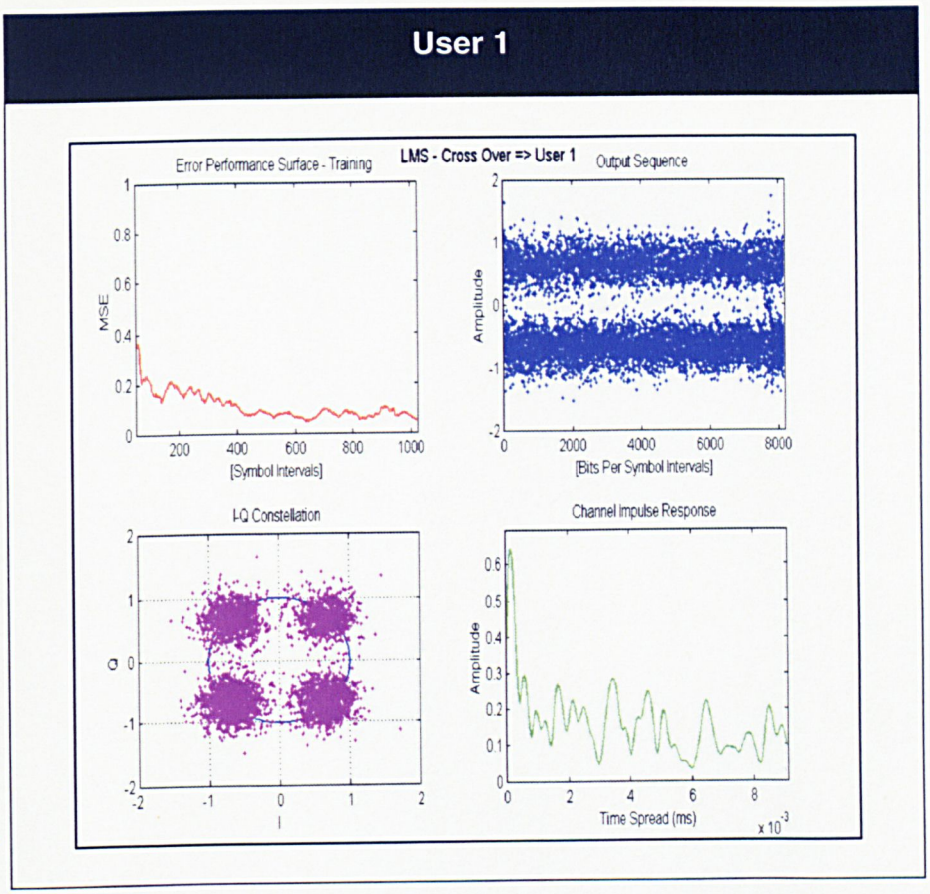

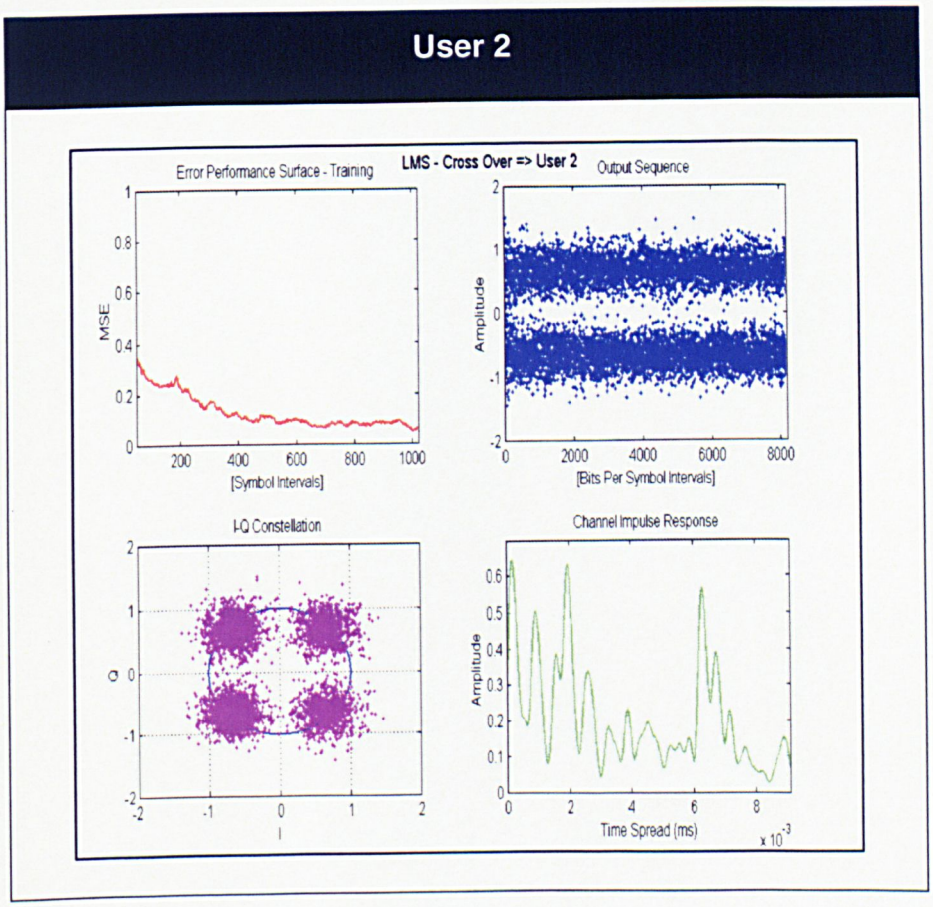

Figure 5-10 Cross-over MUD strategy for equal power reception

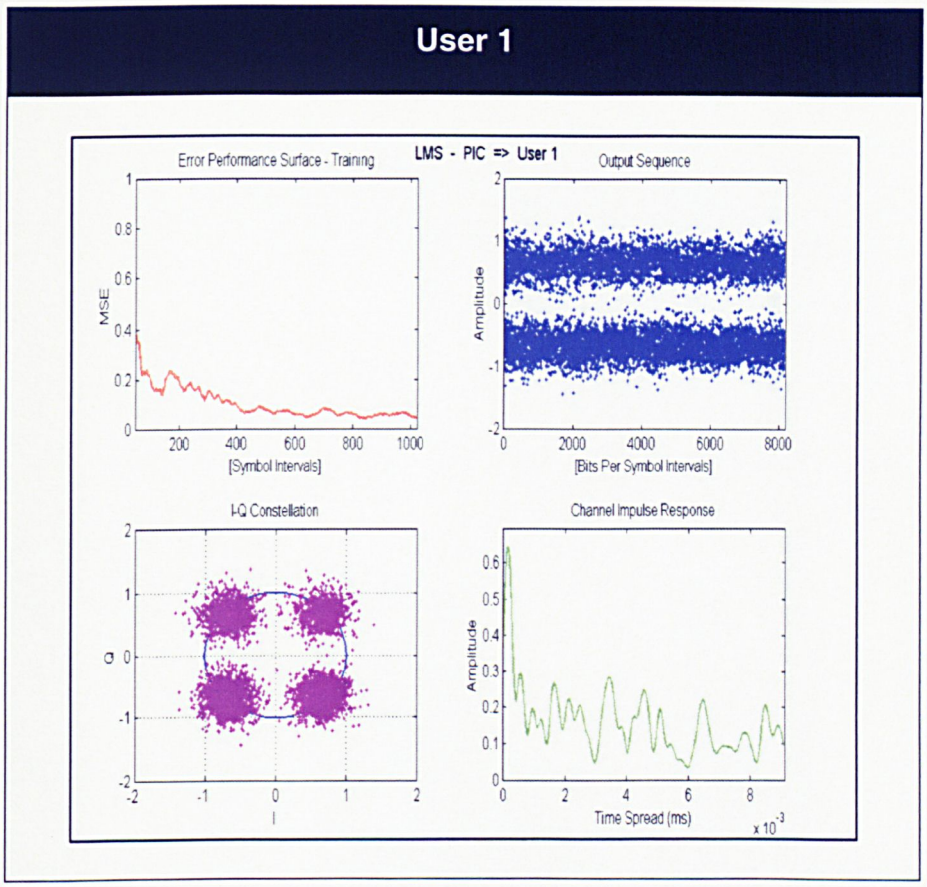

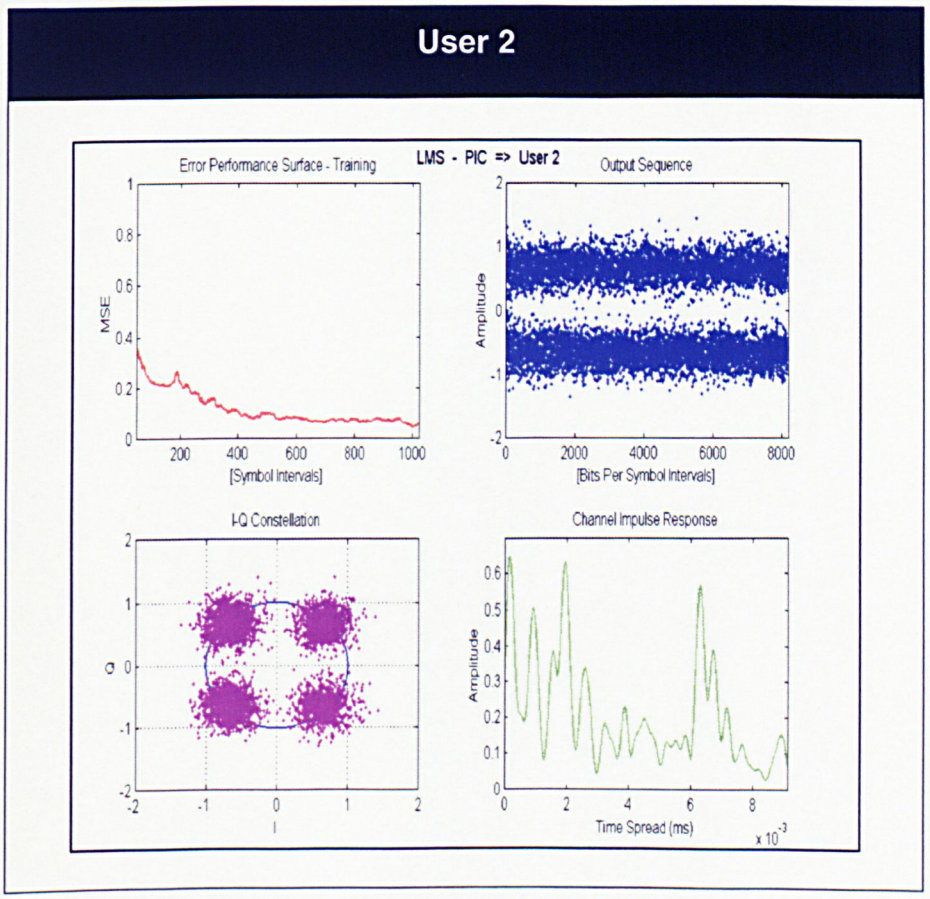

Figure 5-11 PIC MUD strategy for equal power reception

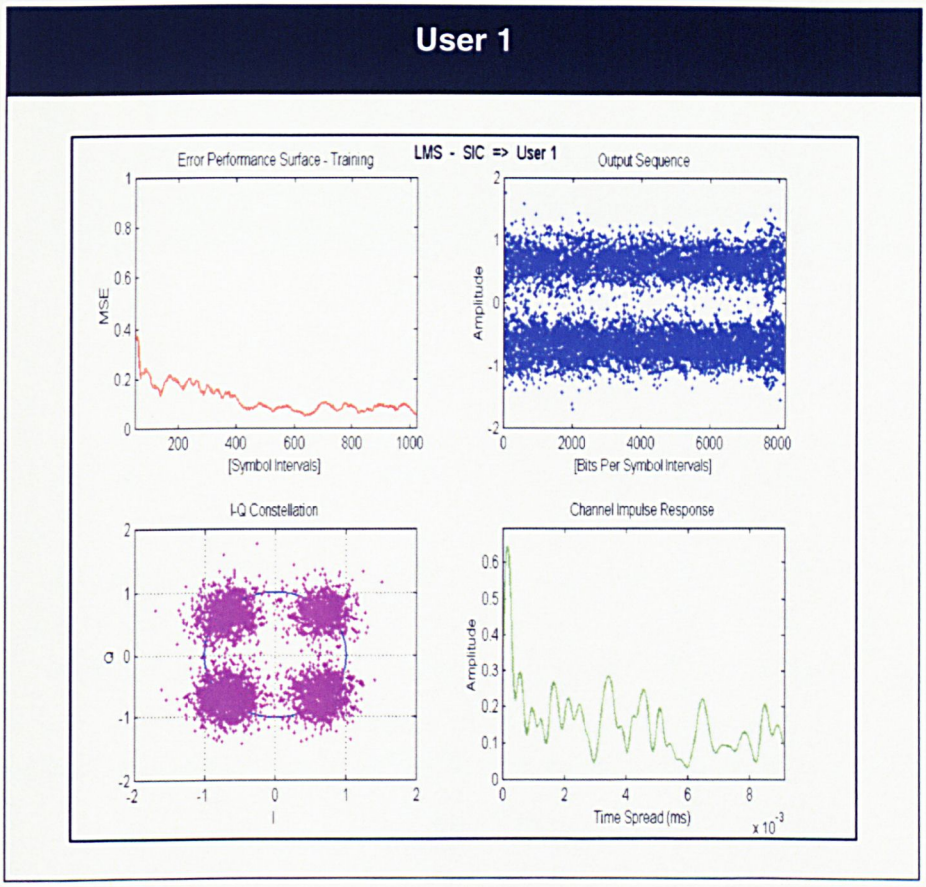

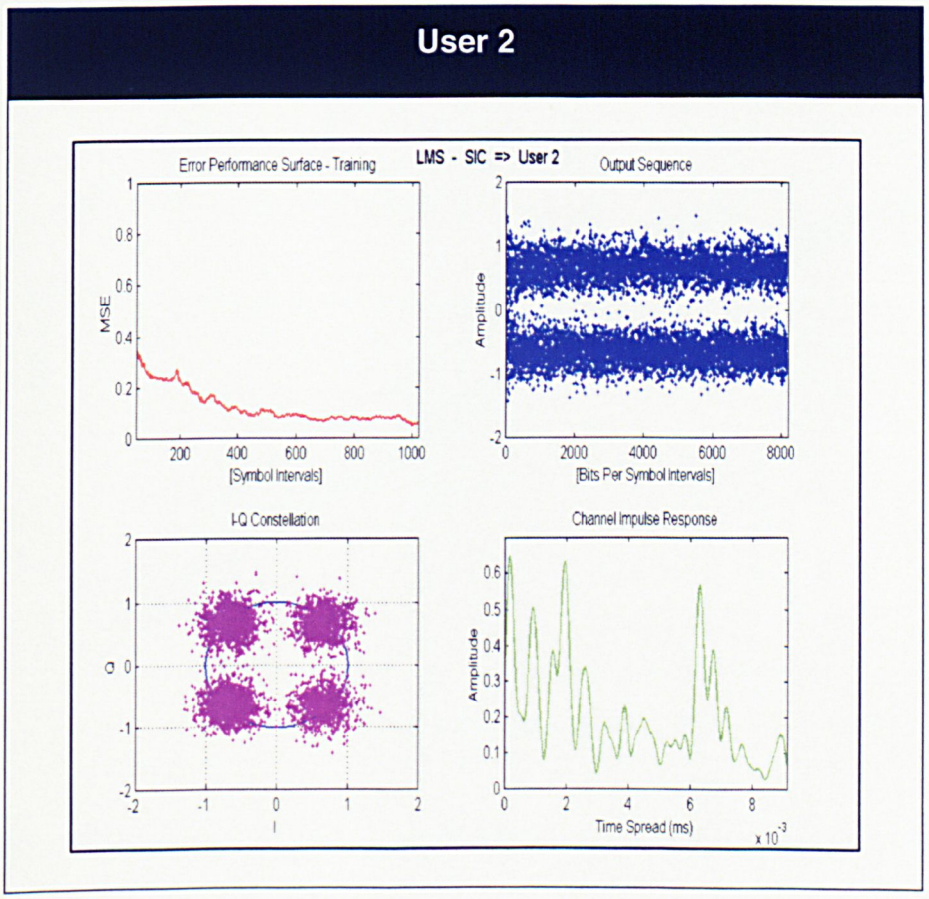

Figure 5-12 SIC MUD strategy for equal power reception

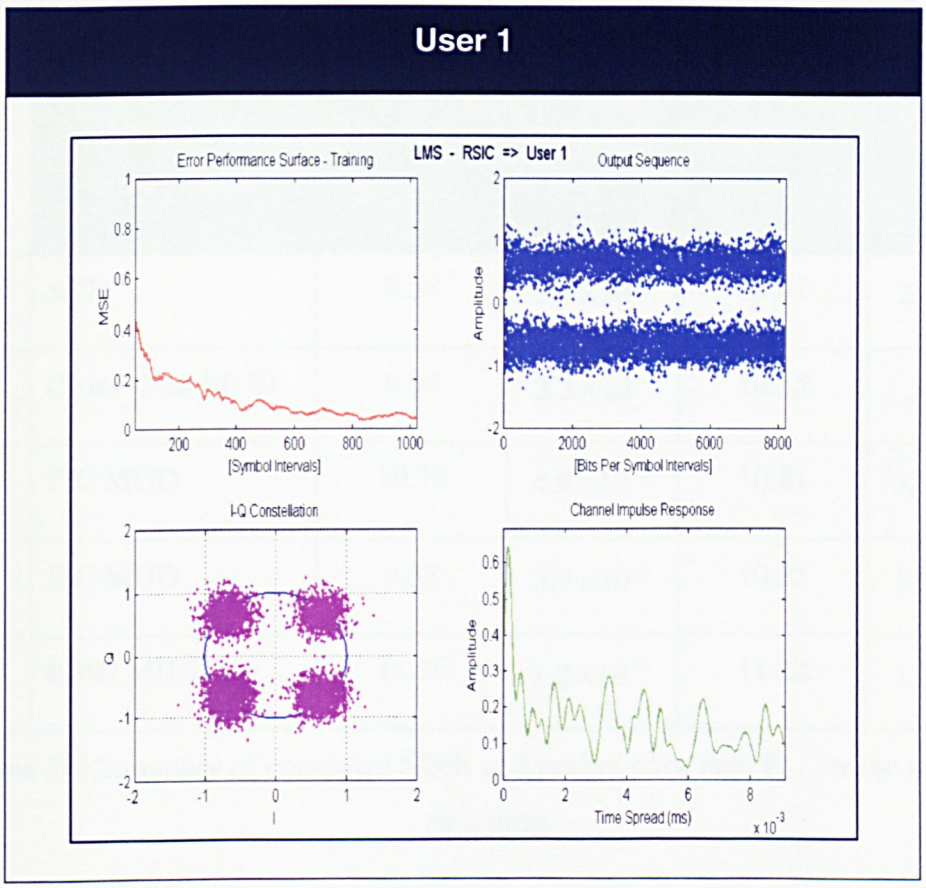

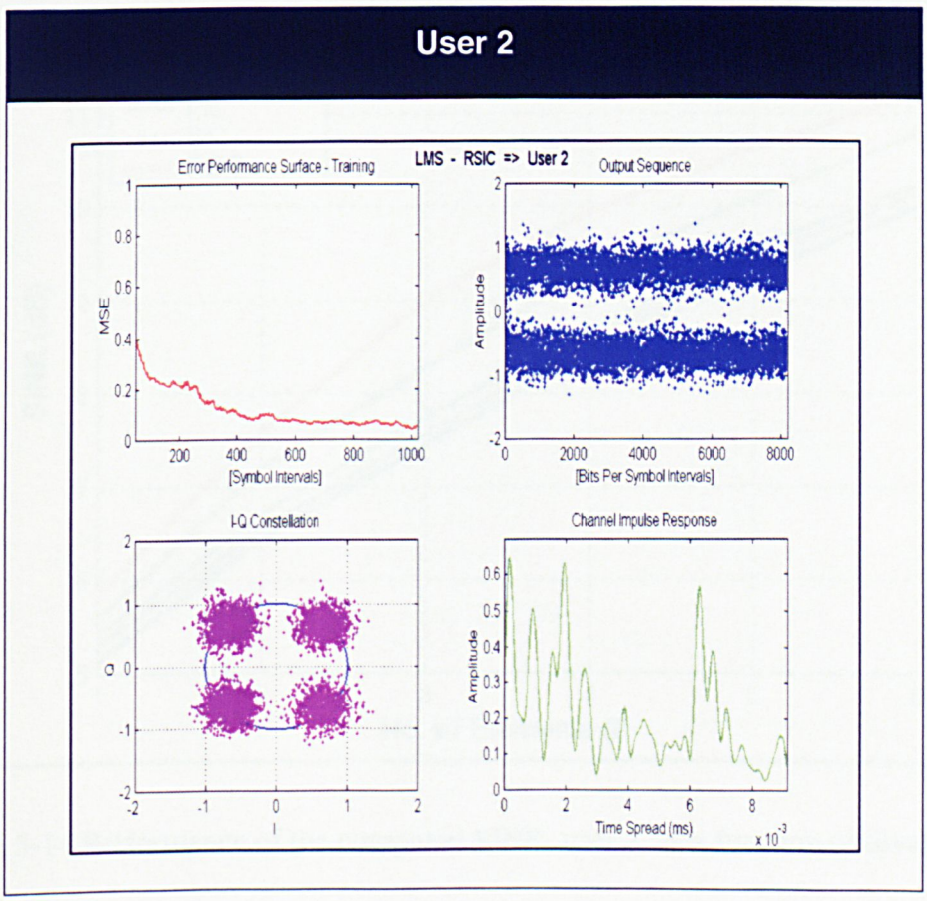

Figure 5-13 RSIC MUD strategy for equal power reception

	Receiver Structures	User 1		User 2	
		SINR (dB)	P_{er}	SINR (dB)	P_{er}
1.	SUD	9.58	3.7×10^{-3}	10.01	2.4×10^{-3}
2.	Cross-Over MUD	9.95	2.2×10^{-3}	10.15	1.95×10^{-3}
3.	PIC MUD	10.78	4.9×10^{-4}	10.81	2.4×10^{-4}
4.	SIC MUD	9.58	3.7×10^{-3}	10.25	1.5×10^{-3}
5.	RSIC MUD	11.36	1.2×10^{-4}	11.22	1.1×10^{-4}

Table 5-2 Summary of computed SINR and packet error rate, P_{er}, for the receiver structures

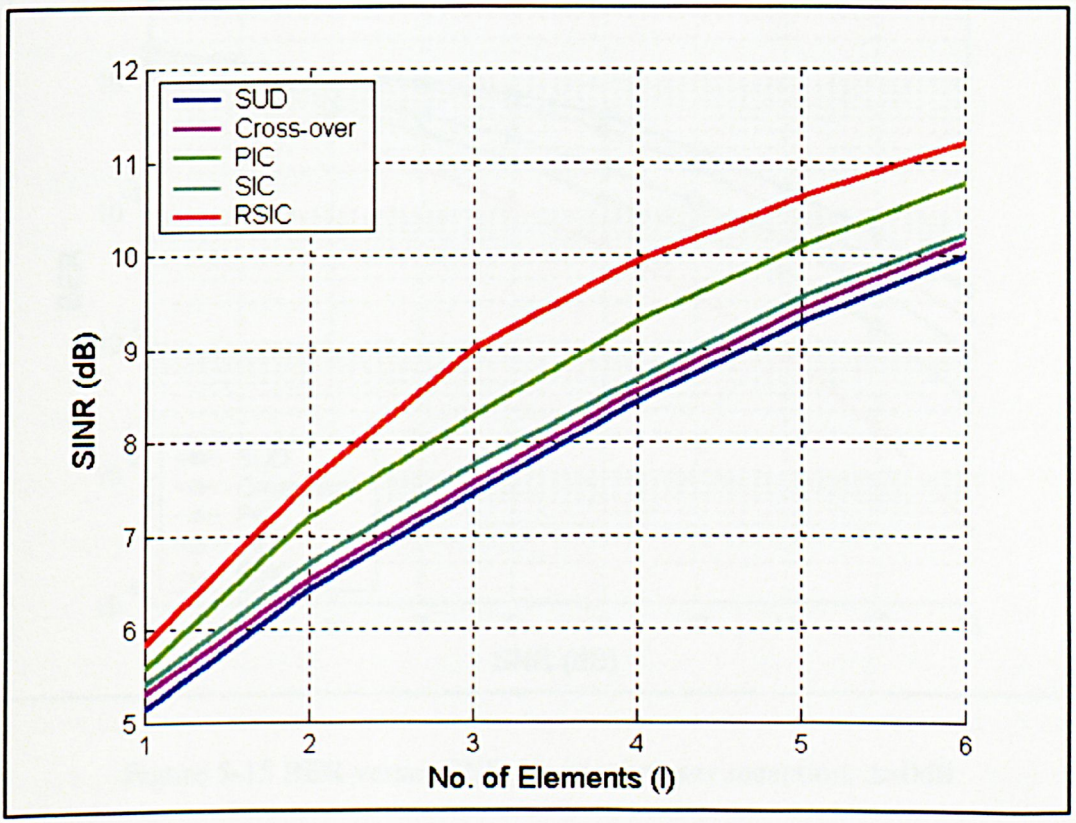

Figure 5-14 Performance of the computed SINR, user 2, as a function of diversity order

5.6.1.2 BER Analysis in AWGN Channel

A 3-user equal power reception is considered when operating in an Additive White Gaussian Noise (AWGN) channel. The received amplitude difference between the users is set such that $10\log_{10}(A_k/A_{k+1})^2 = \Delta\text{dB}$, $k = 1,2,3$. In the equal power reception, the power difference is $\Delta = 0$ dB. The BER obtained by the single user detection strategy falls short from the BER for a single user bound, as shown in Figure 5-15. It was observed that the "cross-over" strategy did not perform well, with its BER performance slightly lower than the single user detection strategy. Both the PIC and RSIC strategies were observed to have BER performances that are closer to the single user bound. At the BER of 10^{-3}, the RSIC had a gain of ~1.2 dB over the PIC strategy, which had in turn a gain of ~1 dB over the SIC strategy.

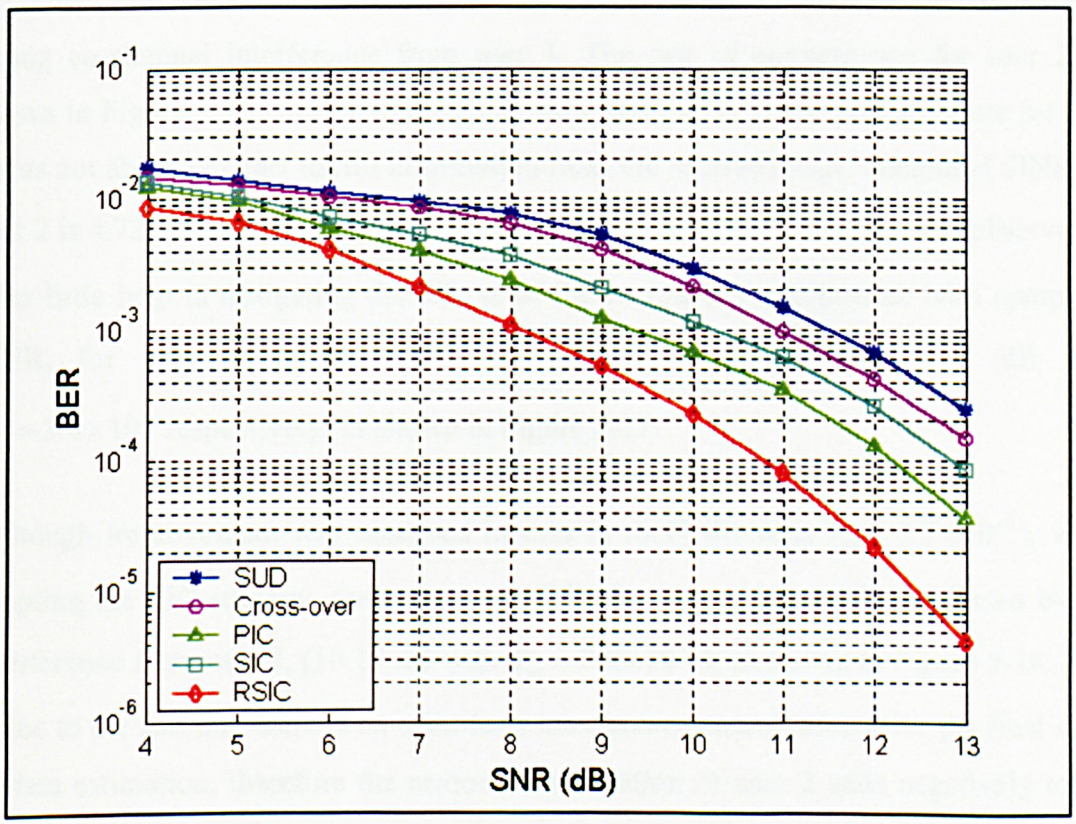

Figure 5-15 BER versus SNR for equal power reception, Δ=0dB

5.6.2 Unequal power (Near-Far) reception

5.6.2.1 Performance in Multipath Propagation Channel

A 2-users unequal power reception is considered here. The user's parameter settings are illustrated in Table 5-3. The feedforward and feedback tap length for both users are 20 and 40 respectively, refer to Appendix Figure 9 of Appendix IX for tap length selection. The step-size values for the canonical complex LMS adaptive algorithm was set at 0.006 and 0.004 for the feedforward and feedback filter taps respectively, refer to Appendix Figure 10 of Appendix IX for optimised stepsize values selection.

Figure 5-16 shows the computed output results for both users by using the single user detection strategy. As user 1 has a higher SNR difference of 8dB, data estimation was not significantly affected much by the interference of user 2, with computed SINR = 10.49 dB with $P_{er} = 2.4 \times 10^{-4}$. However, user 2, being the weaker user was affected by strong co-channel interference from user 1. The rate of convergence for user 2, as shown in Figure 5-16, was observed to be slow and the SUD receiver structure for user 2 was not able to extract useful information from the received data. Computed SINR for user 2 is 4.72 dB with $P_{er} = 3.2 \times 10^{-1}$. The "cross-over " MUD strategy was observed to offer little help in mitigating the effects of the co-channel interference with computed SINR, for user 1 and 2, 10.35 dB with $P_{er} = 4.8 \times 10^{-4}$ and 4.91 dB with $P_{er} = 3.0 \times 10^{-1}$ respectively, as shown in Figure 5-17.

Although improvement was observed in user 2, (6.99 dB with $P_{er} = 2.9 \times 10^{-2}$), when adopting the PIC strategy, the computed SINR for user 1 was slightly affected by the interference from user 2, (10.19 dB with $P_{er} = 2.8 \times 10^{-4}$), as shown in Figure 5-18. This is due to the fact that there is an open-loop interference cancellation prior the final stage of data estimation, therefore the erroneous estimation of user 2 adds negatively to the interference cancellation for user 1. By correctly estimating the data for the stronger user, the SIC structure was able to improve the computed SINR for user 2 to 8.12 dB with $P_{er} = 5.6 \times 10^{-3}$. Since no interference cancellation consideration is made for user 1, the computed result for user 1 is identical to the single user detection strategy, as shown in Figure 5-19.

Significant improvement was observed when the RSIC strategy was used. By performing a single loop-back from the weak user to the stronger user, the output SINR of user 1 shown in Figure 5-20, was improved to 11.45 dB with $P_{er} = 0.0$. The computed SINR for user 2 was 9.62 dB with $P_{er} = 2.1 \times 10^{-4}$, which has a major improvement of ~5.1 dB from the single user detection strategy. A summary of the computed SINR and packet error rate, P_{er}, for the various receiver structures is summarised in Table 5-4.

Figure 5-21 shows a plot of the computed SINR for user 2, by the various detection strategies as a function of diversity order. With the increased use of diversity order, the single user detection strategy still performs poorly. As $L > 2$, the performance of the RSIC structure outweighs the other MUD strategies.

Tx Depth for both		User 1 - 9 m and User 2 – 9 m
Rx Array Depth		First element at 8 m ref. to seabed
Channel		Multipath Channel Model
User 1	**Distance**	2000 m
	I/P SNR	14 dB
User 2	**Distance**	5000 m
	I/P SNR	6 dB

Table 5-3 Parameters for 2-user near-far scenario

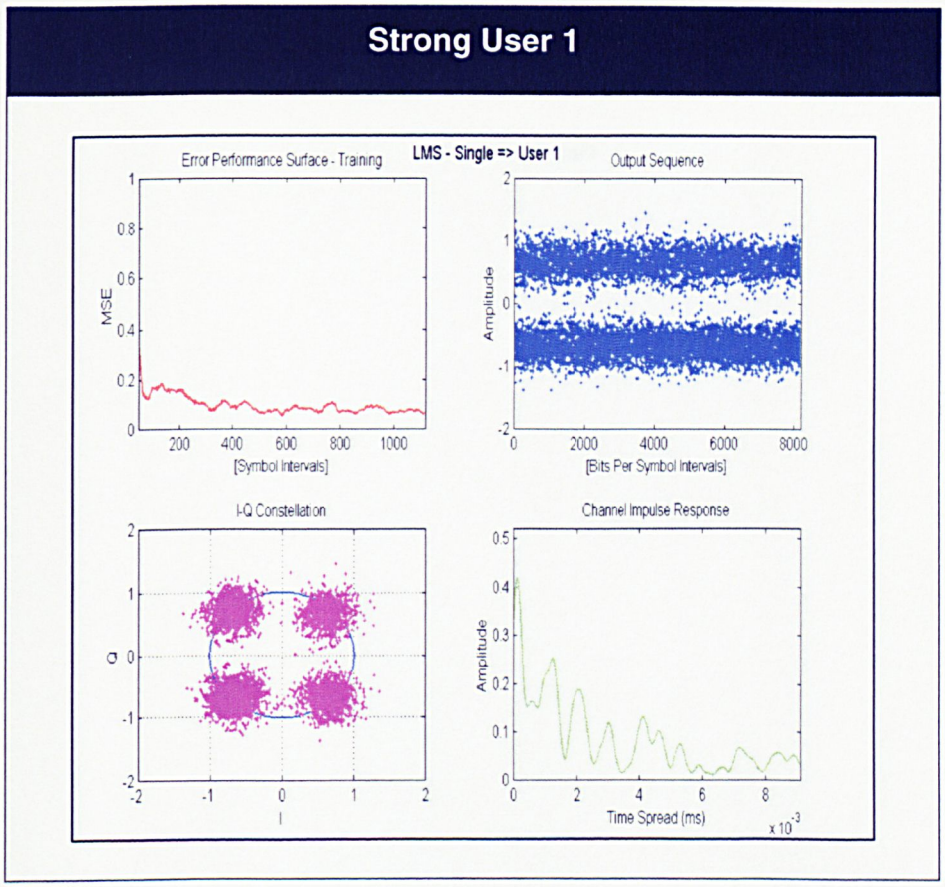

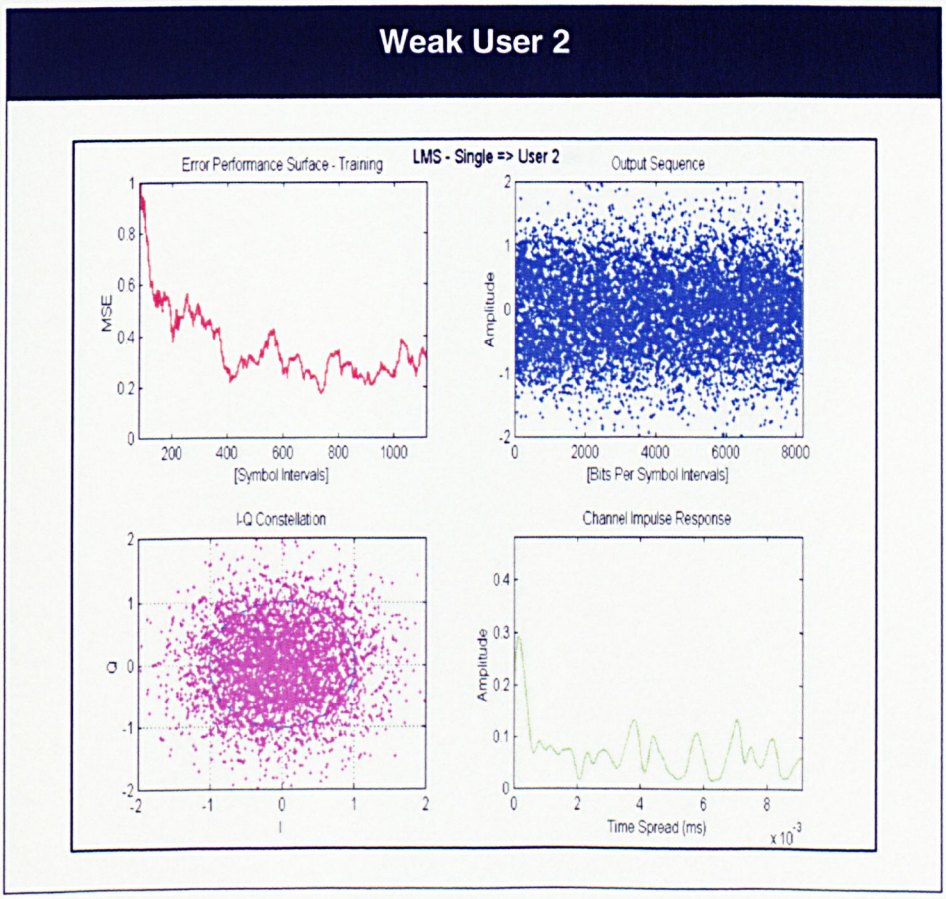

Figure 5-16 Single-user detection strategy for unequal power reception

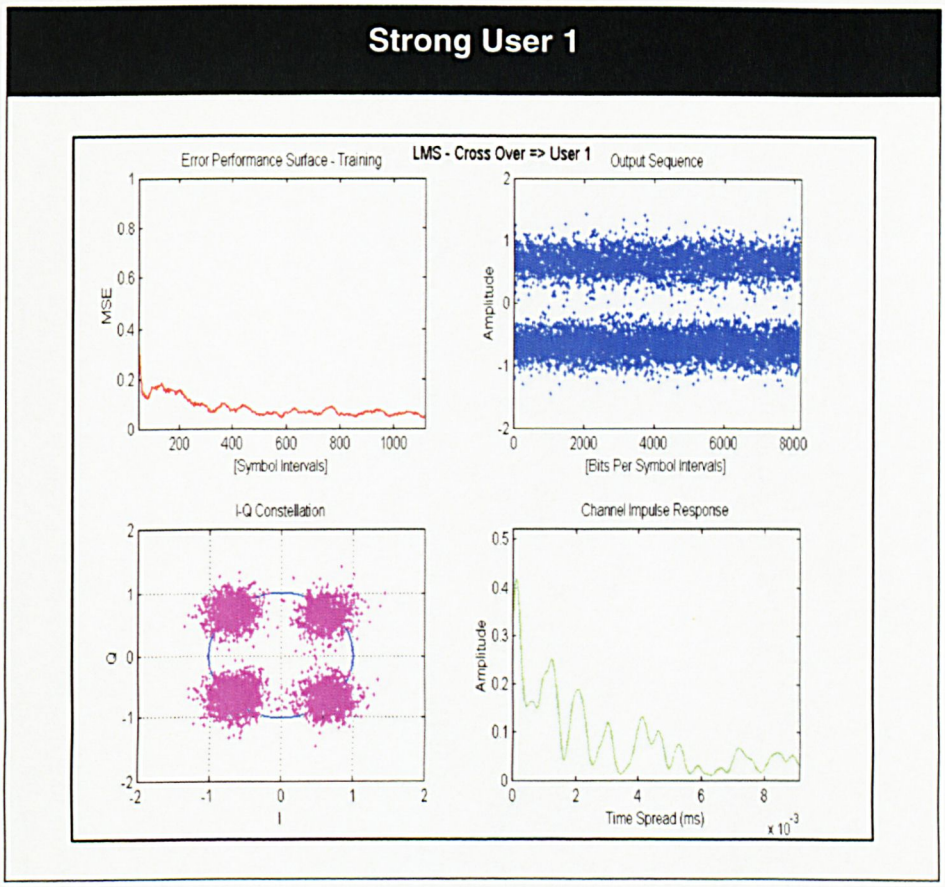

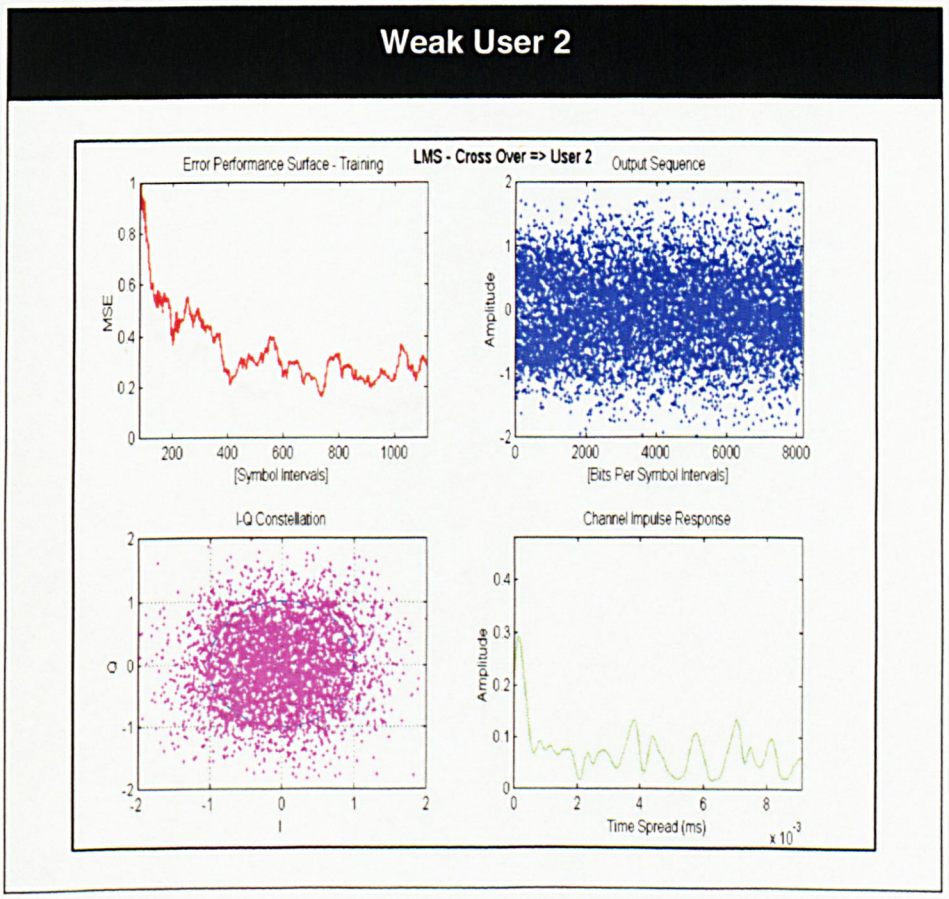

Figure 5-17 Cross-over MUD strategy for unequal power reception

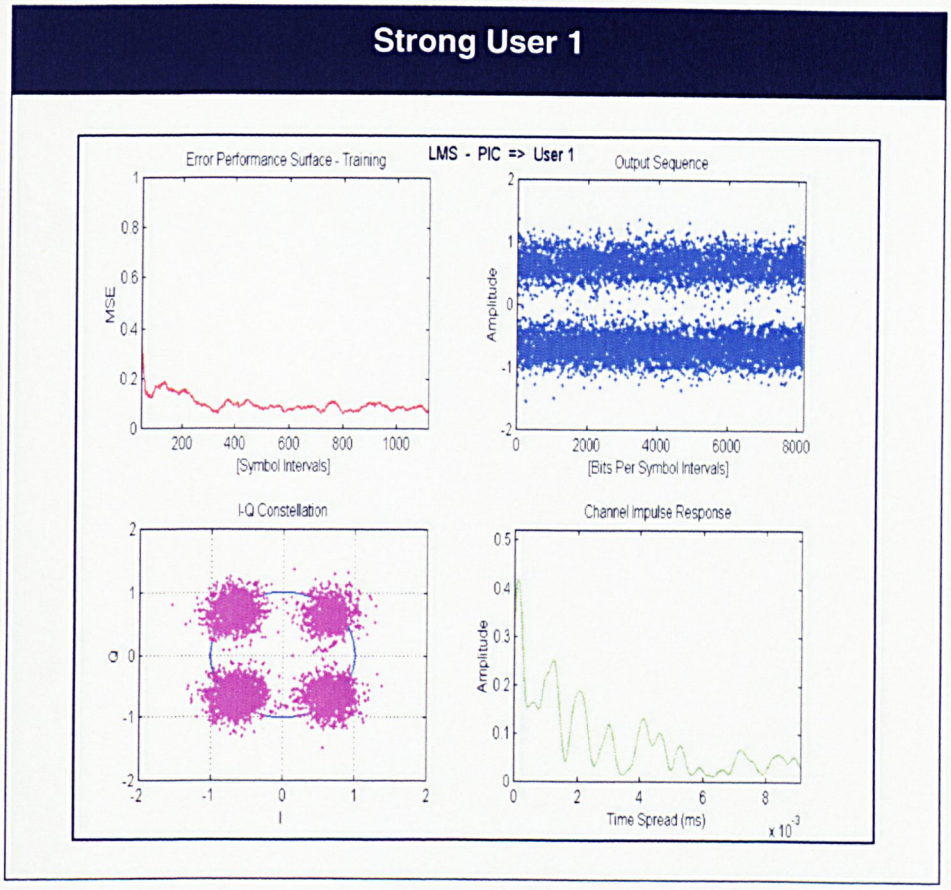

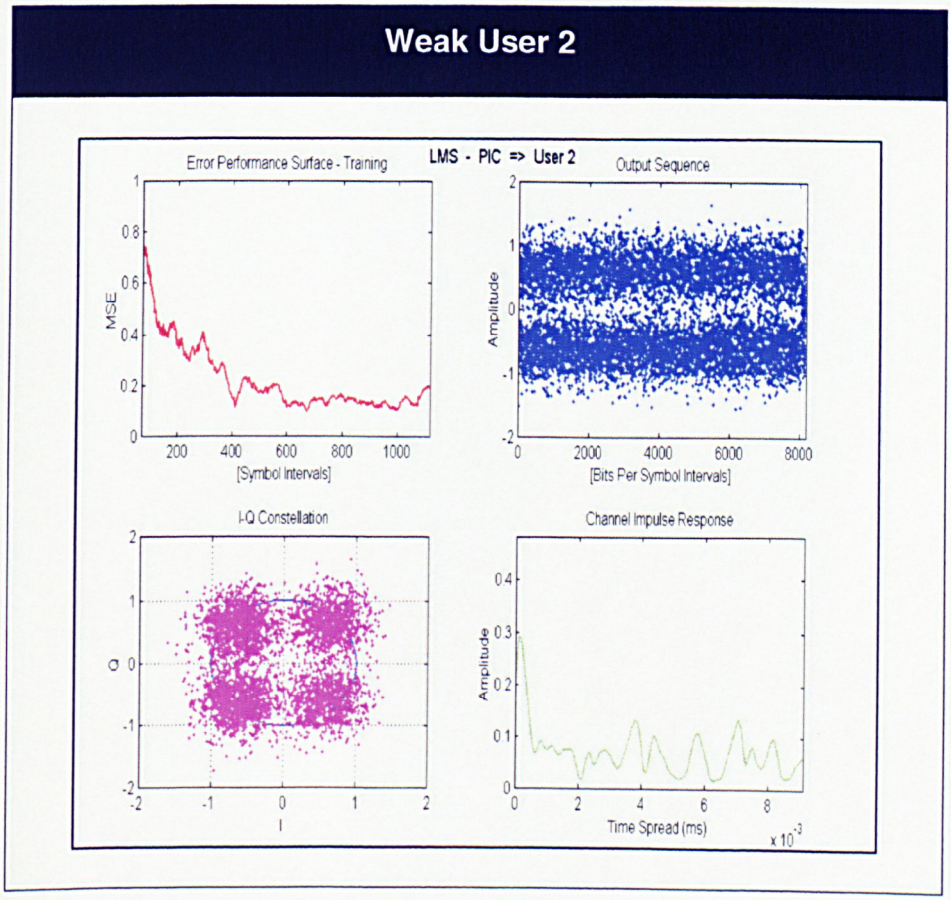

Figure 5-18 PIC MUD strategy for unequal power reception

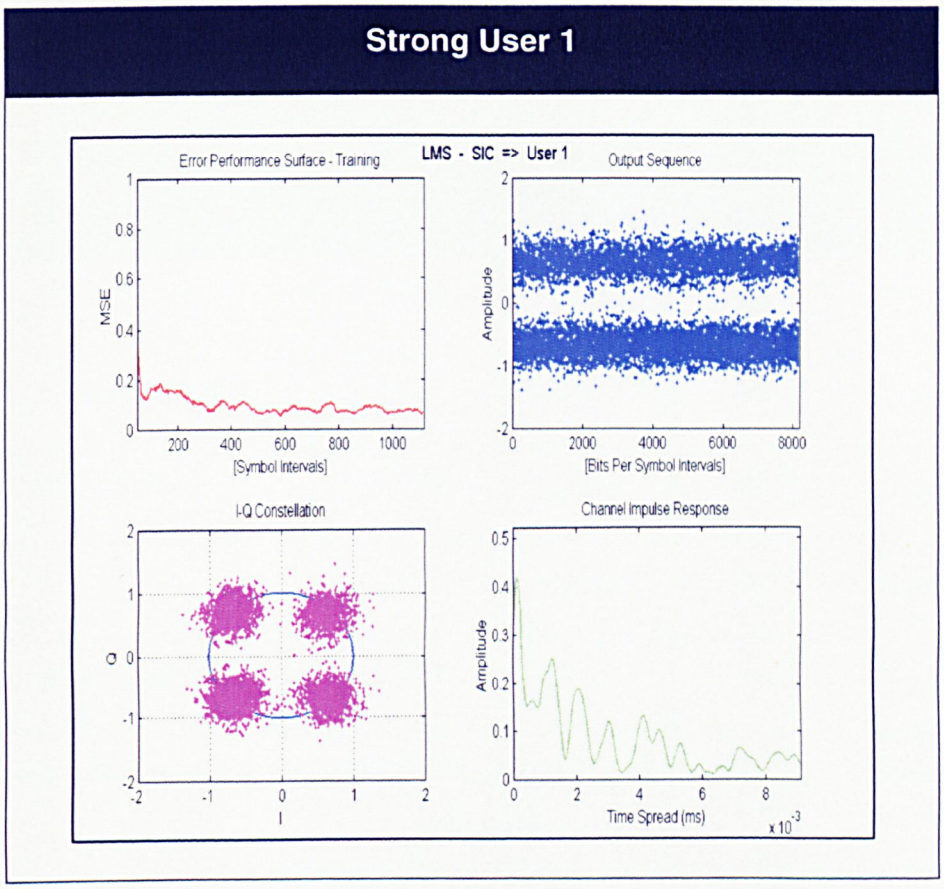

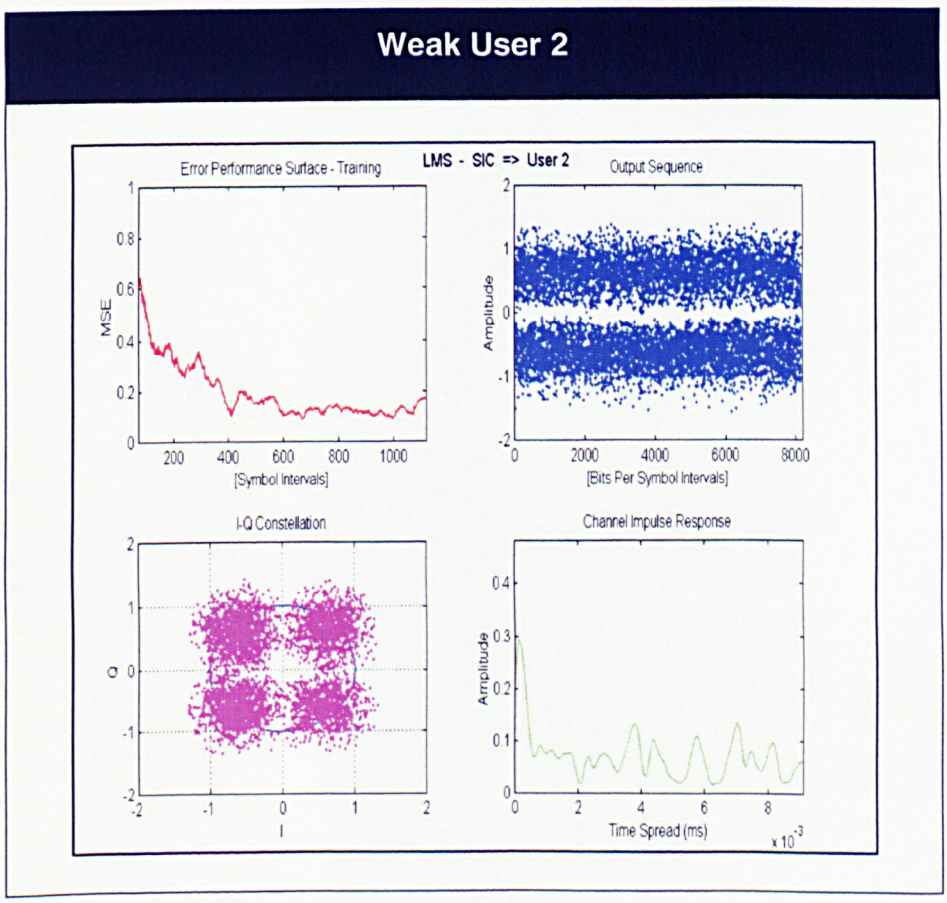

Figure 5-19 SIC MUD strategy for unequal power reception

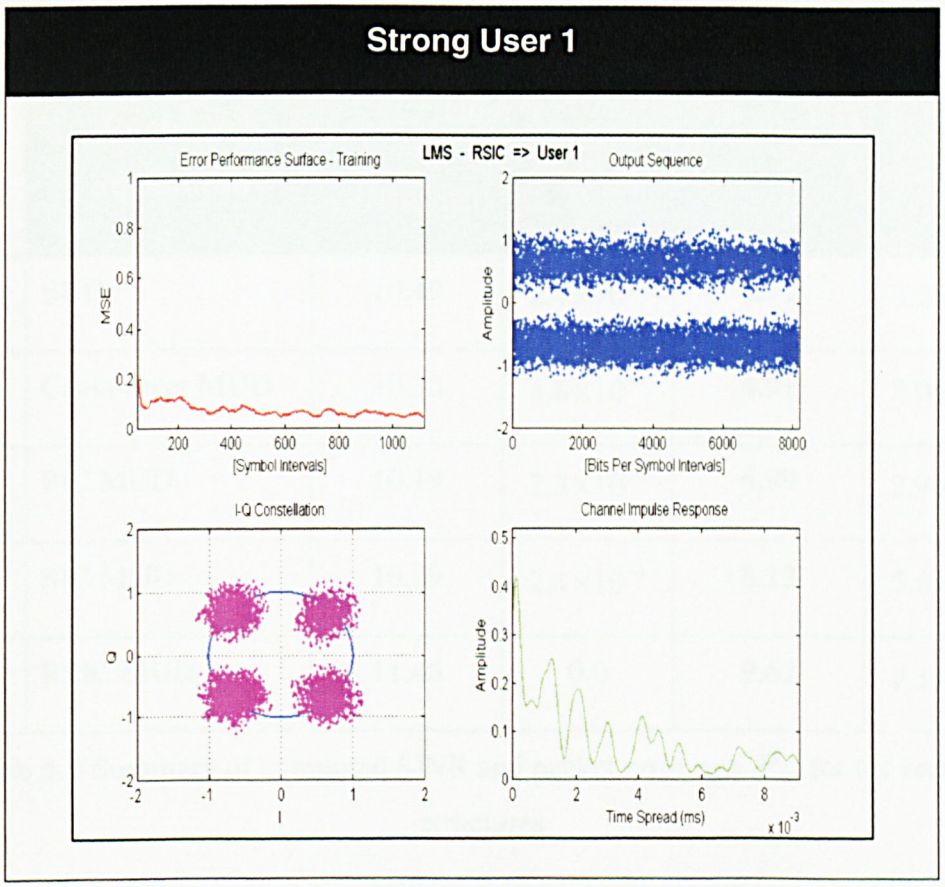

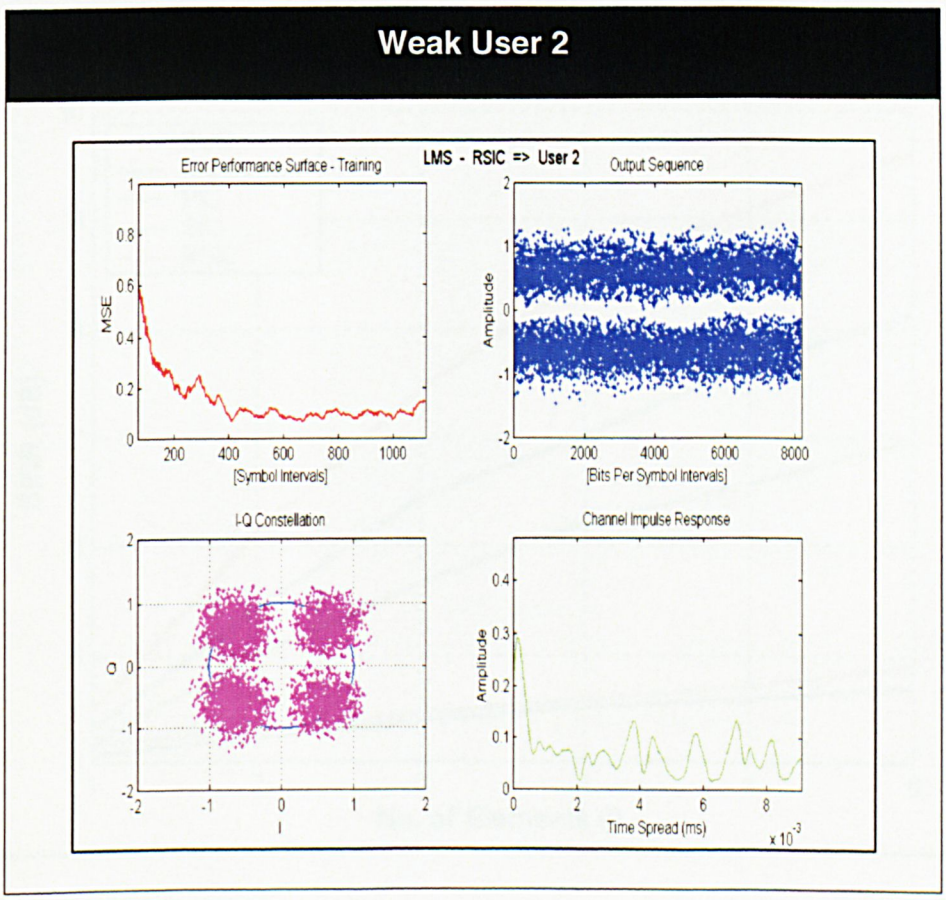

Figure 5-20 RSIC MUD strategy for unequal power reception

	Receiver Structures	User 1		User 2	
		SINR (dB)	P_{er}	SINR (dB)	P_{er}
1.	SUD	10.49	2.4×10^{-4}	4.72	3.2×10^{-1}
2.	Cross-Over MUD	10.35	4.8×10^{-4}	4.91	3.0×10^{-1}
3.	PIC MUD	10.19	2.8×10^{-4}	6.99	2.9×10^{-2}
4.	SIC MUD	10.49	2.4×10^{-4}	8.12	5.6×10^{-3}
5.	RSIC MUD	11.45	0.0	9.62	2.1×10^{-4}

Table 5-4 Summary of computed SINR and packet error rate, P_{er}, for the receiver structures

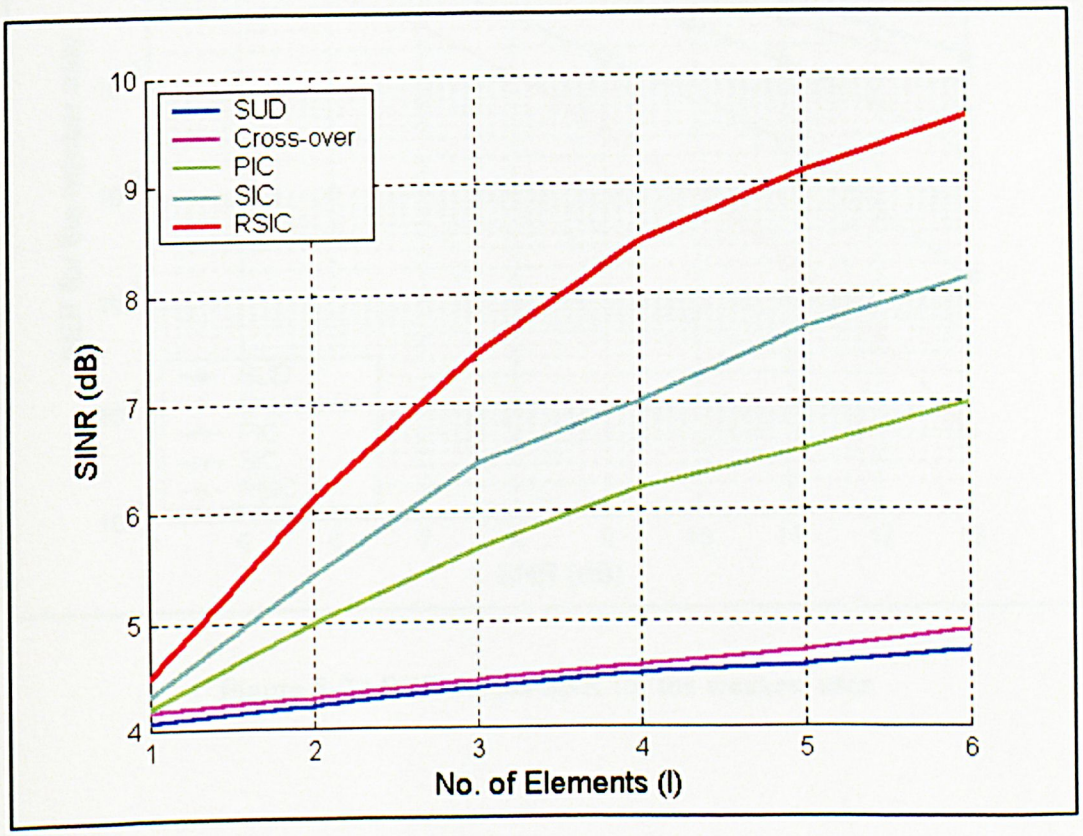

Figure 5-21 Performance of the computed SINR, user 2, as a function of diversity order

5.6.2.2 BER Analysis in AWGN channel

The received amplitude difference between the 3-users unequal power reception is set $10\log_{10}(A_k/A_{k+1})^2 = \Delta\text{dB}$, where power difference is $\Delta = 4\text{dB}$. Figure 5-22 shows the BER versus SNR for the weakest user in an unequal power reception scenario. It is observed that the BER obtained by the single user detection and "cross-over" MUD strategy is much higher than the single user bound. As opposed to the equal power reception, the SIC had a better performance over the PIC when operating with unequal power reception. However, the loop-back feature of the RSIC strategy offers the advantage of gaining an extra improvement for the strong and weakest user. At the BER of 10^{-3}, the RSIC had a gain of ~1.6 dB over the SIC strategy, which had in turn a gain of ~2 dB over the PIC strategy.

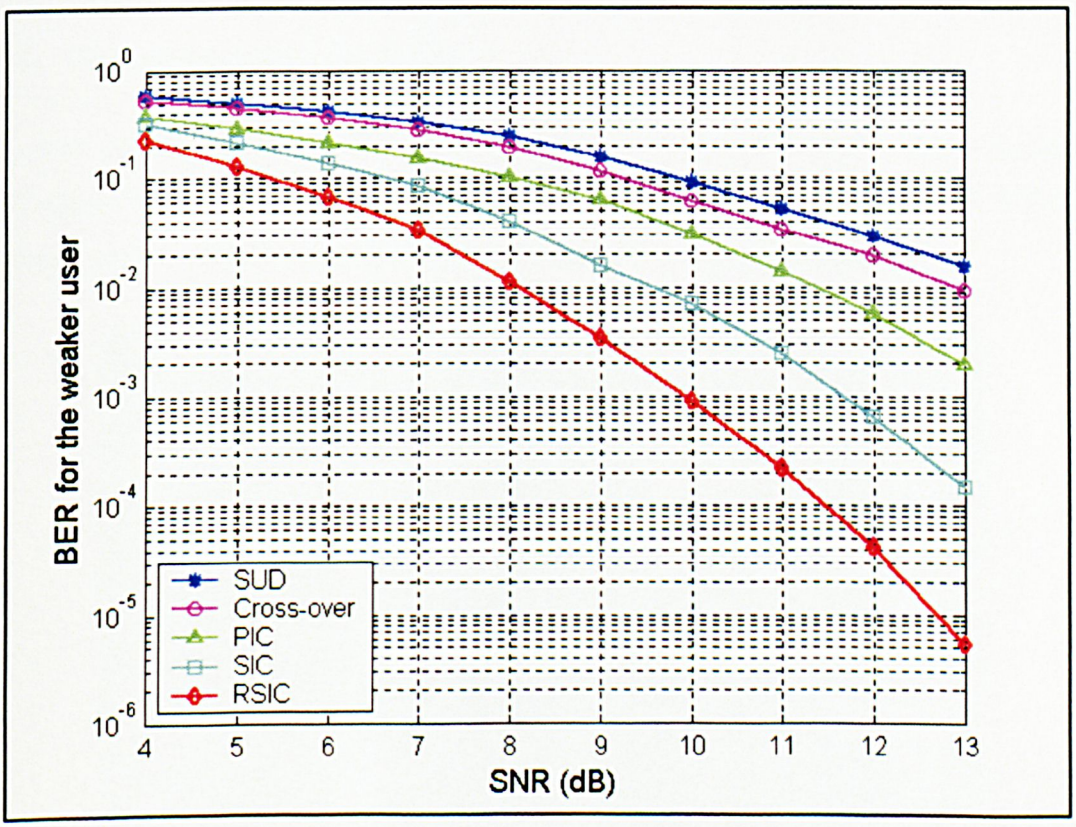

Figure 5-22 BER versus SNR for the weakest user

5.7 Summary

The design of novel multi-user detection strategies is described in this chapter with the aim of mitigating the effects of co-channel interference. Both single and multiuser user systems were tested in scenarios considering equal and unequal power receptions. It was observed from the simulated results that the multi-user detection strategies offer better performance over the single user detection strategy. However, the results achieved by the multi-user strategies exhibit different characteristics. It was observed and suggested that the PIC strategy is more suitable when operating in an equal power reception whereas the SIC was shown to perform better in an unequal power reception. With a slight increase in complexity, the RSIC strategy manifested itself to be a suitable candidate in extracting useful data for users when operating in various types of power reception scenario.

Chapter 6 Experimental Setup and Receiver Software Design

6.1 Introduction

This chapter describes the general organisation for the SWAN-MAST III project field trials that were carried out in both May, 1999 and 2000. The main objective of the sea-trial is to acquire experimental data to enable experimental validation of the MUD strategies.

The multi-user detection strategies described in chapter 5 were developed into a GUI (Graphical User Interface) software based receiver system using the Microsoft Visual C++ 5.0 Studio suite.

6.2 System Configuration Outline

6.2.1 Transmission and Reception

For both sea-trials, the "MeetPost Noordwijk" - MPN, a research and monitoring platform which is positioned at 8 km off the coast of Noordwijk, Netherlands, served as the base station for data reception during the sea-trials, shown in Figure 6-1.

Figure 6-1 Side view of MPN with receiver array attached within the red circle

6.2.2 Configuration for the First Sea-Trial

The experimental setup for the first sea-trial, which was carried out in May 1999, consists of two installations:

1. A *fixed* installation of the receiver array (Rx) was moored on the MPN [6.1]. Six receiving transducers were immersed, moored, powered and connected to the data acquisition hardware and the signals acquired were pre-processed and stored on the MPN.

2. A *mobile* installation, onboard a support ship, where a transmitter (Tx1) and its driving equipment were installed, deployed underwater at each ship stop for each single measurement and recovered after completion of measurement.

The first sea-trial experiment only entailed one transmitter (this is to cater to the needs for other project partner, DUNE, who were investigating on single user blind signal processing algorithms). Measurements with simultaneous transmitted signals were simulated from data obtained from a single source at different positions.

6.2.2.1 Location of Transmitters

Data were gathered at 8 ship locations corresponding to the ranges shown in Figure 6-2 and Table 6-1 respectively. The numbers at each transmission point denotes the individual user transmission in the system [6.2].

6.2.2.2 Receiver Array Geometry

The receiving array consists of 6 hydrophones that were mounted to the MPN [6.2]. The hydrophones were in a 3×2 configuration, with 3 horizontal rows of 2 hydrophones per row. The horizontal spacing is 15 cm or one λ wavelength, and the vertical spacing between the rows is 4 m. The bottom pair of elements were 3 m from the sea bottom. The position of the six hydrophones is shown schematically in Figure 6-3. The hydrophones were fixed onto a frame, which was attached to the sensor pole at the South West corner of the MPN so that the hydrophones were directed to the west of the

platform. The sensor pole was in turn tilted out of the water along the south side of the platform and fixated to allow minimal movement. The relationship between the transmitter and the receiver array fixation is illustrated in Figure 6-4.

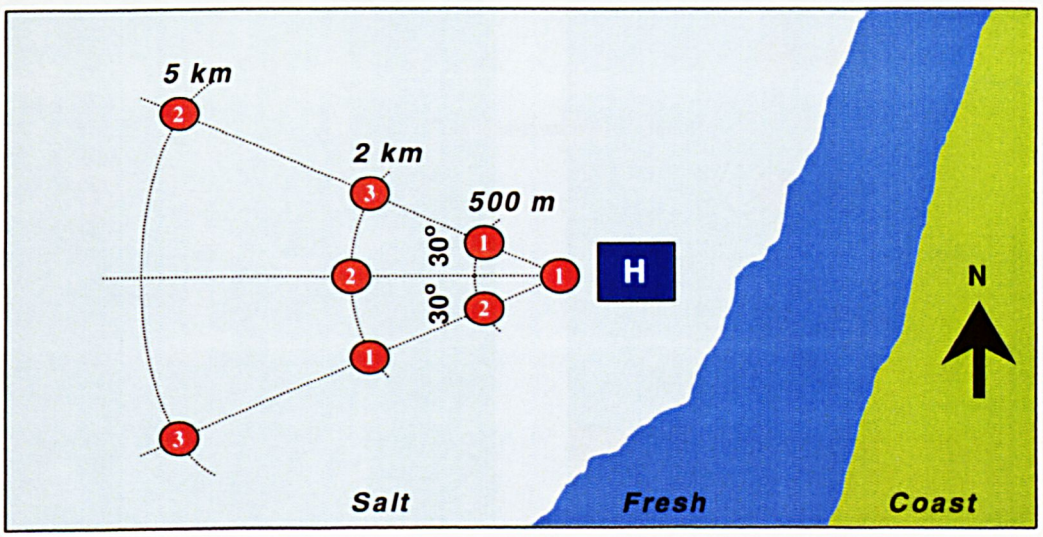

Figure 6-2 Transmitter positions (•), with respect to MPN

Parameter	*Unit*	*Value*
Distance Tx – Rx	**m**	50 500 2000 5000
Angle with respect to West of MPN	**deg**	$+30^0$ and -30^0
Vertical Position of Tx, with ref. to seabed	**m**	9

Table 6-1 Transmitter positions specifications

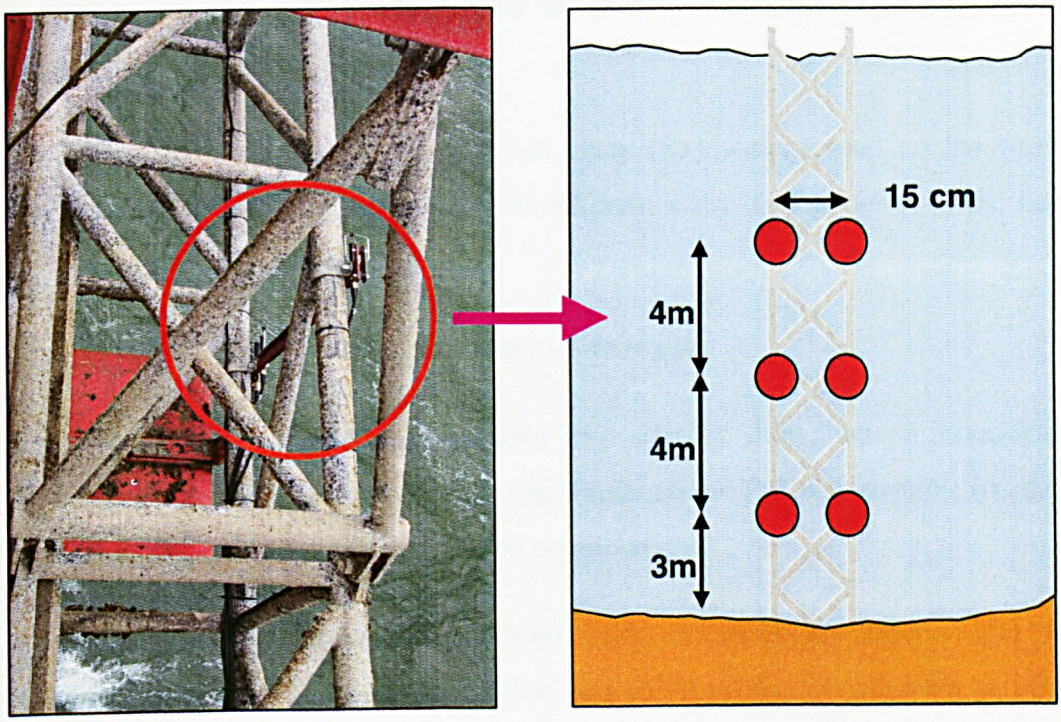

Figure 6-3 Position of hydrophones in receiving array at MPN

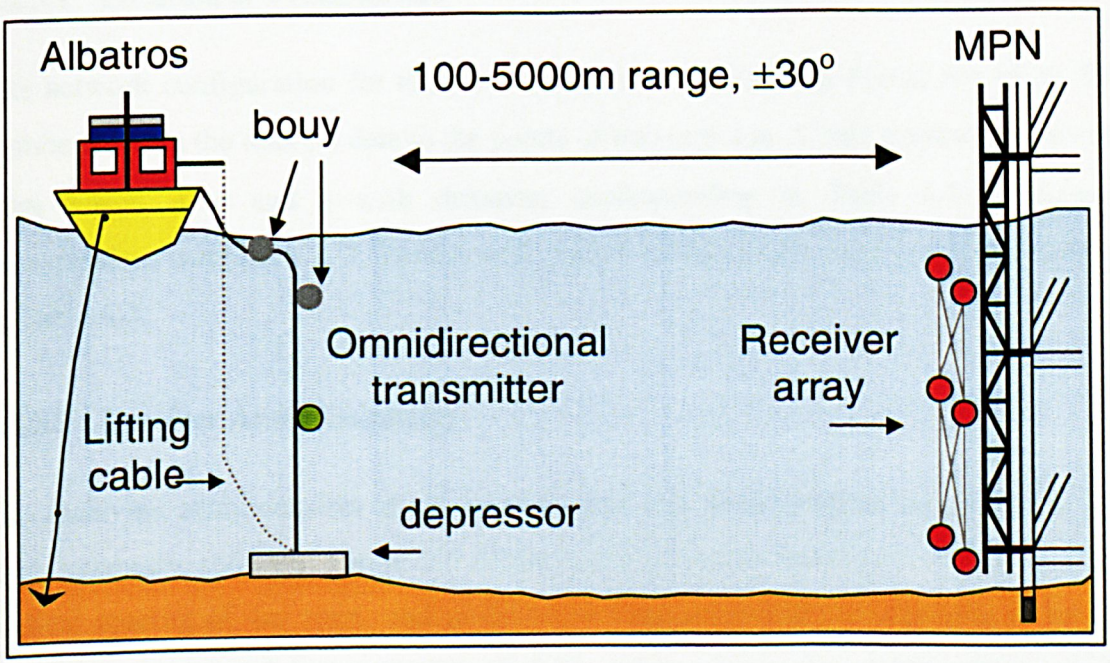

Figure 6-4 Side view configuration of transmitter and receiver array

6.2.3 Configuration for the Second Sea-Trial

In the second sea-trial, which was carried out in May 2000, the experimental set-up consisted of three installations at sea:

1. A *fixed* installation of the receiver array (Rx) was moored on the MPN [6.1]. Six receiving transducers of different array configuration to the first sea-trial was adopted.

2. One *mobile* installation in the fresh water region.

3. Two *mobile* installations, onboard two support ships, where transmitter (Tx1) was fixed at one location while transmitter Tx2 was mobile. At each ship stop, data transmissions were simultaneous.

The second sea-trial experiment entailed both single and multi-user transmission [6.3]. The purpose for the single user transmission was to allow the investigation of system behaviour in the presence of fresh-water to salt-water interface. Measurements with simultaneous transmission were achieved with one mobile installation while the other had a fixed installation.

6.2.3.1 Location of Transmitters

The network configuration for the second field trial is shown in Figure 6-5 [6.3]. The numbers within the dots (•) denote the points of transmission. Single transmissions were from points 2, 4 and 5 with distances corresponding to Table 6-2. Multi-user transmissions were from 1, 2, 3 and 6 with point 6 installed as a fixed point, as indicated in Table 6-3.

6.2.3.2 Receiver Array Geometry

The receiving array consists of six hydrophones that were mounted to the MPN. The array geometry, shown in Figure 6-6 allows spatial diversity technique to be adopted, by vertical spacing of 4m apart, and at the same time achieving beamforming technique with three horizontal hydrophones, of 0.5λ apart, across the middle plane of the geometry. The relationship between the transmitter and the receiver array fixation is illustrated in Figure 6-7.

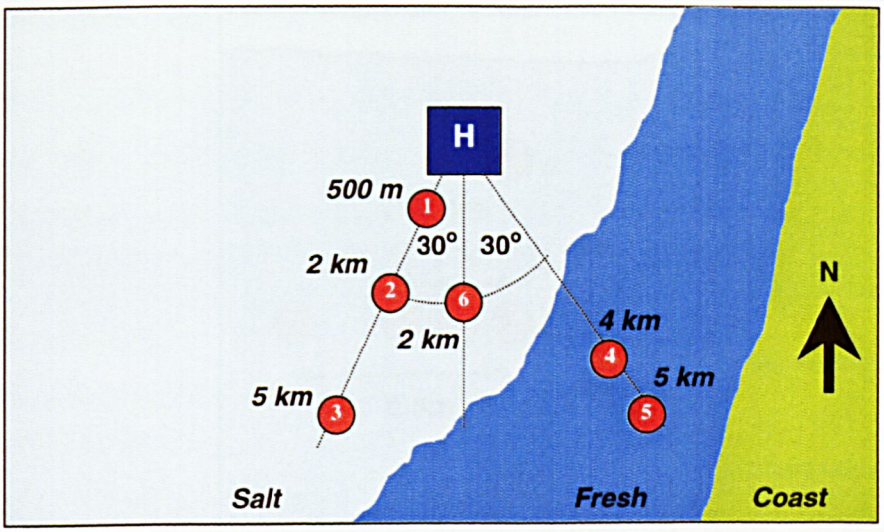

Figure 6-5 Transmitter positions (•), with respect to MPN

Single User Transmission		
Parameter	***Unit***	***Value***
Distance Tx – Rx	**m**	2000 4000 5000
Angle with respect to North of MPN	**deg**	-150° and -210°
Vertical Position of Tx, with ref. to seabed	**m**	9 and 2

Table 6-2 Transmitter positions specifications for single user transmission

Multi User Transmission		
Paramter	***Unit***	***Value***
Distance Tx – Rx	**m**	500 2000 5000
Angle with respect to North of MPN	**deg**	-180° and –210°
Vertical Position of Tx, with ref. to seabed	**m**	9

Table 6-3 Transmitter positions specifications for multi-user transmission

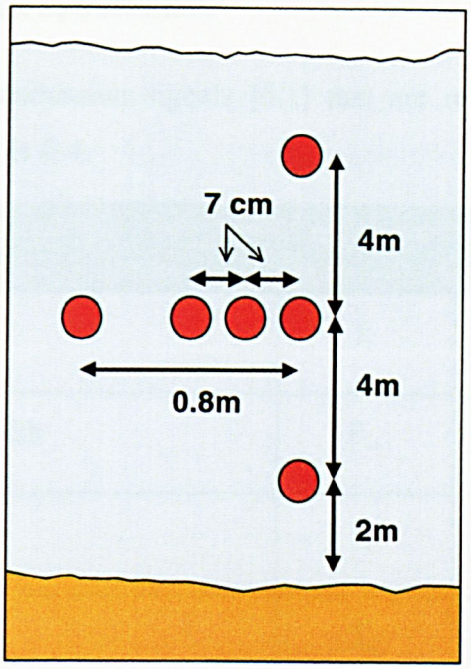

Figure 6-6 Position of hydrophones in receiving array at MPN

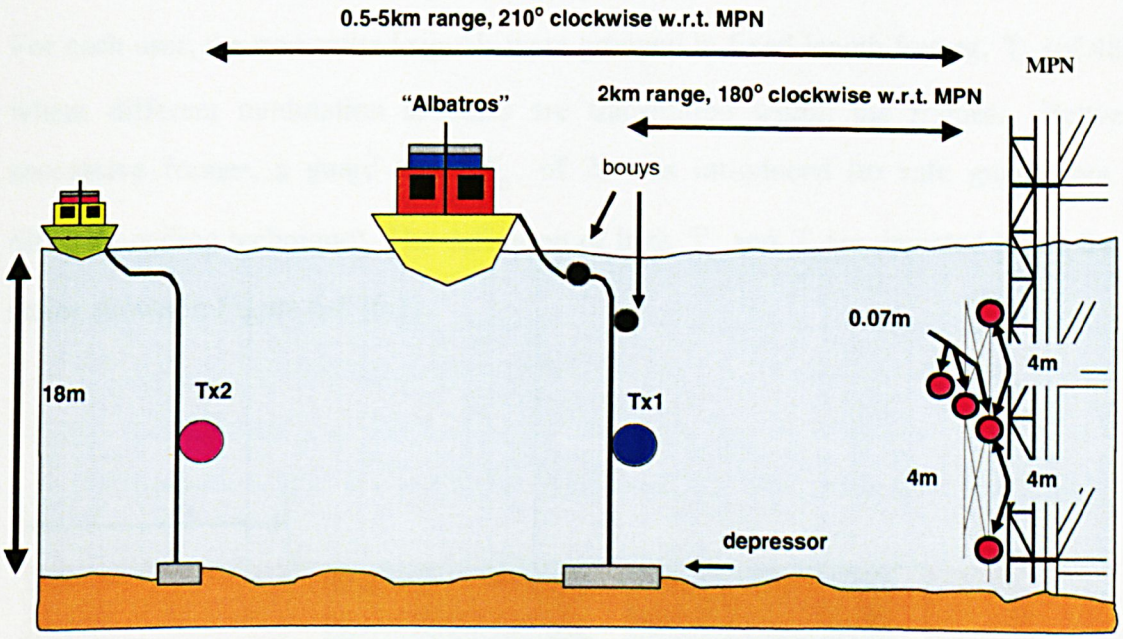

Figure 6-7 Side view configuration of transmitter and receiver array

6.3 Transmission Signal Specification

Specifications of the transmission signals [6.1] that are relevant to the transmitting hardware are given in Table 6-4.

Parameter	Symbol	Unit	Value
Carrier Frequency	f_c	**kHz**	10
Transmission Bandwidth	B_w	**kHz**	4
Tx Sampling rate	f_s	**kHz**	44.1
Frame total Duration	T_o	**s**	48
Guard time between subsequent frames	T_g	**s**	2

Table 6-4 Specifications for transmission data frames

6.3.1 Data Frame Definition

For each user, the transmitted signals were grouped in fixed-length frames, T_o (of 48s), where different modulation schemes are transmitted within the frames. Between successive frames, a guard time, T_g, of 2s was introduced (to safe guard data of different coding technique). The definition of both T_o and T_g are depicted in the frame series shown in Figure 6-8 [6.1].

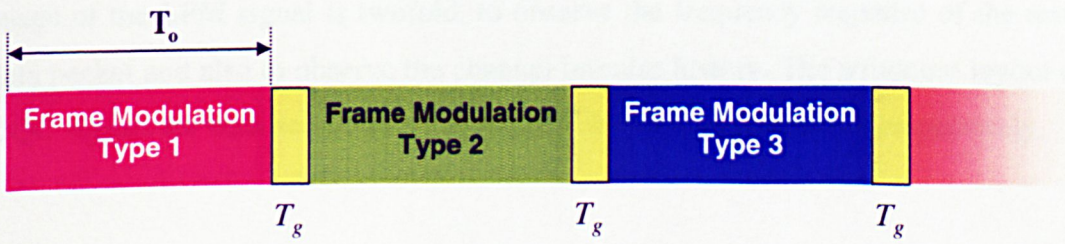

Figure 6-8 Definition of frame and guard time

6.3.2 Data Packet Definition

To fully utilize the 4 kHz of bandwidth, coherent modulation was employed for all users. The data structure consists of a header (synchronizer), a training sequence followed by a variable data sequence, as illustrated in Figure 6-9. The next header of subsequent data packet was used as the trailer to detect if the data sequence was transmitted successively [6.1].

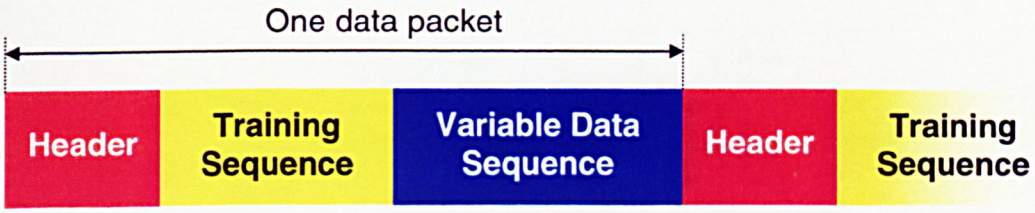

Figure 6-9 Structure of the individual data packets

6.3.3 Signal for Data Quality Check (DQC)

A subset of data quality check (DQC) signals were transmitted prior to any transmission of the data packets [6.4-6.5]. The structure of the DQC signal consists of a 10 kHz pure tone, a Linear Frequency Modulation (LFM) signal and silent period. The purpose of the pure tone served as an observation for harmonic distortion at the receiver end. The usage of the LFM signal is twofold, to observe the frequency response of the received data packet and also to observe the channel impulse history. The structural layout of the DQC signals for both sea-trials are given in Table 6-5 and Table 6-6 respectively.

	Signal	Duration (s)
[1.]	Silent	10
[2.]	10 KHz pure tone	5
[3.]	Silent	10
[4.]	Linear FM (6 – 14 KHz)	10
[5.]	Silent	10
Total Duration		45 s

Table 6-5 Layout of DQC signal for the first sea-trial

	Signal	Duration (s)
[1.]	10 KHz pure tone	55
[2.]	Silent	10
[3.]	Linear FM	55
Total Duration		120

Table 6-6 Layout of DQC signal for the second sea-trial

6.3.4 Signal Generation Specifications

During data acquisition, the primary aim is to accommodate the conditions for sampling, carrier and symbol frequencies, in order to achieve for each symbol an integer number of both the samples and the carrier periods. The first of these conditions is important for the equalisation as it allows data sample extraction in a straightforward manner from the recorded sequences. The definitions and overview of the data signals that were transmitted in both sea-trial are described in the following sections.

6.3.4.1 Data Structure for Transmission – First Sea-Trial

The total number of frames to be transmitted at each ship stop is given in Table 6-7, which corresponds to a 10 min continuous transmission [6.6].

	Modulation	Bit Rate (bps)	No. of Frames	Total No. of Tx bits/symbol	Coding
1.	BPSK	2048	1	96709	-
2.	BPSK	4096	1	193719	-
3.	BPSK (MTS)	4096	1	193719	-
4.	QPSK (255 SYN)	4096	3	581157	Gray
5.	QPSK (511 SYN)	4096	3	575793	Gray
6.	QPSK (128 SYN)	4096	1	194267	Gray
7.	QPSK (MTS)	4096	1	193719	Gray
8.	QPSK (SS)	4096	1	194735	Gray

Table 6-7 Layout of data structure

6.3.4.2 Data Structure for Transmission – Second Sea-Trial

In the second sea-trial, JPEG (QPSK modulation) data files were adopted, as shown in Figure 6-10(a)-(c) where the compression ratio used for the JPEG encoding was 12:1 with respect to the original JPEG file. Coded Division Multiple Access (CDMA) technique with spreading ratio of 7 was also included for the data transmission. A total of 12 frames were transmitted for each data set, with each frame having a duration of 50s, with a 10s guard time between frames [6.7]. The data layout for the various schemes is depicted in Table 6-8.

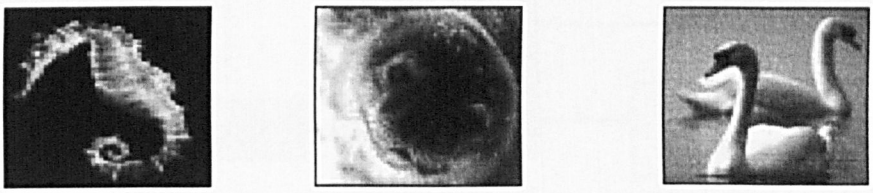

(a) (b) (c)

Figure 6-10 Compressed JPEG file for user (a) 1 (b) 2 and (c) 3

	Modulation	Bit Rate (bps)	No. of Frames	Total No. of Tx bits/symbol	Coding
1.	QPSK	2048	1	96709	Gray
2.	QPSK (JPEG)	4096	3	161262	Gray
3.	7-bit BPSK	585.14	2	167760	-
4.	7-bit QPSK	1170.28	3	167760	Gray

Table 6-8 Time duration of various modulation schemes

6.4 Hardware Equipment for the Sea-Trial

6.4.1 Receiver Acquisition Hardware

The set up of the hardware [6.2] at the receiving end is depicted in depicted in Figure 6-11.

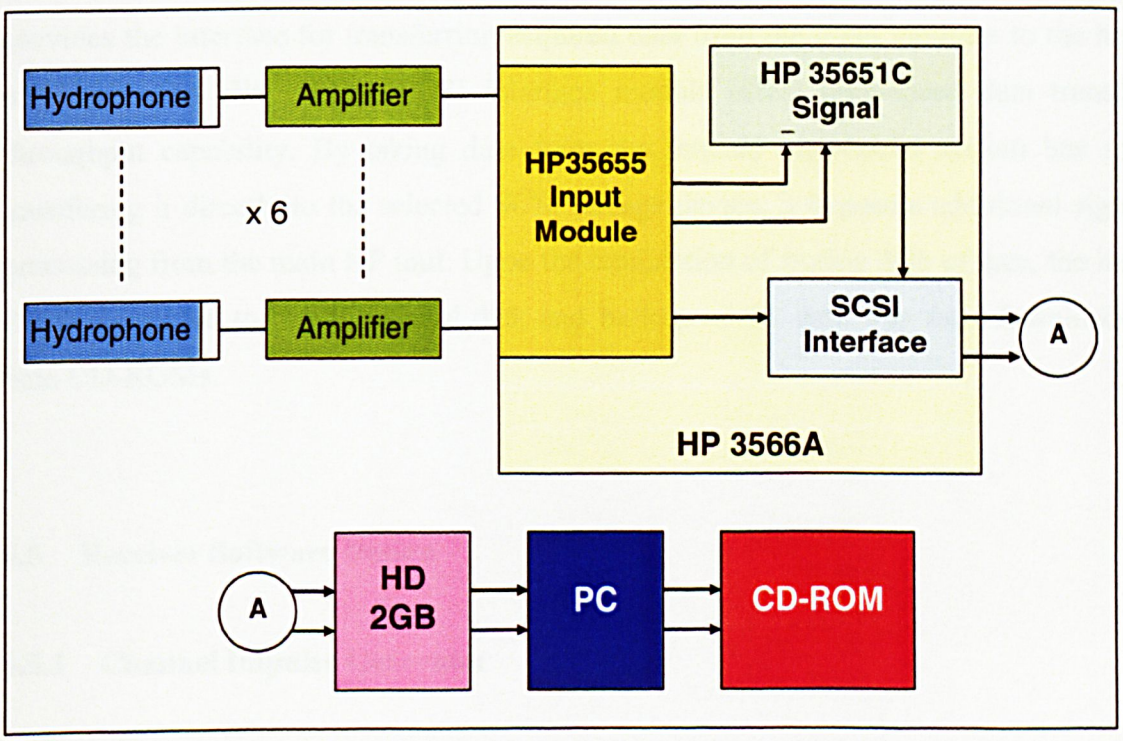

Figure 6-11 Receiver hardware setup

6.4.1.1 Hydrophones

The six receiver hydrophones were of type B&K 8101, which is a wide range waterborne-sound transducer for making absolute sound measurements over the frequency range of 1 Hz to 120 kHz with a receiving sensitivity of –184 dB re 1V/µPa. A built in high quality low-noise preamplifier acts an impedance converter to provide a signal suitable for transmission over long distances.

6.4.1.2 Data Acquisition and Backup system

The HP 3566A signal analyser contains several modules including a 8-channel input module (HP 35655) and a Signal Processing module (HP 35651C). The HP 35655 provides eight separate analogue input channels. The input channels are equipped with an anti-aliasing filter, ADC and digital filter. They are sampled simultaneously to maintain cross-channel phase match. The HP 35651C signal processing module, which has a in-built memory of 16 MB to perform calculations and control tasks. It also provides the interface for transferring acquired data from the input modules to the host computer. The HP 35659A SCSI interface module offers high-speed data transfer throughput capability. By taking data from the internal high-speed system bus and transfering it directly to the selected SCSI storage device, it bypasses additional signal processing from the main HP unit. Upon the completion of storing 2Gb of data, the host PC is connected to the SCSI hard disk and backup of the data was then downloaded onto CD-ROMs.

6.5 Receiver Software Design

6.5.1 Channel Impulse Generator

An easy to use Graphic User Interface (GUI) - Impulse Response Generator, was developed under Microsoft Visual C++ 5.0 is shown in Figure 6-12. This impulse response generator software allows an immediate first check of the channel property for each data transmission performed. Dialog boxes which involve editing of the system parameters and systems files are shown in Figure 6-13, are invoked from the main GUI of Figure 6-12. An example of the computed output for a 2-user reception is shown in Figure 6-14. The flowchart for the channel impulse generator is shown in Figure 6-15.

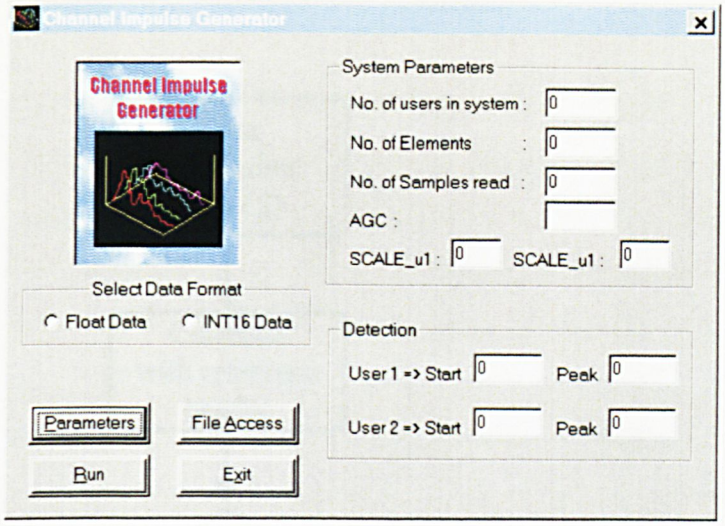

Figure 6-12 GUI display for the channel impulse generator

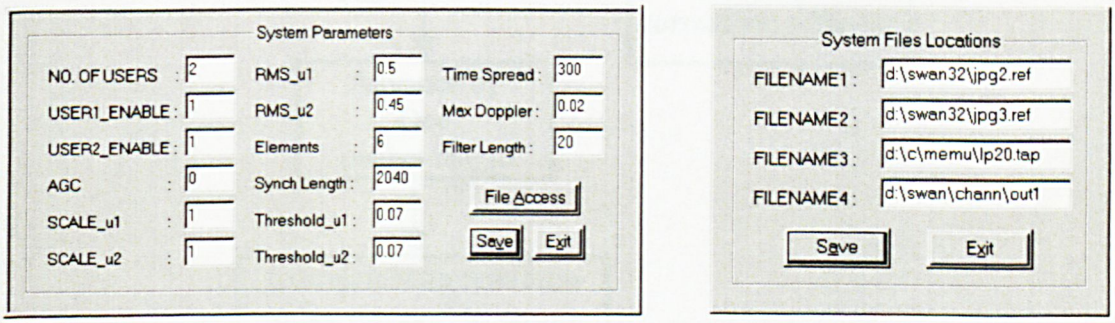

(a) (b)

Figure 6-13 System and files parameters

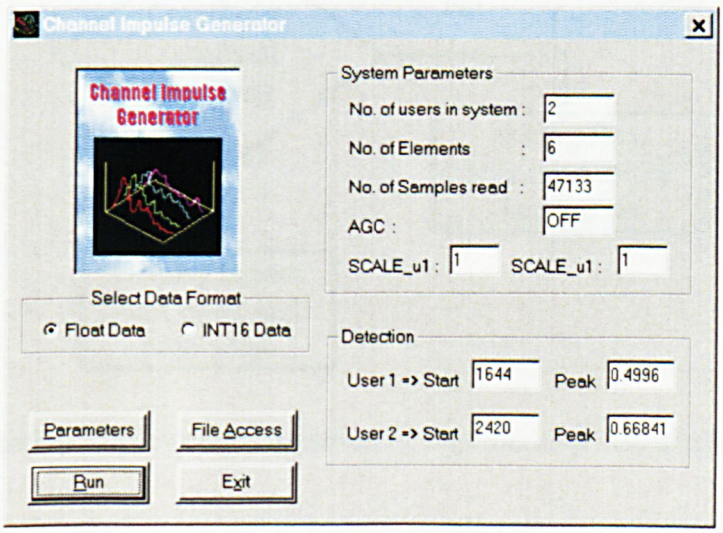

Figure 6-14 Example of a computed output from software

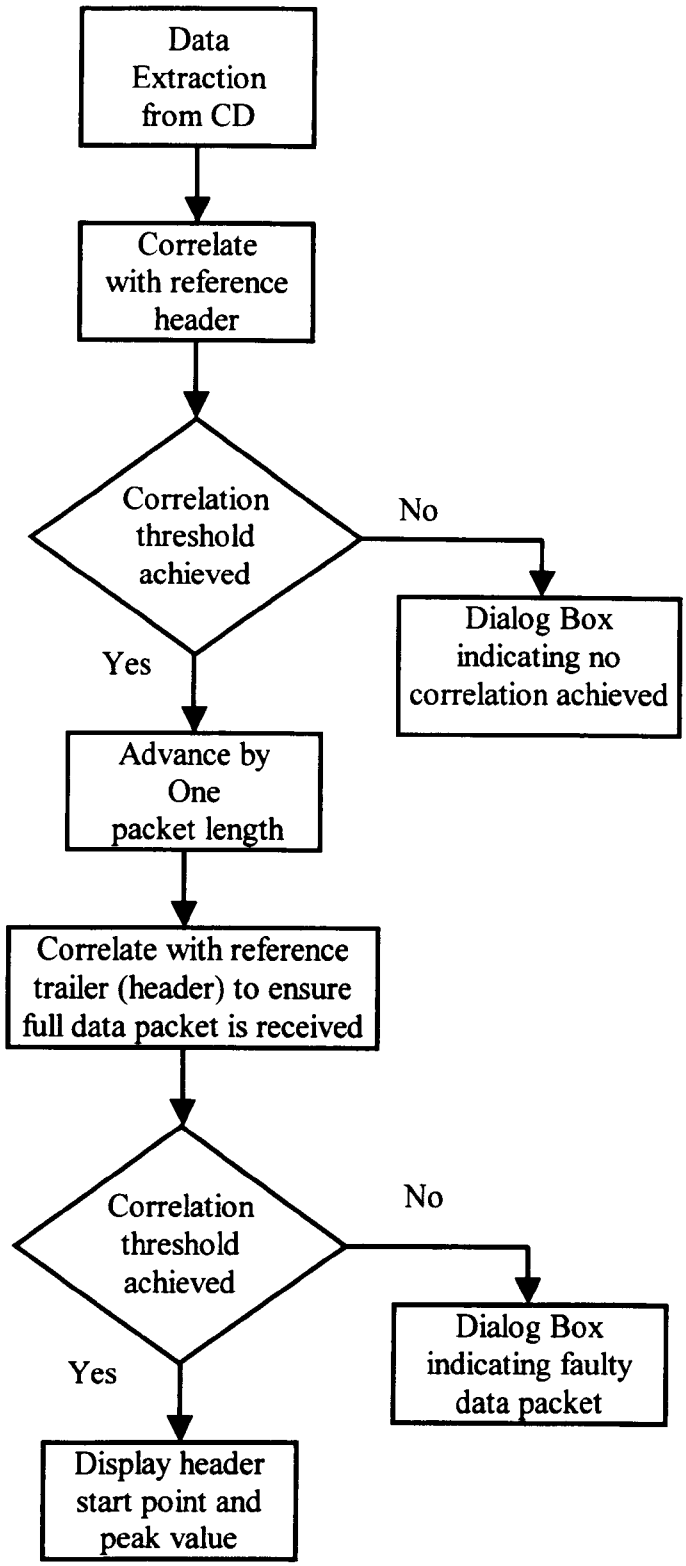

Figure 6-15 Flowchart operation of impulse response generation

6.5.2 Receiver Structures

The adaptive algorithms and multi-user receiver structures described in chapter 4 and 5 were developed into a single GUI platform, as shown in Figure 6-16. The 32-bit platform of the program offers the advantage of faster computation as compared to previous C programs that were developed in the 16-bit platform (receiver software written for the research programme), as reported in [6.8]. The RLS – v.1 and RLS – v.2 algorithms in Figure 6-16 refers to the standard RLS algorithm and the improved RLS (IRLS) algorithm respectively. Both the dialog boxes for editing the system parameters and file locations for the various algorithms, SUD and MUD receiver structures are depicted in Figure 6-17 and Figure 6-18. Upon completion of data demodulation, the GUI displays the end-result of the calculated BER and output SINR of the users, as shown in Figure 6-19, (example for a 2 user reception). The flowchart for the receiver structure is shown in Figure 6-20.

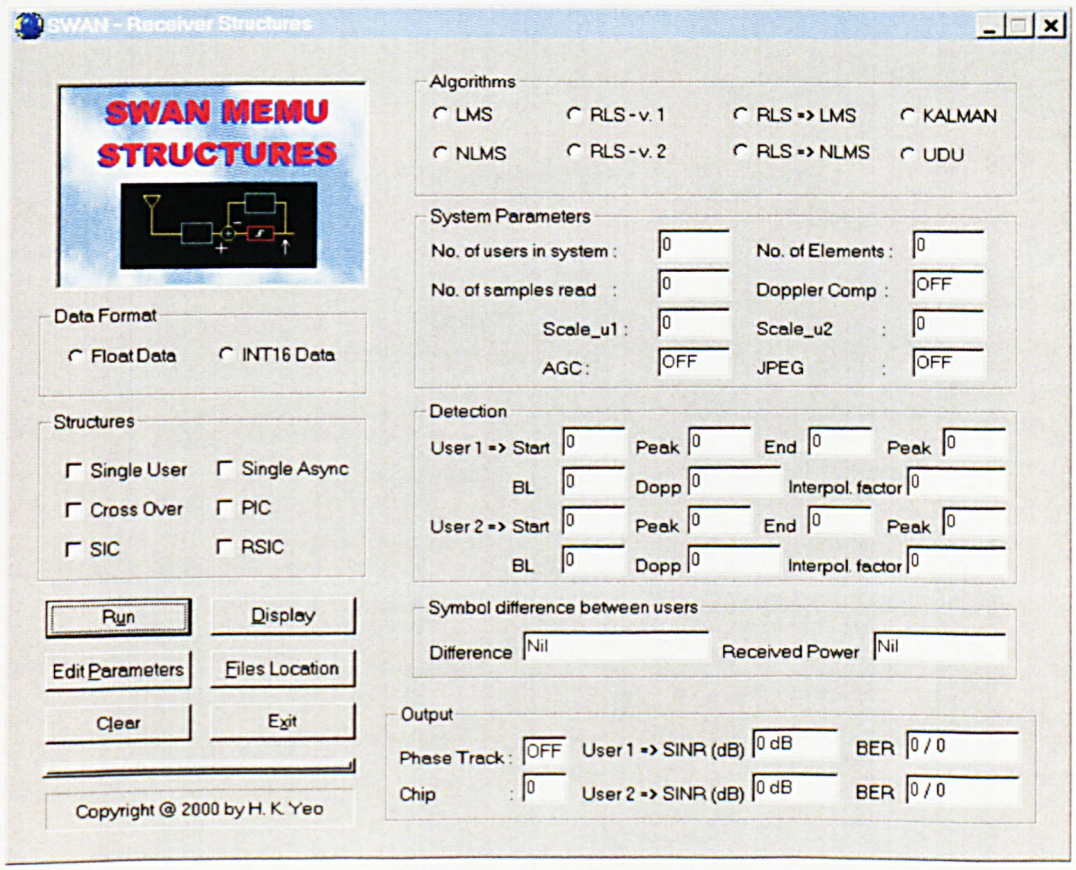

Figure 6-16 GUI display of the various detection strategies with adaptive algorithms

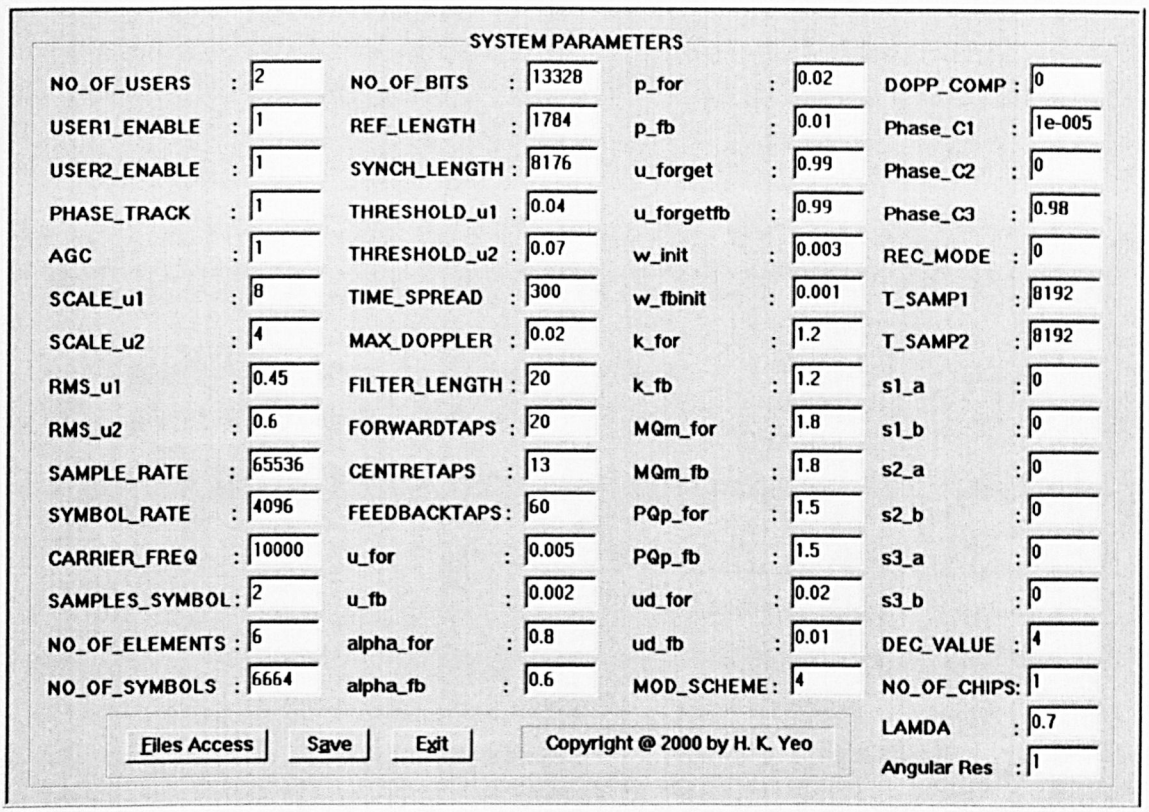

Figure 6-17 System parameters dialog box

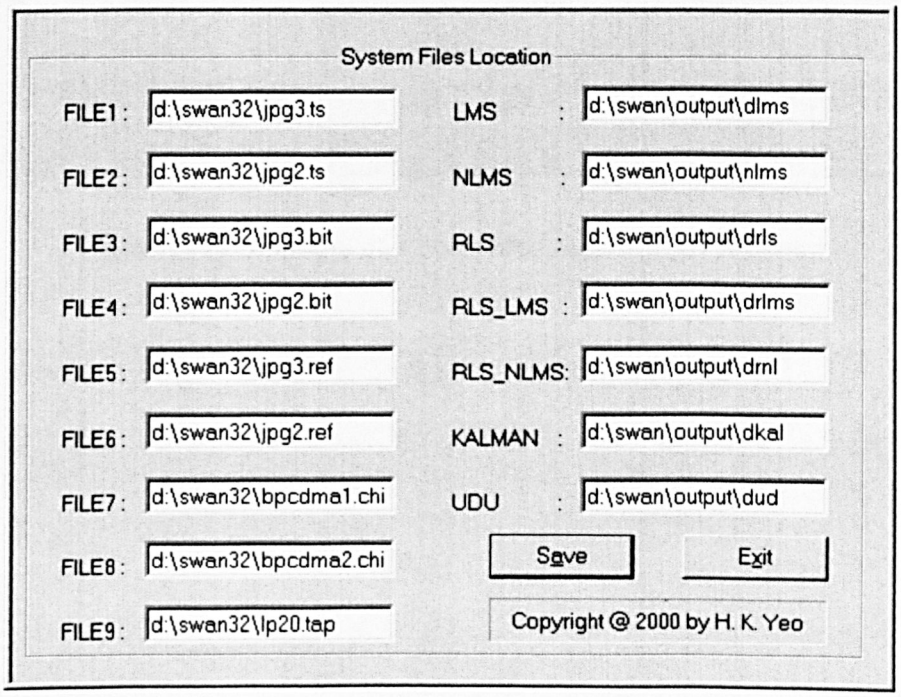

Figure 6-18 System files dialog box

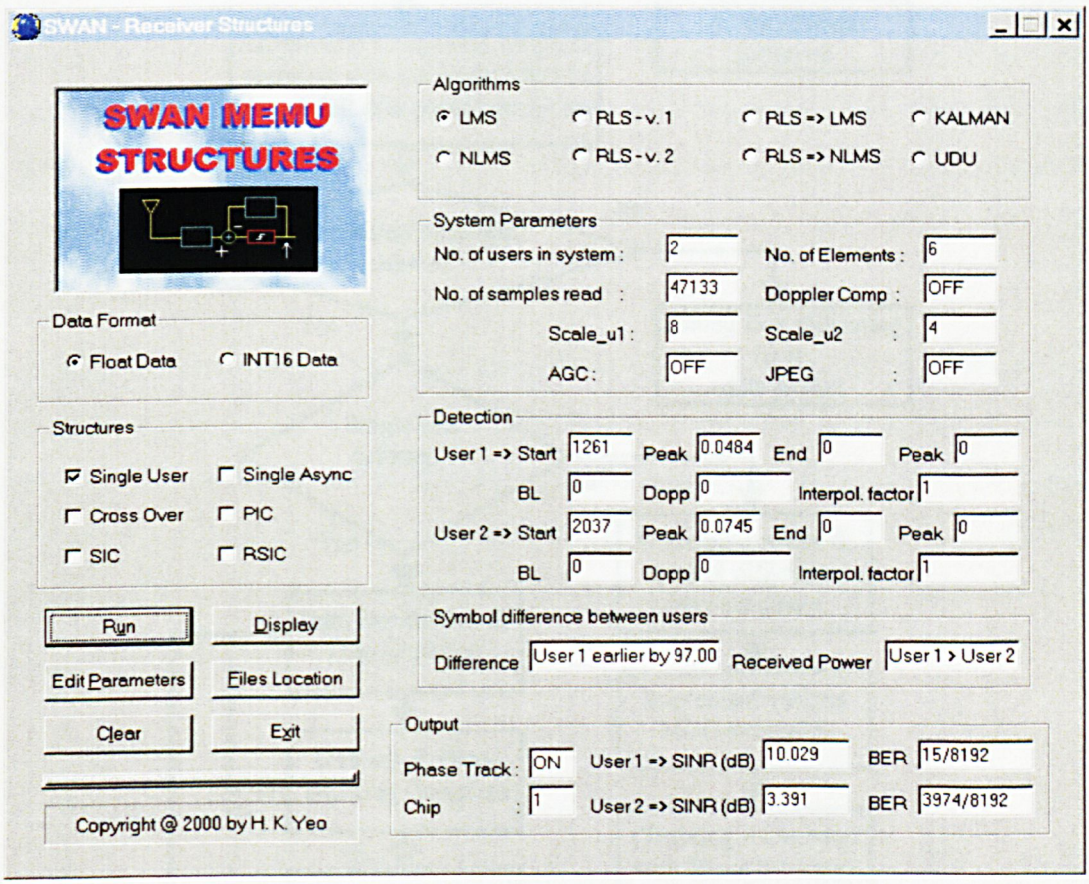

Figure 6-19 Example of a computed output from software

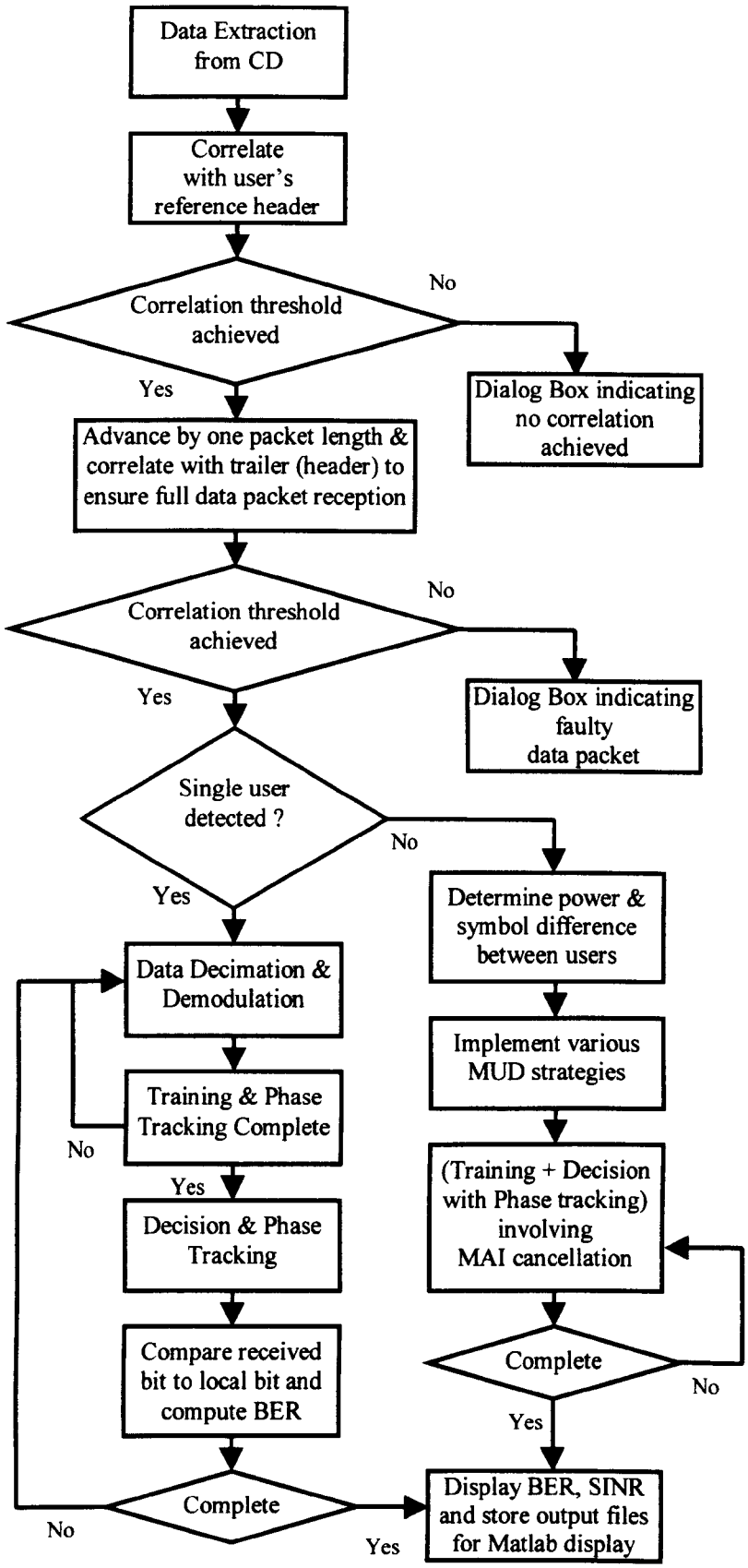

Figure 6-20 Flowchart operation for the receiver structures

6.6 Summary

This chapter outline the system specification for the sea trials conducted in both May 1999 and May 2000 respectively, where the network topologies, positions of transmissions and the receiver array geometry were described.

The signals for transmission were grouped into two classes. The first set was used as a data quality checking (DQC) metric as well as analysing the channel properties. In the second set of data, both BPSK (Binary Phase Shift Keying) and QPSK (Quadrature Phase Shift Keying) were considered from the available modulation schemes because of the advantage of higher bandwidth efficiency and increased data rate with M-ary modulation techniques. In the second sea-trial where multi-user transmission was deployed, both JPEG transmission and spread spectrum were used with QPSK modulation scheme.

The receiver front-end hardware was described and the interface between the front-end hardware was supported by two GUI software-based receivers. The first GUI software-based receiver was written to support the DQC analysis. A second GUI software platform was written to support the demodulation of received signals. The single-user detection (SUD), multi-user detection (MUD) strategies and the adaptive algorithms were embedded within the GUI software.

Chapter 7 Field Trial Results of the Multi-User Detection Strategies

7.1 Introduction

In horizontal underwater network communication, the base-station detector tends to receive a signal composed of the summed signals from multiple users, which overlap in time and frequency. Due to the path-distance difference between users with respect to the base station, there is likelihood that there will be equal or unequal ("near-far") power reception difference between users. Therefore, both equal and unequal power reception scenarios were considered in the sea-trials where the effectiveness of the proposed MUD strategies was validated with data from two separate ocean sea-trials.

As part of the European Community MAST III project – SWAN (MAS3-CT97-0107SWAN), two sea-trials were conducted in May 1999 and May 2000 respectively. The experiments were carried out in the North Sea, 8km from the coast near Noordwijk, in the Netherlands. The measuring platform "MeetPost Noordwijk" (MPN) at position 52°16'25.9"N, 04°17'45.2"E, acted as the base station for all data reception. The SUD and the proposed MUD receiver systems, discussed in chapter 5, were tested with the acquired data from the two experimental trials and a performance analysis for the receiver structures are being carried out in this chapter.

In the equal power reception scenario, a performance analysis for the receiver structures was undertaken for a two user asynchronous reception. As "near-far" effect is considered to be a more predominant issue in network communication, two class of scenarios were considered to study the implication of interferences caused by the stronger users towards weaker users and vice versa. While the first scenario investigates the effects of interference when the stronger user arrives before weaker user during the training mode, the second scenario investigates the effects of interference when the stronger user arrives during the decision mode of the weaker users.

The results from the performance analysis between the SUD and MUD strategies proved useful not only to highlight the benefits to be gained from adopting the MUD strategies but also to bring to light potential weaknesses which may exist within the systems.

The last section of the chapter addresses the performances of the proposed improved RLS algorithm against other adaptive algorithms for adaptation to the proposed RSIC MUD receiver structure. The algorithms are accessed for their rate of convergence, tracking performance and computational complexity.

7.2 Equal Power Reception

The network configuration for the 2 users simultaneous transmission is shown in Figure 7-1. The transmission positions for both users 1 and 2 were 2km from the MPN with direction of transmission at 180° and 210° w.r.t. North of MPN respectively. The observed time of arrival for user 1 and 2 is depicted in Figure 7-2, where the data frames of user 1 were detected ~800 symbols earlier than user 2. The input SNR for both users were observed to be at ~16dB. A summary of the network configuration and system parameters for the sea-trial experiment (May 2000) is illustrated in Table 7-1 with the receiver array as described in Figure 6-6 of chapter 6.2.3.2.

The channel impulse responses observed from the receiver array for both users 1 and 2, are shown in Figure 7-3 and Figure 7-4 respectively. It can be seen from the channel impulse responses that the transmitted signal was underspread. Therefore short filters using 15 and 20 taps were used for the feedforward and feedback filters respectively, refer to Appendix Table 8 of Appendix X for tap length selection. The values of the step-size parameters used by the LMS algorithms are 0.006 and 0.003 for the feedforward and feedback taps respectively, refer to Appendix Table 9 of Appendix X for optimised stepsize values selection.

Being an equal power reception, the SUD receiver structure was able to achieve convergence during the training period, as shown in the error performance surface of Figure 7-5. A small surge in the MSE level was observed at ~800 iteration of user 1, which indicated the introduction of user 2 in the system, but this rise of MSE quickly converges down again within 20 symbol iterations. The computed SINR for both users were 15.17 dB and 14.87 dB with P_{er} of 9.1×10^{-4} and 1.1×10^{-3} respectively. For the cross-over MUD receiver structure, the computed SINR for both users 1 and 2 were 15.42 dB and 14.34 dB with P_{er} of 8.2×10^{-4} and 2.1×10^{-3}, as shown in Figure 7-6. The

performance of the PIC MUD receiver structure manifests itself to be effective in an equal power reception over the SUD receiver structure, where the computed SINR for both users are 16.41 dB and 15.63 dB, both of which are ~1 dB higher, with P_{er} of 0.0 respectively, as shown in Figure 7-7. The result obtained by the SIC MUD receiver structure further confirmed that SIC MUD described in chapter 5.5.3 is not as effective as the PIC in an environment where the received signal powers are equal. While an improvement was noticed in the computed SINR of user 2, 15.59 dB with $P_{er} = 0.0$, the results obtained for user 1 was the same as the one obtained by the SUD receiver structure, as shown in Figure 7-8. Finally, the loop-back feature of the RSIC MUD receiver structure obtained an almost identical result as the PIC strategy, with computed SINR 16.41 dB and 15.64 dB with P_{er} 0.0 for user 1 and 2 respectively, as shown in Figure 7-9. A summary of the computed SINR and P_{er} for the various receiver structures is summarised in Table 7-2.

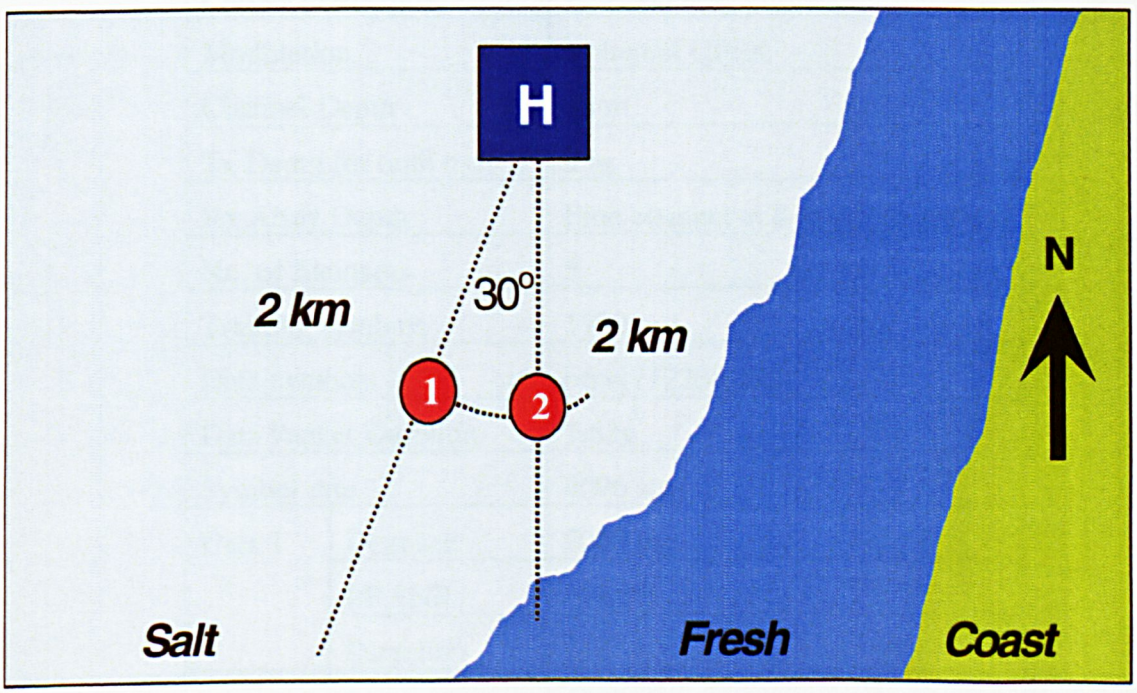

Figure 7-1 Network configuration for a 2 user simultaneous transmission

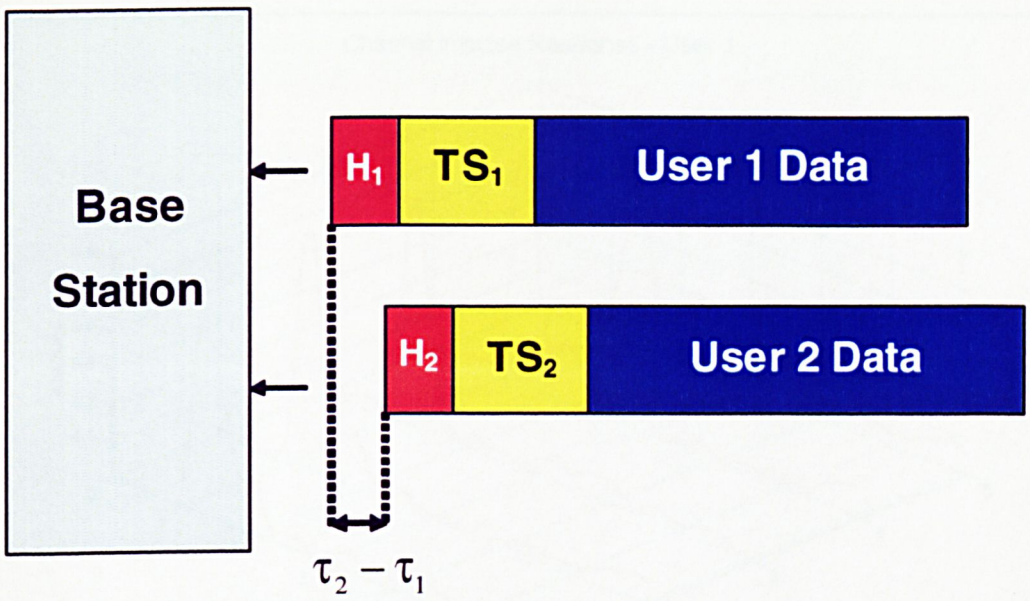

Figure 7-2 Observation window for asynchronous reception

Frequency Bandwidth		B_w = 8-12 kHz
Carrier Frequency		F_c = 10 kHz
Modulation		Coherent QPSK
Channel Depth		18 m
Tx Depth for both user		9 m
Rx Array Depth		First element at 8 m ref. to seabed
No. of Elements		5
Training symbols		1700
Data symbols		6664 (12238 bits)
Data Packet Duration		1.62s
Symbol rate		4096 sps
User 1	Distance	2000 m
	I/P SNR	~16 dB
	Direction	210° w.r.t. to North of MPN
User 2	Distance	2000 m
	I/P SNR	~16 dB
	Direction	180° w.r.t. to North of MPN

Table 7-1 System parameters for 2-user equal power reception

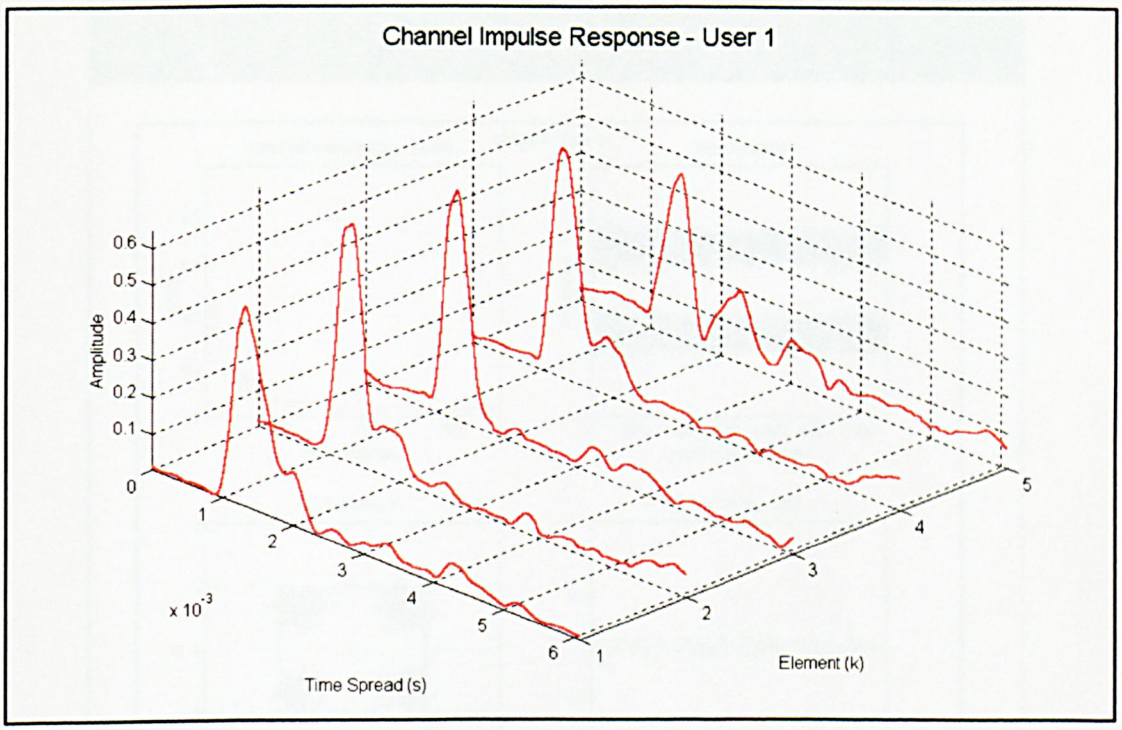

Figure 7-3 Channel impulse response for user 1

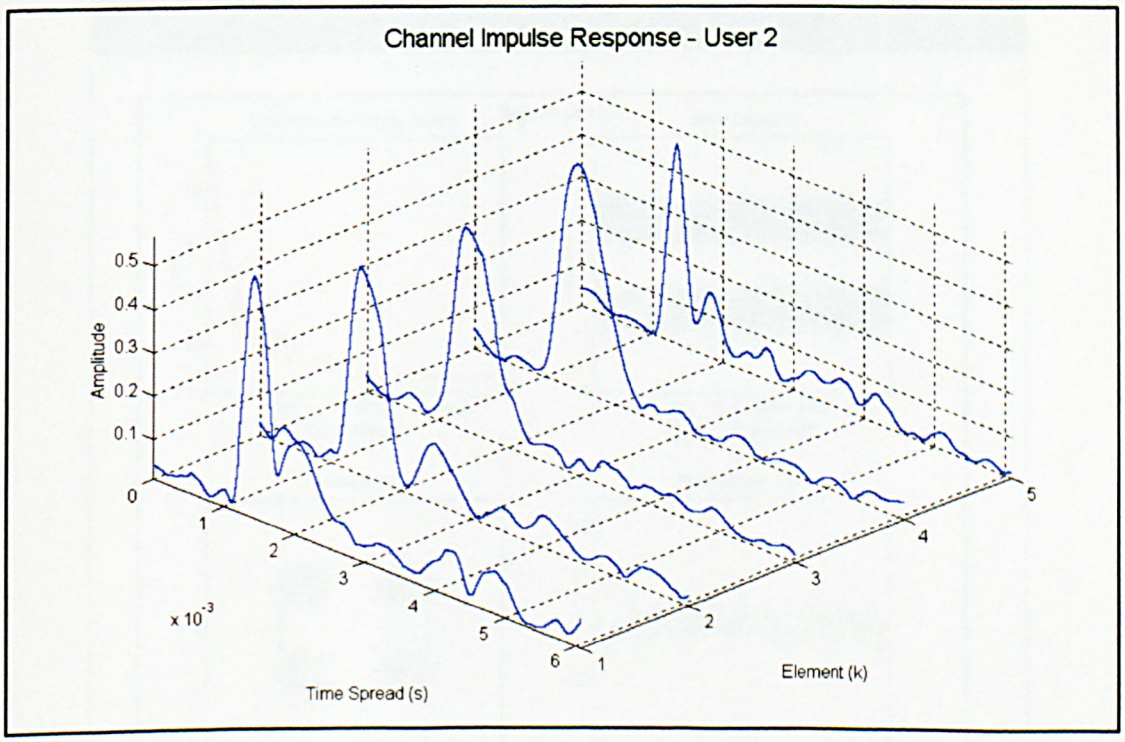

Figure 7-4 Channel impulse response for user 2

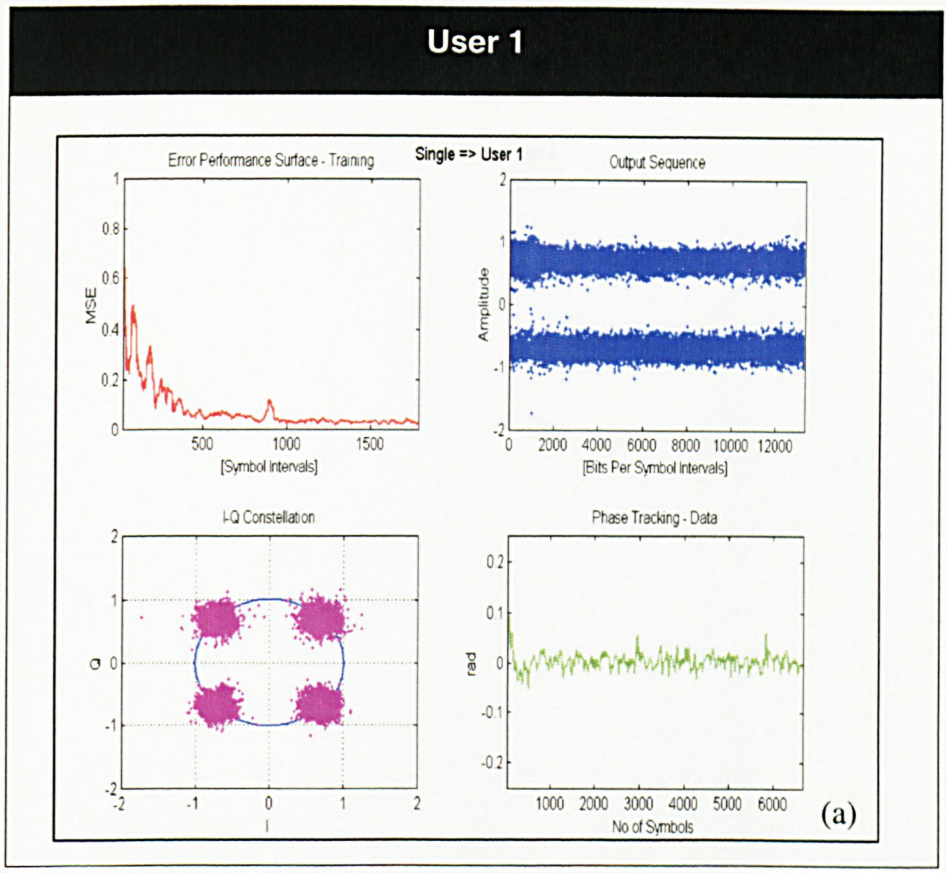

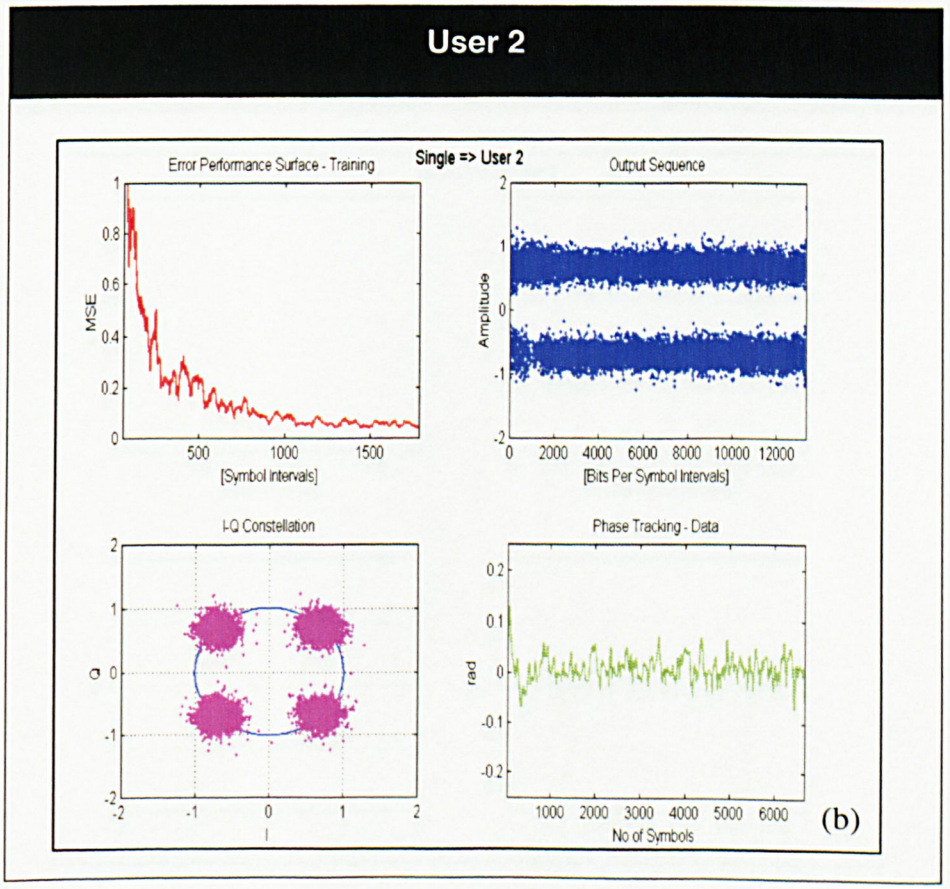

Figure 7-5 SUD strategy for equal power reception

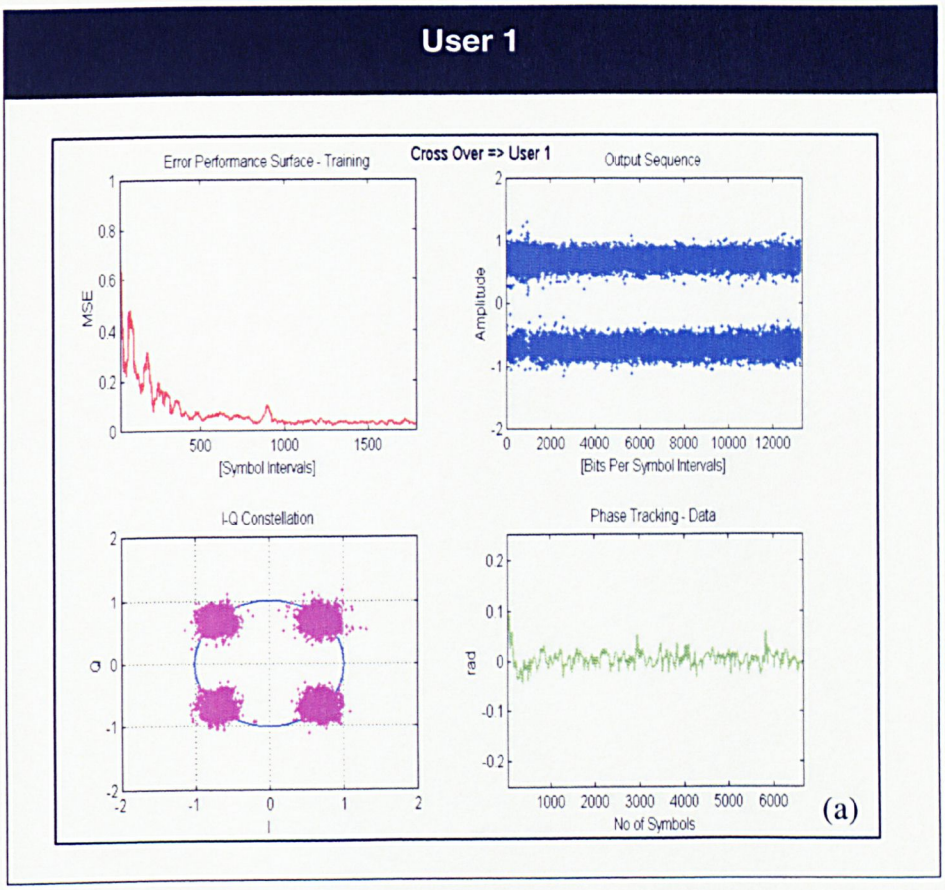

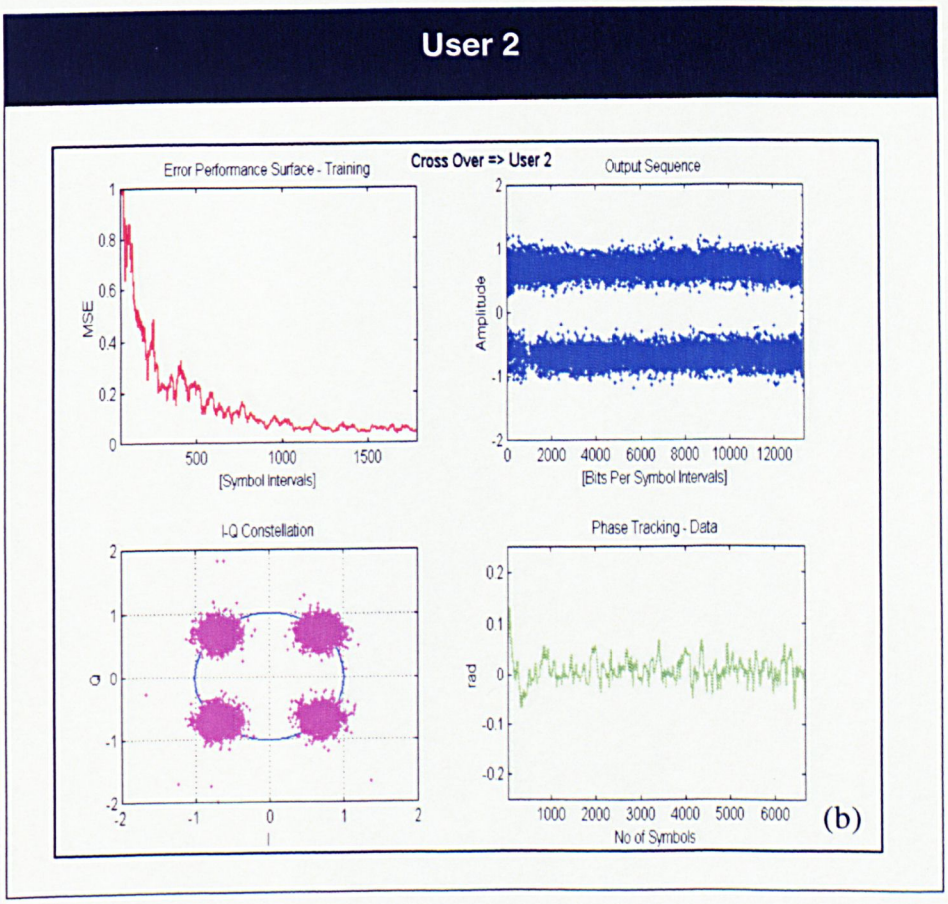

Figure 7-6 Cross-over MUD strategy for equal power reception

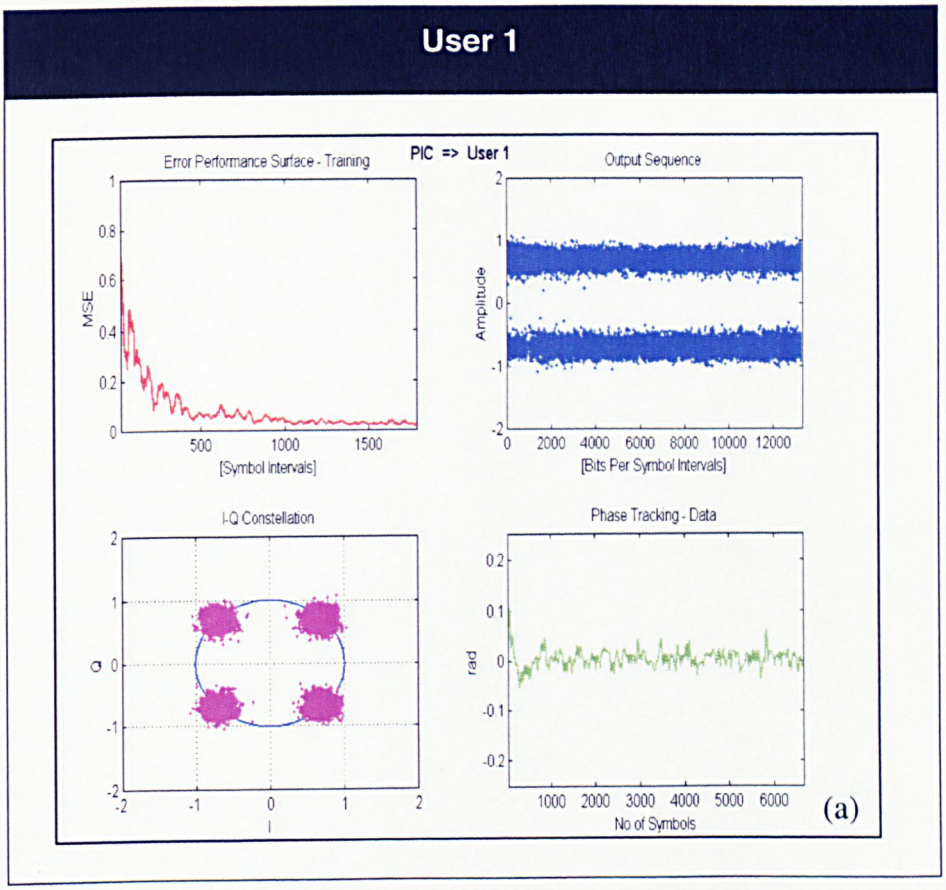

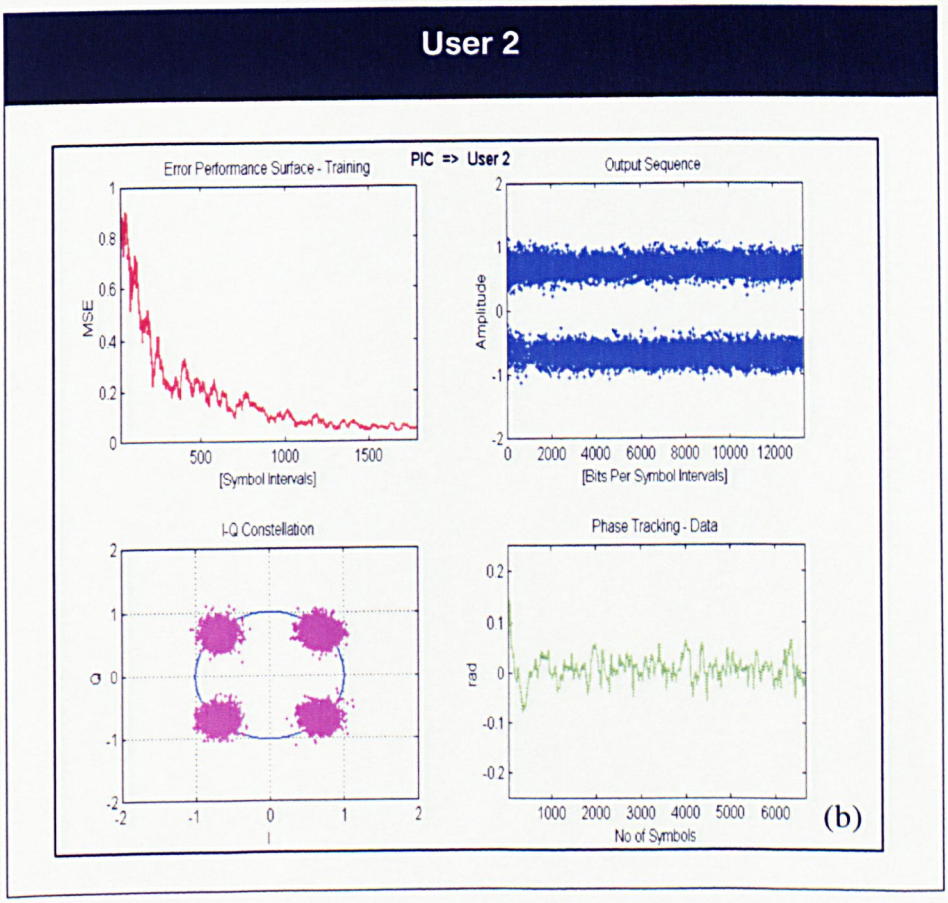

Figure 7-7 PIC MUD strategy for equal power reception

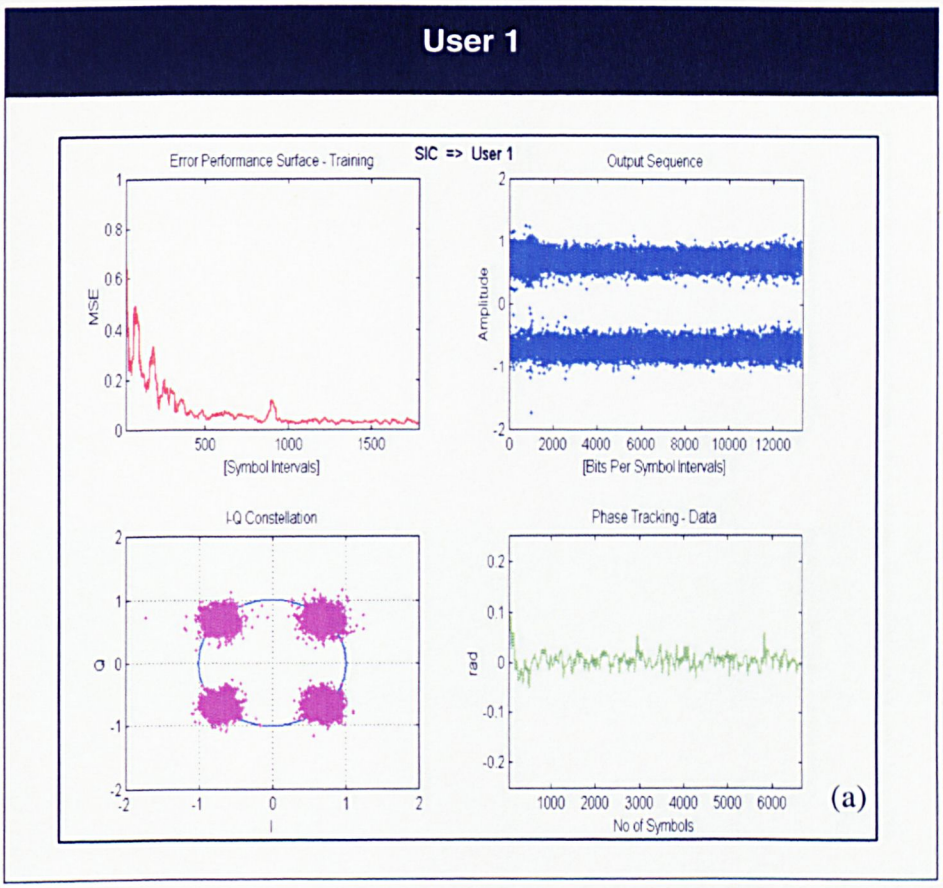

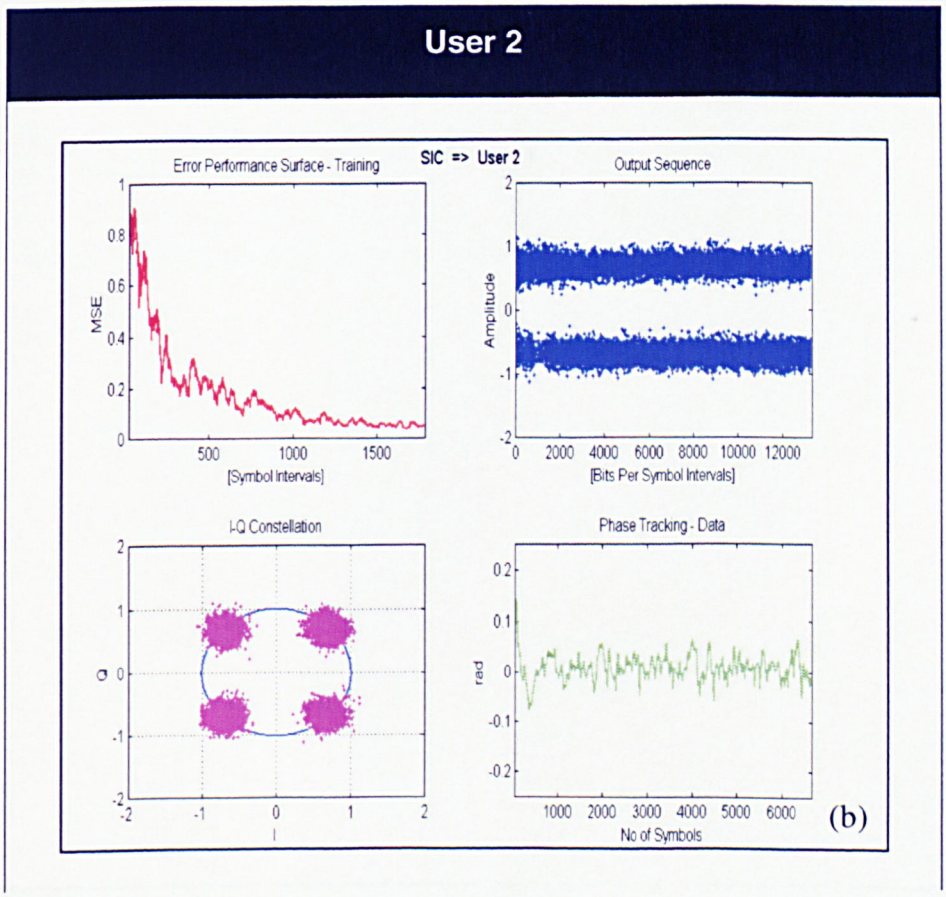

Figure 7-8 SIC MUD strategy for equal power reception

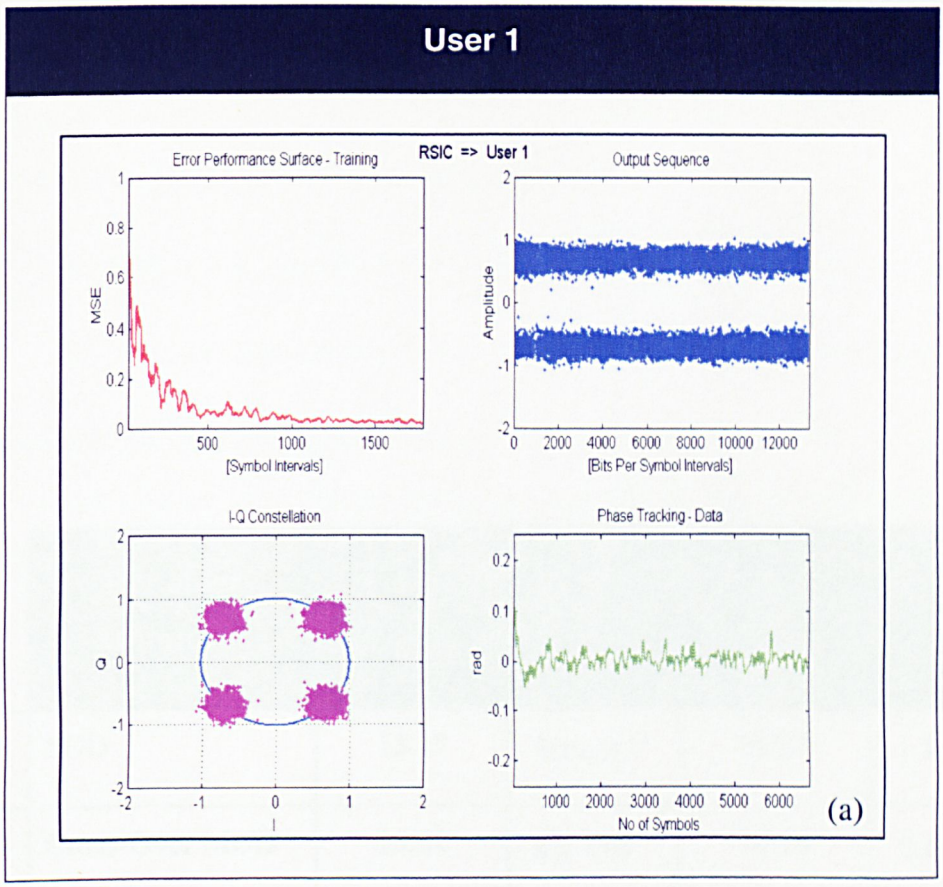

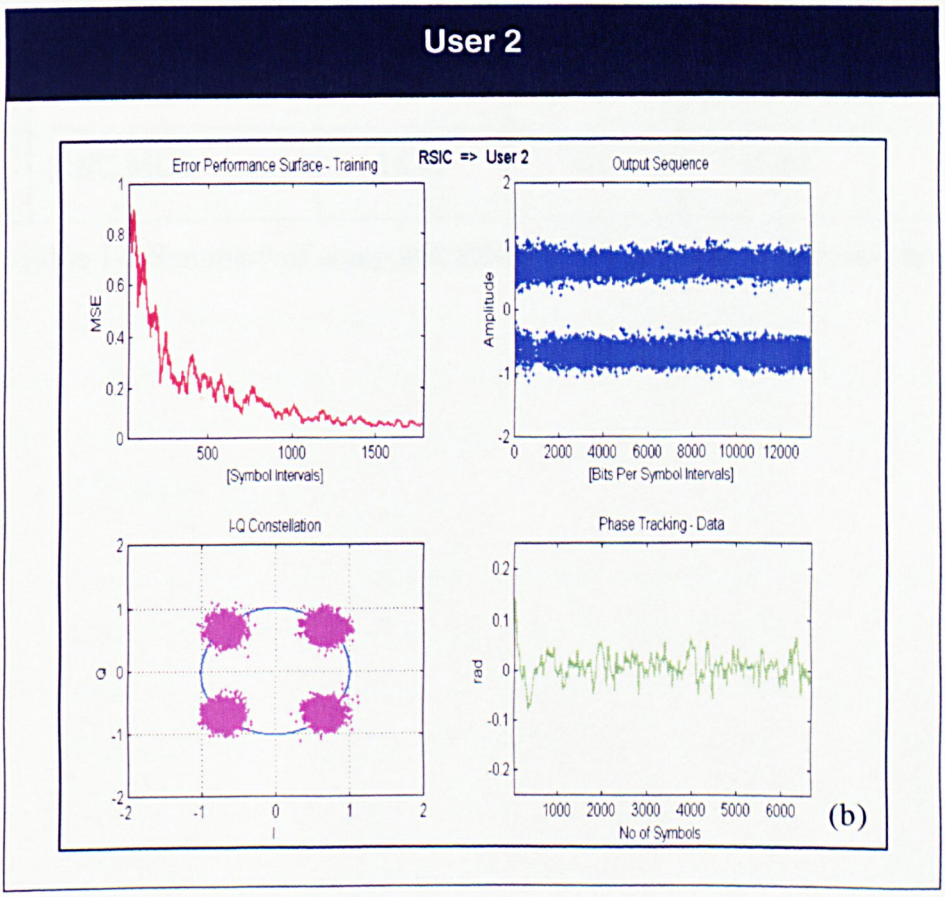

Figure 7-9 RSIC MUD strategy for equal power reception

	Receiver Structures	User 1		User 2	
		SINR (dB)	P_{er}	SINR (dB)	P_{er}
1.	SUD	15.17	9.1×10^{-4}	14.87	1.1×10^{-3}
2.	Cross-Over MUD	15.42	8.2×10^{-4}	14.34	2.1×10^{-3}
3.	PIC MUD	16.41	0.0	15.63	0.0
4.	SIC MUD	15.17	9.1×10^{-4}	15.59	0.0
5.	RSIC MUD	16.41	0.0	15.64	0.0

Table 7-2 Summary of computed SINR and P_{er} for the receiver structures

7.3 Unequal power reception

In this section, the implication of asynchronous reception in an unequal power reception scenario is investigated under the following categories:

A. Strong user arriving before weak user during training mode

B. Weakest user arriving before stronger users during the decision mode

It is envisaged that the first category may not be as difficult to tackle as compared to the second category since MAI occurs during the training mode. Therefore, the receiver having a priori known set of sequences may allow accurate decision estimation for interference cancellation. However, in the latter category, the weaker user had to rely heavily on the accurate estimation of the stronger users when operating in the decision mode. Any wrong decision estimation made for the stronger users will ultimately contribute negatively to the interference cancellation, which results in erroneous estimation of the weakest user.

7.3.1 Scenario A – Strong User Arriving prior Weaker User

A 2-user unequal power asynchronous reception is shown in Figure 7-10. The transmission positions for both users 1 and 2 were 2km from the MPN with direction of transmission at 0° and 30° w.r.t. West of MPN respectively. The observed time of arrival for user 1 and 2 is depicted in Figure 7-11, where the data frames of user 1 were detected ~100 symbols earlier than user 2. The input SNR for both users were observed to differ by ~11dB. A summary of the network configuration and system parameters for the sea-trial experiment is illustrated in Table 7-3 with the receiver array as described in Figure 6-3 of chapter 6.2.2.2.

The channel impulse responses observed from the receiver array for both user 1 and user 2 are shown in Figure 7-12 and Figure 7-13 respectively. The multipath spread was observed to be ~10 ms, which extends for ~50 symbol intervals suggests the need of longer feedback filter taps to remove residual ISI. Filter tap lengths of 20 and 65 were used for the feedforward and feedback filters respectively, refer to Appendix Table 10 of Appendix XI for tap length selection. The values of the step-size parameters used by the LMS algorithms are 0.005 and 0.002 for the feedforward and feedback taps

respectively, refer to Appendix Table 11 of Appendix XI for optimised stepsize values selection.

Figure 7-14 shows the computed outputs obtained by the SUD receiver structure. Although user 1 has a higher SNR compared to that of user 2, it suffers slightly from the interference contributed by user 2. The output SINR for user 1 obtained by the SUD receiver structure was 11.57 dB with $P_{er} = 7.3 \times 10^{-4}$. Being embedded in stronger interference, the SUD was not able to retrieve useful data for user 2, the computed SINR of user 2 was 2.84 dB with $P_{er} = 6.3 \times 10^{-1}$. This poor result obtained for user 2 then renders the data packet of user 2 redundant. Referring to Figure 7-15, it was noted that the "cross-over" structure had relatively poor results where user 1 had a SINR of 9.89 dB with $P_{er} = 2.9 \times 10^{-3}$ and user 2 had a SINR of 4.08 dB with $P_{er} = 4.7 \times 10^{-1}$. This is mainly attributed to the fact that LMS algorithm is sensitive to the eigenvalue spread of the received signal.

Observation from the experimental results confirmed that the adaptive PIC receiver structure does not perform well in the case of unequal power channel. The SINR for user 1 was 10.53 dB with $P_{er} = 1.3 \times 10^{-3}$. This increased error is attributed to the fact that the erroneous decision of user 2 contributed negatively to the subtraction of the received signal, which was to be fed into the adaptive DFE of user 1 in stage 2. Improvement was observed for the weak user where the computed SINR was 8.59 dB, which is an improvement of ~5.7 dB from the SUD structure. However, the detected error obtained by the PIC structure was still deemed high, $P_{er} = 9.3 \times 10^{-3}$. The outputs for user 1 and user 2 are shown in Figure 7-16. Further improvement was observed for user 2 by the SIC structure, shown in Figure 7-17 (b). The SIC MUD receiver structure was able to further improve the SINR of user 2 to 9.43 dB with $P_{er} = 2.8 \times 10^{-3}$. The analysis of the SIC structure in chapter 5 shows that the stronger user does not benefit from any MAI reduction, therefore the SINR of user 1 remains the same as that obtained by the SUD receiver structure, shown in Figure 7-17 (a). Thus, the SIC structure was deemed more appropriate for an unequal power channel, however the strongest user does not benefit from any MAI reduction from other weaker users.

Significant improvement was observed with the adaptive RSIC structure. Convergence of user 2 was better when compared to any of the other proposed structures. An output

SINR of 11.92dB was obtained with $P_{er} = 1.1 \times 10^{-4}$, as shown in Figure 7-18. By performing a single feedback loop to the stronger user to eliminate the interference of user 2, the output SINR of user 1 was improved to 13.72dB with $P_{er} = 0.0$, as shown in Figure 7-18. Hence the RSIC structure had manifested itself to be a superior multi-user detection strategy for MAI in a "near-far" asynchronous scenario.

A summary of the computed SINR and P_{er} for the various receiver structures is summarised in Table 7-4.

Figure 7-19 and Figure 7-20 shows the variation of the measured P_{er} over a period of 36 consecutive packet (~45s) by the various receiver structures. An abrupt change in the channel property at time, t ~ 15s and 26s provided some insight to the performance of the various structures. The performance of the single user detection strategy exhibits a lower measured P_{er} in the stronger user, which corresponds to an increase in the measured P_{er} of the weaker user. The poor performance of the PIC structure for the strong user confirmed the negative contribution of the weak user signal subtraction from the received signal. Throughout the 45s of data reception, the RSIC structure maintains an almost constant low measured P_{er} for both users.

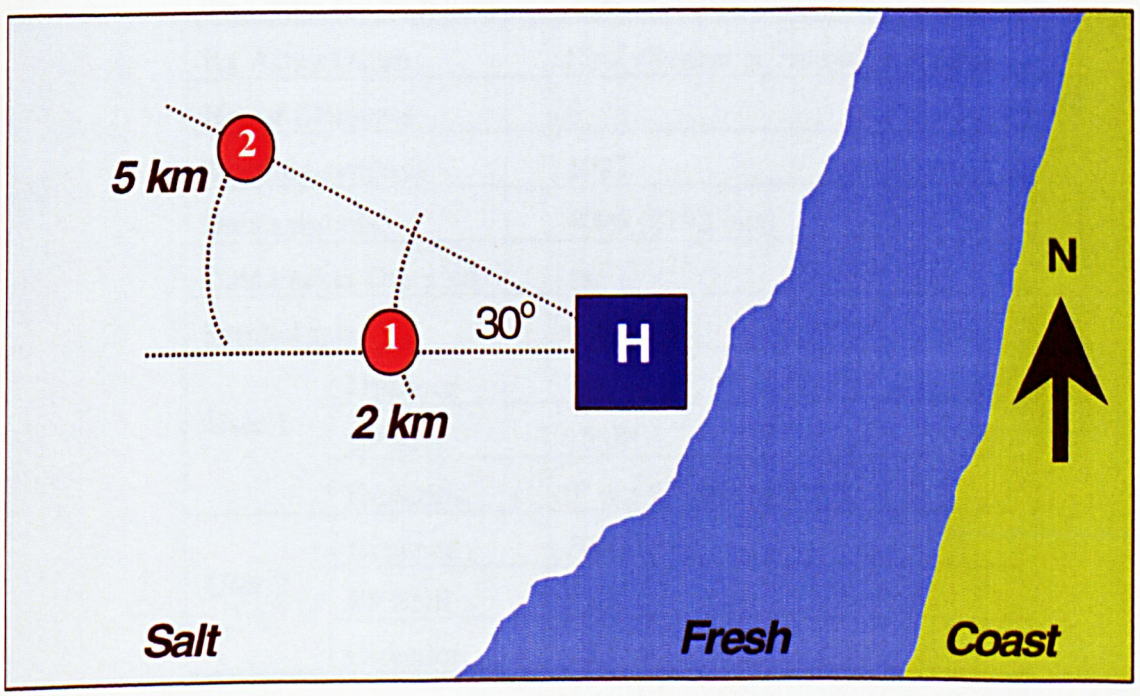

Figure 7-10 Network configuration for a 2 user simultaneous transmission

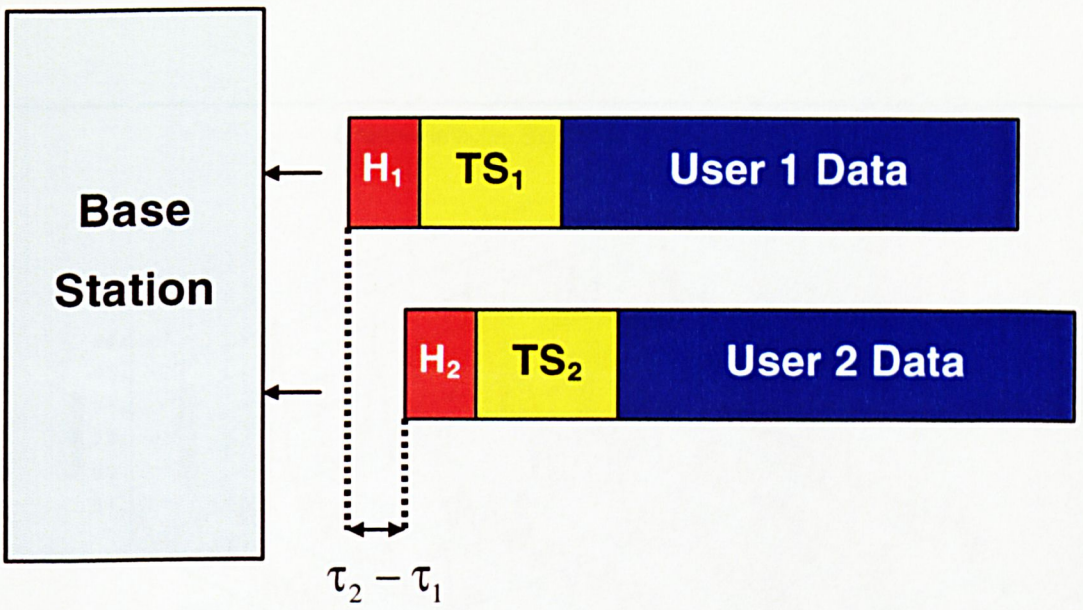

Figure 7-11 Observation window for asynchronous reception

Frequency Bandwidth		B_w = 8-12 kHz
Carrier Frequency		F_c = 10 kHz
Modulation		Coherent QPSK
Channel Depth		9 m
Tx Depth for both user		7 m
Rx Array Depth		First element at 7m ref. to seabed
No. of Elements		6
Training symbols		1023
Data symbols		4096 (8192 bits)
Data Packet Duration		1s
Symbol rate		4096 bps
User 1	Distance	2000 m
	I/P SNR	15 dB
	Direction	0^o w.r.t. West of MPN
User 2	Distance	5000 m
	I/P SNR	5 dB
	Direction	$+30^o$ w.r.t. West of MPN

Table 7-3 System parameters for 2-user unequal power reception

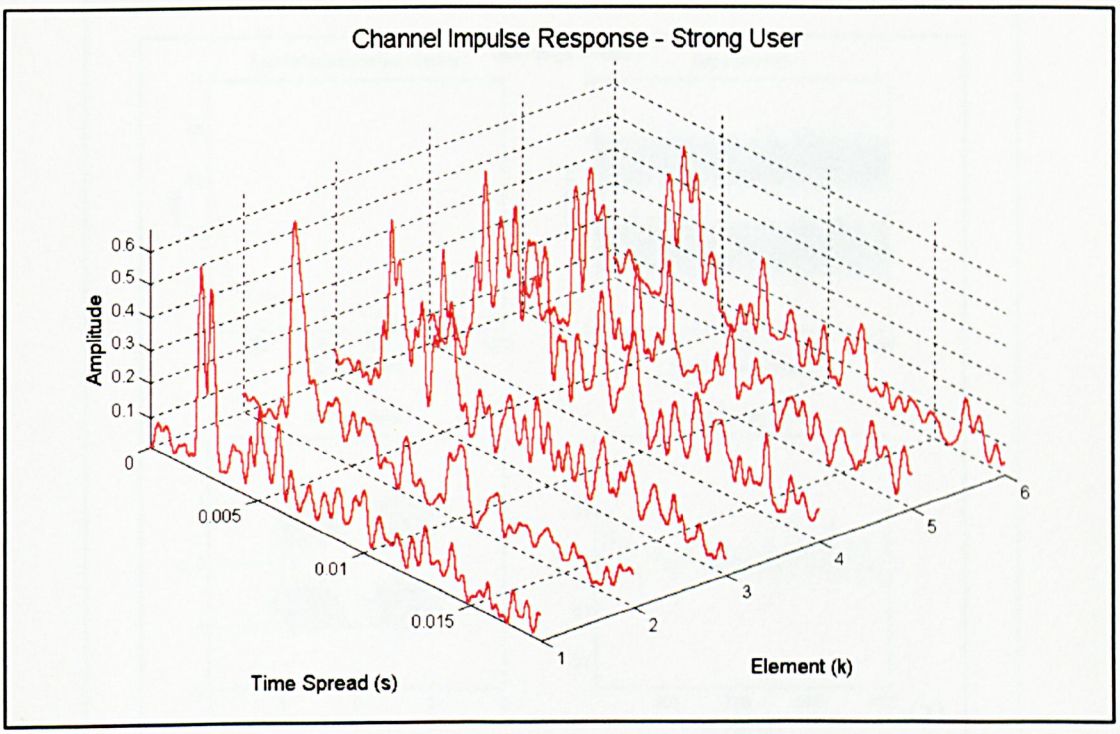

Figure 7-12 Channel impulse response for strong user 1

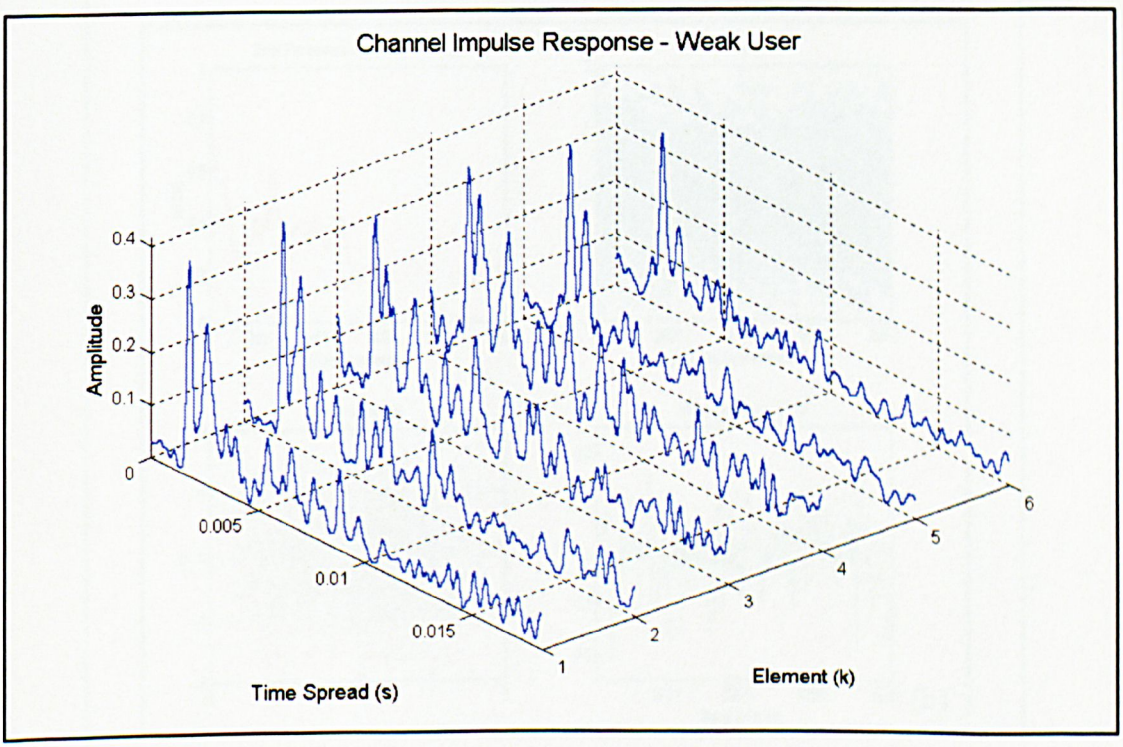

Figure 7-13 Channel impulse response for weak user 2

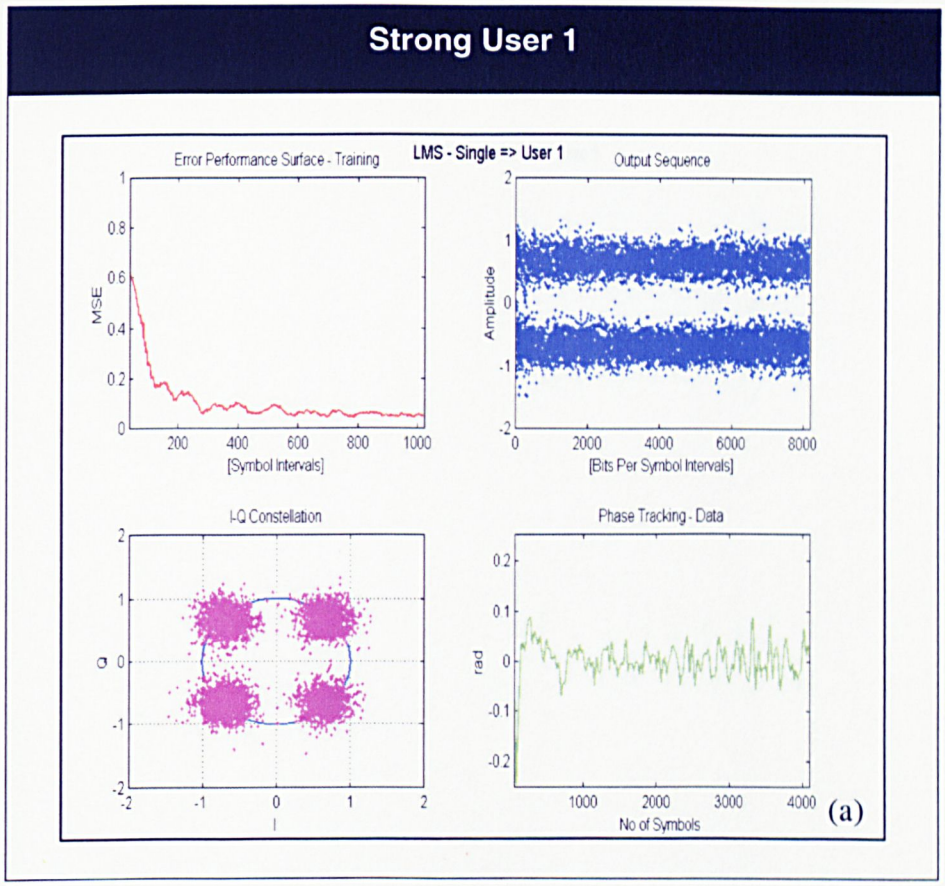

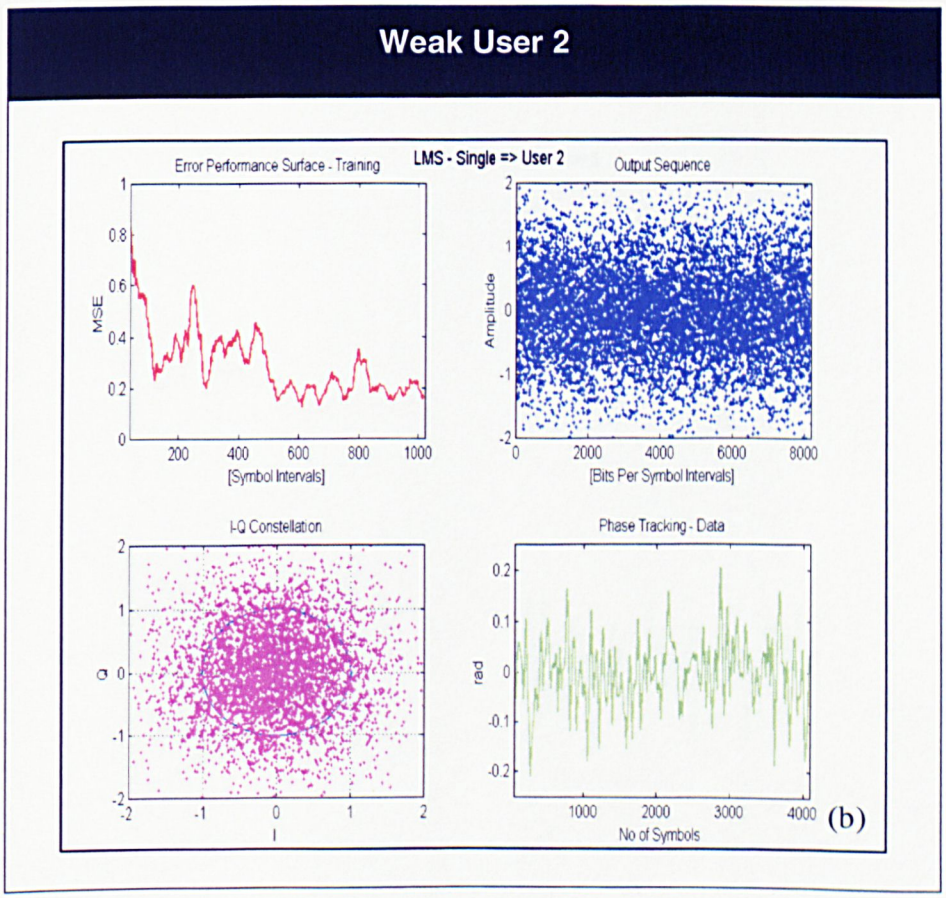

Figure 7-14 SUD strategy for unequal power reception

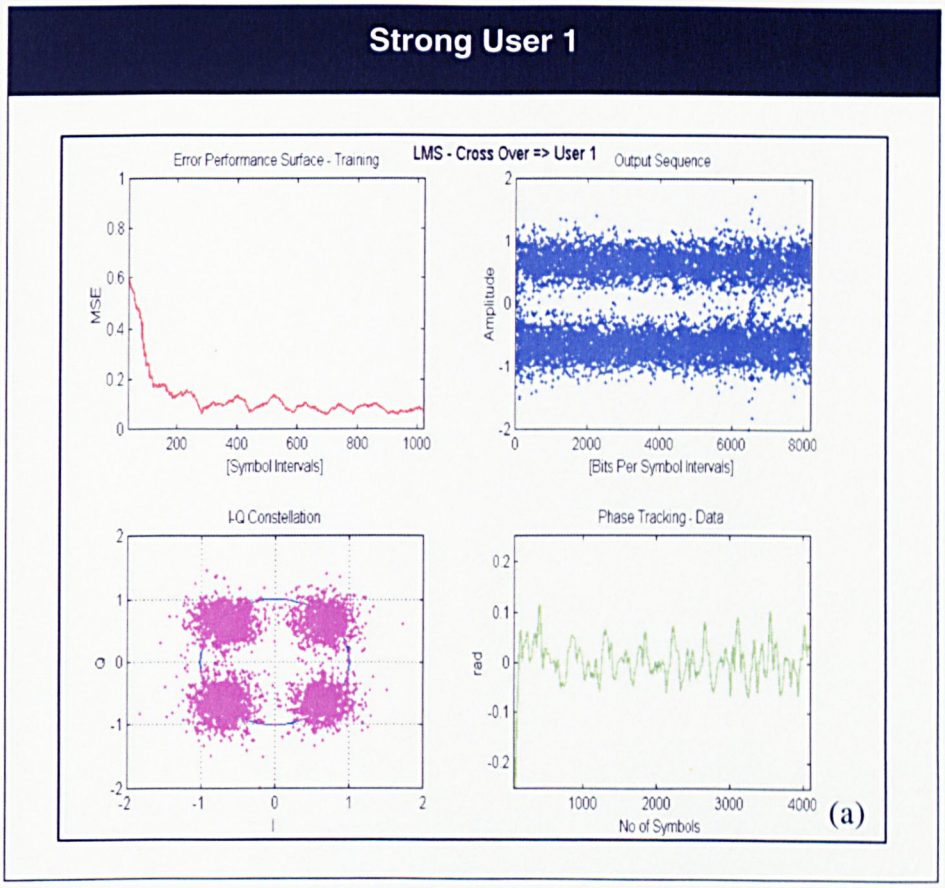

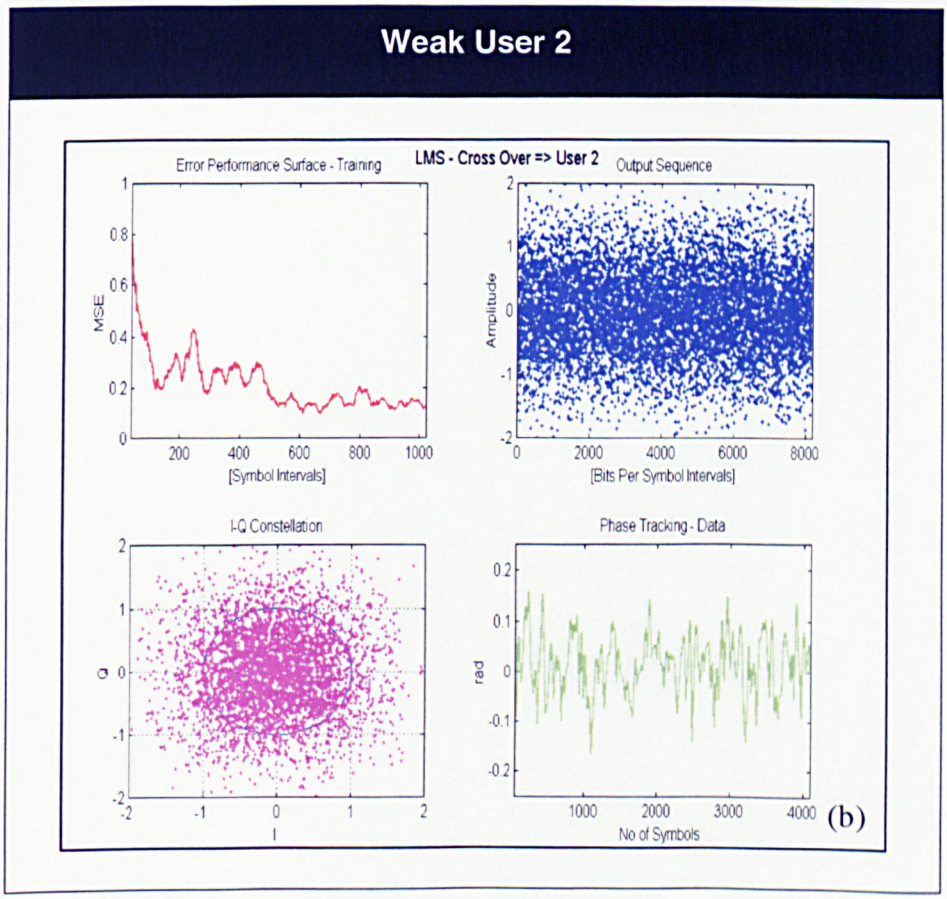

Figure 7-15 Cross-over MUD strategy for unequal power reception

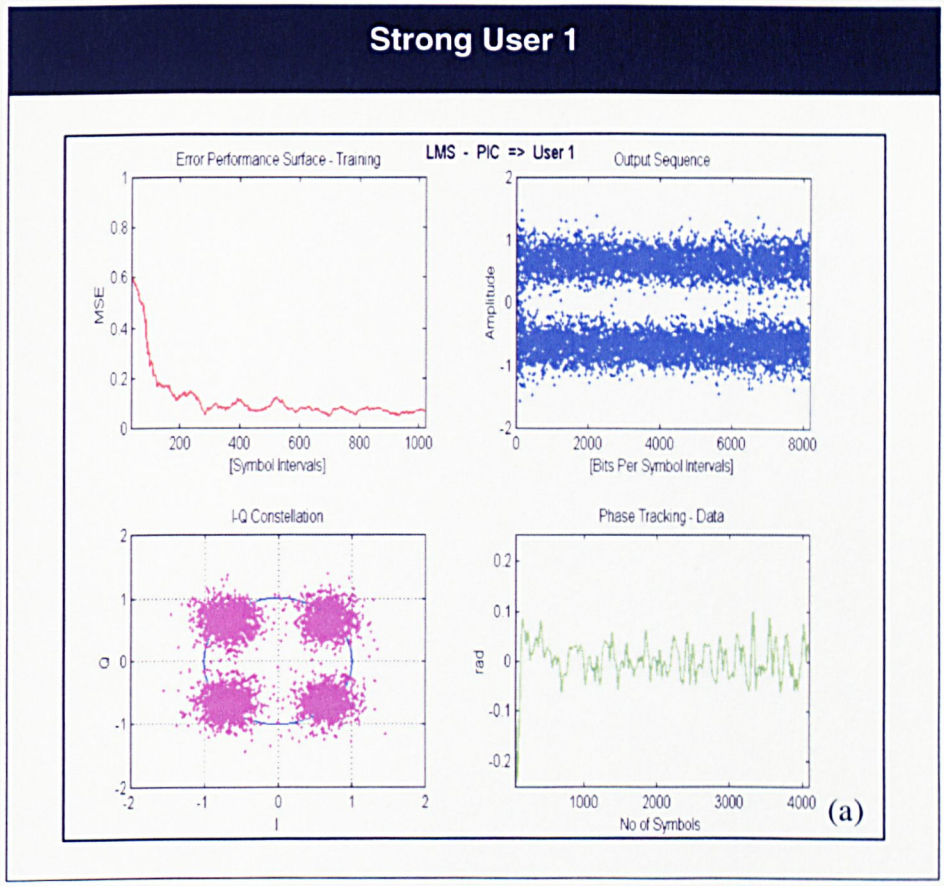

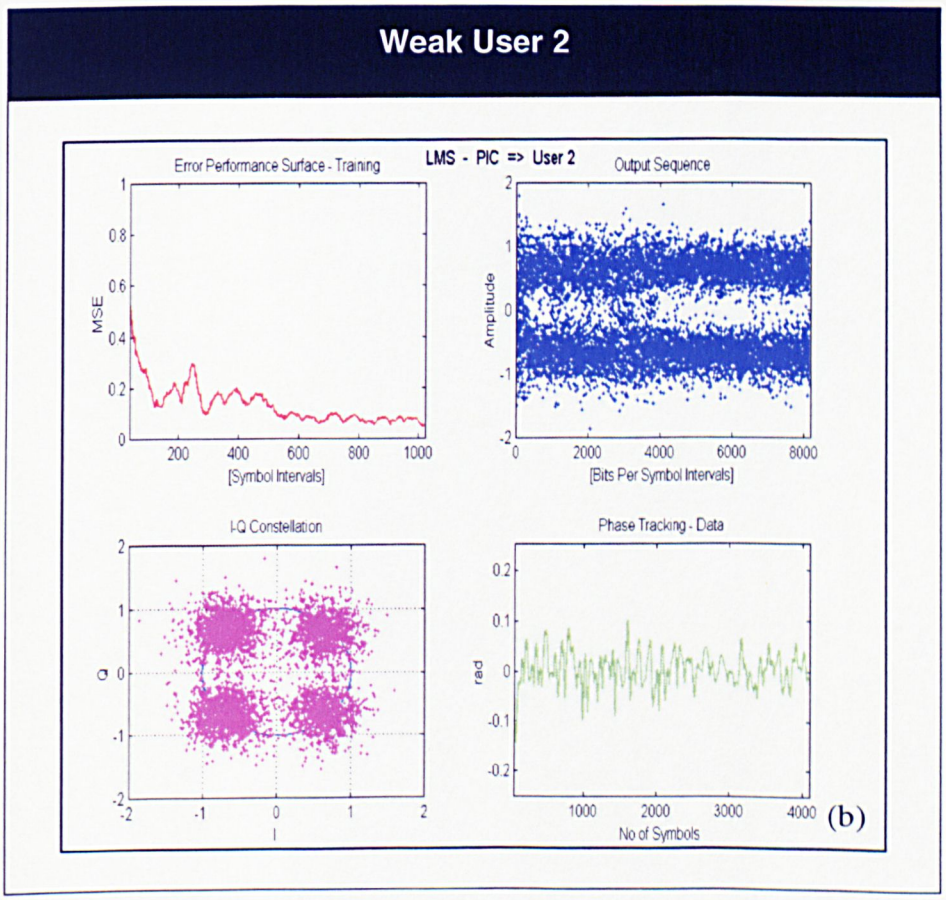

Figure 7-16 PIC MUD strategy for unequal power reception

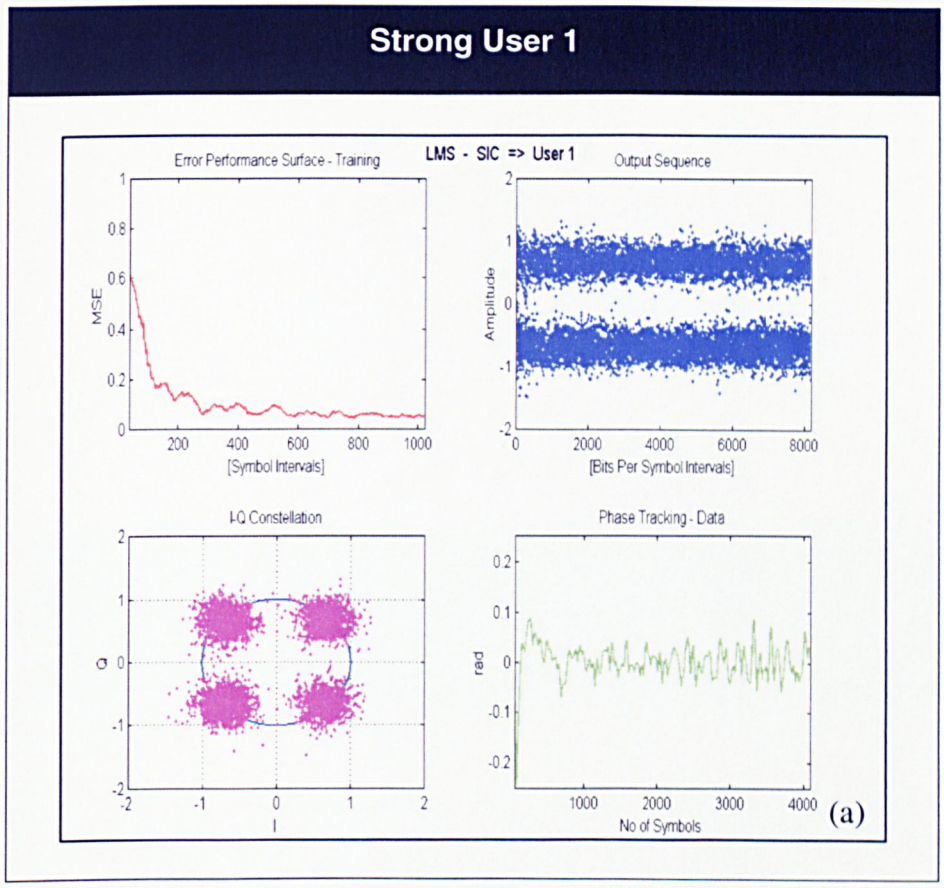

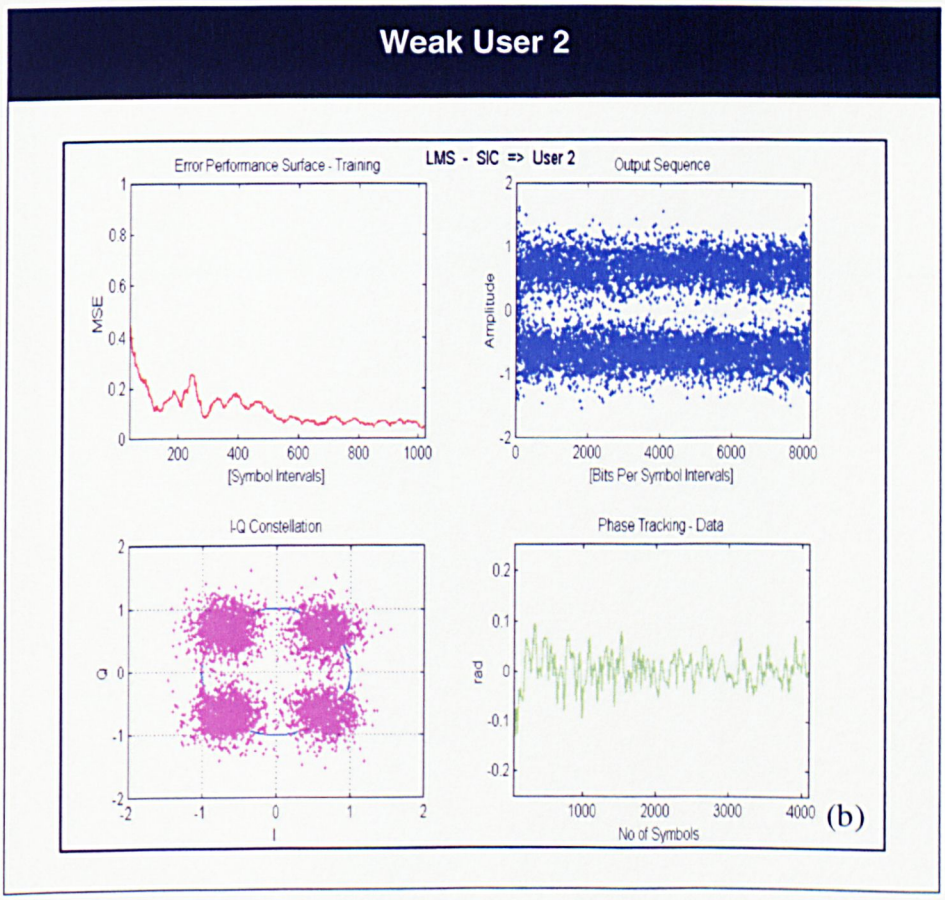

Figure 7-17 SIC MUD strategy for unequal power reception

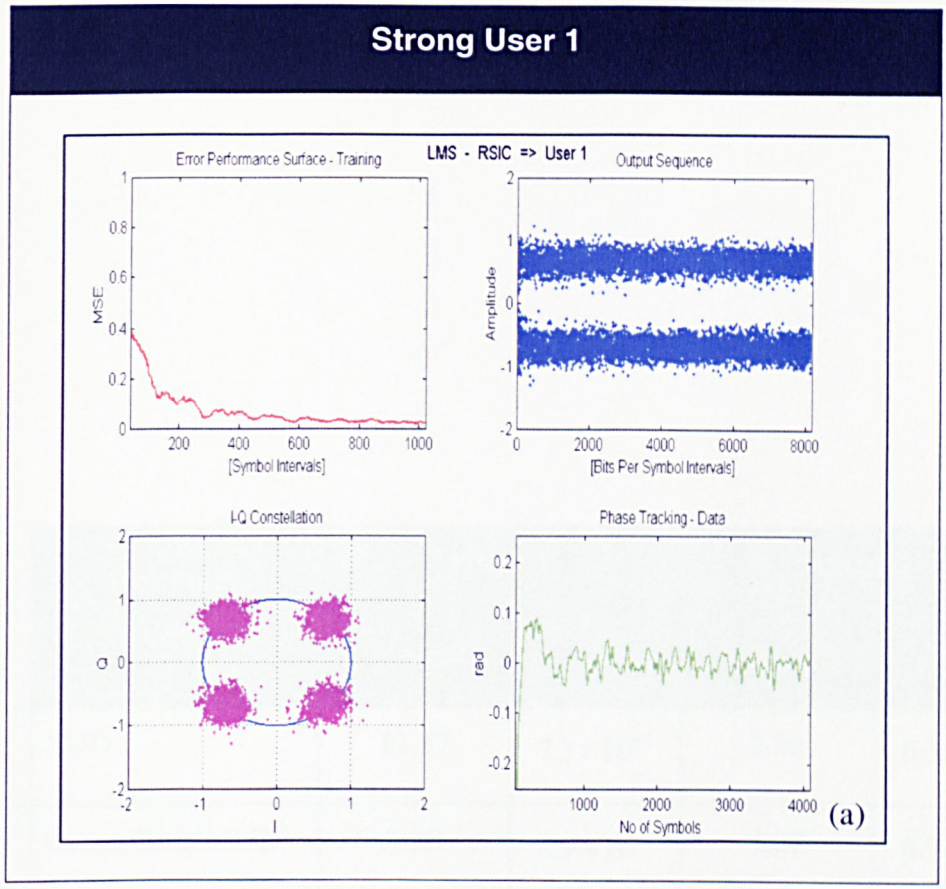

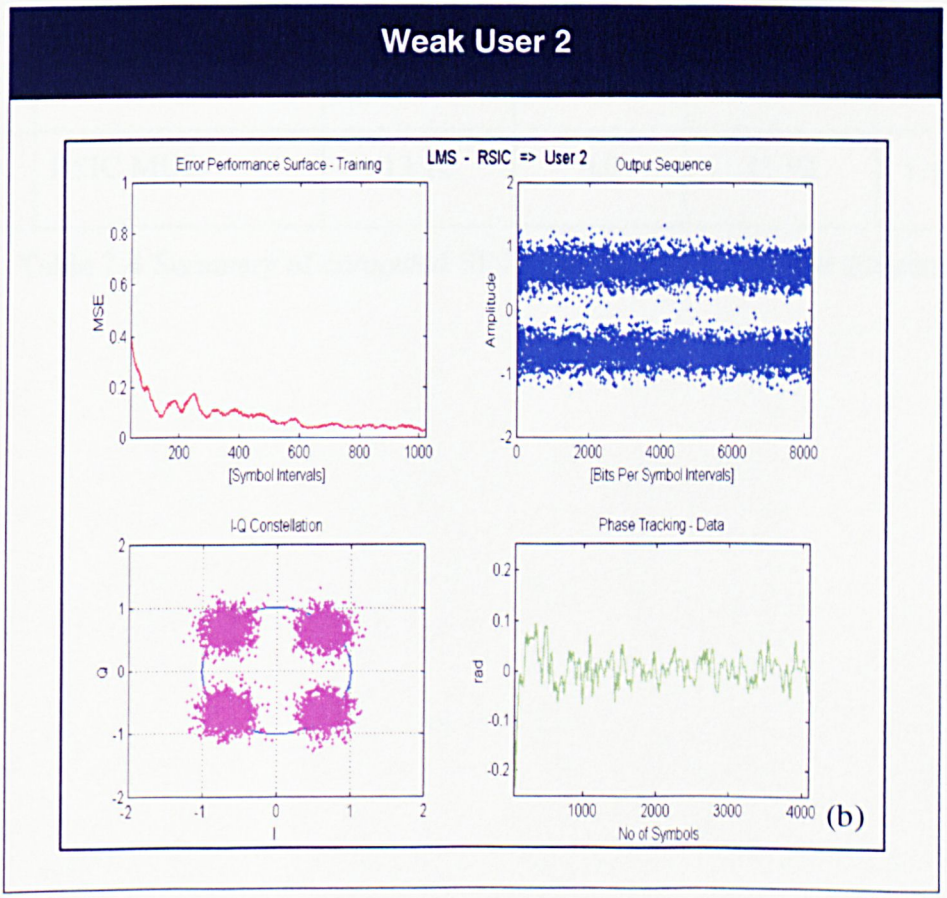

Figure 7-18 RSIC MUD strategy for unequal power reception

	Receiver Structures	User 1		User 2	
		SINR (dB)	P_{er}	SINR (dB)	P_{er}
1.	SUD	11.57	7.3×10^{-4}	2.84	6.3×10^{-1}
2.	Cross-Over MUD	9.89	2.9×10^{-3}	4.08	4.7×10^{-1}
3.	PIC MUD	10.53	1.3×10^{-3}	8.59	9.3×10^{-3}
4.	SIC MUD	11.57	7.3×10^{-4}	9.43	2.8×10^{-3}
5.	RSIC MUD	13.72	0.0	11.92	1.1×10^{-4}

Table 7-4 Summary of computed SINR and P_{er} for the receiver structures

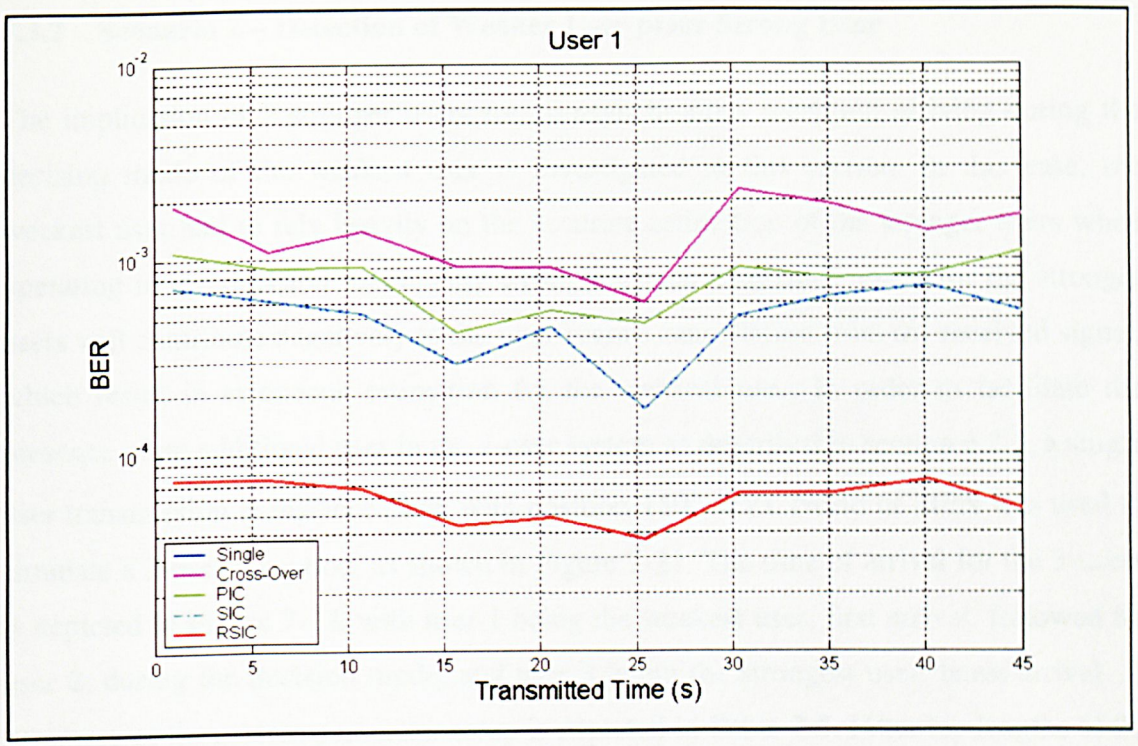

Figure 7-19 Measured P_{er} over 45 s of continuous transmission for user 1

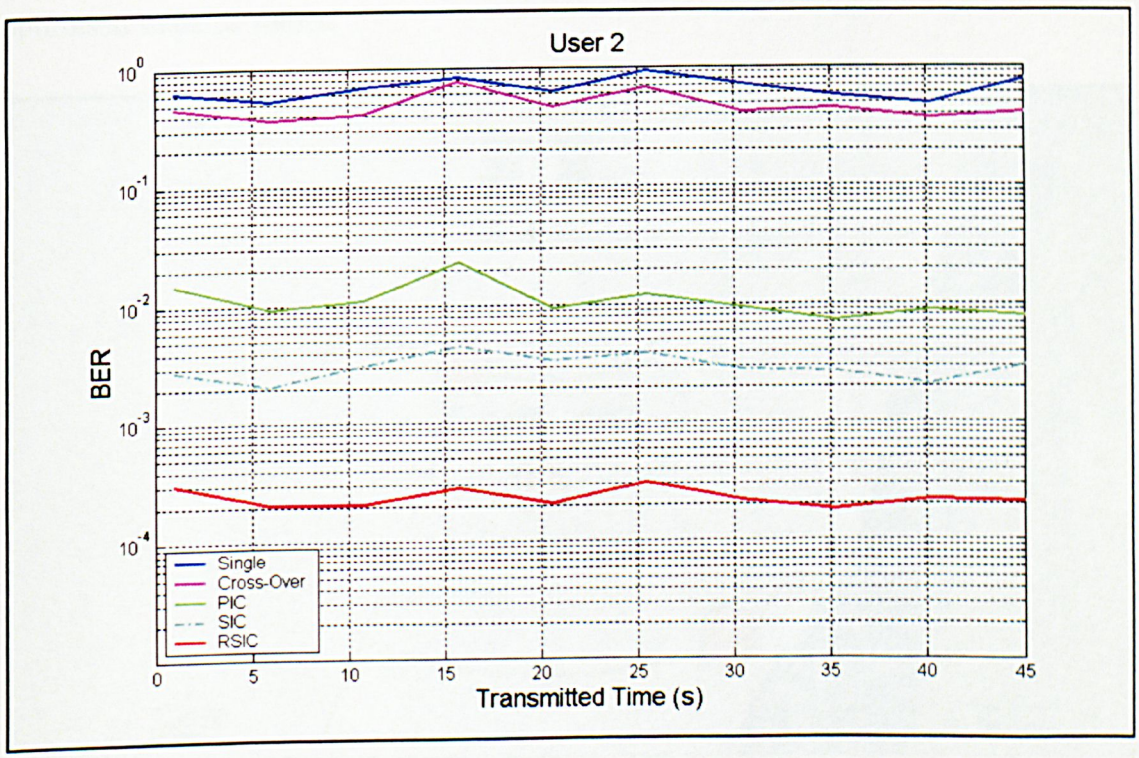

Figure 7-20 Measured P_{er} over 45 s of continuous transmission for user 2

7.3.2 Scenario 2 – Detection of Weaker User prior Strong User

The implication of 2 stronger users for an asynchronous reception arriving during the decision mode of the weakest user is investigated in this section. In this case, the weakest user had to rely heavily on the accurate estimation of the stronger users when operating in the decision mode. Any wrong decision estimation made for the stronger users will contribute negatively to the interference cancellation from the received signal, which result in erroneous estimation for the weakest user. In order to facilitate the presence of an additional user in the 2-user system as described in section 6.2.3, a single user transmission at distance 5km, with position 180° w.r.t. North of MPN was used to simulate a 3-user reception, as shown in Figure 7-21. The time of arrival for the 3-users is depicted in Figure 7-22, with user 1 being the weakest user, first arrival, followed by user 2, during the decision mode, and user 3 being the strongest user, latest arrival. A summary of the system parameter setup is depicted in Table 7-5. Filter tap lengths of 20 and 40 were used for the feedforward and feedback filters respectively, refer to Appendix Table 12 of Appendix XII for tap length selection. The values of the step-size parameters used by the LMS algorithms are 0.006 and 0.004 for the feedforward and feedback taps respectively, refer to Appendix Table 13 of Appendix XII for selection of optimised stepsize values.

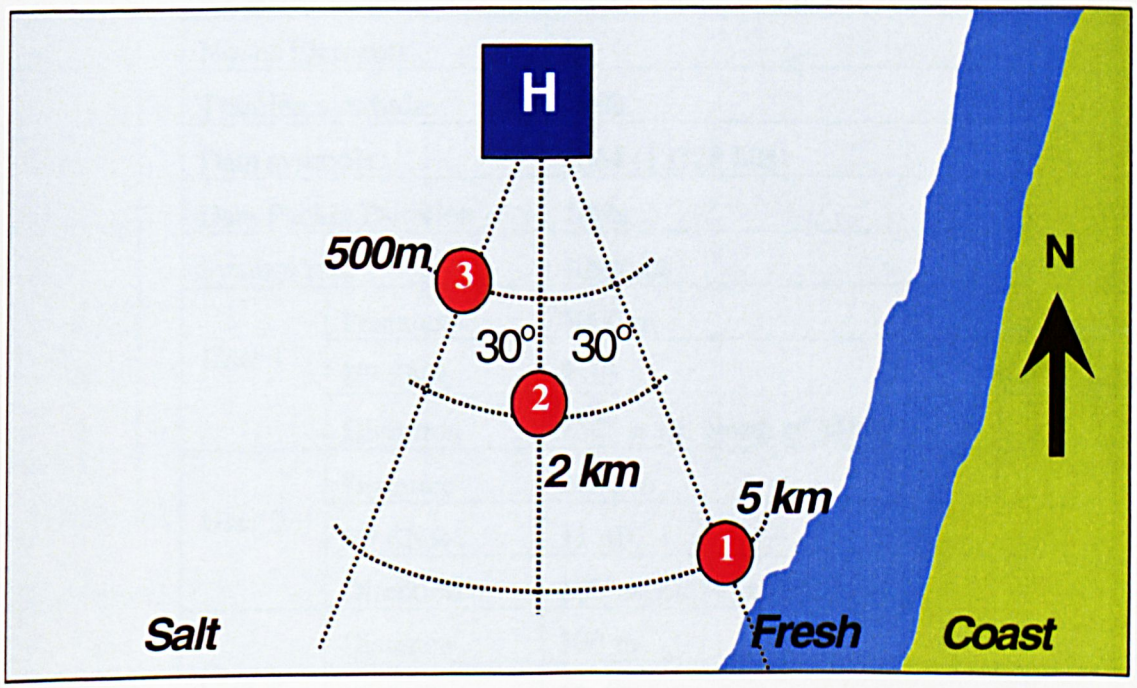

Figure 7-21 Network configuration for a 3 user simultaneous transmission

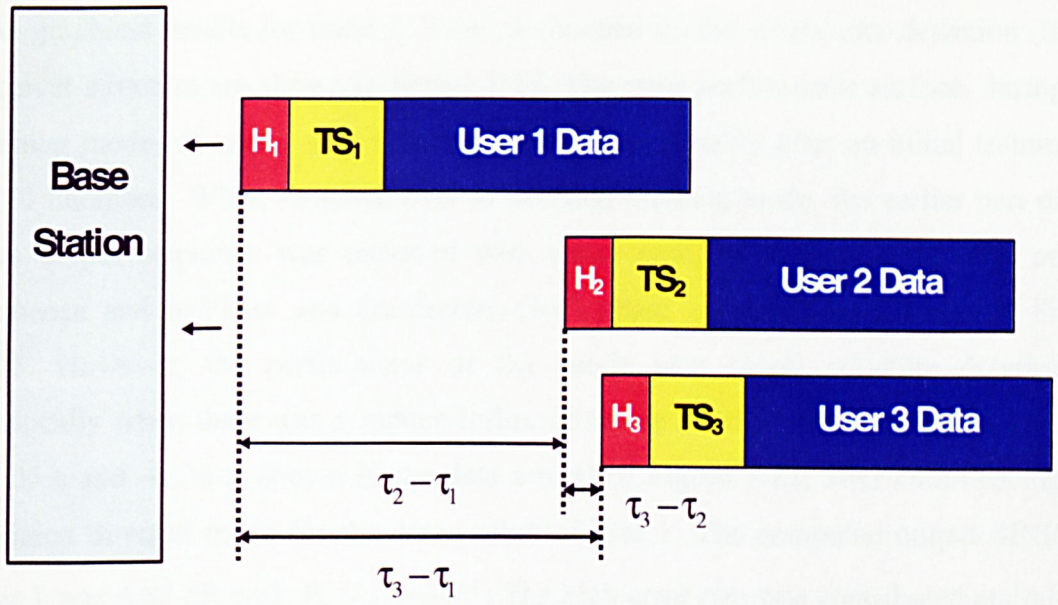

Figure 7-22 Observation window for asynchronous reception

Frequency Bandwidth		B_w = 8-12 kHz
Carrier Frequency		F_c = 10 kHz
Modulation		Coherent QPSK (JPG file)
Channel Depth		18 m
Tx Depth for users		2 m (User 1) 9 m (User 2 & 3)
Rx Array Depth		First element at 8 m ref. to seabed
No. of Elements		5
Training symbols		1700
Data symbols		6664 (13328 bits)
Data Packet Duration		1.62s
Symbol rate		4096 sps
User 1	Distance	5000 m
	I/P SNR	5 dB
	Direction	150° w.r.t. North of MPN
User 2	Distance	2000 m
	I/P SNR	11 dB
	Direction	180° w.r.t. North of MPN
User 3	Distance	500 m
	I/P SNR	19 dB
	Direction	210° w.r.t. North of MPN

Table 7-5 System parameters for 3-users unequal power reception

The graphical results for users 1, 2 and 3 obtained by the single user detection (SUD) receiver structure are shown in Figure 7-23. The error performance surface, during the training mode, of user 1 was observed to converge steadily after an initial training of ~150 iterations. When switched over to decision directed mode, the earlier part of the data output sequence was retrieved with much ease, as shown in the data output sequence and In-Phase and Quadrature (I-Q) phase constellation diagram of Figure 7-23. However, the performance of the single user single structure deteriorated drastically when there was a sudden influx of strong interference from user 2 and 3 at ~1.05 s and ~1.36 s, shown in the data arrival of Figure 7-22, after commencing the decision directed mode for the data packet of user 1. The computed output SINR for user 1 was 6.68 dB with $P_{er} = 1.1 \times 10^{-1}$. The high error rate was contributed entirely by the surge of strong interference from both user 1 and 2. This also resulted in a distorted representation in the latter part of the decoded JPEG (Joint Photographic Experts Group) packet, as shown in Figure 7-28(a). Being embedded in a stronger interference during the training mode, in this case, the SUD receiver structure for user 2 was not able to attain convergence prior to switching to decision mode in order to allow successful decoding of the data sequence. The computed output SINR was 7.53 dB and the detection error, $P_{er} = 3.8 \times 10^{-2}$, rendered the decoded JPEG data packet useless, as shown in picture of Figure 7-28(b). Being the strongest user, user 3 suffers little from the interference from both user 1 and 2, with computed SINR=17.73 dB with $P_{er} = 0.0$, shown in Figure 7-28(c).

The graphical outputs for the method of "cross-over" are shown in Figure 7-24. Also from Figure 7-29(a)-(c), it can be observed that the "cross-over" method of MAI suppression exhibits relatively poor performance in decoding the JPEG packet. The computed output SINR and detection error for user 1, 2 and 3 were 6.42 dB with $P_{er} = 1.3 \times 10^{-1}$, 7.98 dB with $P_{er} = 3.2 \times 10^{-2}$ and 16.33 dB with $P_{er} = 6.1 \times 10^{-4}$ respectively.

Much improvement was observed in the decoded data for the users when adopting the PIC method. The computed results shown in Figure 7-25 for user 1, SINR = 8.98 dB with $P_{er} = 6.4 \times 10^{-2}$, demonstrates that much of the interference contributed by user 2 was removed. However, the strong interference from user 3 remains a hindrance to the successful decoding of the JPEG packet for user 1, as shown in Figure 7-25(a).

Although an improvement was observed for user 2, SINR = 9.89 dB with $P_{er} = 6.8 \times 10^{-3}$, shown in Figure 7-25(b), the MAI contributed by both user 1 and user 2 results in a negative effect for user 3, output SINR = 16.83 dB with $P_{er} = 5.9 \times 10^{-4}$, as shown in Figure 7-25(c). The increased error observed in user 3 can be attributed to the error decision of both user 1 and 2 which contributed negatively to the subtraction of the regenerated weighted data from the received signal. The decoded JPEG packets for the 3 users are depicted in Figure 7-30 (a)-(c).

By adopting the method of SIC suppression, MAI from both user 2 and 3 was suppressed significantly in the output data sequence of user 1. However, interference from user 3 still contributed a reasonably high level of distortion to the decoded data for user 1, with computed SINR = 10.89 dB and $P_{er} = 6.8 \times 10^{-3}$, as shown in the graphical output of Figure 7-26(a) and the JPEG image in Figure 7-31(a). On the other hand, the SIC method managed to achieve convergence in the training mode of user 2, as shown in Figure 7-26(b), with SINR = 12.89 dB and $P_{er} = 0.0$, thus enabling it to successfully decode its output JPEG packet, shown in Figure 7-31(b). Analysis from the SIC method in section 5.5.3 shows that the strongest user does not benefit from any MAI reduction. Therefore the results obtained for user 3 is identical to the result obtained by the single user structure, that is SINR = 17.73 dB with $P_{er} = 0.0$, shown in Figure 7-26(c) and the JPEG image in Figure 7-31(c) respectively.

The best performance was observed from using the RSIC method. The output JPEG packet of user 1 was successfully decoded with output SINR = 14.46 dB with $P_{er} = 0.0$, as shown in the graphical output of Figure 7-27(a) and the JPEG image of Figure 7-32(a). By performing a single feedback loop of the regenerated, weighted signal from both users 1 and 2 to the received signal, the computed SINR for user 3 from the subtracted signal was further improved to 22.02 dB with $P_{er} = 0.0$. The RSIC method also gained an improvement in the decoded JPEG packet for user 2, SINR = 15.38 dB with $P_{er} = 0.0$. The graphical output and JPEG packet for both users 2 and 3 are shown in Figure 7-27(b)-(c) and Figure 7-32(b)-(c) respectively. These results clearly indicate that, amongst the strategies considered for shallow water coherent network communication, the RSIC structure is the most effective multi-user detection strategy

for MAI suppression in coherent acoustic communication. A summary of the computed SINR and P_{er} for the various receiver structures is summarised in Table 7-6.

The time evolution of beamforming pattern obtained for user 1 by the SUD method and RSIC method receiver structures are shown are shown in Figure 7-33 and Figure 7-34 respectively. The beamforming pattern were based on the 3 horizontal elements of Figure 6-6 between the time duration 0.9s~1.50s of the received data packet. Figure 7-33 clearly illustrates that in the presence of strong interruption from strong MAI at ~1.05s and ~1.36s (yellow dotted lines), the single user adaptive beamformer loses its nulling effectiveness. But the RSIC detection strategy gained a significant improvement when interference cancellation had been performed prior to any beamforming. It was observed that no nulling was performed for user 2, at 0^{o}, the most probable reason for this is that the interference from user 2 had been completely eradicated prior to beamforming. A deep null was formed to mitigate the interference of user 3 in the direction $+30^{o}$ while generating a main lobe in the direction -30^{o}.

Figure 7-35 and Figure 7-36 shows the variation of the measured P_{er}, for both user 1 and 2 over a period of 18 consecutive packet (~40s) by the various receiver structures. The measured P_{er} for both users remains rather constant throughout the ~40s transmission. This can be cross-examined with the channel impulse history for user 1 and 2, as shown in Figure 7-37 and Figure 7-38 respectively, which did not exhibits signs of multipath spread. Throughout the 40s of data reception, the RSIC strategy was observed to have maintained a low measured P_{er} for both users in the 10^{-4} range.

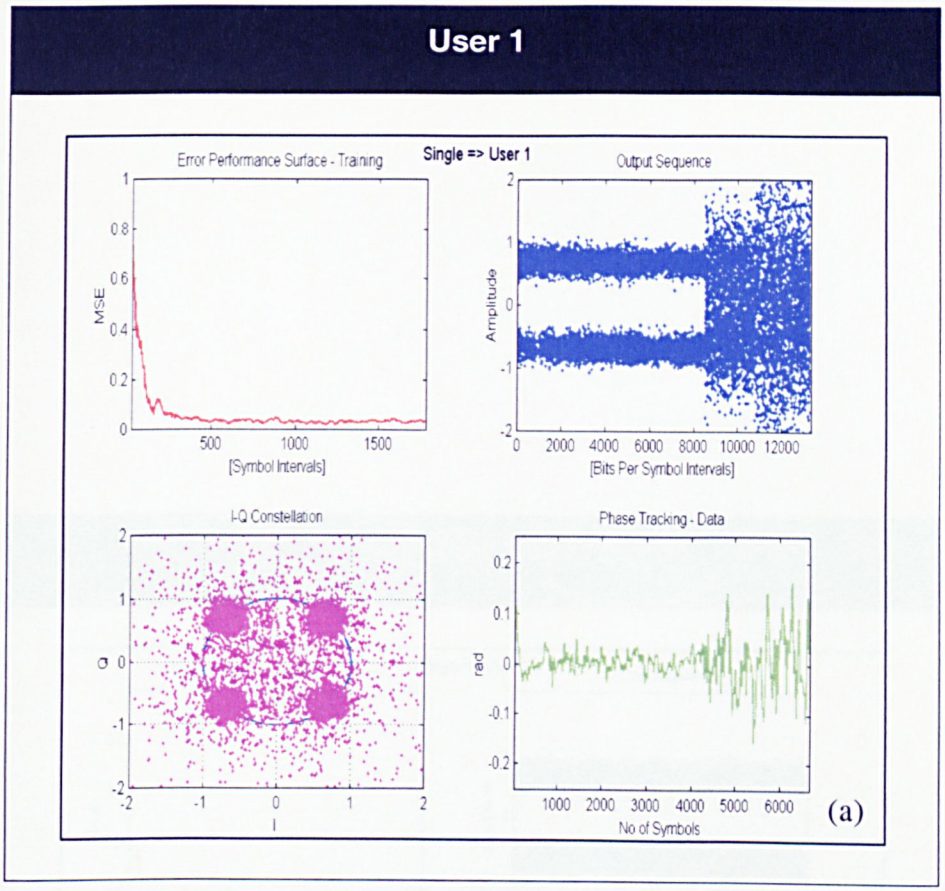

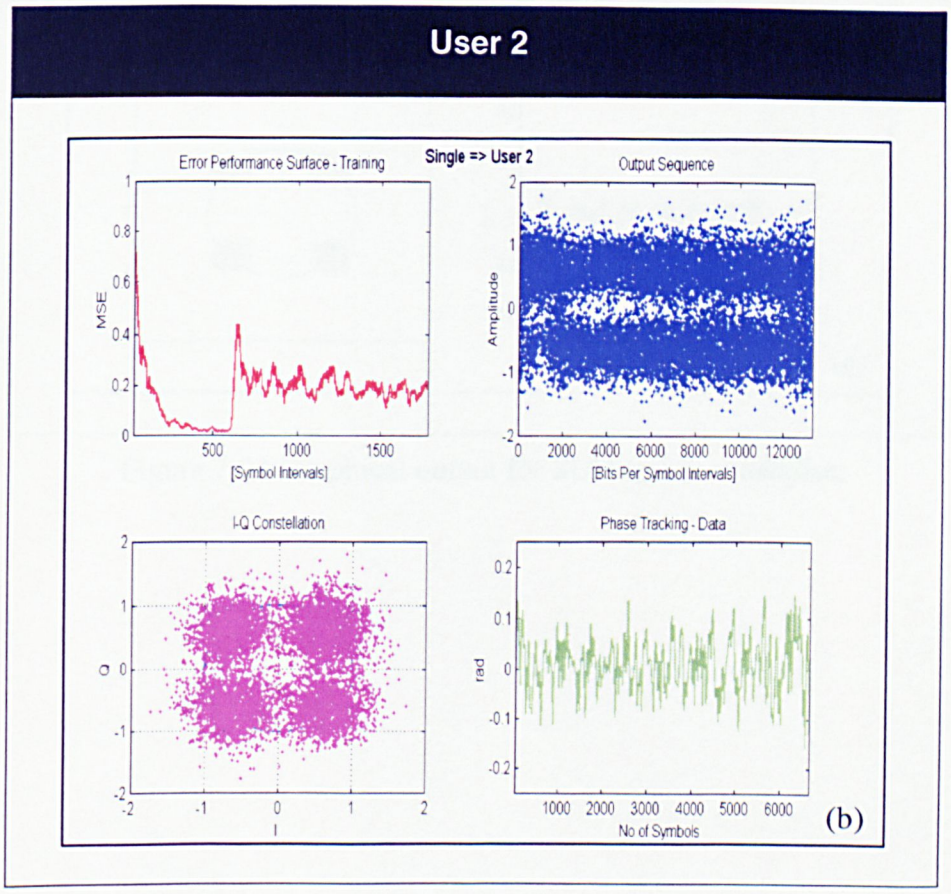

Figure 7.23 Graphical output for SUD receiver structure

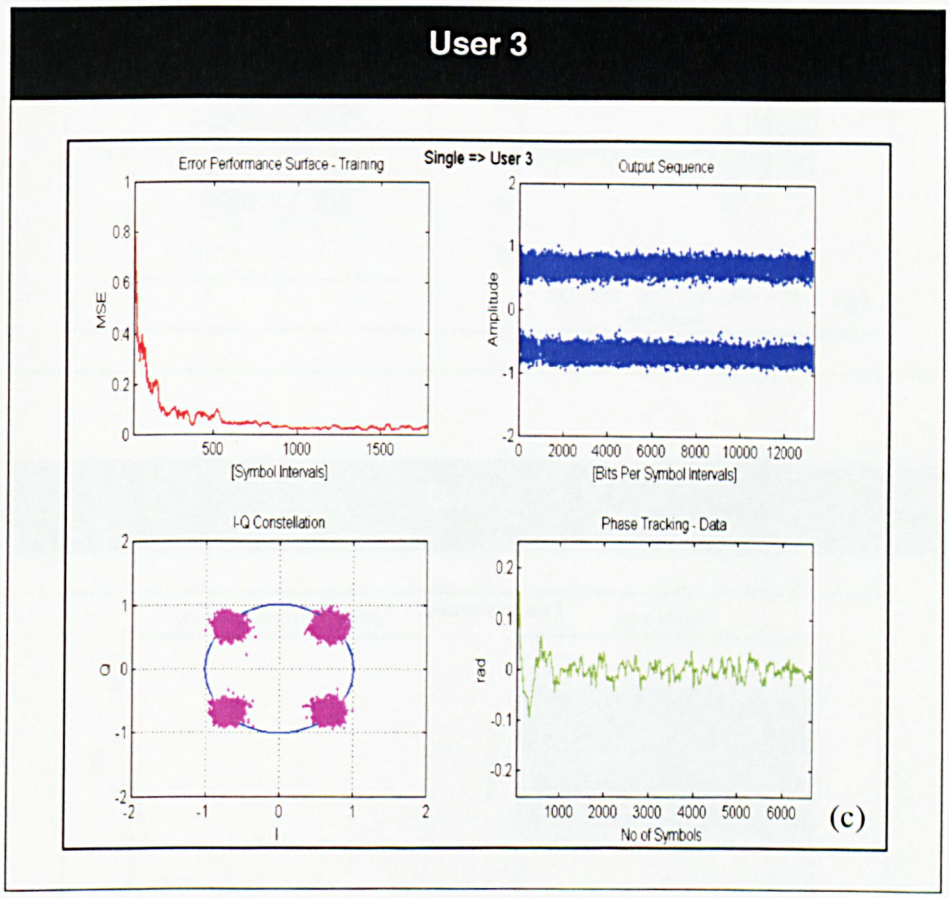

Figure 7-23 Graphical output for SUD receiver structure

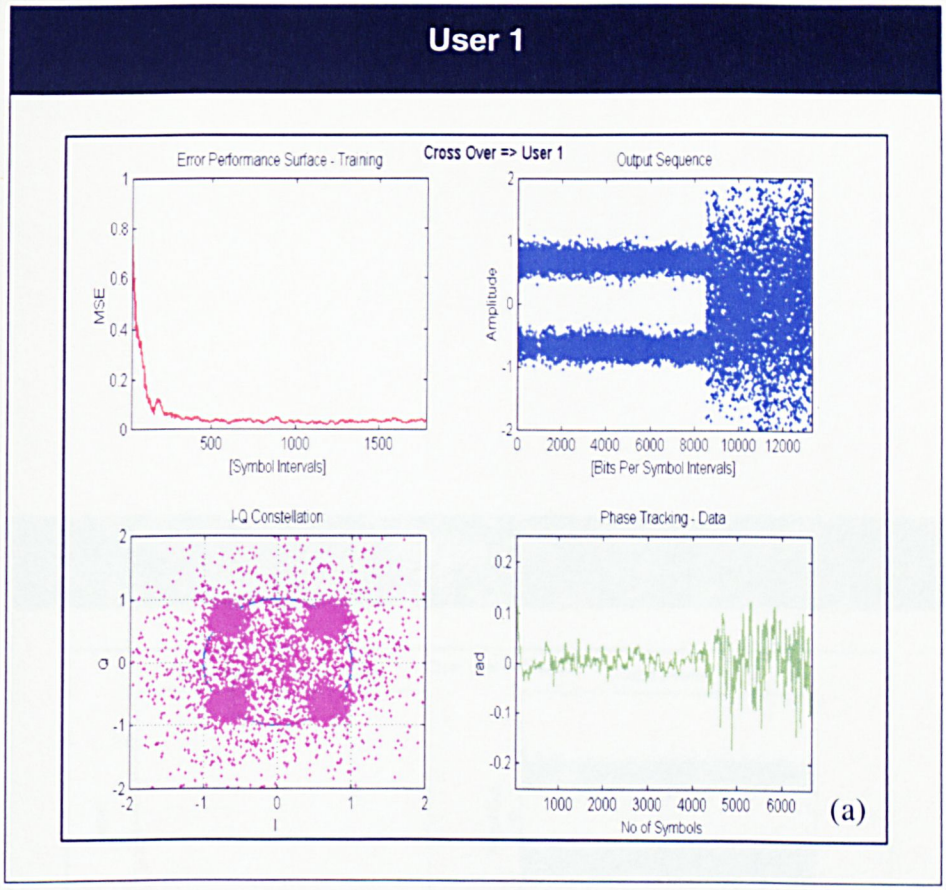

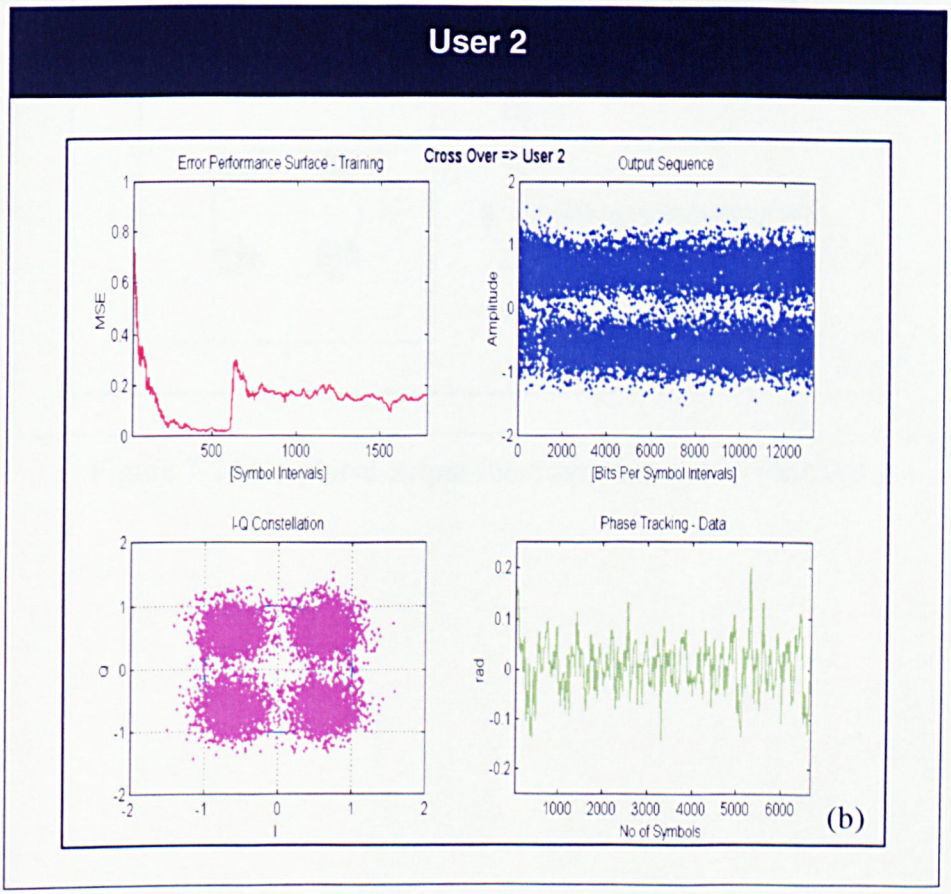

Figure 7.24 Graphical output for cross-over receiver structure

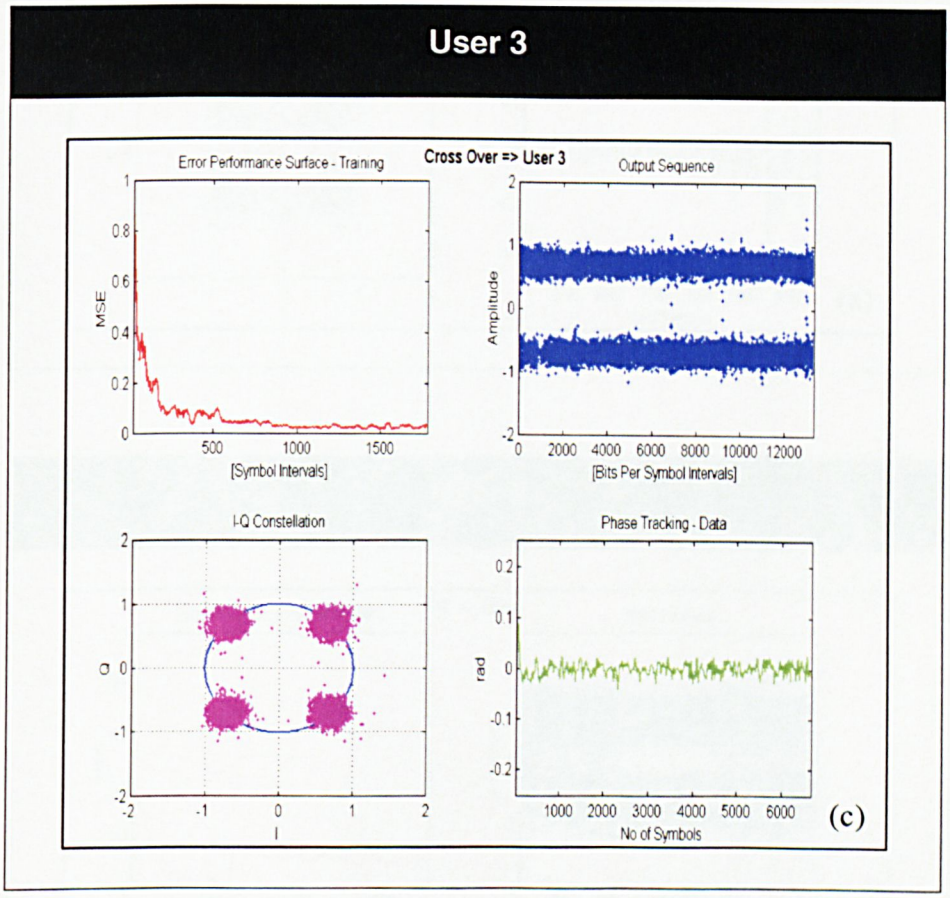

Figure 7-24 Graphical output for cross-over receiver structure

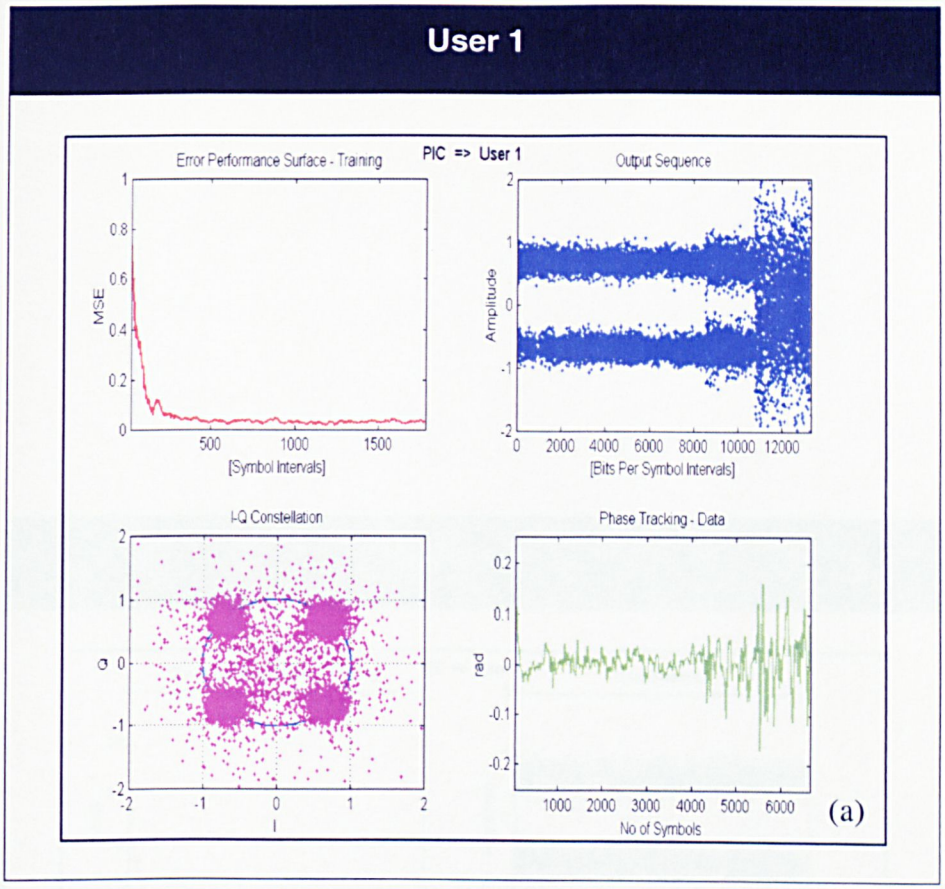

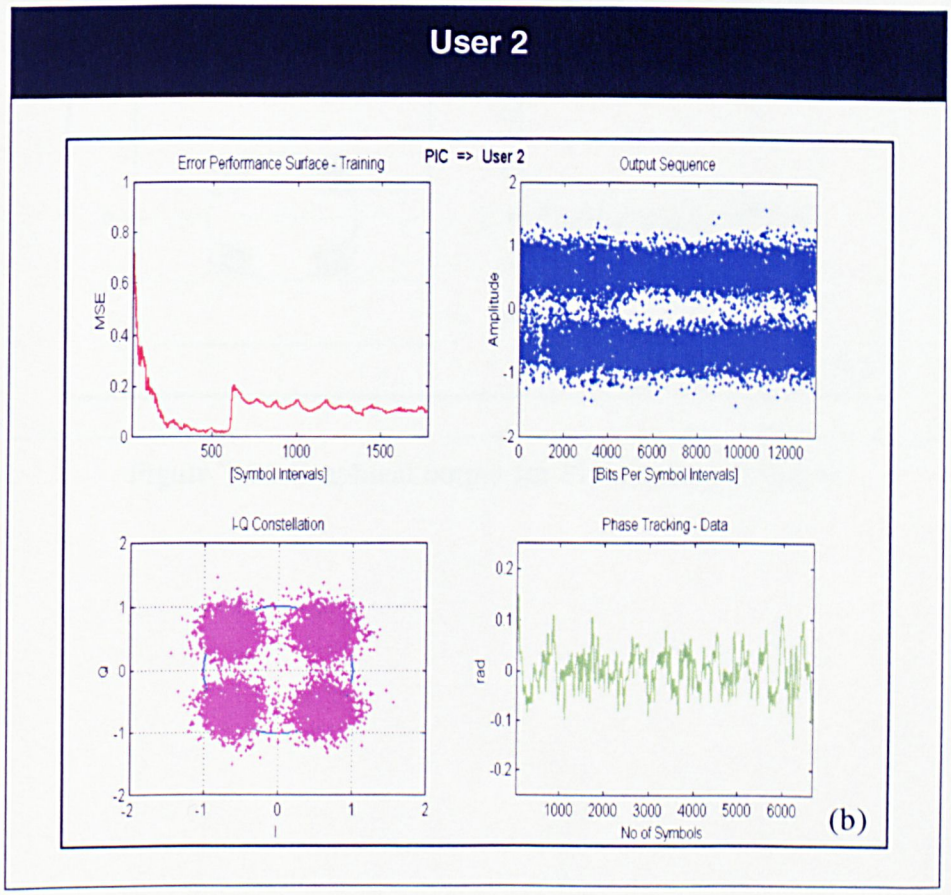

Figure 7.25 Graphical output for PIC receiver structure

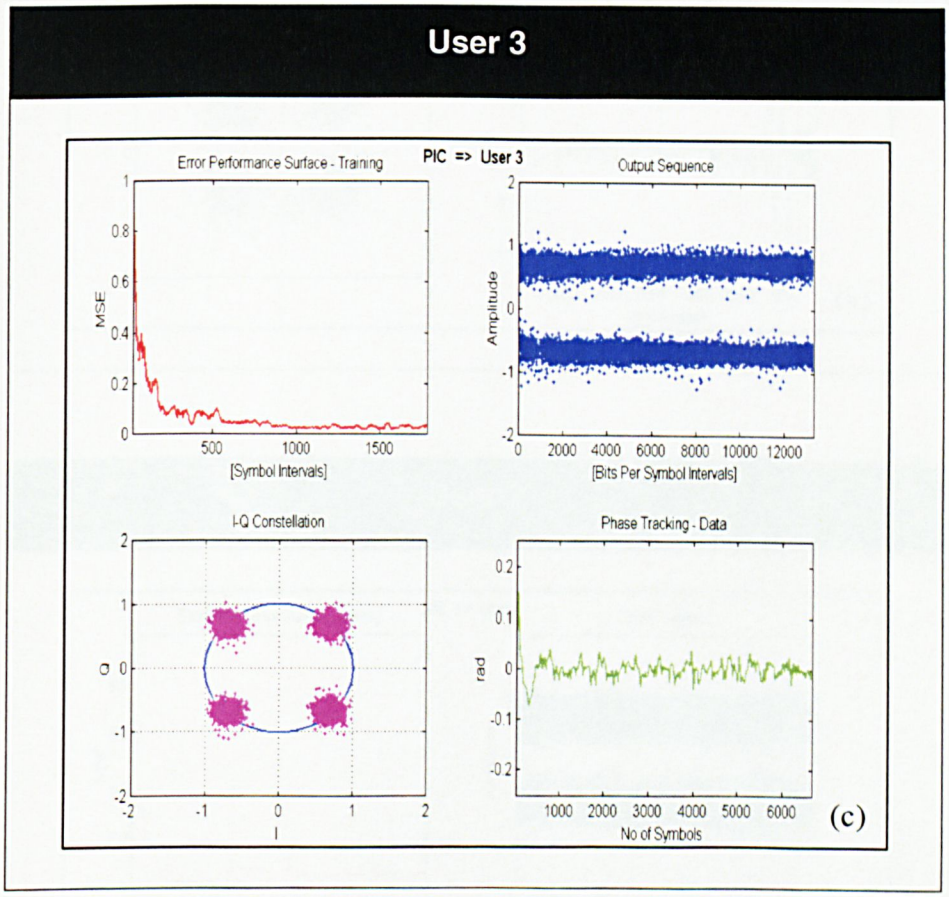

Figure 7-25 Graphical output for PIC receiver structure

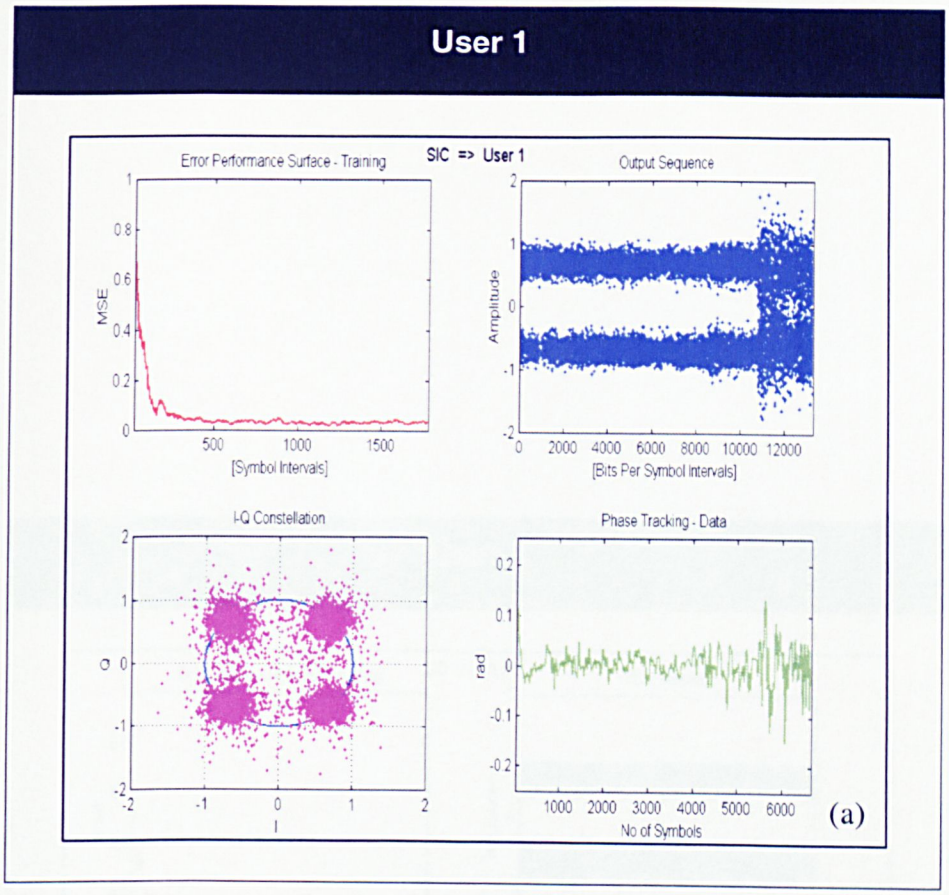

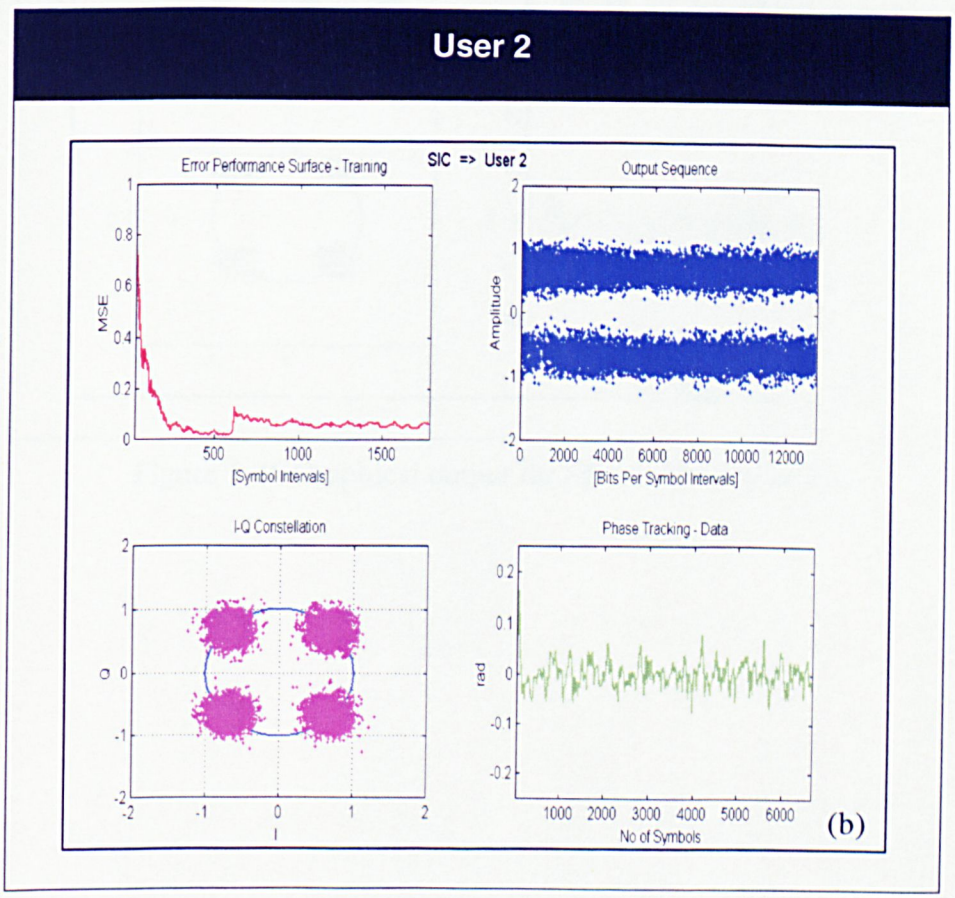

Figure 7.26 Graphical output for SIC receiver structure

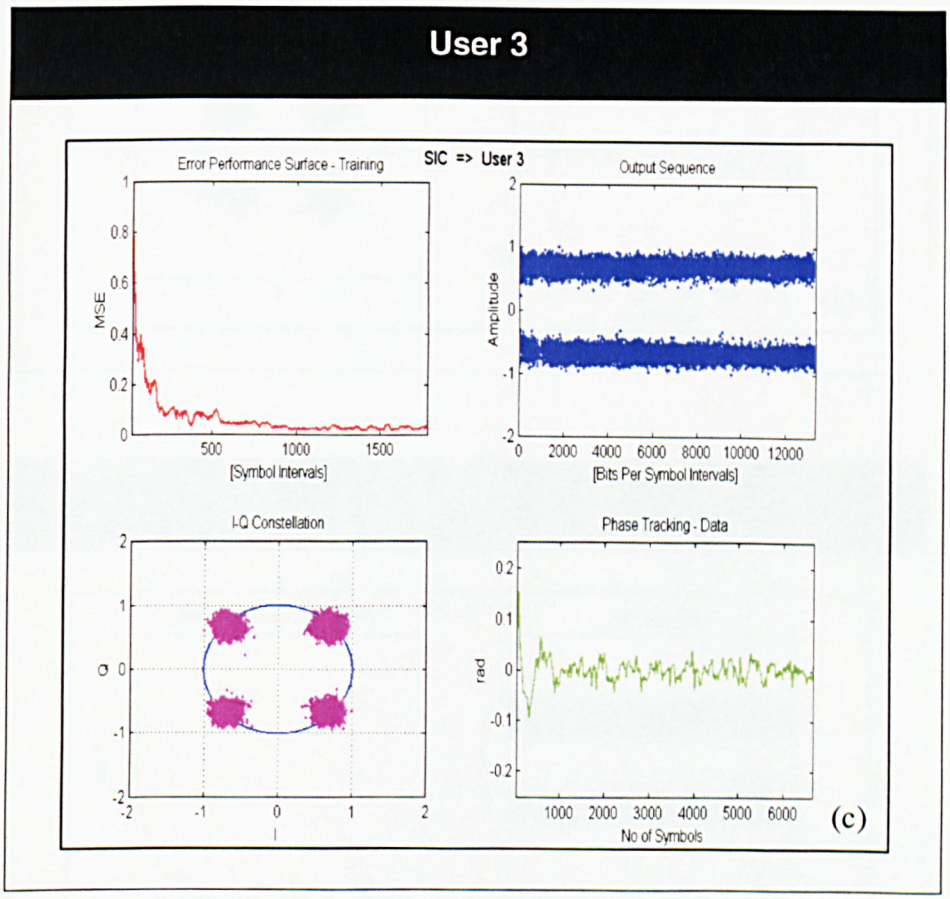

Figure 7-26 Graphical output for SIC receiver structure

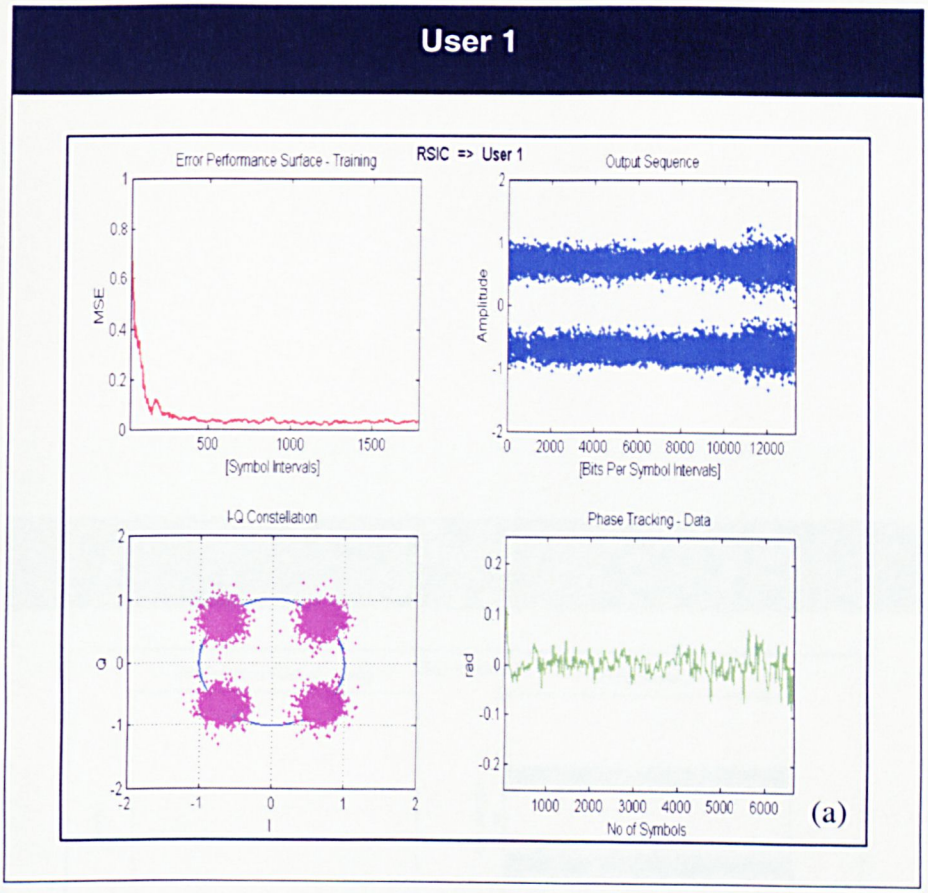

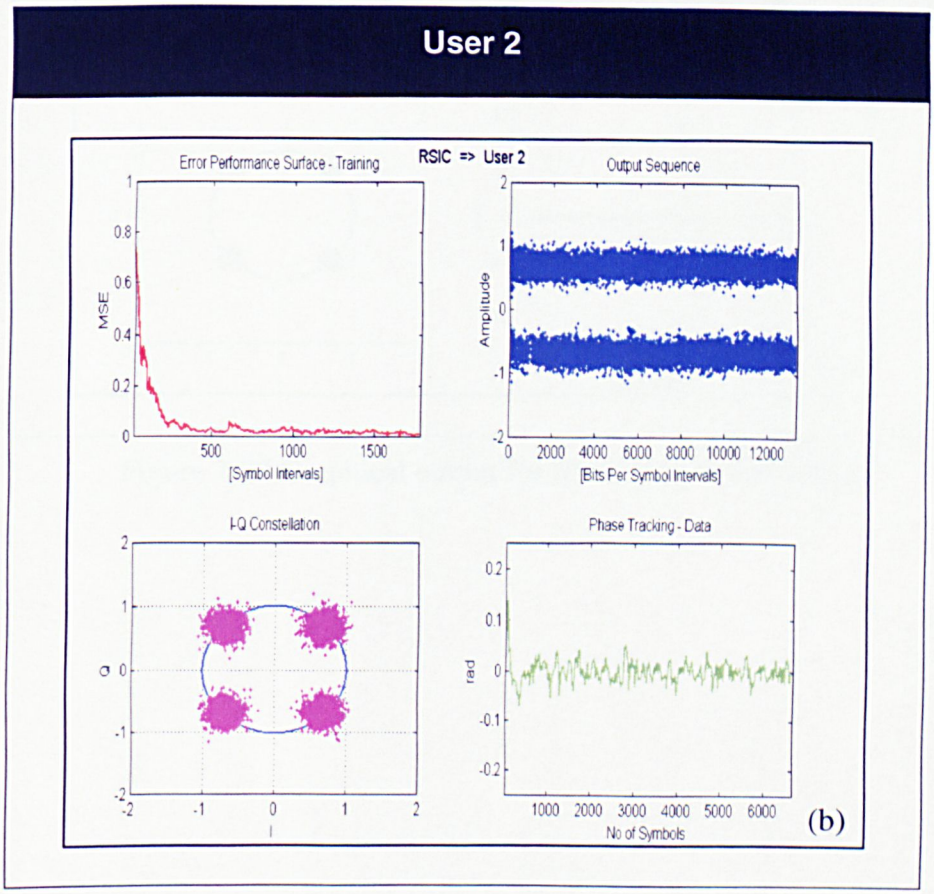

Figure 7.27 Graphical output for RSIC receiver structure

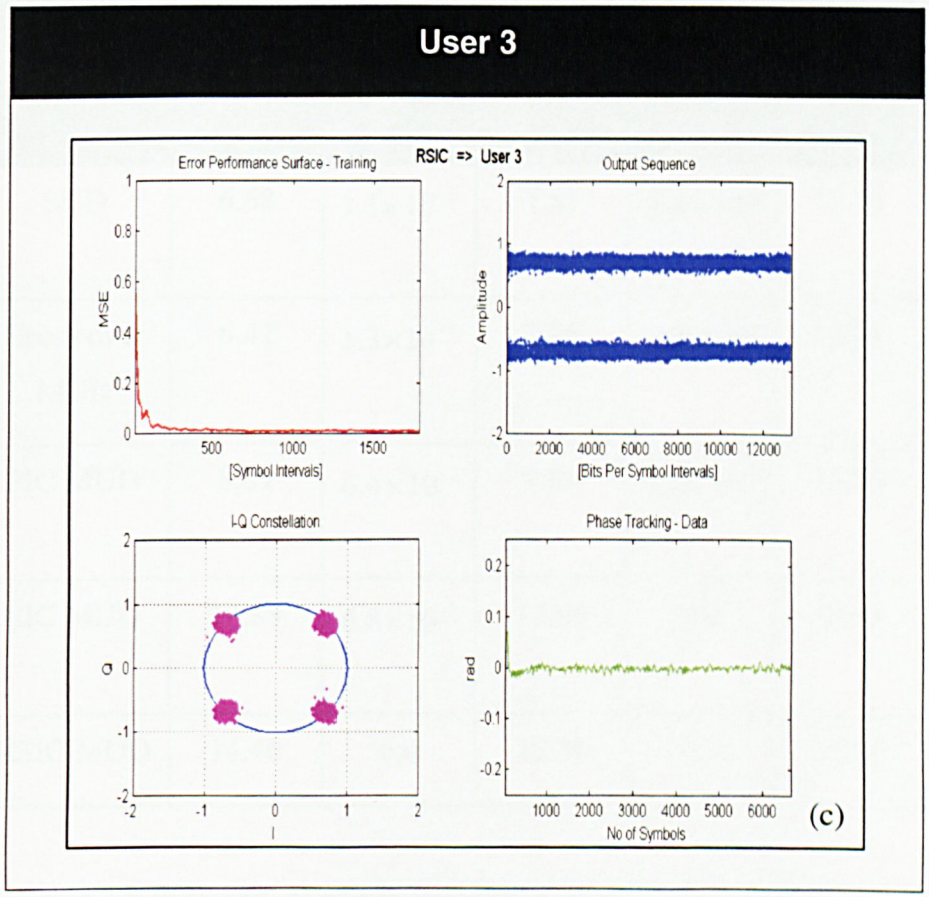

Figure 7-27 Graphical output for RSIC receiver structure

	Receiver Structures	User 1		User 2		User 3	
		SINR (dB)	P_{er}	SINR (dB)	P_{er}	SINR (dB)	P_{er}
1.	SUD	6.68	1.1×10^{-1}	7.53	3.8×10^{-2}	17.73	0.0
2.	Cross over MUD	6.42	1.3×10^{-1}	7.98	3.2×10^{-2}	16.33	6.1×10^{-4}
3.	PIC MUD	8.89	6.4×10^{-2}	9.89	6.8×10^{-3}	16.83	5.9×10^{-4}
4.	SIC MUD	10.89	6.8×10^{-3}	12.89	0.0	17.73	0.0
5.	RSIC MUD	14.46	0.0	15.38	0.0	22.02	0.0

Table 7-6 Summary of computed SINR and P_{er} for the receiver structures

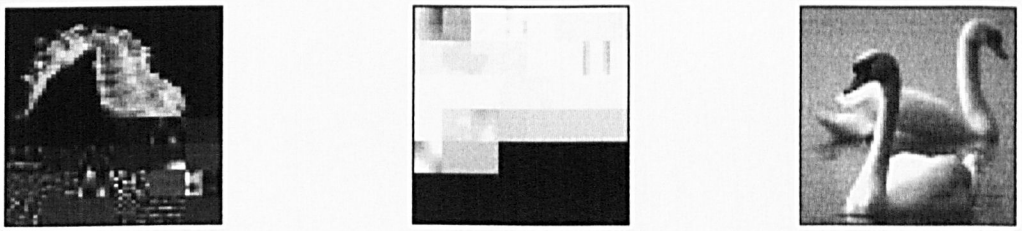

(a) (b) (c)

Figure 7-28 Decoded JPEG files by SUD receiver structure:
(a) User 1 (b) User 2 (c) User 3

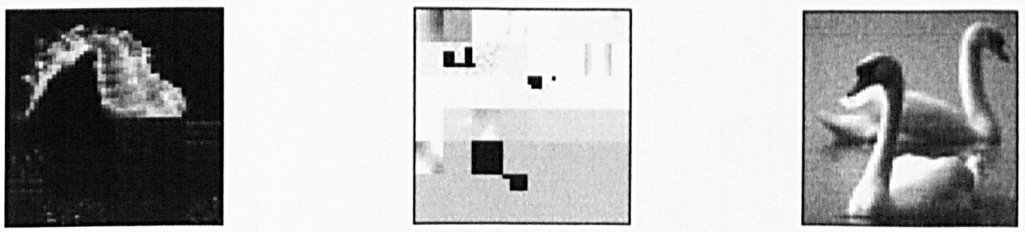

(a) (b) (c)

Figure 7-29 Decoded JPEG files by cross over receiver structure:
(a) User 1 (b) User 2 (c) User 3

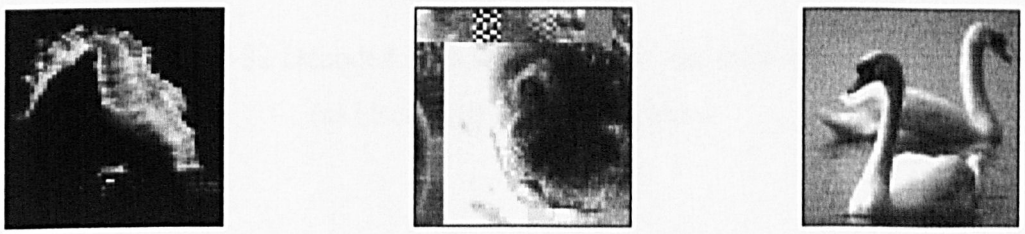

(a) (b) (c)

Figure 7-30 Decoded JPEG files by PIC receiver structure:
(a) User 1 (b) User 2 (c) User 3

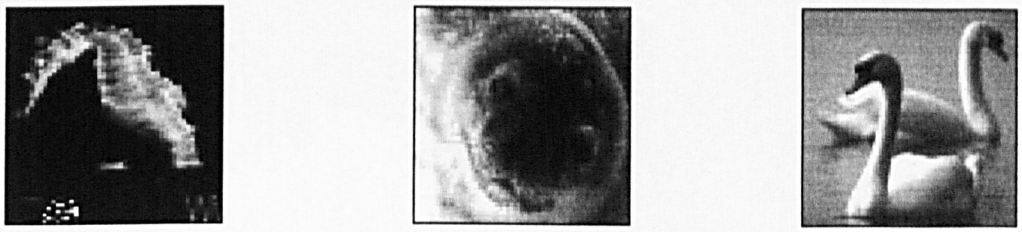

(a) (b) (c)

Figure 7-31 Decoded JPEG files by SIC receiver structure:
(a) User 1 (b) User 2 (c) User 3

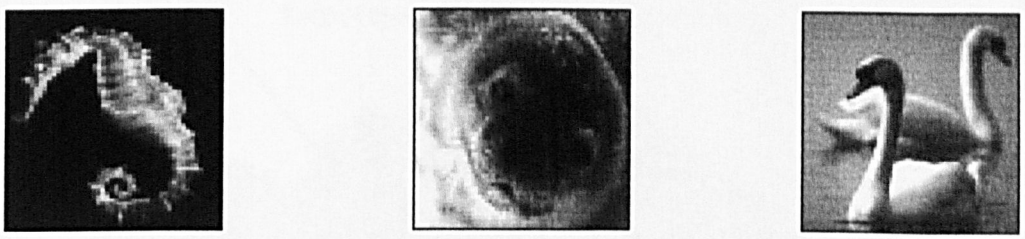

(a) (b) (c)

Figure 7-32 Decoded JPEG files by RSIC receiver structure:
(a) User 1 (b) User 2 (c) User 3

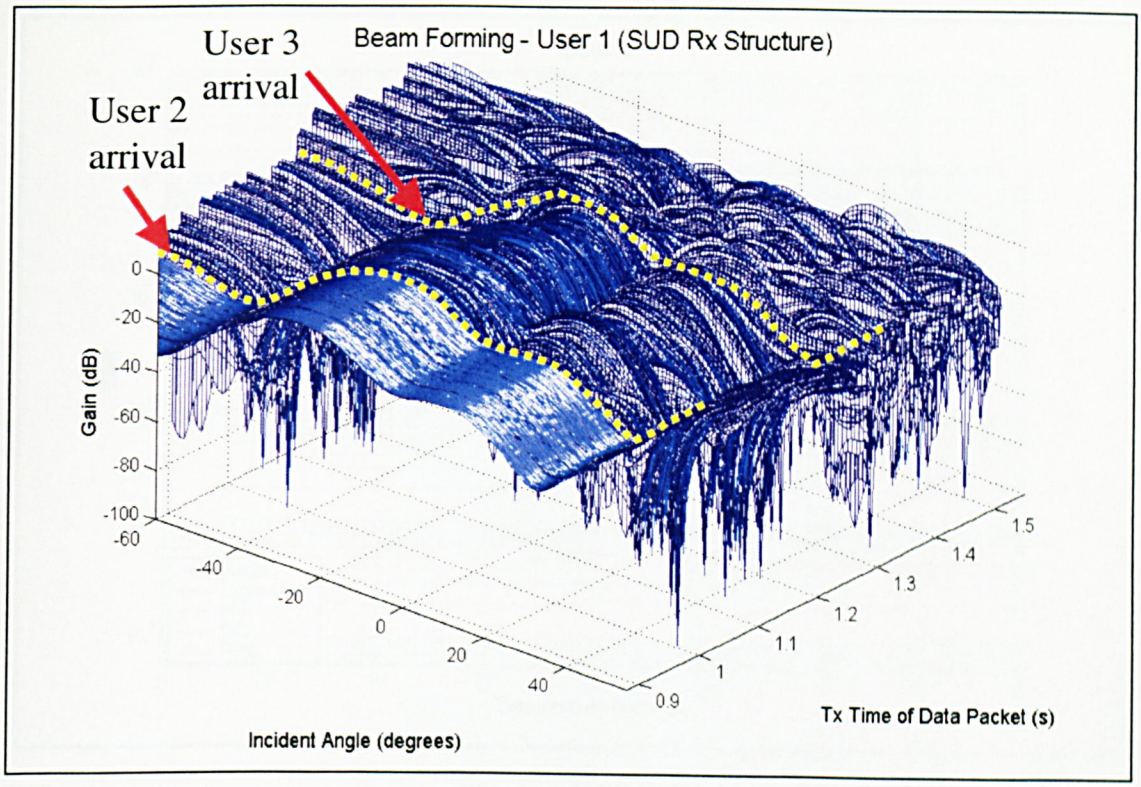

Figure 7-33 Beamforming by SUD strategy

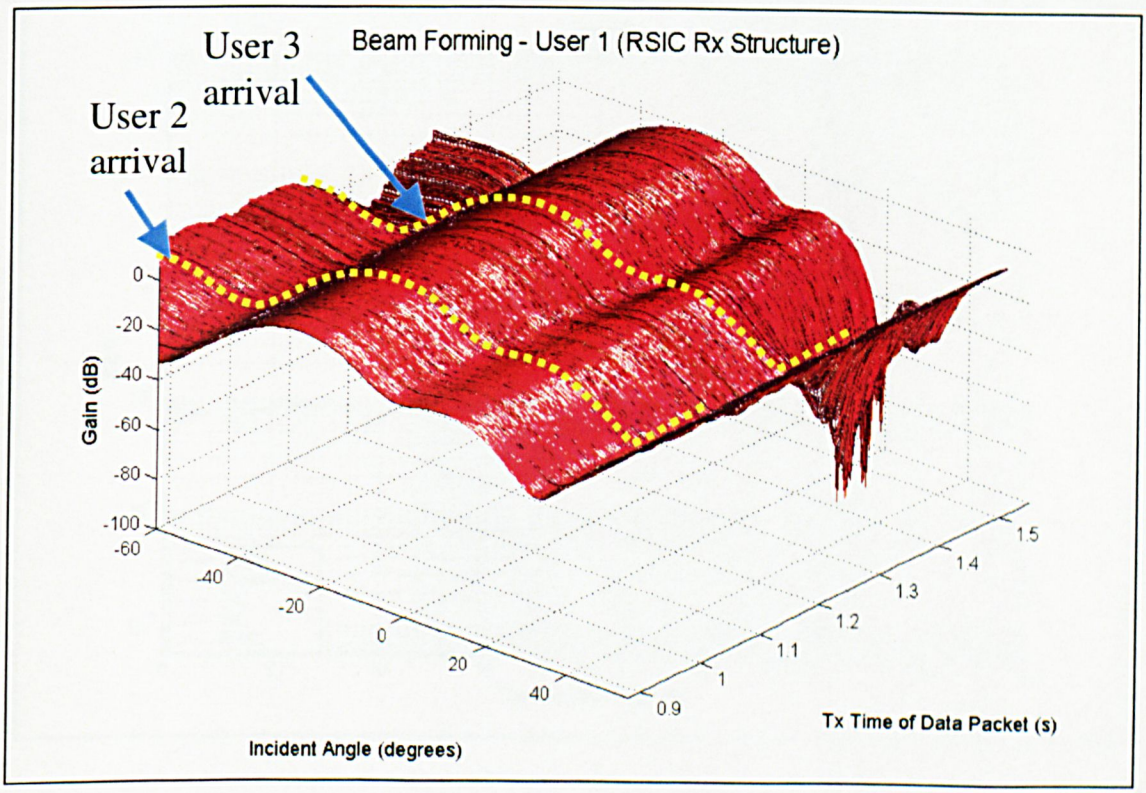

Figure 7-34 Beamforming by RSIC strategy

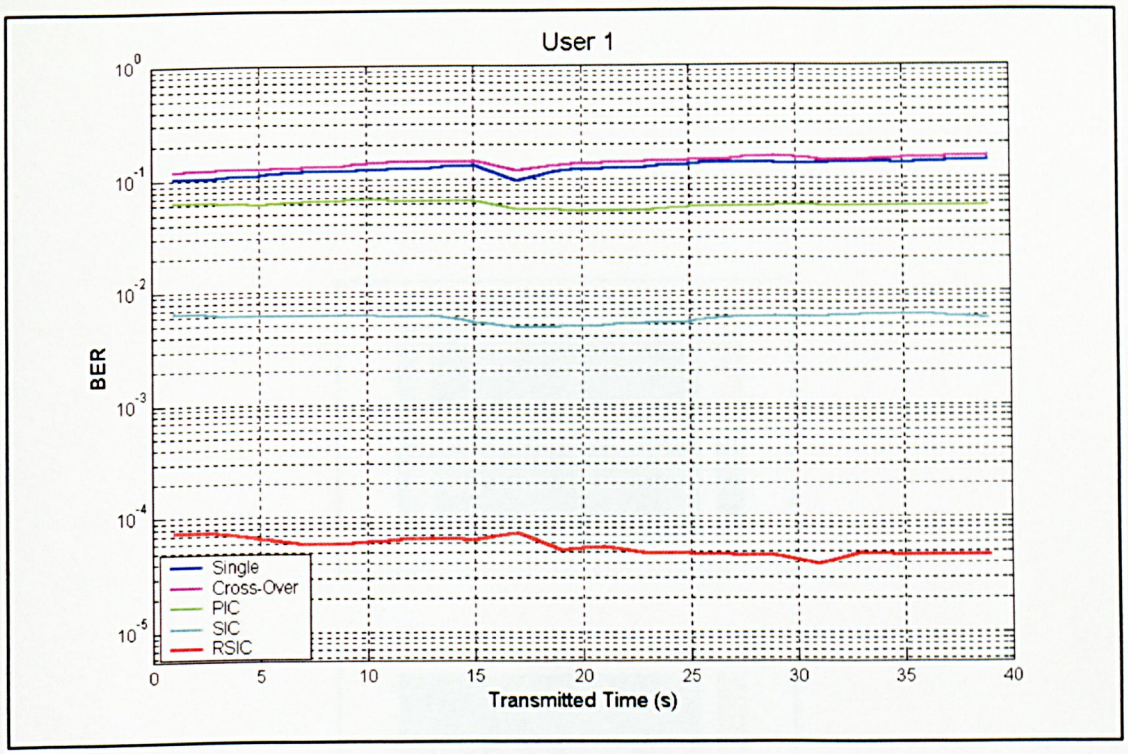

Figure 7-35 Measured P_{er} over 40 seconds of continuous transmission for user 1

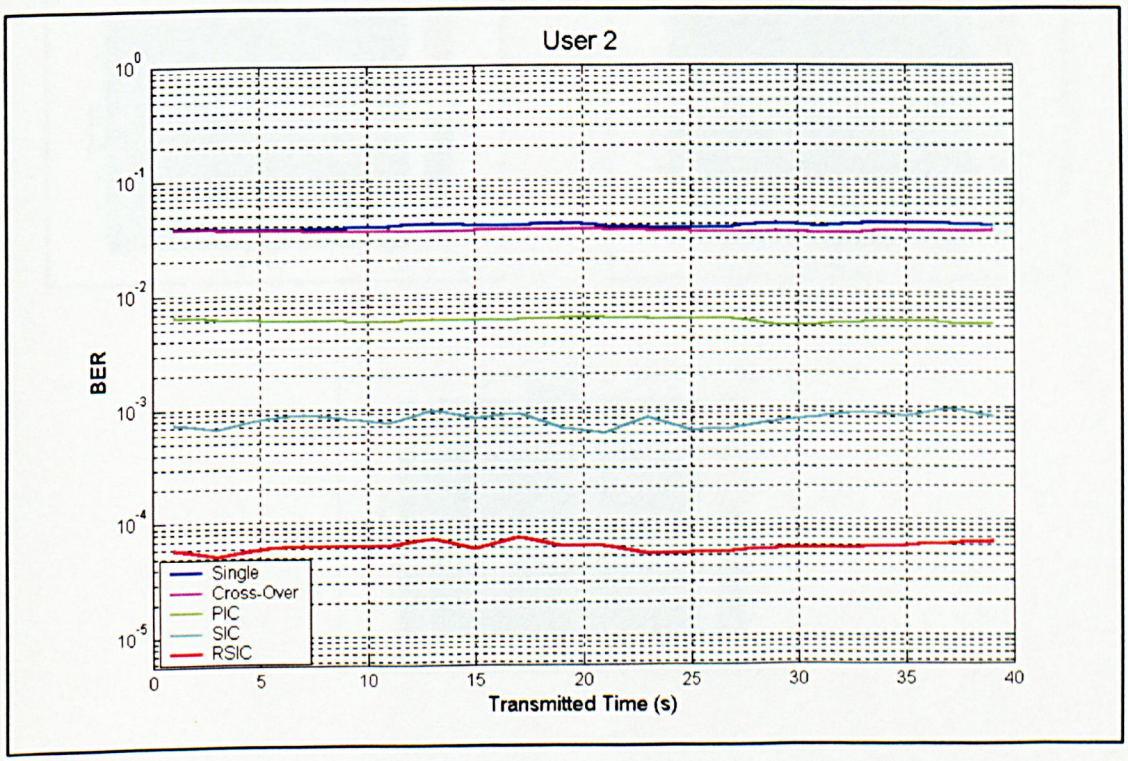

Figure 7-36 Measured P_{er} over 40s of continuous transmission for user 2

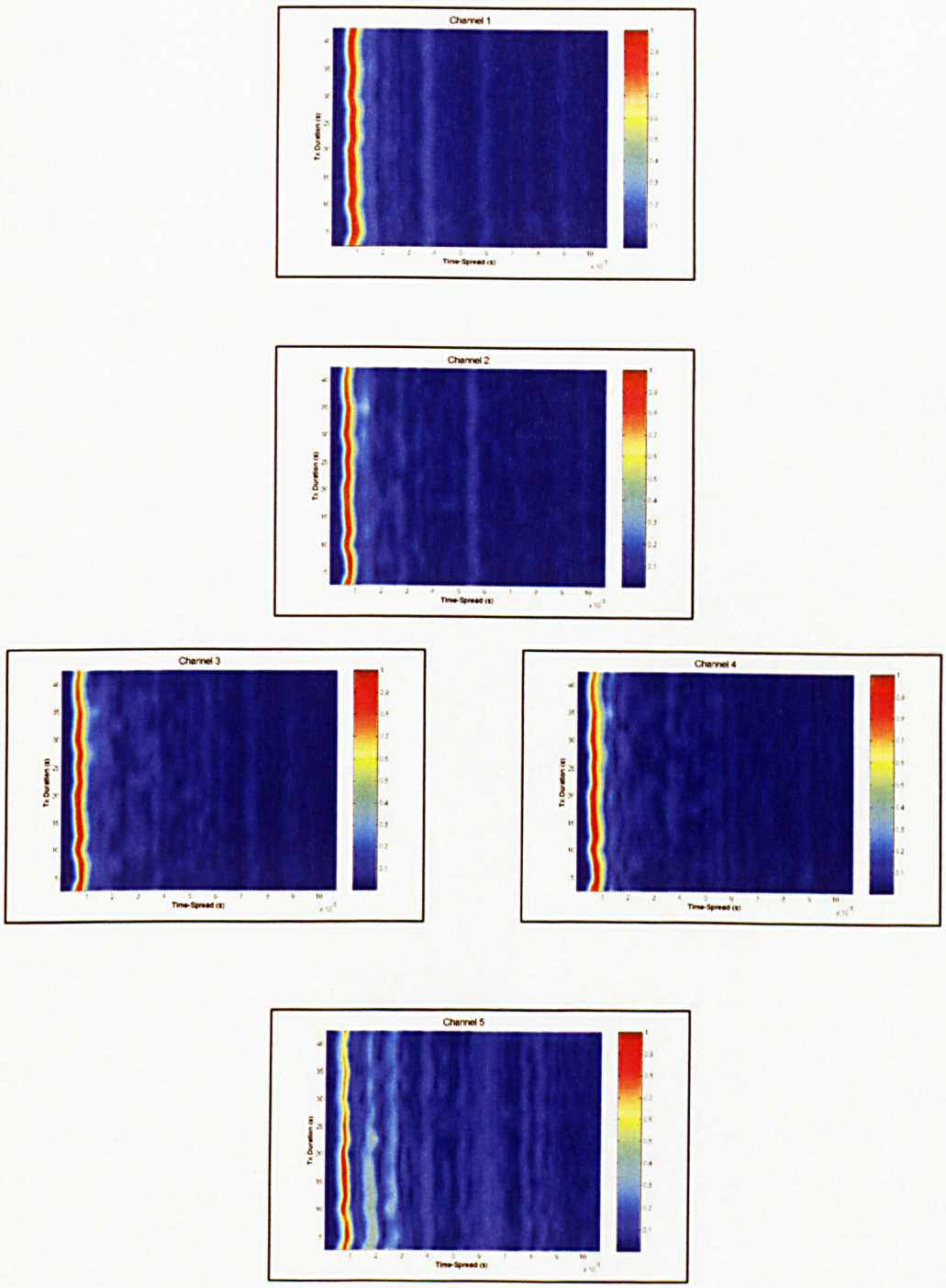

Figure 7-37 Channel impulse history at 5000 m

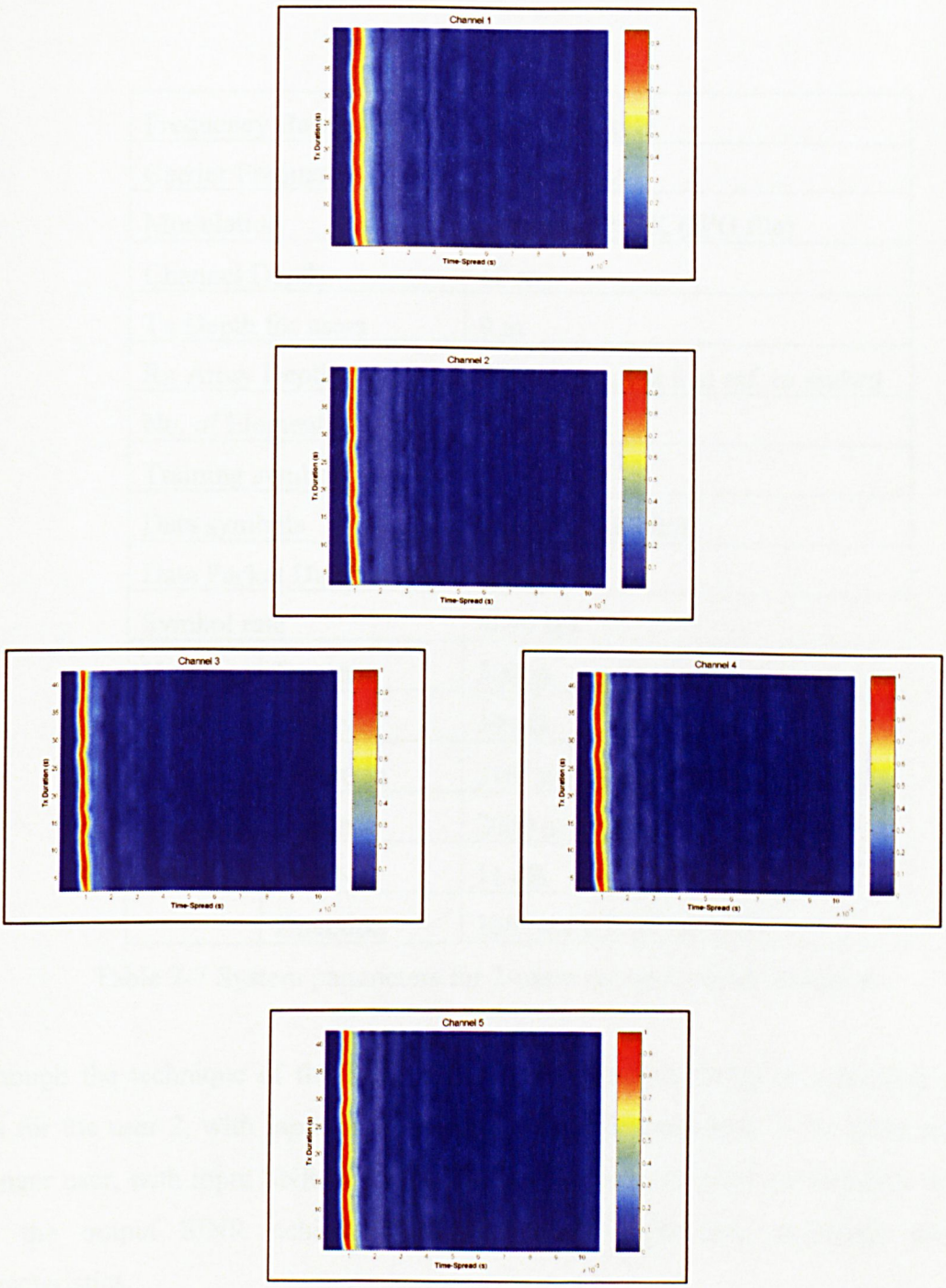

Figure 7-38 Channel impulse history at 2000 m

7.4 Comparison of Supervised Adaptive Algorithms for the RSIC Technique

The performance of the supervised adaptive algorithms adopted by the RSIC MUD receiver structure is examined in this section. The experimental system setup is illustrated in Table 7-7.

Frequency Bandwidth		B_w = 8-12 kHz
Carrier Frequency		F_c = 10 kHz
Modulation		Coherent QPSK (JPG file)
Channel Depth		18 m
Tx Depth for users		9 m
Rx Array Depth		First element at 8 m ref. to seabed
No. of Elements		5
Training symbols		1700
Data symbols		6664 (13328 bits)
Data Packet Duration		1.62s
Symbol rate		4096 sps
User 1	Distance	500 m
	I/P SNR	19 dB
	Direction	210° w.r.t. North of MPN
User 2	Distance	2000 m
	I/P SNR	11 dB
	Direction	180° w.r.t. North of MPN

Table 7-7 System parameters for 2-users unequal power reception

Although the technique of the RSIC strategy exhibits robustness in extracting useful data for the user 2, with input SNR of 11dB, which is embedded in the presence of a stronger user, with input SNR of 19dB. The results from the error performance surface and the output SINR achieved by the various algorithms displayed different characteristics.

The faster convergence rate achieved by the standard RLS algorithm over the LMS algorithm during the transient state (training mode) is by no means surprising, as shown in the computed error performance surface of Figure 7-39. However, the introduction of

the exponential weighting factor inhibits the standard RLS algorithm from tracking abrupt changes in the channel during the steady state (decision mode). Results obtained using the standard RLS algorithm, in Figure 7-40(b) with output SINR = 11.3 dB and error detection, $P_{er} = 0.0$, exhibits a poorer tracking compared to the LMS algorithm as in Figure 7-40(a), with SINR = 13.2 dB and $P_{er} = 0.0$, which is due mainly to the divergence of the inverse correlation matrix. The MSE plot is shown in Figure 7-41.

The VSLMS algorithm achieved a better convergence rate over the LMS and RLS algorithms with SINR = 14.5 dB with $P_{er} = 0.0$, shown in Figure 7-39 and Figure 7-40(c). However, the improved RLS algorithm gave the best performance in terms of rate convergence and tracking over the rest of the algorithms when switching from the transient state to the steady state, with SINR = 15.6 dB and $P_{er} = 0.0$, shown in Figure 7-39 and Figure 7-40(d). In terms of computational complexity, both the LMS and VSLMS offers an attractive approach when operating in real-time mode, while the improved RLS algorithm is desirable when off-line data analysis is required.

A summary of the computed SINR and P_{er} for the various algorithms is summarised in Table 7-8.

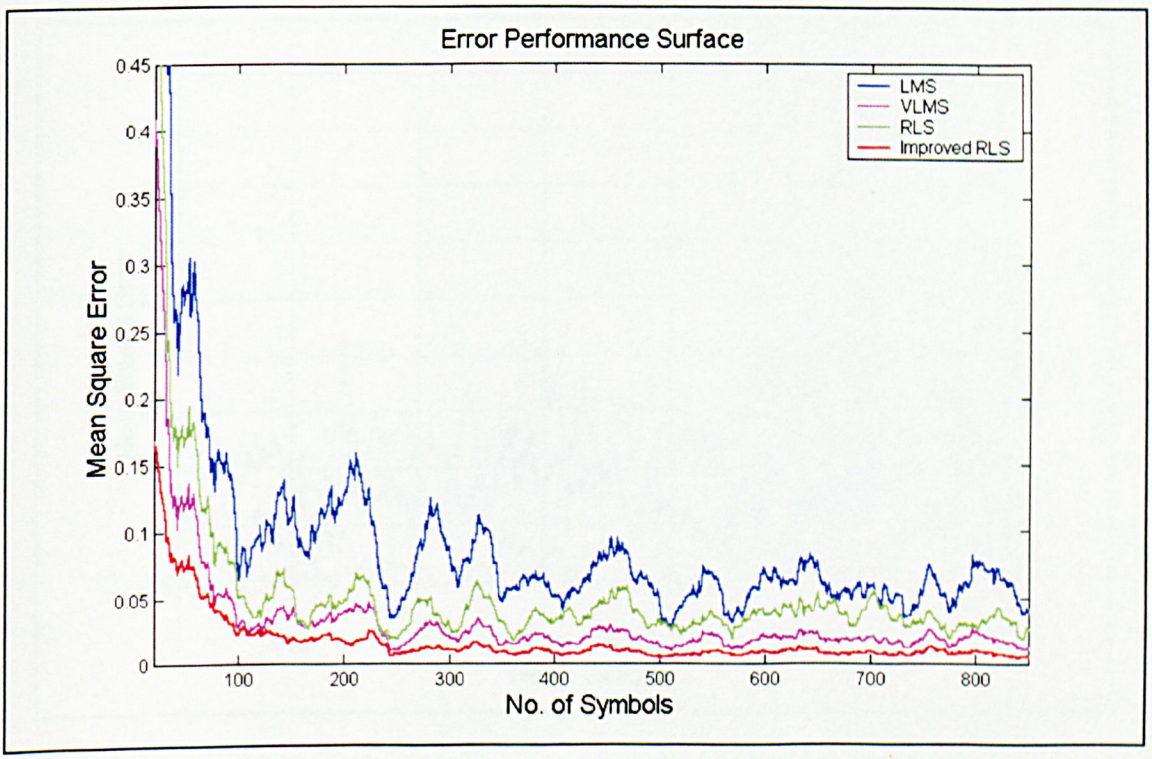

Figure 7-39 Error performance surface

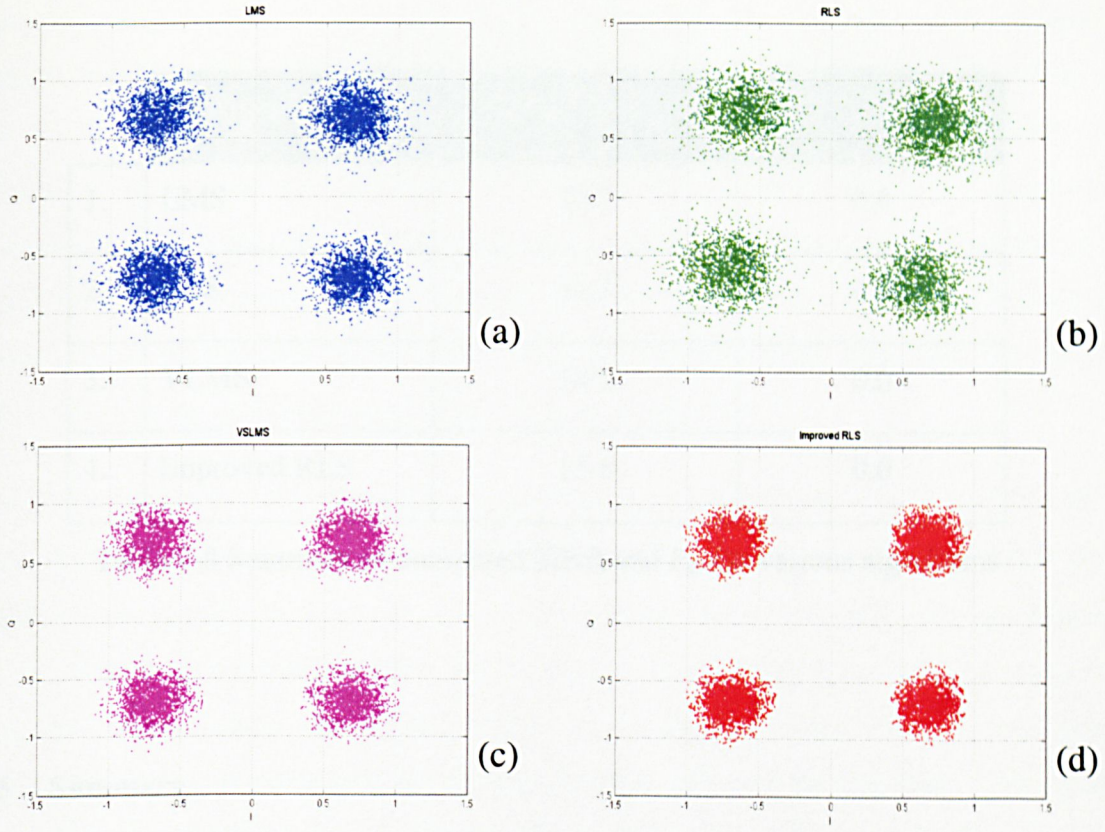

Figure 7-40 Phase constellation plot for (a) LMS (b) RLS (c) VLMS (d) Improved RLS

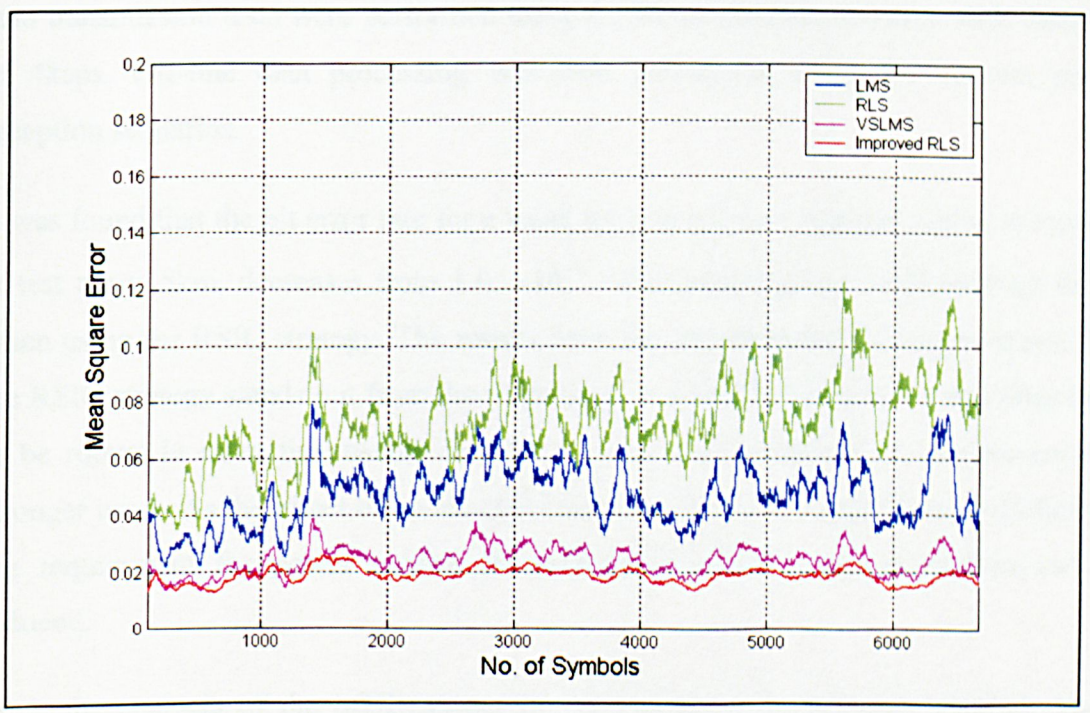

Figure 7-41 MSE plots for the (i) LMS (ii) RLS (iii) VSLMS and iv) Improved RLS algorithms operating in decision directed mode

	Algorithms	SINR (dB)	P_{er}
1.	LMS	13.2	0.0
2.	RLS	11.3	0.0
3.	VLMS	14.5	0.0
4.	Improved RLS	15.6	0.0

Table 7-8 Summary of computed SINR and P_{er} for various algorithms

7.5 Summary

Two field trials were carried out in the North Sea to validate the functionality and performance of the various proposed multi-user detection strategies. Various scenarios of asynchronous power reception were considered and investigated upon. Simultaneous data transmission tests were performed using QPSK modulation scheme, with data rate of 4ksps. Off-line data processing was then performed using the various power reception scenarios.

It was found that the bit error rate for a weak user, in a 3-user unequal power reception, at test range 5km, decreases from 1.05×10^{-1} when adopting the SUD strategy to 0.0 when using the RSIC strategy. The results from the experimental data demonstrate that the RSIC strategy stands out from the other proposed MUD strategies by showing itself to be robust in extracting useful data for a weak user embedded in the presence of stronger users. As the effect of co-channel interference has been significantly mitigated, the requirement for power control in underwater acoustic communication can be reduced.

From the analysis of the MUD strategies, the adaptive PIC receiver structure has a processing load of *(K* x *M)*, *K* and M are the number of users and stages of cancellation respectively. As compared to the PIC structure, the adaptive SIC receiver structure has only a processing load of *M*. Although the adaptive RSIC receiver structure has twice

the processing load, (*2M*), as compared to the SIC structure, it requires a much lower computational load than the PIC structure. The slightly increased design complexity of the RSIC receiver structure at the base-station over the SIC structure, offers the advantage of reduced complexity at the network nodes. However, the computational load of the RSIC structure is still low compared to the PIC structure. The computational load of the RSIC structure can be further reduced by adopting the LMS algorithm which provided a more compact design to the receiver structure, which is an important factor when considering real-time, stand alone implementation.

Although the complexity of adaptive beamforming is much lower than that of the MAI cancellation techniques, however the nulling capability of the beamformer relies very much on the angular position of the interfering user to the intended user and also on having a sufficient number of elements to provide for k-1 solutions. In contrast to the adaptive beamformer, the effectiveness of multistage interference cancellation techniques are not restricted by these constraints but rather on the accuracy of parameter estimation for interference cancellation. The results show that the performance of the adaptive joint spatial-beamforming receiver structure with recursive successive interference cancellation technique offers significant advantages over the other types of multistage interference cancellation technique in an asynchronous "near-far" scenario.

Chapter 8 Summary, Conclusion and Suggestions for Further Work

8.1 Summary

The primary objective in this research work was to develop multi-user detection strategies for a coherent shallow water acoustic network.

Transmission of simultaneous coherent data, as required by a communication network, is hampered by both channel distortion and co-channel interference. Whilst channel distortion occurs as a result of multipath propagation, co-channel interference is due to users sharing the same channel for data transmission. The adaptive decision feedback equalisation receiver structure adopting spatial diversity scheme has been reported to be effective in combating against multipath propagation problem. However, in a shallow water acoustic network, the receiver structure has the added task of suppressing co-channel interference from other users.

Using the principle of the adaptive decision feedback equaliser and single user detection, several novel methods of adaptive multi-user detection strategies namely Parallel Interference Cancellation (PIC), Successive Interference Cancellation (SIC) and Recursive Successive Interference Cancellation (RSIC), were proposed to overcome the effects of co-channel interference. Whilst the multi-user detection strategy based on parallel interference cancellation was deemed effective in an equal power reception, the multi-user detection strategy based on successive interference cancellation was effective in an unequal power scenario. However, these two methods have conversing strengths and weaknesses. Therefore, to circumvent the short falls of the parallel and successive interference cancellation techniques, a multi-user detection strategy based on recursive successive interference cancellation technique was proposed. Based on these adaptive multi-user detection strategies, a software based receiver structure was developed.

The work concluded with the validating of the multi-user detection strategies by considering both equal and unequal asynchronous power receptions with field trials, for ranges up to 5km.

8.2 Conclusions

The effects of the underwater medium, which are detrimental to acoustic telemetry, were highlighted in chapter 2. Although the transmission loss and background noise were the fundamental limitations for an acoustic telemetry system, the effect of multipath propagation due to sea-surface and bottom boundary reflections were considered to be the most serious.

Apart from the effects of multipath propagation in underwater acoustic communication, the other problem facing the system design was that of the co-channel interference by other users sharing the underwater resources. The problem of multiple transmissions arriving simultaneously at the receiver resulting in data packet collision was highlighted in chapter 3. The practical difficulties of implementation of the multiple access techniques were discussed. Although the advantage of the time-division multiple access operation is to ease data packet collision by assigning each user with different transmission and reception time slots. However, this implies that the receiver system has the added operation of acting as a master where system timing has to be established with the individual network nodes in order to ensure correct time slot arrival and framing and to cope with multipath delays. Frequency-division multiple access technique has the advantage of assigning users with different operating frequency bands, thus ensuring that users are orthogonal to each other (with additional guard bands inserted). However, utilising the frequency-division multiple access wastes the already limited underwater channel bandwidth. The advantage of code-division multiple access is its ability to provide protection against narrowband interfering signals, but the result of spreading the signal is a lower data throughput. Therefore, advantages in employing multiple access techniques to help resolve the problem of co-channel interference are offset by the increased demand of the limited channel bandwidth, resulting in poor network efficiency.

The effect of multipath propagation was extended to the analysis of shallow water medium by using a geometrical multipath channel model. The channel model provided an insight to the effects of ISI on the transmitted acoustic signal. While it was anticipated that severe ISI tends to occur at short-range transmissions, signal fading is a predominant issue in long distance transmission.

Adaptive filtering algorithms, which are the driving force for designing an effective adaptive equaliser to resolve the distortion introduced by the channel, were investigated in chapter 4. The performance comparison between supervised and blind adaptive algorithms was accomplished in the chapter, using both simulated and experimental data. From the simulated results using the multipath channel model, the performances between the supervised algorithms were close to each other due to the fact that the algorithms are basically tracking a statistically time-invariant channel. The performance of the blind algorithms were observed to be slightly lagging behind when compared to the supervised algorithms, where their rate of convergence is generally much slower as compared to the supervised algorithms. This is due to the fact that they require a much larger sample size for attaining minima at the error performance surface. In this case, they required almost twice the symbol iterations compared to the supervised algorithms to achieve convergence.

The performance gap between the supervised and blind algorithms widened when tested with experimental data, which had a severe multipath spread. In supervised algorithms, the standard RLS algorithm had a poorer tracking capability over the class of LMS algorithms in a time-variant channel, while the improved RLS (IRLS) algorithm resulted in improved performance in both convergence and tracking when compared to the other supervised algorithms. Although, the classes of LMS algorithms are attractive in real-time operation, the IRLS algorithm is desirable when off-line data analysis is required. Convergence of the blind algorithms cannot be guaranteed as the cost function of the blind algorithms, which operates with a finite length filter and no training sequence is non-convex, thus generating false local minima during the convergence period. The poor rate of convergence of the blind algorithms during the training mode was considered unacceptable to provide a good transient into the decision directed mode.

The design and implementation of three types of novel multi-user detection strategies for co-channel interference cancellation was described in chapter 5. The proposed multi-user strategy based on parallel interference cancellation (PIC), which uses adaptive decision feedback equaliser system as its fundamental building block, estimates and subtracts co-channel interference for all users concurrently. The second type of multi-user detection strategy based on successive interference cancellation (SIC) uses a successive approach towards co-channel interference. The fundamental operation

of the recursive successive interference cancellation (RSIC) is identical to the SIC technique. The unique feature of the RSIC strategy is its ability to loop-back the summed effects of all weak users to the strongest user. By doing so, it allows the strongest user to cancel out the summed effects from other weaker users. Decoding of the weaker users is then performed again for a predefined number of times.

Both the single and multiuser receiver systems were tested in simulation for equal and unequal power reception scenarios. From both scenarios, the multi-user detection strategies had produced added benefits over the single user detection strategy. However, the results achieved by the multi-user strategies exhibited different characteristics. It was observed that the PIC strategy had a better performance over the SIC strategy in an equal power reception. This is due to the fact that the SIC strategy does not take into account any interference cancellation for the stronger user, in this case the first detected user since the received power for both users are equal. Therefore users of equal power reception are demodulated with disparate reliability. The difference in performance between the PIC and SIC strategies had an opposite switch when operating in an unequal power reception. Since the PIC strategy performs interference cancellation for all users concurrently, the weaker user, which is embedded in a strong interferer, will have a lower probability of correctly estimating the data. The novel RSIC strategy coped well in both cases of equal and unequal power reception by successfully extracting useful data for the users. And the RSIC strategy provided the best result when operating in both equal and unequal power receptions. When operating in a 3-user AWGN channel, the RSIC strategy was able to achieve BER performance that is close to the single user bound.

The general organisation of the sea trials for the research project was described in chapter 6. A software based receiver structure which was developed to accommodate the various proposed multi-user detection strategies was also discussed in the chapter.

The performances of the multi-user detection strategies, with adaptive beamforming, were tested with experimental data in chapter 7. Although the complexity of the adaptive joint spatial-beamforming is much lower than that of the MAI cancellation techniques, the nulling capability of the spatial-beamformer relies very much on the angular position of the interfering user to the intended user and also on having a sufficient number of receiver elements to perform beamforming. In contrast to the

adaptive beamformer, the effectiveness of the multistage interference cancellation techniques is not restricted by these constraints but rather on the accuracy of the parameter estimation for interference cancellation. The results show that the performance of the RSIC receiver structure offers advantages over the other types of multistage interference cancellation technique both in an asynchronous equal and unequal power reception scenario, with packet error rate, $P_{er} = 0.0$ at ranges up to 5km.

8.3 Suggestions for Further Work

8.3.1 Further Experimentation

The results obtained from the sea-trials do explain the MAI cancellation capabilities of the proposed multi-user detection strategies. However, more experimental measurements are essential for building up a complete picture of the capabilities of the receiver system. The recording of yet more data of different network configuration would be desirable, especially when the environmental parameters are continuously changing.

8.3.2 Multi User Detection (MUD) Modem

One of the main reasons for choosing QPSK modulation technique was that it offered higher bandwidth efficiency with increased data rate as compared to the BPSK modulation technique.

Both BPSK and QPSK modulation techniques were used during the research work. However, from the results obtained from the sea-trials lead the author to believe that higher modulation techniques may be viable. An approach in reducing the complexity of the receiver structure is to adopt non-coherent detection schemes with DPSK (Differential Phase Shift Keying). However, considerations have to be made for the poorer performance of DPSK receiver systems, which are usually 3dB down from coherent detections. The other modulation schemes that can be considered to increase data rate while maintaining the bandwidth spectral is M-ary Quadrature Amplitude Modulation (QAM). It is believed that M-ary QAM may be embedded in advanced techniques like Discrete Multi Tone (DMT) signalling to further increase data rate,

however, further research work has to be perform to explore novel techniques in using the already bandwidth limited channel.

In this work, spread spectrum techniques (CDMA) were not employed in order to investigate the effectiveness of the MUD strategies. From the results obtained by the proposed MUD strategies, the author believe that more processing gain (co-channel rejection) can be achieved by adopting spread spectrum techniques. However, it is recommended that the spreading ratio is to be consider for, especially when operating in a bandwidth limited channel.

During the implementation of the software-based MUD strategies for asynchronous reception, a buffer-window is required to capture the full data packets for all users so that MAI cancellation can be performed, as shown in Figure 8-1. To implement this in hardware system requires large memory storage, leading to higher system complexity. A possible way to reduce this complexity is to store only the frame synchronising sequences (preamble) signals for all users in the network. Background detection of users arriving asynchronously at the base-station is then performed. Thus, discriminating the need for full data packet buffering.

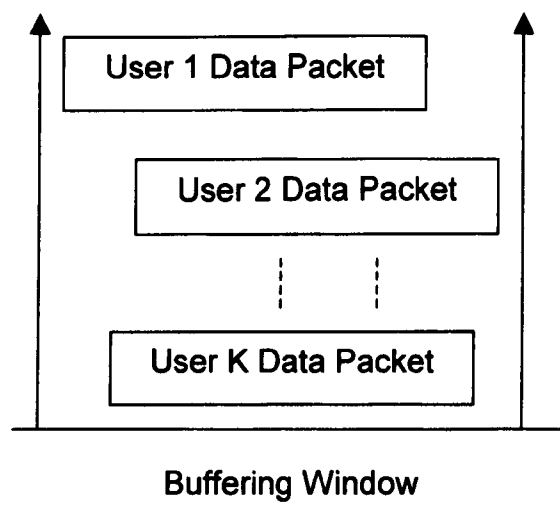

Figure 8-1 Buffering window for data capturing

Appendix

I Near-Field Anomaly Factor for Shallow Water Transmission Loss

Near- Field anomaly, β, in dB [2.21].

Sea-State	0		1		2		3		4		5	
f, kHz	Sand	Mud	Sand	Mud	Sand	Mud	Sand	Mud	Sand	Mud	Sand	Mud
0.1	7.0	6.2	7.0	6.2	7.0	6.2	7.0	6.2	7.0	6.2	7.0	6.2
0.2	6.2	6.1	6.2	6.1	6.2	6.1	6.2	6.1	6.2	6.0	6.2	6.0
0.4	6.1	5.8	6.1	5.8	6.1	5.8	6.1	5.8	6.1	5.8	4.7	4.5
0.8	6.0	5.7	6.0	5.6	5.9	5.6	5.3	5.0	4.3	3.9	3.9	3.6
1.0	6.0	5.6	5.9	5.5	5.7	5.3	4.6	4.2	4.1	3.7	3.8	3.4
2.0	5.8	5.4	5.3	4.9	4.2	3.8	3.8	3.4	3.5	3.1	3.1	2.8
4.0	5.7	5.1	3.9	3.5	3.6	3.1	3.2	2.8	2.9	2.4	2.6	2.2
8.0	4.3	3.8	3.3	2.8	2.9	2.5	2.6	2.2	2.3	1.9	2.1	1.7
10.0	3.9	3.4	3.1	2.6	2.7	2.2	2.4	2.0	2.2	1.7	2.0	1.6

II Attenuation Coefficient for Shallow Water Transmission Loss

Attenuation coefficient, α_T, in dB [2.21].

Sea-State	0		1		2		3		4		5	
f, kHz	Sand	Mud	Sand	Mud	Sand	Mud	Sand	Mud	Sand	Mud	Sand	Mud
0.1	1.0	1.3	1.0	1.3	1.0	1.3	1.0	1.3	1.0	1.3	1.0	1.3
0.2	1.3	1.7	1.3	1.7	1.3	1.7	1.3	1.7	1.3	1.7	1.4	1.7
0.4	1.6	2.2	1.6	2.2	1.6	2.2	1.6	2.2	1.7	2.4	2.2	3.0
0.8	1.8	2.5	1.8	2.5	1.9	2.6	2.2	3.0	2.4	3.8	2.9	4.0
1.0	1.8	2.7	1.9	2.7	2.1	2.9	2.6	3.7	2.9	4.1	3.1	4.3
2.0	2.0	3.0	2.4	3.5	3.1	4.4	3.3	4.7	3.5	5.0	3.7	5.2
4.0	2.3	3.6	3.5	5.2	3.7	5.5	3.9	5.8	4.1	6.2	4.3	6.4
8.0	3.6	5.3	4.3	6.3	4.5	6.7	4.7	6.9	5.0	7.3	5.1	7.5
10.0	4.0	5.9	4.5	6.8	4.8	7.2	5.0	7.5	5.2	7.8	5.3	8.0

III Pseudorandom Sequences

The maximal-length (ML) sequences have several randomness properties that made them attractive in communication applications.

- **Property 1**: ML sequences has $0.5(N+1) = 2^{n-1}$ ones and $2^{n-1} - 1$ zeros.

- **Property 2**: A sliding observation window of length *n* along the output sequence for N shifts, except for all zeros sequence, at each *n*-tuple will appear exactly once.

- **Property 3**: ML sequence with definition for a run as a sequence of identical symbols, there are

  $\Rightarrow$ One run of 1's of length *n*

  $\Rightarrow$ One run of 0's of length *n*-1

  $\Rightarrow$ One run of 1's and one run of 0's of length *n*-2

  $\Rightarrow$ Two runs of 1's and two runs of 0's of length n-3

  $\Rightarrow$ 2^{n-3} runs of 1's and 2^{n-3} runs of 0's of length 1

- **Property 4**: For a periodic autocorrelation defined as

$$\rho_b(r) = \frac{1}{N}\sum_{k=1}^{N} b_k + b_{k+r}$$

The periodic autocorrelation of the ML sequence is

$$\rho_b(r) = \begin{cases} 1 & r = 0,N,2N,... \\ -\dfrac{1}{N} & \text{otherwise} \end{cases}$$

- **Property 5**: The sum of a modulo-2 sequence and any shifted sequence is itself a shifted version of the original sequence

IV JPEG – "Joint Photographic Experts Group" Encoding

With the ongoing research of possible deployment of LAN for underwater acoustic environmental monitoring, it opens up the needs for transmitting and receiving digital images to monitor the underwater environment. However, in a bandwidth-limited channel, the use of high quality images is a barrier to system design. Assuming one byte per pixel, a relatively small image of 320×240 pixels (grey scale) will require a storage space of 76,800 bytes, which is equivalent to 150s of transmission for a BPSK system of data rate 4096 bps and 75s for a QPSK system. Therefore JPEG compression techniques is needed to reduce the size of the image packets. A grey scale compressed image of a picture of "swan" is shown in Appendix Figure 1b with pixel size 70×74, with storage size 1.6 KB, from the original "swan" colour image of 320×240, with storage size 280 KB. Applying a QPSK modulation with symbol rate of 4096sps, the compression had literally reduced the transmission time from ~34.2s to ~1.9s.

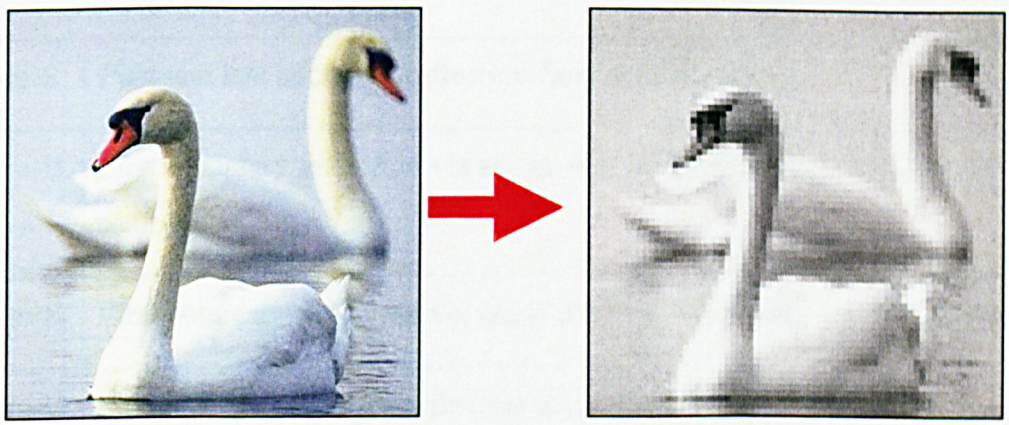

(a) (b)

Appendix Figure 1 (a) Original image 320x240 (b) Compressed image 70x74

V Multipath Channel Model

The transmitted signal can be classified into the direct path signal, *DD*, and multi-path components which can be grouped into four types, as illustrated in Appendix Table 1. The reflection characteristics at the boundaries depend on the Rayleigh parameter [3.15], given by

$$R = \frac{2\pi f_c}{c}\sigma.\sin(\varphi) \qquad \text{Eqn. (1)}$$

where f_c, σ and φ is the operating frequency, r.m.s. crest to trough surface wave-height and the acoustic ray grazing angle. The relationship between the wind speed, ω, and σ for a fully developed sea has been derived by [3.16] which is given by

$$\sigma = (3.6576 \times 10^{-3})\omega^2 \qquad \text{Eqn. (2)}$$

S-to-S	First and last boundary reflection from the sea-surface
S-to-B	First boundary reflection via sea surface and last boundary reflection via sea-bed
B-to-S	First boundary reflection via sea-bed and last boundary via sea surface
B-to-B	First and last boundary reflection from the sea-bed

Appendix Table 1 Notations of multipath signals

In the case where the Rayleigh parameter, $R << 1$, the surface is primarily a reflector and produces a coherent reflection at the specular angle equal to the angle of incidence. When $R >> 1$, the surface acts as a scatterer, sending incoherent energy in all directions. The condition that has been used for the coherent specular reflection is given by [3.16]

$$\lambda > 8H\sin(\varphi) \qquad \text{Eqn. (3)}$$

where H is the height between the crest and trough of the roughness feature. Assuming sinusoidal waves, the peak-to-peak amplitudes H is related to its r.m.s. values

$$H = 2\sqrt{\frac{2}{3.\sigma}} \qquad \text{Eqn. (4)}$$

The computation of the length of signal paths and delay time of the channel model in Figure 3-14 can be visualised using the Lloyds mirror effect [3.17].

a) Angle of Arrival

Using basic trigonometric properties, the angle of arrival of the acoustic ray at the receiver is given by

$$\psi = k\tan^{-1}\left(\frac{B}{L}\right) \qquad \text{Eqn. (5)}$$

where *k* is a constant denoting the angle of arrival, B and L are the signal components with multipath order, n, and distance given in Appendix Table 2.

1.	$B = D_r - D_a$	$k = -1$	DD
2.	$B = 2nh\text{-}D_r\text{-}D_a$	$k = 1$	S-to-S_n
3.	$B = 2nh + D_r\text{-}D_a$	$k = -1$	S-to-B_n
4.	$B = 2nh\text{-}D_r + D_a$	$k = 1$	B-to-S_n
5.	$B = 2(n\text{-}1)h + D_r + D_a$	$k = -1$	B-to-B_n

Appendix Table 2 Path length of the direct and multipath component

b) Delayed Time of Arrival

The distance length of each signal path shown in Figure 3-14 of chapter 3 can be expressed as

$$\sqrt{L^2 + B^2} \qquad \text{Eqn. (6)}$$

Using a shallow channel ratio, $(L/h) >> 2n+1$, and the signal components of Appendix Table 2, Eqn. (6) can be expanded by binomial expansion. The multipath signals can be expressed in the form given in Appendix Table 3,

1.	$DD \cong \left[L + \frac{1}{2L}(D_r - D_a)^2 \right]$
2.	$S\text{-to-}S_n \cong \left[L + \frac{1}{2L}(2nh - D_r - D_a)^2 \right]$
3.	$S\text{-to-}B_n \cong \left[L + \frac{1}{2L}(2nh + D_r - D_a)^2 \right]$
4.	$B\text{-to-}S_n \cong \left[L + \frac{1}{2L}(2nh\text{-}D_r + D_a)^2 \right]$
5.	$B\text{-to-}B_n \cong \left[L + \frac{1}{2L}(2(n\text{-}1)h + D_r + D_a)^2 \right]$

Appendix Table 3 Path length distance of the direct and multipath components

Therefore the delayed time of arrival, τ, that is the relationship between the direct path and its multipath components can be expressed as

$$\tau = t_d - t_{DD} = \frac{D_d - DD}{c} \qquad \text{Eqn. (7)}$$

where t_d, D_d, t_{DD}, DD are the time of arrival and distance of propagation of the multipath and direct path components respectively and c is the sound speed. Hence, the delayed time of arrival for the various multipath components can be calculated and expressed in Appendix Table 4.

1.	$\tau_{S\text{-to-}S_n} \cong \frac{2}{Lc}\left[n^2h^2 - nh(D_r + D_a) + D_rD_a\right]$
2.	$\tau_{S\text{-to-}B_n} \cong \frac{2}{Lc}\left[n^2h^2 + nh(D_r - D_a)\right]$
3.	$\tau_{B\text{-to-}S_n} \cong \frac{2}{Lc}\left[n^2h^2 + nh(D_a - D_r)\right]$
4.	$\tau_{B\text{-to-}B_n} \cong \frac{2}{Lc}\left[(n-1)^2h^2 + (n-1)h(D_r + D_a) + D_aD_r\right]$

Appendix Table 4 Relationship between the direct path and multipath time of arrival

c) Amplitudes of arrived signals

The transmitted acoustic pressure decrease from boundary reflections can be determined by the complex surface or bottom pressure reflection coefficient, $\bar{r}_s$ and $\bar{r}_b$, respectively. Generally, the boundary reflections are dependent on the grazing angle of the acoustical transmission, and therefore on the order of the multipath. The surface

reflection coefficient proposed by Coates [3.18], using the Bechmann-Spezzichino model [3.19], was given as

$$\left|\bar{r}_S\right| = \sqrt{\frac{1+\left(\frac{f_c}{f_a}\right)^2}{1+\left(\frac{f_c}{f_b}\right)^2}} \qquad \text{Eqn. (8)}$$

where

$$f_a = f_b\sqrt{10} \qquad \text{Eqn. (9)}$$

and

$$f_b = 378w^{-2} \qquad \text{Eqn. (10)}$$

where f_c and w is the carrier frequency, in kHz, and the wind speed, in knots.

Considering that the boundary reflection of the transmitted signal at the sea surface causes a phase shift of π, the complex surface pressure reflection coefficient is expressed as

$$\bar{r}_S = -\left|\bar{r}_S\right| \qquad \text{Eqn. (11)}$$

The bottom reflection coefficient proposed by [3.14] observed that for carrier frequency, $f_c < 50\text{kHz}$, with grazing angle, $\varphi < 5^\circ$ and bottom porosity less than 0.5, the magnitude of the bottom pressure reflection coefficient, $\bar{r}_b$, was approximately unity. Therefore, it was assumed that the phase shift due to the bottom boundary reflection is π. The combined pressure loss due to repeated boundary reflections, n order, for each of the multi-path signal component can be expressed as

1.	$R_{S\_to\_S_n} \cong -\left\|\bar{r}s\right\|^n$
2.	$R_{S\_to\_B_n} \cong \left\|\bar{r}s\right\|^n$
3.	$R_{B\_to\_S_n} \cong \left\|\bar{r}s\right\|^n$
4.	$R_{B\_to\_B_n} \cong -\left\|\bar{r}s\right\|^{n-1}$

Appendix Table 5 Pressure loss for the boundary reflections

The received signal of (3.22) of chapter 3 constructed in terms of the summation of the image signal can then be expressed as

$$x_b(t) = \frac{e^{jw(t-t_{DD})}}{DD} + \sum_{n=1}^{\infty}\left[\frac{R_{S-to-S_n}}{S-to-S_n}e^{jw(t-t_{S-to-S_n})} + \frac{R_{S-to-B_n}}{S\text{-}to\text{-}B_n}e^{jw(t-t_{S-to-B_n})}\right.$$

$$\left. + \frac{R_{B-to-S_n}}{B\text{-}to\text{-}S_n}e^{jw(t-t_{B-to-S_n})} + \frac{R_{B-to-B_n}}{B\text{-}to\text{-}B_n}e^{jw(t-t_{B-to-S_n})}\right] \qquad \text{Eqn. (12)}$$

The received signal nomalised by the direct path can be simplified as

$$x_b(t) = 1 + \sum_{n=1}^{\infty}\left[a_{S-to-S_n}e^{-\tau_{S-to-S_n}} + a_{S-to-B_n}e^{-\tau_{S-to-B_n}}\right.$$

$$\left. + a_{B-to-S_n}e^{-\tau_{B-to-S_n}} + a_{B-to-B_n}e^{-\tau_{B-to-S_n}}\right\} \qquad \text{Eqn. (13)}$$

where τ_{S-to-S_n}, τ_{S-to-B_n}, τ_{B-to-S_n}, τ_{B-to-B_n} are the delayed time of arrivals for the multipath components and a_{S-to-S_n}, a_{S-to-B_n}, a_{B-to-S_n}, a_{B-to-B_n} are the normalised amplitude of the multipath components.

VI Optimised parameters values for a simulated channel model at 2000m

Appendix Figure 2 shows the BER performance of the DFE for various tap length selection where n/m represents the forward and feedback tap length respectively. The f_n / f_m values from simulation of Appendix Figure 3 to Figure 6, represents the forward and feedback parameters values respectively.

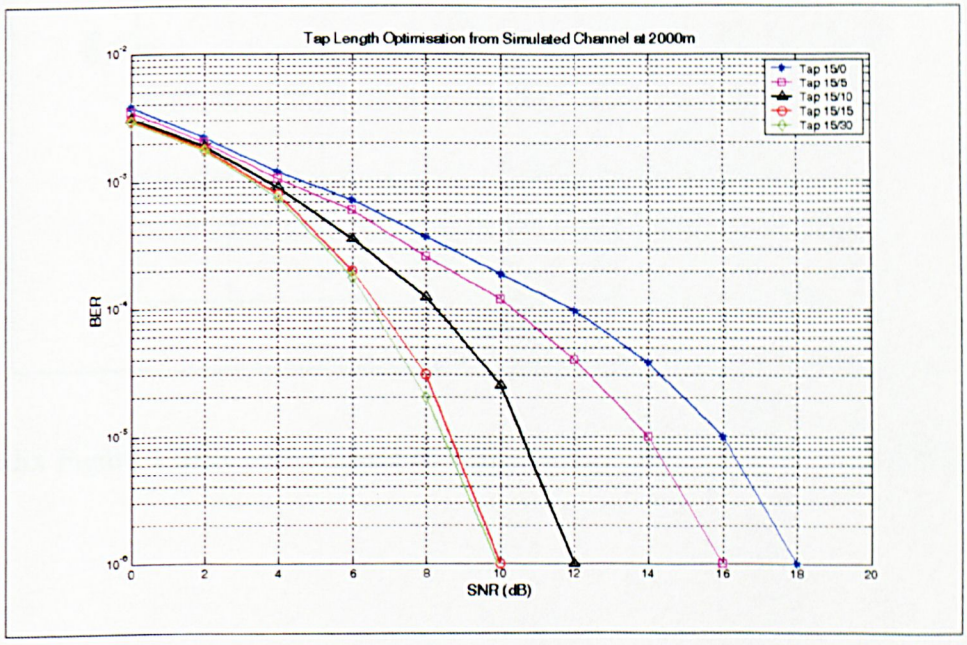

Appendix Figure 2 BER performance for various tap length selection vs. SNR

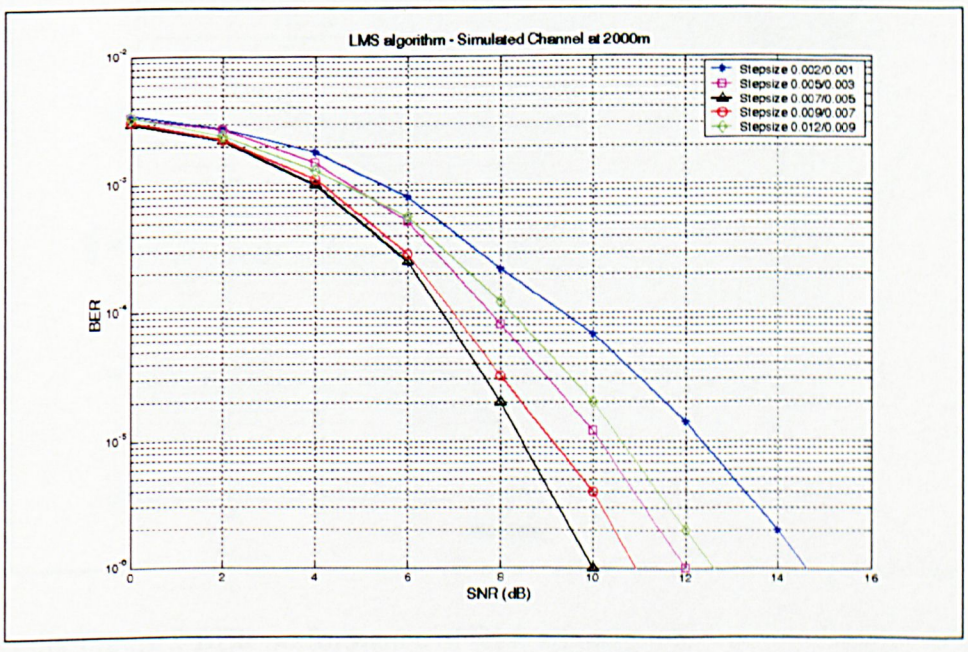

Appendix Figure 3 BER performance of LMS algorithm for various step-sizes values

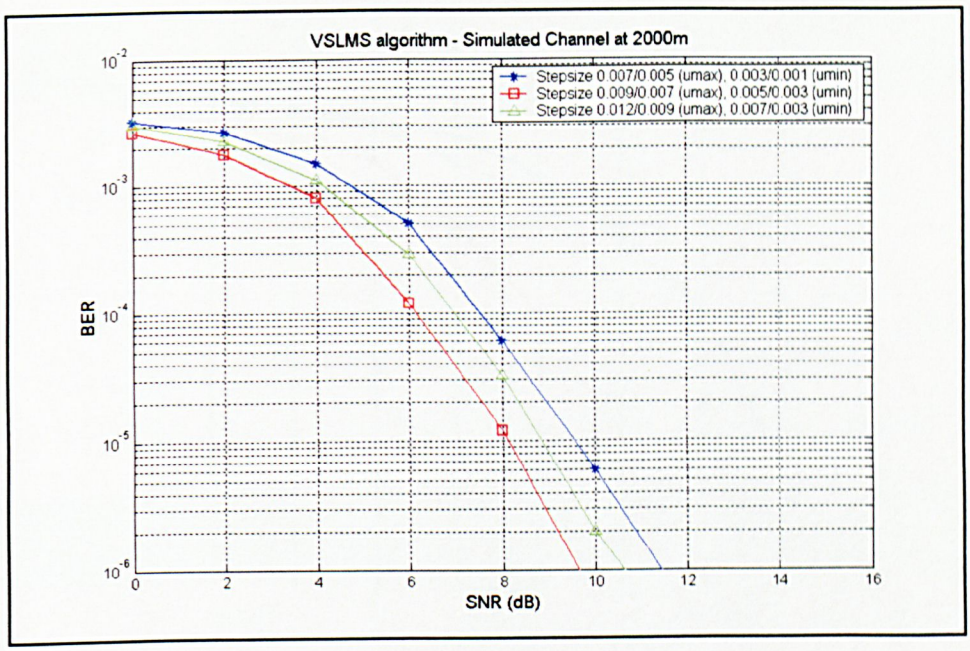

Appendix Figure 4 BER performance of VSLMS algorithm for various step-sizes values

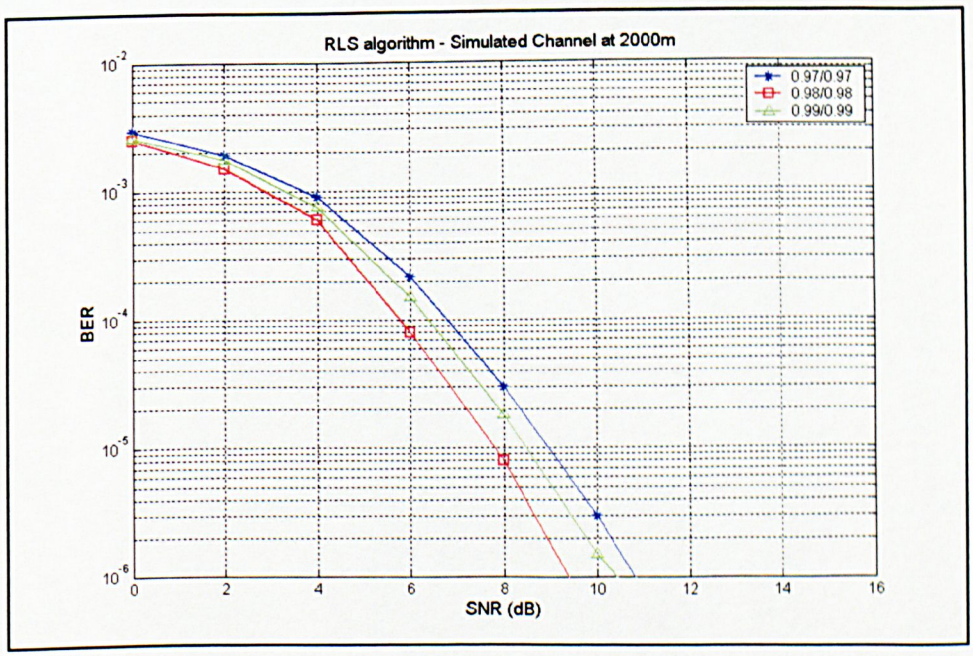

Appendix Figure 5 BER performance of RLS algorithm for various forgetting values

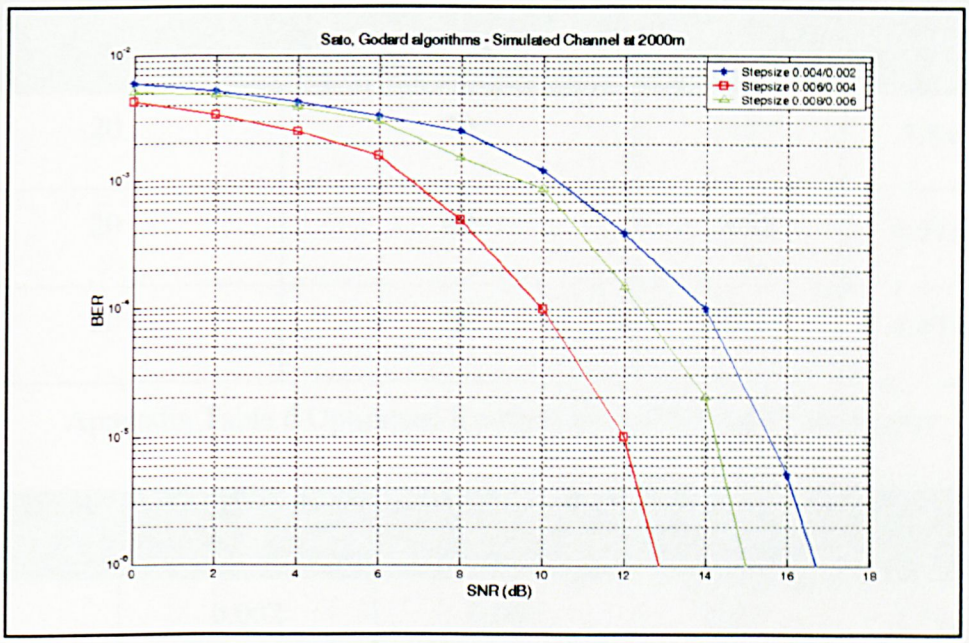

Appendix Figure 6 BER performance of Sato algorithm for various forgetting values

VII Optimised parameters values for a experimental channel at 1800m

Forward Tap Length	Feedback Tap Length	SINR (dB)	P_{er}
20	30	9.2	7.8×10^{-4}
20	40	10.01	4.57×10^{-4}
20	50	10.2	4.47×10^{-4}

Appendix Table 6 Optimised feedforward and feedback tap lengths

Algorithms	Forward	Feedback	SINR (dB)	P_{er}
LMS	0.002	0.001	8.35	2.19×10^{-3}
	0.005	0.003	10.48	7.32×10^{-4}
	0.007	0.005	10.51	7.39×10^{-4}
VSLMS (max/min)	0.005/0.003	0.003/0.001	9.21	1.15×10^{-3}
	0.007/0.003	0.005/0.001	11.65	2.44×10^{-4}
	0.009/0.005	0.007/0.003	11.71	2.47×10^{-4}
RLS class	0.97	0.97	7.91	2.14×10^{-2}
	0.98	0.98	9.20	3.42×10^{-3}
	0.99	0.99	9.41	3.48×10^{-3}
Blind	0.0015	0.001	4.20	5.9×10^{-1}
	0.004	0.002	7.65	1.36×10^{-2}
	0.006	0.004	7.83	1.61×10^{-2}

Appendix Table 7 Optimised feedforward and feedback values

VIII Optimised parameters for a simulated 2-user equal power reception

Appendix Figure 7 shows the BER performance for a single user bound for equal power reception for various tap length selection where n/m represents the forward and feedback tap length respectively. The f_n / f_m values from simulation of Appendix Figure 8, represents the forward and feedback parameter values respectively.

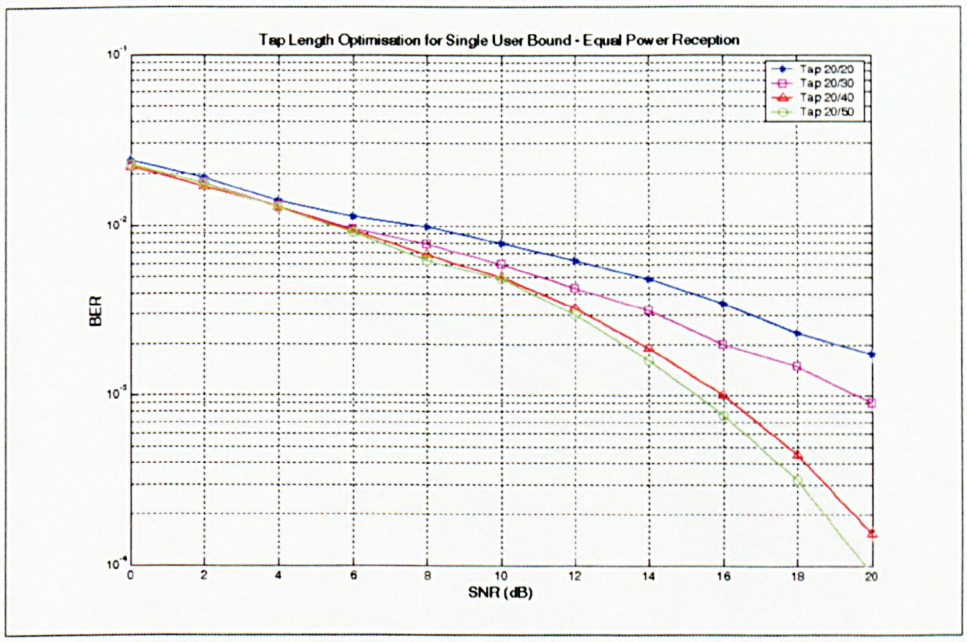

Appendix Figure 7 BER performance for various tap length selection vs. SNR

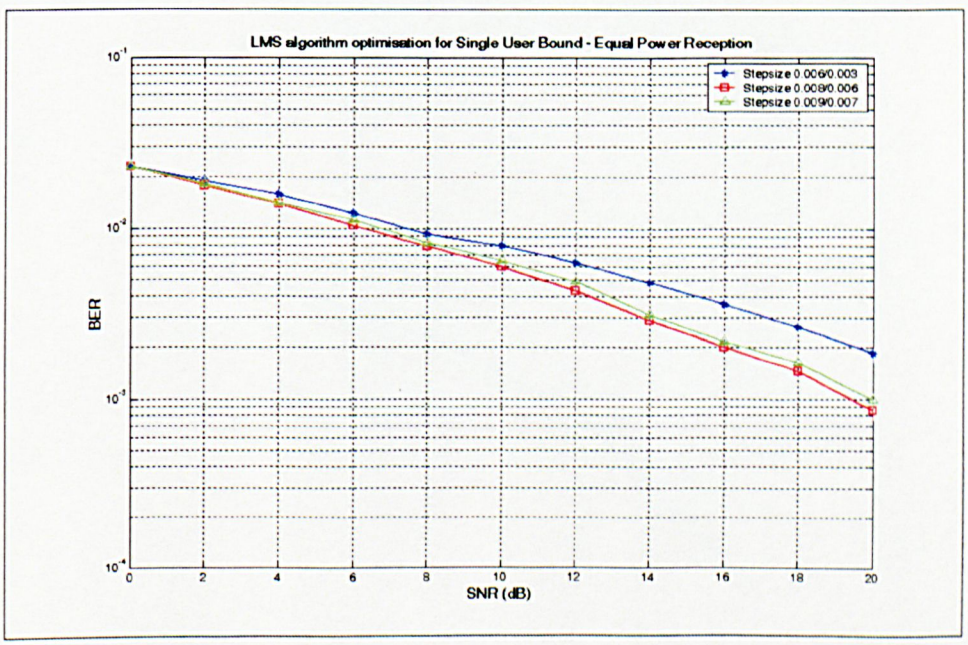

Appendix Figure 8 BER performance of LMS algorithm for various step-sizes values

IX Optimised parameters for a simulated 2-user unequal power reception

Appendix Figure 9 shows the BER performance for a single user bound for unequal power reception for various tap length selection where n/m represents the forward and feedback tap length respectively. The f_n / f_m values from simulation of Appendix Figure 10, represents the forward and feedback parameter values respectively.

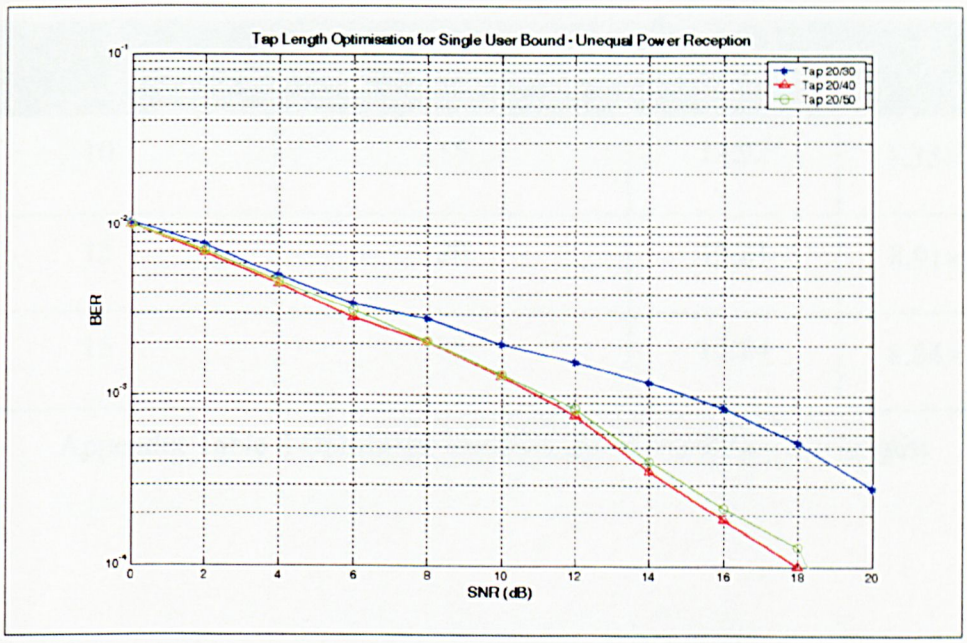

Appendix Figure 9 BER performance for various tap length selection vs. SNR

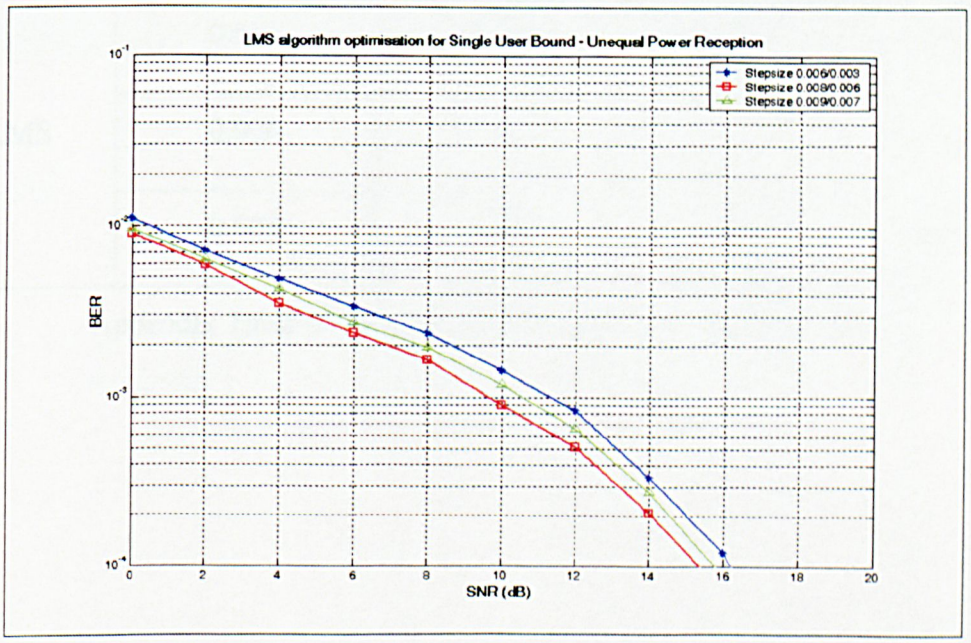

Appendix Figure 10 BER performance of LMS algorithm for various step-sizes values

X Optimised parameters for a experimental 2-user equal power reception

Appendix Table 8 and 9 illustrated the optimisation of different taps length and stepsize values respectively for a 2-user experimental sea-trial with equal power reception. The optimised values were based on the first detected user in the system.

Forward Tap Length	Feedback Tap Length	SINR (dB)	P_{er}
10	15	13.92	1.35×10^{-3}
15	20	15.21	8.91×10^{-4}
15	25	15.24	8.84×10^{-4}

Appendix Table 8 Optimised feedforward and feedback tap lengths

Algorithms	Forward	Feedback	SINR (dB)	P_{er}
LMS	0.004	0.002	12.95	4.49×10^{-3}
	0.006	0.003	15.17	9.1×10^{-4}
	0.008	0.005	15.26	9×10^{-4}

Appendix Table 9 Optimised feedforward and feedback values

XI Optimised parameters for a experimental 2-user unequal power reception

Appendix Table 10 and 11 illustrated the optimisation of different taps length and stepsize values respectively for a 2-user experimental sea-trial with unequal power reception, where the stronger user arrived before the weaker user during the training mode. The optimised values were based on the strongest user in the system.

Forward Tap Length	Feedback Tap Length	SINR (dB)	P_{er}
20	40	9.28	2.15×10^{-3}
20	65	11.77	7.12×10^{-4}
20	75	12.01	5.83×10^{-4}

Appendix Table 10 Optimised feedforward and feedback tap lengths

Algorithms	Forward	Feedback	SINR (dB)	P_{er}
LMS	0.003	0.001	8.56	5.19×10^{-3}
	0.005	0.002	11.57	7.3×10^{-4}
	0.007	0.004	11.95	8.51×10^{-4}

Appendix Table 11 Optimised feedforward and feedback values

XII Optimised parameters for a experimental 3-user unequal power reception

Appendix Table 12 and 13 illustrated the optimisation of different taps length and stepsize values respectively for a 3-user experimental sea-trial with unequal power reception, where the weaker user arrived before the stronger user during the decision mode. The optimised values were based on the strongest user in the system.

Forward Tap Length	Feedback Tap Length	SINR (dB)	P_{er}
20	30	15.89	0.0
20	40	17.83	0.0
20	50	18.12	0.0

Appendix Table 12 Optimised feedforward and feedback tap lengths

Algorithms	Forward	Feedback	SINR (dB)	P_{er}
LMS	0.003	0.001	14.96	0.0
	0.006	0.004	17.73	0.0
	0.007	0.004	18.02	0.0

Appendix Table 13 Optimised feedforward and feedback values

List of References

References for Chapter 1

[1.1] R. Conot, "*Thomas A. Edison: A Streak of Luck*," Da Capo, New York, 1979.

[1.2] Shallow Water Acoustic Network, MAST-III project web page: http://www.mclink.it/com/swan/.

[1.3] I. Dyer, M. J. Crocker, "*Handbook of Acoustic*," 1st Edition, John Wiley & Sons, 1998, Chapter 30, pg. 339-344.

[1.4] MacCurdy, E. "*The Notebooks of Leonardo da Vinci*," Garden City, N. Y., Garden Publishing Co. Inc, 1942, Chapter X.

[1.5] "*Sound*," The New Encyclopaedia Britannica, vol. 17, Chicago: Encyclopaedia Britannica, pg. 19, 1974.

[1.6] Strutt, John W. (Lord Rayleigh), "*Theory of Sound*," vols. I and II, MacGraw Hill, New York, Chapter 1, 1967.

[1.7] William S. Burdic, "*Underwater Acoustic System Analysis*," 2nd Edition, Prentice Hall, Englewood Cliffs, 1991.

[1.8] Robert J. Urick, "*Principles of underwater sound*," 3rd Edition, McGraw Hill, 1983.

[1.9] H. O. Berktay, B. Gasey, and C. A. Teer, "*Underwater Communication, Past, Present and Future*," J. Sound Vib., vol. 7, pg. 62-70, 1968.

[1.10] A. Baggeroer, "*Acoustic Telemetry – An Overview*," IEEE Journal of Oceanic Eng., vol. 9, No. 4, pg. 229-235, October 1984.

[1.11] IEEE J. Oceanic Eng., "*Special Issue on Ocean Acoustic Data Telemetry*," vol. 16, no. 1, pp. 1-177, 1991.

[1.12] A. Clark, "*Diver Communication – The Case for Single Sideband*," Underwater System Design, pp. 16-18, 1989.

[1.13] W. Dow, "*A Telemetering Hydrophone*," Deep-Sea Research, vol. 7, pp. 142-147, 1960.

[1.14] P. Hearn, "*Underwater Acoustic Telemetry*," IEEE Trans. Communication Tech., vol. CT-14, pp. 839-843, 1966.

[1.15] F. R. Mackelburg, S. J. Watson, A. Gordon, "*Benthic 4800 bits/second Acoustic Telemetry*," Proc. Oceans, pp. 78-82, 1981.

[1.16] John Proakis, "*Digital Communications*," 3rd Edition, Mcgraw Hill, New York, 1995.

[1.17] J. Catipovic, A. B Baggeroer, K. Von Der Heydt, D. Koelsch, "*Design and Performance Analysis of Digital Acoustic Telemetry Systems for the Short Range Underwater Channel*," IEEE J. Ocean Eng., vol. 9., no. 4, pp. 242-252, 1984.

[1.18] http://www.datasonic.com/products/modems/atm850.htm

[1.19] J. Catipovic, M. Deffenbaugh, L. Freitag and D. Frye, "*An Acoustic Telemetry System for Deep Ocean Mooring Data Acquisition and Control*," Proc. Oceans, Seattle, WA, pp. 887-892, October 1989.

[1.20] S. J. Roberts, "*An Echo Cancellation Technique Applied to an Underwater Acoustic Data Link*," Ph.D Thesis, Department of Electrical and Electronic Engineering, Herriot Watt University, Edinburgh, Scotland, September 1983.

[1.21] G. Sandsmark, "*The Feasibility of Adaptive Equalisation in High Speed Underwater Acoustic Data Transmission*," Ph.D Thesis, NTH, Trondheim, Norway, 1990.

[1.22] A. Kaya and S. Yauchi, "*An Acoustic communication System for Subsea Robot*," Proc. Ocean'89, Seattle, WA, no. 765-770, Oct. 1989.

[1.23] M. Suzuki and T. Sasaki, "*Digital Acoustic Image Transmission System for Deep Sea Research Submersile*," Proc. Ocean'92, Newport, RI, pp. 567-570, Oct 1992.

[1.24] J. Fischer, K. Bennett, S. Reible, J. Cafarella and I. Yao, "*A High Rate, Underwater Acoustic Data Communication Transceiver*," Proc. Ocean'92, Newport, RI, pp. 571-576, Oct. 1992.

[1.25] M. Johnson, D. Herold and J. Catipovic, "*The Design and Performance of a Compact Underwater Acoustic network Node*," Proc. Oceans'94, Brest, France, pp. 467-471, Sept. 1994.

[1.26] M. Stojanovic, J. A. Catipovic and J. G. Proakis, "*Phase Coherent Digital Communications for Underwater Acoustic Channels*," IEEE J. Oceanic Eng., vol. 19, pp. 100-111, Jan. 1994.

[1.27] R. Galvin and R. F. W Coates, "*Analysis of the Performance of An Underwater Acoustic Communication System and Comparison with a Stochastic Model*," Proc. Oceans'94, Brest, France, pp. 478-482, Sept. 1994.

[1.28] G. S. Howe, P. S. D. Tarbit, O. R. Hinton, B. S. Sharif and A. E. Adams, "*Sub-sea Acoustic Remote Communications Utilizing an Adaptive Receiving Beamformer for Multipath suppression*," Proc. Ocean'94, Brest, France, pp. 313-316, Sept. 1994.

[1.29] P. S. D Tarbit, G. Howe, O. R. Hinton, A. E. Adams and B. S. Sharif, "*Development of a Real-Time Adaptive Equaliser for a High-Rate Underwater Acoustic Data Communication Link*," Proc. Oceans'94, Brest, France, pp. 307-312, Sept. 1994.

[1.30] B. S. Sharif, J. Neasham, O. R. Hinton & A. E. Adams. "*A computationally Efficient Doppler Compensation System for Underwater Acoustic Communications*," IEEE J. Oceanic Eng., vol. 25, no.1, January 2000.

[1.31] B. S. Sharif, J. Neasham, O. R. Hinton & A. E. Adams. "*Adaptive Doppler compensation for coherent acoustic communications*," IEE Proc. Radar, Sonar Navigation, Vol. 147(5), Oct 2000.

[1.32] S. Verdu, "*Adaptive Multiuser Detection*," Proc. IEEE 3rd Int. Symp. Spread Spectrum Tech. Applicat., Oulu, Finland, pp. 43-50, July 1994.

[1.33] M. Stojanovic and Z. Zvonar, "*Multichannel Processing of Broadband Multiuser Communication Signals in Shallow Water Acoustic Channels*," IEEE J. Ocean Eng., vol. 12, pp. 156-166, April 1996.

[1.34] Sato Y., "*A Method for Self-Recovering Equalization*," IEEE Trans. on Comms., vol. 23, pp. 679-682, 1975.

[1.35] Godard D., "*Self Recovering Equalization and Camier tracking in Two-Dimensional Data Communication Systems*," IEEE Trans. on Comms., vol 28, pp. 1867-1875, 1980.

[1.36] Simon Haykin, "*Blind Deconvolution*," 1st Edition, Prentice Hall, 1994.

References for Chapter 2

[2.1] J. R. Lovett, "*Merged Seawater Sound Speed Equation*," *Journal Acoustic. Soc. Am.*, vol. 52, pg. 837, 1972.

[2.2] R. J. Urick, "*Principles of Underwater Sound*," 3rd Edition, McGraw Hill, pg. 129, 1983.

[2.3] Lord Rayleigh, "*Theory of Sound*," vol. II, pg. 89- 94, Dover Publications, New York, 1945.

[2.4] Robert J. Urick, "*Sound Propagation in the Sea*," 1st Edition, Peninsula Publishing, Chapter 10, pg. 10-1, 1982.

[2.5] Marsh, H. W., M. Schulkin, and S. G. Kneale, "*Scattering of Underwater Sound by the Sea Surface*," *Journal Acoust. Soc. Am.*, vol. 33, pg. 334-342, 1976.

[2.6] R. Coates, "*An Empirical Formula for Computing the Beckhamn-Spizzichino Surface Reflection Loss Coefficient*," *IEEE Trans. Ferroelectrics Frequency Control*, vol. 35, no. 4, pg. 522-523, 1988.

[2.7] R. B. Patterson, "*Intensity Fluctuation of Direct and Surface Reflected Signals from a Deep Source*," Journal Underwater Acoust., vol. 12, pg. 41, 1962.

[2.8] R. Urick and H. L. Saxton, "*Surface Reflection of Short Supersonic Pulses in the Ocean*," *Journal Acoust. Soc. Am.*, vol. 19, pg. 8, 1947.

[2.9] L. N. Libermann, "*Reflection of Underwater Sound from the Sea surface*," *Journal Acoust. Soc. Am.*, vol. 20, pg. 498, 1948.

[2.10] W. S. Burdic, "*Underwater Acoustic System Analysis*," 2nd Edition, Prentice Hall, Englewood Cliffs, New Jersey, 1984.

[2.11] E. L. Hamilton, "*Compressional Wave Attenuation in Marine Sediments*," GeoPhysics, vol. 37, pg. 620, 1972.

[2.12] R. J. Urick, "*Principles of Underwater Sound*," 3rd Edition, McGraw Hill, pg. 237-287, 1983.

[2.13] R. J. Urick and R. M. Hoover, "*Backscattering of Sound from the Sea Surface*," *Journal Acoust. Soc. Am.*, vol. 28, pg. 1038, 1956.

[2.14] R. P. Chapman and H. H. Harris, "*Surface Backscattering Strengths Measured with Explosive Sound Sources*," *Journal Acoust. Soc. Am.*, vol. 34, pg. 1592, 1962.

[2.15] G. M. Wenz, "*Acoustic Ambient Noise in the Ocean*," *Journal Acoust. Soc. Am.*, vol. 34, pg. 1936-1956, 1962.

[2.16] R. J. Collier, "*Ship Noise*," 1st Edition, Chapter 3, New York, 1974.

[2.17] F. H. Fisher and P. F. Worcester, "*Essential Oceanography*," *Encyclopedia of Acoustics*, Wiley, Chapter 35, 1998.

[2.18] F. Ingenito and S. N. Wolf, "*Site Dependence of Wind-Dominated Ambient Noise in Shallow Water*," *Journal Acoust. Soc. Am.*, vol. 85, pg. 141-145, 1989.

[2.19] R. W. Coates, "*Underwater Acoustic Systems*," 1st Edition, MacMillian Publishing Ltd., U. K., pg. 18, 1990.

[2.20] F. H. Fisher and V. P. Simmons, "*Sound Absorption in Sea Water*," *Journal Acoust. Soc. Am.*, vol. 62, pg. 558-564, 1977.

[2.21] H. W. Marsh and M. Schulkin, "*Shallow Water Transmission*," *Journal Acoust. Soc. Am.*, vol. 35, pg. 542, 1963.

References for Chapter 3

[3.1] Jennifer L. T., Timothy E. T., David B., "*An Efficient Store-and-Forward Protocol for a Shallow-Water Acoustic Local Area Network*," Ocean Proc. of the IEEE, vol. 1, pp. 883-888, 1994.

[3.2] J. Jubin and J.D. Tornow, "*The DARPA packet radio network protocols*," Proc. of the IEEE, vol 75, pp 21-32, January 1994.

[3.3] Marco V. Arbolino, Ing. Claudio Camporeale, "*System Outline Configuration Report*," SWAN Technical Report, March 1998.

[3.4] A. B. Baggeroer, "*Acoustic Telemetry – An Overview*," *IEEE Jornal. Oceanic Eng.*, vol. 9, pp. 229-235, Oct. 1984.

[3.5] Qureshi S. H., "*Adaptive Equalization*," Proc. IEEE, vol. 73, pp. 1349-1387, 1985.

[3.6] Sarwate D. V. and Pursley D. J., "*Crosscorrelation Properties of Pseudorandom and Related Sequences*," Proc. IEEE, vol. 68, pp. 593-619, May 1980.

[3.7] Gold R., "*Optimal Binary Sequences for Spread-Spectrum Multiplexing*," IEEE Trans. Inf. Theory, vol. 13, pp. 619-621, 1967.

[3.8] Gold R., "*maximal Recursive Sequences with 3-valued recursive Cross-Correlation Functions*," IEEE Trans. Inf. Theory, vol. 14, pp. 154-156, 1968.

[3.9] Simon Haykin, "*Analog and Digital Communication*," 1st Edition, Prentice Hall, 1989.

[3.10] Korn I., "*Digital Communications*," Van Nostrand Reinhold Compnay, New York, 1985.

[3.11] Jhong Sam Lee, Leonard E. Miller, "CDMA Engineering Handbook," 1st Edition, Artech House Publishers, 1998.

[3.12] John G. Proakis, "*Digital Communication*," 3rd Edition, 1995.

[3.13] Lindsey W. C. and Simon M. K., "*Telecommunication Systems Engineering*," Prentice Hall, Englewood Cliffs, 1973.

[3.14] Adam Zelinski, Young Hoon Yoon, Lixue Wu, "*Performance Analysis of Digital Communication in a Shallow Water Channel*," IEEE J. of Oceanic Eng., vol. 20, no. 4, October 1995.

[3.15] R. J. Urick, "*Principles of Underwater Sound*," 3rd Edition, McGraw Hill, New York, pp. 129, 1983.

[3.16] W. S. Burdic, "*Underwater Acoustic System Analysis*," 2nd Edition, Prentice Hall, New York, pp. 121, 1991.

[3.17] L. M. Brekhovskikh, "*Waves in Layered Media*," 1st Edition, Academic Press, New York, pp. 325-331, 1960.

[3.18] R. Coates, "*An Empirical Formula for computing the Beckmann-Spizzichino Surface Reflection Loss Coefficient*," IEEE Trans. Ultrason. Ferroelec. Frequency Control, vol. 35, no. 4, pp. 522-523, July 1988.

[3.19] R. Diamond, "*Extend Users Manual*," Imagine That, San Jose, CA, 1988.

References for Chapter 4

[4.1] Mazo, J. E., "*Analysis of Decision-Directed Equalizer Convergence*," Bell System Tech. J., vol. 59, pp 1857-1876, 1980.

[4.2] H. K. Yeo, B. S. Sharif, O. R. Hinton and A. E. Adams, "An improved RLS algorithm for time-variant underwater acoustic communications," *IEE Electronics Letter*, vol. 36, No. 2, pg. 191-192, 20th January 2000.

[4.3] Simon Haykin, "*Unsupervised Adaptive Algorithms*," 1st Edition, Prentice Hall, New York, 2000.

[4.4] Widrow, B. and M. E. Hoff, Jr., "*Adaptive Switching Circuits*," *IRE WESCON Conv. Rec.*, pt. 4, pg. 96-104, 1960.

[4.5] Luenberger, D. G., "*Optimisation of Vector Space Methods*," Wiley, New York, 1969.

[4.6] John G. Proakis, Dimitris G. Manolakis, "*Digital Signal Processing – Principles, Algorithms, and Applications*," 3rd Edition, Prentice Hall, 1996.

[4.7] B. Farhang Boroujeny, "*Adaptive Filters, Theory and Applications*," 1st Edition, John Wiley & Sons, New York, Chap. 3, 1998.

[4.8] Simon Haykin, "*Adaptive Filters Theory*," 2nd Edition, Prentice Hall, New York, Chap. 5, 1991.

[4.9] Simon Haykin, "*Adaptive Filters Theory*," 3rd Edition, Prentice Hall, New York, Chap. 3, 1996.

[4.10] Widrow, B. and S. D. Stearns, "*Adaptive Signal Processing*," Prentice Hall, Englewood Cliffs, N. J., Chapter 6, 1985.

[4.11] Nitzberg, R., "*Application of the normalized LMS algorithm to MSLC*," *IEEE Trans. Aerospace and Electronic Syst.*, AES-21, no. 1, pg. 79-91, 1985.

[4.12] Goodwin, G. C., and K. S. Sin, "*Adaptive Filtering, Prediction and Control*," 1st Edition, Prentice Hall, Englewood Cliffs, NJ, 1984.

[4.13] Dorny, C. N., "*A Vector Space Approach to Models and Optimisation*," Wiley-Interscience, New York, 1975.

[4.14] Widrow, B. and M. Lehr, "*30 years of Adaptive Neural Networks: Perceptron Madaline, and Backpropagation*," *Proc. IEEE, Special Issue on Neural Network I*, vol. 78, September, 1990.

[4.15] Harris, R. W., D. M. Chabries and F. A. Bishop, "*A Variable Step (VS) adaptive filter algorithm*, " *IEEE Trans. Acoustics, Speech and Signal Process*, ASSP-39, no. 11, pg. 1953-1958, 1986.

[4.16] Matthew, V. J. and Z. Xie, "*A stochastic gradient adaptive filters with gradient adaptive step size*," *IEEE Trans. Signal Process*, SP-41, no. 6, pg. *2075-2087*, 1993.

[4.17] Farhang-Boroujeny, "*Variable Step-Size LMS algorithm: new developments and experiments*, " *IEE Proc. – Vis. Image and Signal Process*, 141, no. 5, pg. 311-317, 1994.

[4.18] Lawrence R. E. and H. Kaufman, "*The Kalman filter for the equalisation of a digital communication channel*," *IEEE Trans. Commun. Technology* vol. COM-19, pg. 11377-1141, 1971.

[4.19] Godard D. N., "*Channel Equalisation using a Kalman filter for fast data transmission*," *IBM J. Res. Dev.*, vol. 18, pp. 267-273, 1974.

[4.20] Geld, A, "*Applied Optimal Estimation*," MIT Press, Cambridge, Mass., 1974.

[4.21] Kailath, T, "*Estimating Filters for Linear Time-Invariant Channels*," Quarterly Progress Rep., MIT Research Lab. for Electronics, Cambridge, Mass. Pp. 185-197, 1960.

[4.22] Peterka V., "*A Square Root filter for real-time multivariate regression*," *Kybernetika*, 11, pg. 53-67, 1975.

[4.23] Verhagen, M. H., "*Round-off error propagation in four generally-applicable, recursive, least-squares estimation schemes*," *Automatica*, vol. 25, pg. 437-444, 1989.

[4.24] Woodbury, M. "*Inverting Modified Matrices*," *Mem. Rep. 42*, Statistical Research Group, Princeton University, Princeton, N. J., 1950.

[4.25] E. Eleftheriou and D. D. Falconer, "*Tracking properties and steady-state performance of the RLS adaptive filter algorithms*," Proc. IEEE Trans. Acoust. Speech, Signal Processing, vol. 34, pp. 1097-1110, 1986.

[4.26] A. Benveniste, "*Design of Adaptive Algorithms for the Tracking of time-varying Systems*," In. J. Adaptive Contr. Signal Processing, vol. 1, pp. 3-29, 1987.

[4.27] E. Eweda, "*Comparison of RLS, LMS and sign Algorithms for Tracking randomly time-varying channels*," IEEE Trans. Signal Processing, vol. 42, pp. 2937-2944, 1994.

[4.28] Sayed A. H. and T. Kailath, "*A state-space approach to adaptive RLS filtering*," *IEEE Signal Processing Mag.*, vol. 11, pg. 18-60, 1994.

[4.29] Simon Haykin, Ali H. Sayed, James R. Zeidler, Paul Yee, Paul C. Wei, "*Adaptive tracking of linear time-variant systems by extended RLS algorithms*," *IEEE Trans. Signal Proc.*, vol. 45, no. 5, pp. 1118-1128, May 1997.

[4.30] Bellini S., "*Bussgang Technique for blind equalisation*," *GLOBECOM*, Houston, Tex, pg. 1634-1640, 1986.

[4.31] Sato Y., "*Two extensional applications of the zero-forcing equalisation method*," *IEEE Trans. Commun.*, vol. COM-23, pg. 684-687, 1975.

[4.32] Godard D. N., "*Self-recovering equalisation and carrier tracking in a two-dimensional data communication system*," *IEEE Trans. Commun.*, vol. COM-28, pg. 1867-1875, 1980.

[4.33] Treichler J. R. and B. G. Agee, "*A New Approach to Multipath Correction of Constant Modulus Signals*," IEEE Trans. Acoust. Speech Signal Process., vol. 31, pp. 459-471, 1983.

[4.34] Benvensite A., P. Priouret, "*Adaptive Algorithms and Stochastic Approximations*," Springer-Verlag, New York, 1987.

[4.35] Austin M. E., "*Decision Feedback Equalization for Digital Communication over Dispersive Channel*," Tech. Rep 437, MIT Lincoln Laboratory, Lexington, Mass, 1967.

[4.36] Field trial, "ESPRC – Centre for Marine & Petroleum Technology", 1st April 1997-31st 1999.

[4.37] Ding Z., "*Blind Channel Identification and Equalization using Spectral Correlation Measurements, Part I: Frequency-domain Approach*," IEEE Press, pp.417-736, New York, 1994.

[4.38] Widrow B, "*Stationary and nonstationary learning characteristics of the LMS adaptive filter*," Pro. IEEE, vol. 64, pp. 1152-1162, 1976.

References for Chapter 5

[5.1] S. Verdu, "*Minimum Probability of Error for Asynchronous Gaussain Multiple Access Channels*," IEEE Trans. Inform. Theory, vol. 32, no. 1, pp. 85-96, 1986.

[5.2] L. E. Franks, "*Carrier and Bit Synchronization in Data Communications: A Tutorial Review*," IEEE Trans. Comms, vol. 28, no. 8, pp. 1107-121, 1980.

[5.3] A. B. Carlson, "*Communication Systems*," McGraw Hill, 1989.

[5.4] John Proakis, "*Digital Communication,*" 3rd Edition, pp. 781, McGraw Hill, Singapore, 1995.

[5.5] B. S. Sharif, Jeff Neasham, A. E. Adams, O. R. Hinton, "*Adaptive Doppler Compensation for Coherent Acoustic Communications*," IEE Proceedings, 2000.

[5.6] M. Stojanovic, L. A. Catipovic and J. G. Proakis, "*Phase Coherernt Digital Communications for Underwater Acoustic Channels*," IEEE J. Oceanic Eng., vol. 19, pp. 100-111, 1994.

[5.7] Barry D. Van Veen and Kevin M. Buckley, "*Beamforming: A Versatile Approach to Spatial Filtering*," IEEE ASSP Magazine, pp. 4-24, April 1988.

[5.8] M. Stojavonic, Zoran Zvonar, "*Multichannel processing of broad-band multiuser communications signals in shallow water acoustic channels*," IEEE Journal of Oceanic Engineering, vol. 21, no. 2, pp. 156, April 1996.

[5.9] M. K. Varanasi and B. Aazhang, "*Multistage Detection in Asynchronous Code-Division Multiple Access Communications*," IEEE Transactions on Communications, vol. 38. No 4, pp. 509-519, April 1990.

[5.10] R. M. Buehrer and B. D. Woerner, "*Analysis of Adaptive Multistage Interference Cancellation for CDMA Using an Improved Gaussian Approximation*," IEEE Trans. on Comms, vol. 44, no. 10, pp. 1308-1321, Oct 1996.

[5.11] R. M. Buehrer and S. P. Nicoloso, "*Comments on "Partial Parallel Interference Cancellation for CDMA"*," IEEE Trans. on Comms, vol. 47, no. 5, pp. 658-661, May 1999.

[5.12] D. Divsalar, M. K. Simon and D. Raphelli, "*Improved Parallel Interference Cancellation*," IEEE Trans. of Comms, vol. 46, pp. 258-268, 1998.

[5.13] N. Correal, R. M. Buehrer and B. D. Woerner, "*A DSP based DS CDMA Multiuser Receiver Based on Partial Interference Cancellation*," IEEE J. of Select. Areas Comm., vol. 17, pp 613-630, April 1999.

[5.14] H. K. Yeo, B. S. Sharif, A. E. Adams and O. R. Hinton, "Performances of Multi-Element Multi-User detection strategies in Shallow Water Acoustic Network (SWAN)", *IEEE Journal of Ocean Engineering*, vol. 26, Issue 4, pg. 604 -611, October 2001.

[5.15] Pulin Patel, Jack Holtzman, "*Analysis of a simple successive interference cancellation scheme in a DS/CDMA system*," IEEE Journal on selected areas in Comms, pp. 798 – 807, June 1994.

[5.16] Y. Cho, J. H. Lee, "*Analysis of an Adaptive SIC for Near-Far Resistant DS-CDMA*," IEEE Transactions on Communications, pp. 1429 – 1433, November 1998.

[5.17] Andrew L. C. Hui and Khaled Ben Letaief, "Successive Interference Cancellation for multiuser asynchronous DS/CDMA detectors in multipath fading links," IEEE Trans. of Communications, vol. 46, no. 3, pp. 384-391, March 1998.

[5.18] A. Duel-Hallen, J. Holtzman and Z. Zvonar, "*Multi-User Detection for CDMA systems*," IEEE Pers. Commun., vol. 2, pp. 46-58, 1995.

[5.19] R. Kohno, "*Combination of an Adaptive Array Antenna and a Canceller of Interference for Direct-Sequence Spread-Spectrum Multiple Access System*," IEEE JSAC, vol. 8, no. 4, pp. 675-682, 1990.

[5.20] H. K. Yeo, B. S. Sharif, A. E. Adams and O. R. Hinton, "Multi-user Detection for a Time-Variant Multipath Environment," IEEE Proceedings of the 2000 International Symposium for Underwater Technology, Tokyo, Japan, pp. 399-404, May 2000.

[5.21] H. K. Yeo, B. S. Sharif, A. E. Adams and O. R. Hinton, "Implementation of Multi-user Detection Strategies for Coherent Underwater Acoustic Communication", *IEEE Journal of Ocean Engineering,* vol. 27, Issue 1, pg. 17-27, January 2002.

References for Chapter 6

[6.1] Marco V. Arbolino, Claudio Camporeale, Otello Gasparini, "*Preliminary Contributions on the Hardware for the SWAN Sea-Trials*," SWAN Technical Note, June 1998.

[6.2] Machteld de Kroon, "*Report Specification and Planning First Sea Trial*," SWAN Technical Note, December 1998.

[6.3] Machteld de Kroon, "*Report Specification and Planning Second Sea Trial*," SWAN Technical Note, December 1999.

[6.4] H. K. Yeo, "Technical Report for DQC Signal Characterization", SWAN Technical Note, March 1999.

[6.5] H. K. Yeo, "Technical Report for DQC Signal Characterization", SWAN Technical Note, March 2000.

[6.6] H. K. Yeo, " *Technical Report "Signal for Transmission"*," SWAN Technical Note, April 1999.

[6.7] H. K. Yeo, " *Technical Note by UNC for "Signal for Transmission"*," SWAN Technical Note, April 2000.

[6.8] H. K. Yeo, "Signal Processing Expert Guide", SWAN Technical Note, June 2000.